EUROPEAN COMMISSION

Community Research

MATISSE

Materials' Innovations for Safe and Sustainable nuclear in Europe

Support to the development of joint research actions between national programmes on advanced nuclear materials

FP7-Fission-2013
Combination of Collaborative project (CP) and Coordination and Support Actions (CSA)

Grant agreement no: 604862
Start date: 01/11/2013 Duration: 48 Months

D.5.21

Summary Report "Functional coatings and modified surface layersNumber of the deliverable"

MatISSE – Contract Number: 604862

Document title	Summary Report "Functional coatings and modified surface layers"
Main Author(s)	Alfons Weisenburger (KIT), Adrian Jianu (KIT), Peter Skalaloz (KTH), Marco Utili (ENEA), Espedito Vassallo (CNR), Enrica Ricci (CNR), Vasile Radu (RATEN, ICN), Fosca Di Gabriele (CVR), Cornelia Heintze (HZDR), Yong Dai (PSI)
Number of pages	138
Document type	Deliverable
Work Package	5
Document number	5.21
Issued by	Karlsruhe Institute of Technology
Date of completion	19/12/2017
Dissemination level	Confidential, only for consortium members (including the Commission Services)

Summary

The collected information describes the work of several partners in Task 5.2 of the MATISSE project and within the SAFE_COAT pilot project of EERA-JPNM. KTH and KIT further developed the composition of FeCrAl+RE alloys to optimize their behaviour in Pb-alloys aiming a corrosion resistant material for the temperature range Pb-alloy cooled nuclear reactors require. While KTH target bulk FeCrAl-RE alloys that require specific attention on formation of brittle sigma phases (Cr-content needs to be around 10wt%), the KIT approach to use an corrosion optimized FeCrAl+RE composition as base for surface alloying allows a wider range of compositions. Both explored the optimum composition that allows the formation of protective Al-rich oxide scales in Pb-alloys between 400 and 600°C at least. Avoiding the formation of Cr-carbides by controlling the C content and the ratio between RE like Ti and Zr e.g. and C is one of the key issues for the formation of protective Al-rich scales. 10wt% Cr and 4 wt% Al, given that the RE and C concentrations are strictly controlled and optimized are the values to be respected. These results show that it is feasible to design ductile alumina-forming FeCrAl alloys as construction materials in corrosive environments at temperatures as low as 450°C. For Fe-Cr-Al-based alloys and modified surface layers exposed to molten lead with 10^{-6} wt.% oxygen in the 400-600°C temperature range an experimental criterion was defined concerning the aluminium and chromium content necessary to form a highly protective Al_2O_3 layer. It was found that higher Cr content leads to alumina formation at lower Al concentration. Outside this alumina stability domain, a concentration of 4 wt.% Al is sufficient, in synergy with 16 wt.% Cr content, to reduce drastically the growth rate of $Fe(Cr,Al)_2O_4$ sub-layer with spinel structure, on Fe-Cr-Al alloys exposed to oxygen-containing molten lead.

Two FeCrAl bulk tensile specimens were tested in PbBi and at both the fracture was fully ductile. That means that the potential problem with sigma formation was avoided. Beside ductile dimples, there were plate-like features that were connected with the specific fracture along the hot rolling direction. The surface of the specimens, where no cracks were detected, showed initiation of degradation, which might be due to the very low oxygen content that does not foster the formation of protective Al-rich oxide sales. Further tests especially with more material are required to address all open points in that development.

AlTiN coatings on T91 were tested in PbBi under harsh tensile load conditions (up to 550MPa) and exhibit almost no delamination. However, all the coatings cracked and the cracks usually stopped at the coating bulk interface. Only in notched areas crack formation in the bulk T91 was observed. The extreme high loads applied and the testing procedure does not allow to conclude on the allowable stress respectively strain until the coating starts cracking. Less severe stress

levels or alternative testing procedure are required to explore the coatings further. Anyhow the non-delamination is a very promising results for such applied coatings.

The Detonation Gun process was investigated and optimized to coat 316 stainless steel plates and small tensile specimens. Especially the coating of small scaled substrates and the application of relatively thin (some tens of µm tick only) coatings was one of the major efforts and results of this exercise. Such coated specimens of 316L were loaded in air and PbBi at 550°C and showed that the coating was resistant. No delamination occurred, nor penetration of PbBi was observed, which both clearly shows the potential of this coating technology that requires further investigations.

The tensile tests of the 316L surface alloyed specimens showed in pre- and post investigation the missing of Al in the surface region. Knowing that at least 4wt% Al is required for protective scale formation, the results obtained in the tensile tests reflect the behaviour of uncoated 316L. Tests with proper surface alloyed steels having the required Al-content are required for meaningful and successful tensile test in liquid PbBi.

Tensile tests of surface alloyed T91 performed at RATEN clearly show the benefit of surface alloying. At the just coated side exfoliation at large strains is observed while the surface alloyed layer do not show such inappropriate behaviour. Slow strain tensile tests of 316l with an Al2O3 coating deposited by a detonation gun (ENEA) exhibit fully ductile behaviour of the bulk 316L while the coating did not show any delamination during the test.

Detailed TEM post investigations of surface alloyed FeCrAl coatings on T91 that were irradiated in contact with PbBi at 300°C with 72MeV protons to a dose of 2.5dpa were performed. Different precipitates (Al, Y, oxygen rich and Cr rich) were found throughout the surface alloyed layer varying in size, morphology and composition. This variation is attributed to the different cooling rates achieved at the surface alloying process. The hardening observed due to the irradiation can not be attributed to this precipitates, but is expected to originate like for other ferritic materials in the defect structure of such materials. Fe irradiation done at HZDR at 300 and 450 °C and significant hardening is observed for all alloys at 300°C and 450°C. The combined effects of the Al mediated shift of the Cr solubility limit and potentially Cr content dependent partial suppressing of α'-phase precipitation by the implanted ions are considered as the main reasons for the variation of hardening observed for the different alloys. A significant contribution of impurity clusters to the observed hardening is expected.

Alumina forming alloys and surface layers and insoluble coatings are promising corrosion mitigation methods that showed their potential in this research. However, aspects like stress tolerance, delamination, irradiation stability are issues that require further attention. The investigations in this work are starting points that need to be continued to understand in detail the potential benefits and continue from such knowledge the optimization and the required scale up. Additional topics to be addressed are reliability, reproducibility and optimization that finally must end in a kind of standardization.

Approval

Rev.	Date	First author	WP leader	Project Coordinator
1	Nov. 2017	A. Weisenburger, KIT	K-F. Nilsson, JRC	P.F. Giroux, CEA
		24.11.17	04.12.2017	19.12.2017

Distribution list

Name	Organisation	Comments
All beneficiaries	MatISSE	

Table of contents

1 Introduction

Steel corrosion in liquid Pb-alloys

Compatibility of materials with Pb is mainly driven by the temperature dependant solubility of the alloying elements in the liquid Pb. Ni, Mn, Al and Si have substantial solubility of up to some wt% at 550°C as shown in Figure 1[1]. The main elements of steel, Fe and Cr, are less soluble but still some 10^{-5}wt% can't be neglected. Practically insoluble are refractory alloys like W, Mo and Ta and most ceramics. Therefore Ni containing metals like austenitic steels suffer more from dissolution attack than Ni free f/m steels like T91. However, mechanical tests performed in liquid Pb-alloy exhibit the susceptibility of f/m steels to LME [8, 9]. Therefore, f/m steels are beside their improved corrosion resistance and higher irradiation stability not considered any longer in the design of fast reactors cooled with Pb-alloys. To mitigate dissolution any direct contact between the steel and the liquid Pb should be avoided. The most appropriate method is the in-situ oxidation by dissolved oxygen [10]. The oxygen concentration is determined by the operating temperature range of the reactor (see Figure 2). PbO formation to avoid any related coolant channel blockage at the low temperature side and avoiding of corrosion attack on the other side limit both the temperature and the oxygen content. But, the limit by the Fe_3O_4 formation line as indicated in figure 2 was shown to be too low [3]. E.g. at 450° 10^{-8}wt% dissolution attack was reported [1].

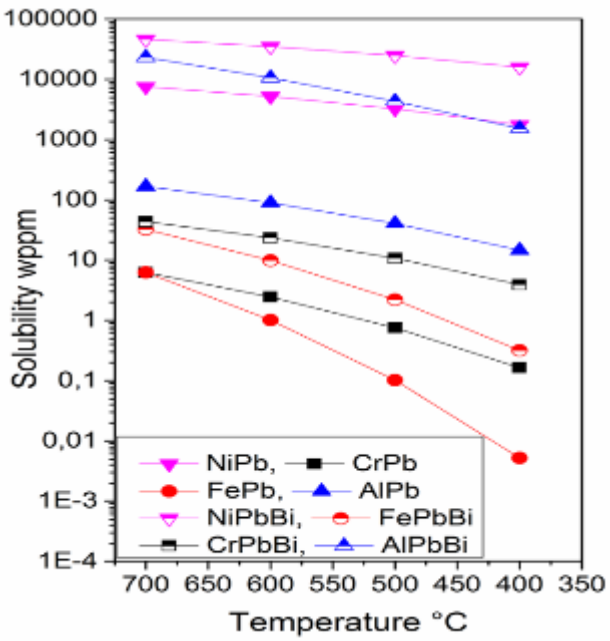

Figure 1: solubility of main Ni, Cr, Fe and Al in Pb and PbBi as function of temperature

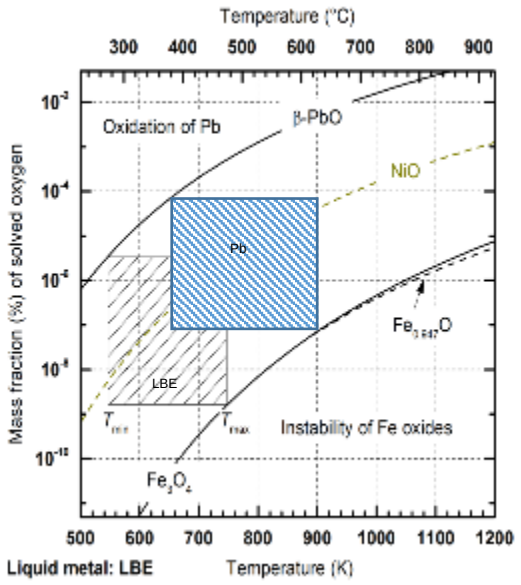

Figure 2: Operating window in terms of oxygen content and temperature of Pb alloy cooled nuclear reactors

The general corrosion mechanism for both coolants, Pb and PbBi, the dissolution of Ni accompanied by penetration of Pb into the steel matrix, is equivalent. However, the rate of dissolution and the resulting temperature and oxygen concentration limits might differ. Below 430°C, the maximum temperature of the reactor vessel of a Pb cooled fast reactor, even in LBE no dissolution attack was observed as long as the oxygen content is sufficiently high for the formation of oxide scales. In Pb an improved behaviour of the steels can be expected. However, if the oxygen concentration drops to low values even at this temperature dissolution attack will become an issue. The use of austenitic steels of 316 type is limited to temperatures below 450°C due to corrosion attack [1]. But, even at this temperature localized corrosion was observed at oxygen concentrations in the HLM of about 10^{-7} wt% (2).

Advanced mitigation measures

To enlarge the operation window of HLM cooled nuclear reactors advanced mitigation measures are under investigation since several years [1]. Two different advance mitigation measures are presented: Insoluble ceramic coatings like TiN, TiAlN and Al_2O_3 and formation of alumina scales during operation either by surface alloying or by new developed bulk FeCrAl-alloys. Evaluation criteria based on requirements are beside

corrosion resistant up to 600 °C at least the stability regards delamination for the coatings and the self-healing capability of the alumina formers. The latter is in any case the preferential one. Insoluble coatings were applied by many different methods including HiPIMS - and RF-Sputtering and PLD (pulsed laser deposition). Corrosion resistance was proven in tests at 550°C for 1200h. Irradiation experiments in contact with PbBi performed at PSI Switzerland exhibit the brittle behaviour on such coatings especially under combined load of corrosion, irradiation and strain [1]. All methods relying on coatings have inherently no self-healing capability. If the coating has a defect the underlying base steel will be attacked. This aspect requires new strategies for service and maintenance. Mitigation measures that rely on the formation of alumina scale during operation have the advantage of being capable to heal scratched or re-new destroyed protective scales. Alloying of strong oxide formers like Al into steels and steel surfaces or alloying of FeCrAlY surface layers can shift the operating temperature window to 600°C [4].

Work performed in WP5.2 of Matisse

The bulk FeCrAlYs are made by KTH and KIT, who is also performing the surface alloying using pulsed electron beams. CNR produced the TiN and TiAlN coatings by different sputtering methods and ENEA used a detonation gun for Al_2O_3 deposition. Corrosion tests of samples are performed by the institution that made and prepared the materials. CV Rez and INR performed mechanical tests in Pb-alloy environment, and HZDR did ion irradiation on selected FeCrAl -Bulk and surface alloys and finally PSI made a detailed TEM post-investigation of FeCrAl- surface alloyed T91 that was irradiated in the LISOR-6 experiment.

The contribution compiles all reports delivered by the partners added by a common summary. Material development and sample preparation done at KTH and KIT and CNR (partially) is reported separately while the sample preparation efforts at CNR and ENEA are included in the reports describing the mechanical tests performed and described by CVR and RATEN.

2 Modified surface layers for mitigation of material degradation in HLM - KIT contribution

Adrian Jianu, Hao Shi, Renate Fetzer, Annette Heinzel, Wladimir An, Alfons Weisenburger, Georg Müller

Abstract

The report gives experimental results concerning the morphology, composition, structure and thickness of the oxide scales grown on model Fe-Cr-Al-based bulk alloys and on Al-containing surface layers, modified by melting with intense pulsed electron beam, during exposure to oxygen-containing molten lead.

The results provide information the alumina stability domain and also the criterion of the Al/Cr ratio for the formation of a highly protective alumina layer on the surface of Fe-Cr-Al-based alloys and on modified surface layers exposed to molten lead with 10^{-6} wt.% oxygen at 400-600°C. The protective oxide scales, grown on alumina-forming Fe-Cr-Al alloys under the given experimental conditions, were transient aluminas, namely, *kappa*-Al_2O_3 and *theta*-Al_2O_3.

The information presented in this report was also published in three papers:

- Oxide scale formation of modified FeCrAl coatings exposed to liquid lead; Fetzer Renate; Weisenburger Alfons; Jianu Adrian; Mueller G., Corrosion science 55 (2012) 213-218;

- Oxide scales formed on Fe-Cr-Al - based model alloys exposed to oxygen containing molten lead, A. Weisenburger, A. Jianu, S. Doyle, M. Bruns, R. Fetzer, A. Heinzel, M. DelGiacco, W. An, G. Müller J. of Nuclear Materials, 437 (2013) 282–292;

- Stability domain of alumina thermally grown on Fe-Cr-Al-based model alloys and modified surface layers exposed to oxygen-containing molten Pb. A. Jianu, R. Fetzer, A Weisenburger, A, M. Bruns, P. Doyle, A. Heinzel, P. Hosemann, G. Mueller, J. of Nuclear Materials, 470 (2016), 68-75;

2.1 Introduction

Heavy liquid metals (HLM), namely lead and lead-based alloys, have lower chemical reactivity to oxygen and water in comparison to other liquid metals, such as sodium and beneficial thermal and neutronic properties [1-4]. Therefore they are under consideration for energy-related applications like advanced nuclear reactors, concentrated solar power and hydrogen production.

However, HLMs have the issue of the compatibility with structural steels, in terms of corrosion and mechanical resistance, which causes considerable concerns [5-13]. The addition of small quantities of oxygen into HLMs forms a protective oxide scale of Fe-Cr-based oxides at temperatures below 500 °C. The formation of the protective oxide scale addresses both austenitic and ferritic/martensitic steels [6]. At higher temperatures, the enhanced solubility of steel alloying elements in HLMs and the faster kinetics make the controlling of the corrosion of the deployed structural materials significantly more difficult. Therefore, passivating films need to be developed to provide a better protection of the structural material in HLMs.

In order to push the temperatures above 500°C without serious corrosion, steels were alloyed with strong oxide-forming elements (e.g. Al, Si) and tested in molten lead and lead-based alloys containing small amounts of oxygen (10^{-8} - 10^{-6} wt.%) [5, 14-18].

These steels were protected by a thin, continuous oxide scale that was formed during

the exposure to oxygen-containing HLM at temperatures above 500°C. It was found that the appropriate Al or Si concentration was the key factor for the formation of a slowly growing, protective, adherent and stable oxide layer.

However, it has to be considered that the required minimum content of aluminium (4-6 wt% depending on Cr content) can negatively affect the workability and mechanical properties (especially ductility) of the steel [19-21]. Therefore, to avoid the impact on the mechanical properties, it has been proposed to deploy aluminium only into the steel surface (around 20-30 μm thick surface layer), at a concentration necessary to provide corrosion protection. This approach was developed at Karlsruhe Institute of Technology (KIT). Al-containing layers (e.g. Fe-Cr-Al-Y) are deposited by plasma spraying and subsequently modified by melting using intense pulsed electron beam processing. The approach is called "GESA-method" where GESA is the abbreviation of the facility German name: "**G**epulste **E**lektron**S**trahl **A**nlage" [22, 23].

Different system concept designs with HLMs as working fluids are currently under evaluation and development. Depending on the application, the HLM temperature may vary within a certain range. In order to provide valuable input data for modelling and design codes in the field of heat management and life-prediction of different structural parts, material corrosion behaviour experiments should be performed for a very finely sampled temperature range.

It was found that, for Al contents below a certain threshold, (Fe–Cr–Al) spinel-type oxides are formed, allowing the growth of magnetite on top [22, 24-26]. In order to find the minimum Al content and the Al/Cr ratio necessary to form a protective alumina scale, a systematic study was performed concerning the corrosion behaviour of the Fe-Cr-Al-based model alloys and modified surface layers exposed to oxygen-containing (10^{-6} wt. %) molten lead in the temperature range 400 - 600 °C. A map of the alumina stability domain for this temperature range has been drawn in Fe-Cr-Al ternary diagrams and the type of alumina polymorph, formed at different temperatures, was determined.

2.2 Corrosion specimens and experimental procedure

Twelve Fe-Cr-Al-based alloys were prepared as ingots starting from high purity elements by arc-melting in argon atmosphere. Their nominal and measured compositions are shown in Table 1. After drawing the first conclusions regarding the corrosion behaviour of model alloys, eight Fe-Cr-Al-Y modified surface layers on T91 steel, were prepared using GESA-method. Manufacturing of modified FeCrAl coated steel specimens was done by low pressure plasma spraying (LPPS) combined with pulsed intense electron beam treatment by GESA. Samples of 9Cr f/m steel T91 with dimensions 33.5x 6.5x2.0 mm^3 were coated with FeCrAl by LPPS (Sulzer Metco AG, Switzerland). Two different compositions of the coating were used: Fe15-Cr11.5Al0.5Y (called type A hereafter), Fe9Cr12Al0.5Y (type B).

Their nominal and measured compositions are shown in Table 1. The Cr and Al contents were measured within 1 wt.%.

Table 1

Composition of Fe-Cr-Al-based bulk alloys and modified surface layers on T91, analyzed with EDX. (BA: bulk alloy; MSL: modified surface layer).

	Sample	Nominal composition	Cr [wt.%]	Al [wt.%]	Y [wt.%]	Fe	Investigation techniques
BA	P1	Fe-6Cr-6Al	6.2	6.8	-	Bal.	OM/SEM/EDS/XRD
	P2	Fe-8Cr-6Al	8.4	6.6	-	Bal.	OM/SEM/EDS/XRD
	P3	Fe-10Cr-5Al	10.8	5.6	-	Bal.	OM/SEM/EDS/XRD
	P4	Fe-14Cr-4Al	14.5	4.2	-	Bal.	OM/SEM/EDS/XRD
	P5	Fe-16Cr-4Al	16.4	4.7	-	Bal.	OM/SEM/EDS/XRD
	P6	Fe-6Cr-8Al	6.4	8.8	-	Bal.	OM/SEM/EDS/XRD
	P7	Fe-10Cr-7Al	10.4	7.6	-	Bal.	OM/SEM/EDS/XRD
	P8	Fe-12Cr-7Al	12.4	7.5	-	Bal.	OM/SEM/EDS/XRD
	P9	Fe-16Cr-6Al	16.9	6.4	-	Bal.	OM/SEM/EDS/XRD/XPS/TEM
	P10	Fe-12Cr-5Al	12.3	5.8	-	Bal.	OM/SEM/EDS/XRD
	P11	Fe-12Cr-8Al	12.2	8.2	-	Bal.	OM/SEM/EDS/XRD/XPS
	P12	Fe-16Cr-8Al	16.5	8.7	-	Bal.	OM/SEM/EDS/XRD/XPS
MSL	A1	Fe-15Cr-11.5Al-0.5Y	14	11	0.3	Bal.	OM/SEM/EDS
	A2	Fe-15Cr-11.5Al-0.5Y	14.5	10	0.3	Bal.	OM/SEM/EDS
	A3	Fe-15Cr-11.5Al-0.5Y	14.5	10	0.3	Bal.	OM/SEM/EDS
	A4	Fe-15Cr-11.5Al-0.5Y	13.5	9	0.4	Bal.	OM/SEM/EDS
	B1	Fe-9Cr-12Al-0.5Y	9.5	10	0.3	Bal.	OM/SEM/EDS
	B2	Fe-9Cr-12Al-0.5Y	9.5	9	0.3	Bal.	OM/SEM/EDS
	B3	Fe-9Cr-12Al-0.5Y	9.5	10	0.3	Bal.	OM/SEM/EDS
	B4	Fe-9Cr-12Al-0.5Y	9.5	8.5	0.4	Bal.	OM/SEM/EDS

The ingots P1-P12 were cut into discs with a thickness of around 1.2 mm. All specimens were prepared using standard metallographic grinding with abrasive SiC paper down to 4200 grit.

After processing, the specimens from P1-P12 model alloys were exposed to stagnant molten lead containing 10^{-6} wt.% oxygen in the COSTA facility [27] at 400 °C, 450 °C, 500 °C, 550 °C and 600 °C, while the specimens with modified surface layers were exposed 400°C, 450°C, 500°C and 550°C.

After the extraction from molten lead, the specimens were cooled in air and then cleaned with a solution of ethanol, acetic acid and hydrogen peroxide (1:1:1) to remove the remaining adherent lead.

The evaluation of the specimens from the model alloys was performed using the following characterization techniques: scanning electron microscopy (SEM), energy dispersive X-ray spectroscopy (EDX), X-ray diffraction using conventional and synchrotron radiation (XRD), and for some selected samples, X-ray photoelectron spectroscopy (XPS).

SEM-EDX examination was performed with Philips XL40 equipped with a SAMx - EDX system.

The phase composition of the majority of grown oxides was analysed using a Seyfert C3000 powder diffractometer (Cu K_α radiation) with $\theta-2\theta$ conventional geometry. For a batch of selected samples the evaluation of the grown oxide was made with grazing incidence – X-ray diffraction (GI-XRD). In the latter case, the measurements were made using synchrotron radiation at the ANKA synchrotron [28], PDIFF beamline, with the wave length λ=0.117945 nm. Incidence angles between 1-3° were used.

XPS measurements were performed on P9 samples using a K-Alpha XPS spectrometer (ThermoFisher Scientific). Data acquisition and processing using the Thermo Avantage software is described elsewhere [29]. The samples were analyzed using a microfocused, monochromated Al Kα X-ray source (200 μm spot size). The K-Alpha charge compensation system was employed during analysis, using electrons of 8 eV energy, and low-energy argon ions to prevent any localized charge

build-up. The spectra were fitted with one or more Voigt profiles (BE uncertainty: ±0.2 eV). The analyzer transmission function, Scofield sensitivity factors [30] and effective attenuation lengths (EALs) for photoelectrons were applied for quantification. EALs were calculated using the standard TPP-2M formalism [31]. All spectra were referenced to the C1s peak of hydrocarbon at 285.0 eV binding energy, controlled by means of the well-known photoelectron peaks of metallic Au, Ag and Cu. XPS sputter depth profiling for evaluation of the composition of the grown oxides was performed using a 2 keV Ar^+ ion beam at a raster size of 1 x 2 mm^2 and a 30° angle of incidence. The depth of sputtering was measured at the end of the evaluation by profilometry (DektakXT Stylus Profilometer, Bruker AXS).

The corrosion behaviour of Fe-Cr-Al-based, GESA-modified surface layers with refined microstructure (grain size 0.5 – 2 μm) in oxygen-containing molten lead was studied using scanning electron microscopy combined with energy dispersive spectroscopy (SEM/EDX).

A summary of the experimental works performed on Fe-Cr-Al bulk alloys P1-P12 and modified surface layers A1-A4 and B1-B4 is given in Table 2.

Table 2

Experiments performed on iron-rich Fe-Cr-Al-based bulk alloys and modified surface layers on T91, exposed to molten lead containing 10^{-6} wt.% oxygen.

Sample	400°C	450°C	500°C	550°C	600°C
			molten Pb		
			10^{-6} wt.% oxygen		
P1-P12	840 h	840 h	930 h	840 h	1830 h
A1 & B1 on T91	900 h	-	-	-	-
A2 & B2 on T91	-	900 h	-	-	-
A3 & B3 on T91	-	-	900 h	-	-
A4 & B4 on T91	-	-	-	900 h	-

2.3 Results

Prior to corrosion testing, the microstructure of the alloys was evaluated using light microscopy (LM). The original grain size of all alloys was in the range of 0.5 – 2 mm, so that a possible influence of grain boundary diffusion on the formation of oxide scales can be considered very low. Figure 1 reveals examples of the samples microstructure in the original state. The grains are preferentially oriented due to solidification conditions.

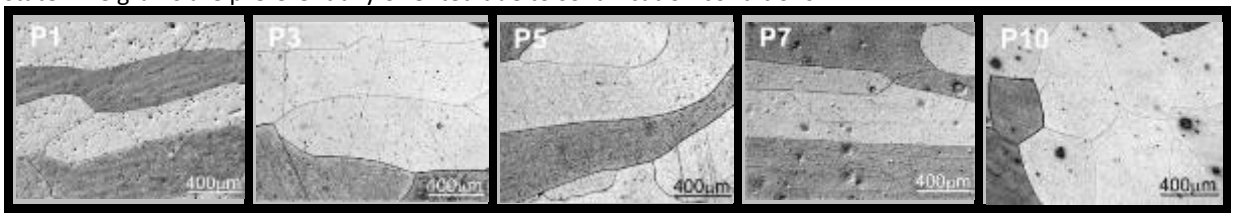

Fig. 1. Examples of the original microstructure of P1 (Fe6Cr6Al), P3 (Fe10Cr5Al), P5 (Fe16Cr4Al), P7 (Fe10Cr7Al) and P10 (Fe12Cr5Al) samples. Large grains in the range of 0.5 – 2 mm and a slight texture characterized all samples.

The surface morphology and elemental composition of the oxide scales, that grown on specimens from Fe-Cr-Al-based bulk alloys and modified surface layers on at all exposure temperatures, were evaluated by SEM/EDX. No dissolution attack was observed for any of the samples tested. Based on the morphology of the oxide grown on the surface, the samples were classified into two categories: samples with "granular" surface aspect and samples with relatively "smooth" surfaces.

The oxide scales of the first category exhibit grains protruded above the original surface and have dark-gray and wrinkled appearance with pores. The first category comprises samples of the bulk alloys P1-P7 and P10 and modified surface layer B2.

The second category, with generally flat surfaces, contains P9, P11 and P12 bulk alloys and modified surface layers A1-A4, B1 and B3. The samples from this category are covered by a green-yellow oxide scale.

Figs. 2-4 show examples of surface morphologies with "granular" and "smooth" aspect observed on different samples after exposure to oxygen-containing molten lead (10^{-6} wt.%) at different temperatures.

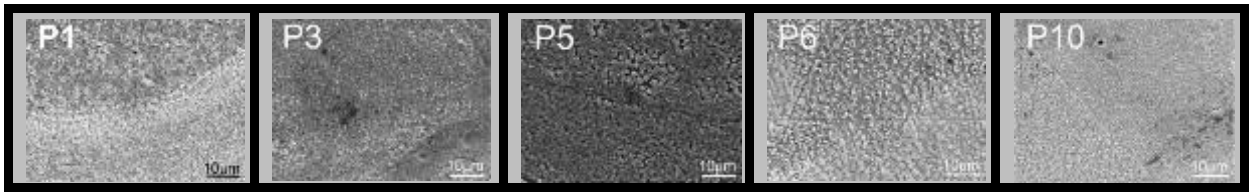

Fig. 2. SEM micrographs of "granular" oxide scale grown on the surface of Fe-Cr-Al-base alloys exposed to oxygen containing liquid lead for 840 hours at 400°C: P1 (Fe6Cr6Al), P3 (Fe10Cr5Al), P5 (Fe16Cr4Al), P6 (Fe6Cr8Al) and P10 (Fe12Cr5Al).

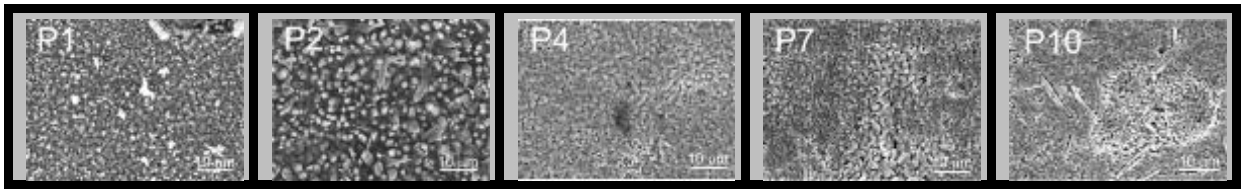

Fig. 3. SEM micrographs of "granular" oxide scale grown on the surface of Fe-Cr-Al-base alloys exposed to oxygen containing liquid lead for 1830 hours at 600°C: P1 (Fe6Cr6Al), P2 (Fe8Cr6Al), P4 (Fe14Cr4Al), P7 (Fe10Cr7Al), P10 (Fe12Cr5Al).

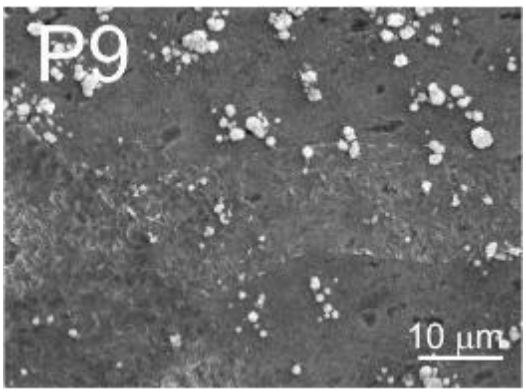

a)

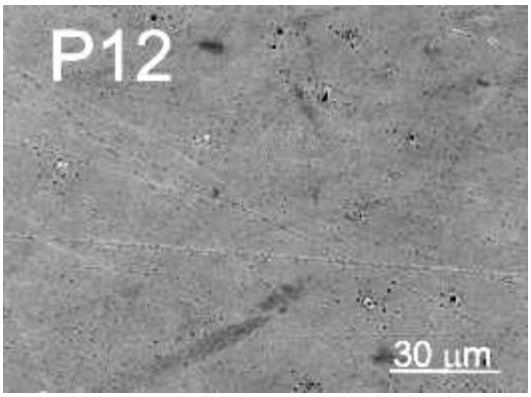

b)

Fig. 4. SEM micrographs of "smooth" oxide scale grown on the surface of Fe-Cr-Al-base alloys exposed to oxygen containing liquid lead at 600°C: P9 (Fe16Cr6Al), P12 (Fe-16Cr-8Al)

The P8 alloy and B4 modified layer show both morphologies, granular and smooth, over considerable areas; 20-40% of the surfaces show a granular aspect. Therefore, P8 and B4 does not clearly fall in any of the two categories and represents the transition region.

The cross section examination of the specimens revealed that samples showing a “granular” surface aspect form a duplex-type oxide scale. Figure 5 shows as examples the EDX sectional line scan patterns obtained on P3, P4 and B2 which has “granular” surface aspect. They were exposed at 450 °C, 400°C and 450°C, respectively to molten lead with 10^{-6} wt.% oxygen. The line scans in Fig. 5 shows an outer magnetite layer and an inner Fe-Cr-Al-O layer grown on the samples during exposure to oxygen-containing molten lead. An internal oxidation zone of around 1 μm was also observed beneath the Fe-Cr-Al-O layer, in case of P3 sample.

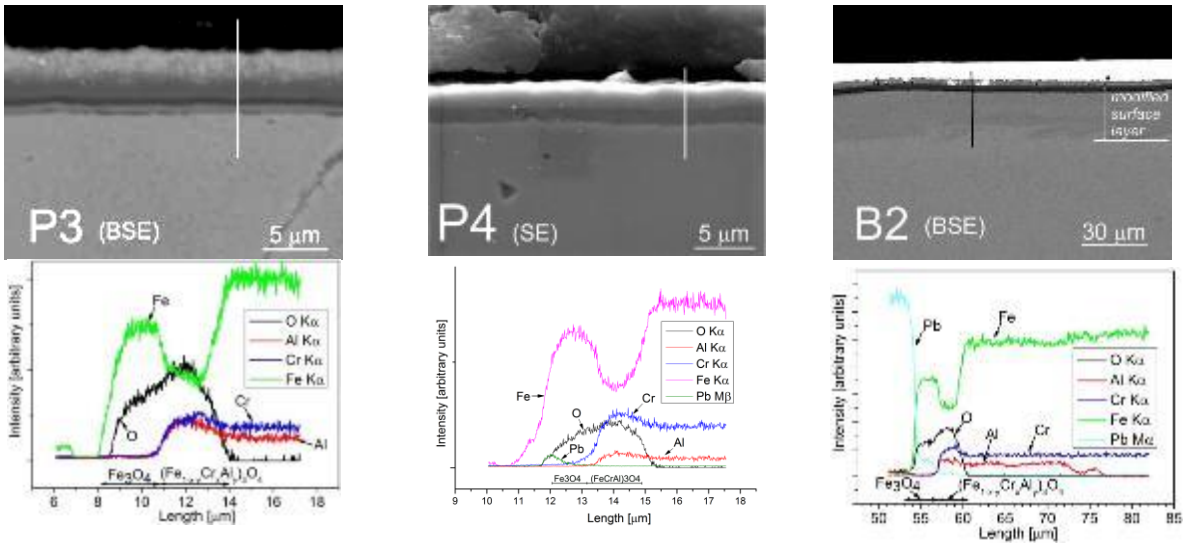

Fig. 5. Examples of SEM cross section images (backscattered electrons) and EDX line scans of the duplex oxide scale (Fe_3O_4 + $(Fe_{1-x-y}Cr_xAl_y)_3O_4$) with rough-granular aspect, grown on P3 (Fe-10Cr-5Al) during exposure at 450 °C, on P4 (Fe14Cr4Al) during exposure at 400°C and on B2 (Fe-9.5Cr-9Al) exposed at 450°C, to molten Pb with 10^{-6} wt.% oxygen.

The samples with “smooth” surfaces were covered by a very thin Al-rich oxide scale, as found by EDX line scan analysis. Fig. 6 shows examples of EDX line scans of the P9 (Fe-16Cr-6Al) samples with smooth surface exposed at 550 °C and 600°C, and A4 (Fe-13.5Cr-9Al) exposed at 550°C to molten lead with 10^{-6} wt.% oxygen. The signals corresponding to aluminium and oxygen reach a maximum before the Cr and Fe signals reach their nominal values. This fact leads to the conclusion that the oxide scale consists mainly of an aluminium oxide.

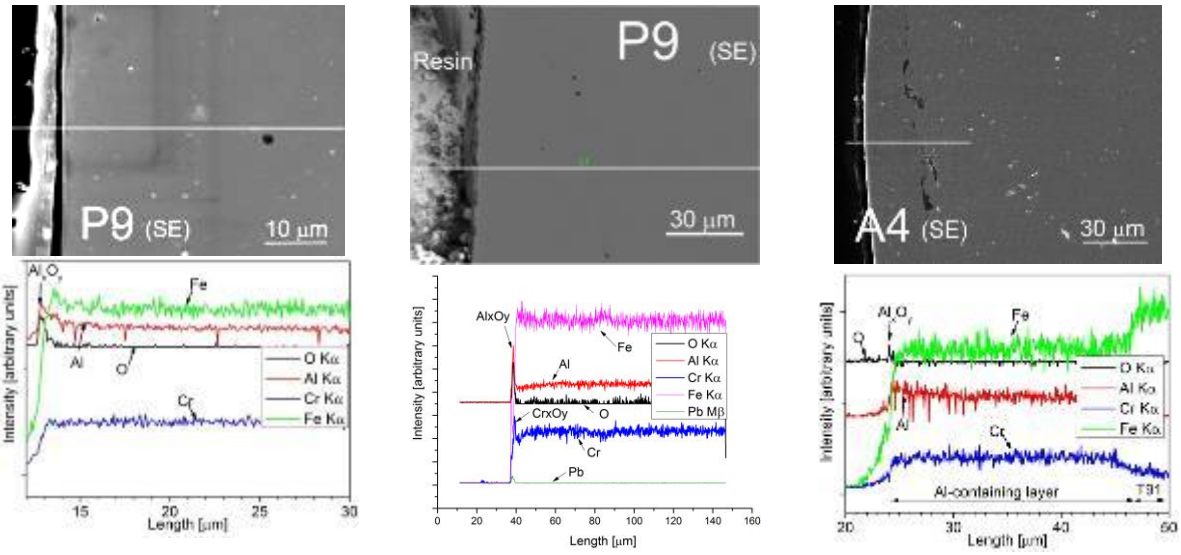

Fig. 6. SEM cross section images and EDX line scans of thin Al-rich oxide scales with smooth aspect, grown on P9 (Fe-16Cr-6Al) during exposure at 550 °C and 600°C and on A4 (Fe-13.5Cr-9Al) exposed at 550°C to molten lead with 10^{-6} wt.% oxygen.

For identification of the phase constituents in the oxide scale, grown on the samples with granular surface, XRD analysis using Cu$K\alpha$ radiation (λ=0.15405 nm) was conducted. The XRD patterns obtained on the bulk alloy samples P1-P7 and P10 show spinel-type structure, identified as magnetite Fe_3O_4 (PDF-card no. 89-0688) and chromite $Fe(Cr,Al)_2O_4$ (PDF-card no. 34-0140). The cubic structure α - Fe(Cr) (PDF-card no. 34-0396), which corresponds to the substrate, is also found. Fig. 7a depicts, as example, XRD patterns of the P7, P1 and P6.

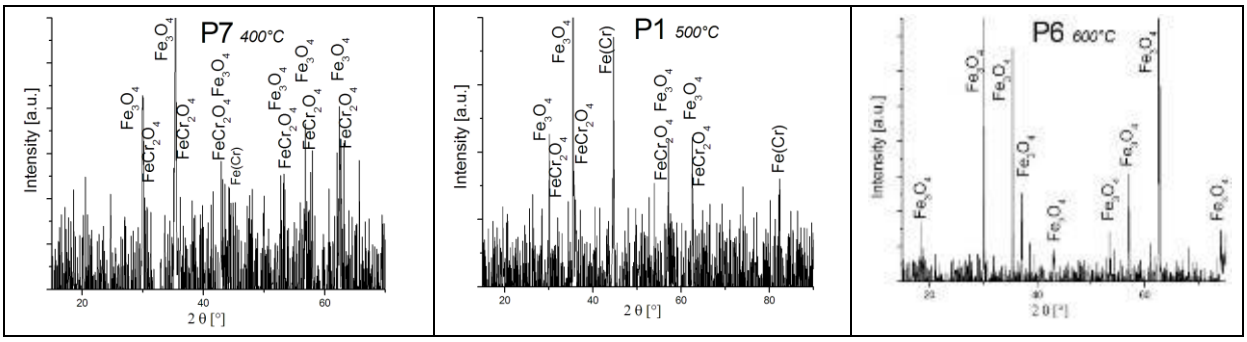

Fig. 7. Examples of XRD patterns measured on samples with granular surface scales after exposure in molten lead containing 10^{-6} wt.% oxygen.

The structure of the oxide with smooth surface was examined using Grazing Incidence XRD (GI-XRD) at the ANKA synchrotron, with two wavelengths: λ=0.11794 nm and λ=0.12397 nm.

The oxide, grown on P9, P11, P12 and partially on P8 is either (i) κ-Al_2O_3 transient alumina (PDF card No. 26-31), as can be concluded from the example shown in Fig. 8 (P8 exposed at 550 °C), or (ii) a mixture of two alumina polymorphs (κ-Al_2O_3 and θ-Al_2O_3, PDF card No. 86-1410), in case of P11 and P12 exposed at 600°C. XRD patterns of P8, P9 and P11 samples also contain peaks of magnetite.

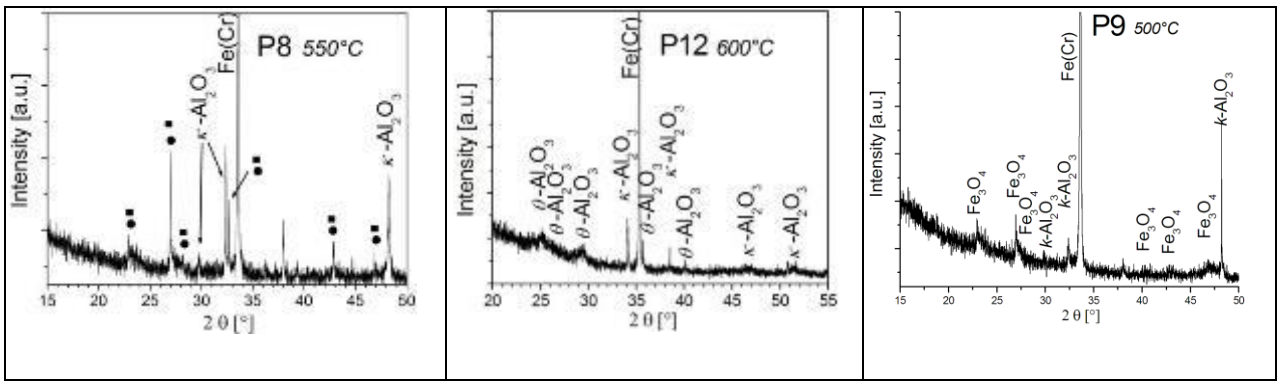

Fig. 8. Examples of XRD patterns measured on samples with "smooth" surface scales after exposure in molten lead containing 10^{-6} wt.% oxygen.

The magnetite has grown on some 20-40% of the P8 sample surface and only at grain boundaries or around some surface defects in case of P9 and P11 samples.

XPS compositional sputter depth profile evaluations were performed on the P9 bulk alloy samples, that formed transient aluminas as protective scale at all temperatures (Fig. 9). Following a semi-quantitative procedure [32], the average thickness of the alumina layer, grown on the P9 sample exposed at 400, 450, 500, 550 and 600 °C to oxygen-containing molten lead, was estimated from the full width at half-maximum (FWHM) of the AlOx peak, to be 35 nm, 60 nm, 84 nm, 140 nm and 500 nm respectively.

Transmission electron microscopy was conducted on FIB lift-out samples to evaluate the alumina scales grown on P9 samples during their exposure to oxygen-containing molten lead. The average scale thicknesses of these samples exposed at 450 °C and 600 °C are around 60 nm and 500 nm, respectively (Fig. 10).These measurements confirm the scale thickness estimation based on XPS sputter depth profile.

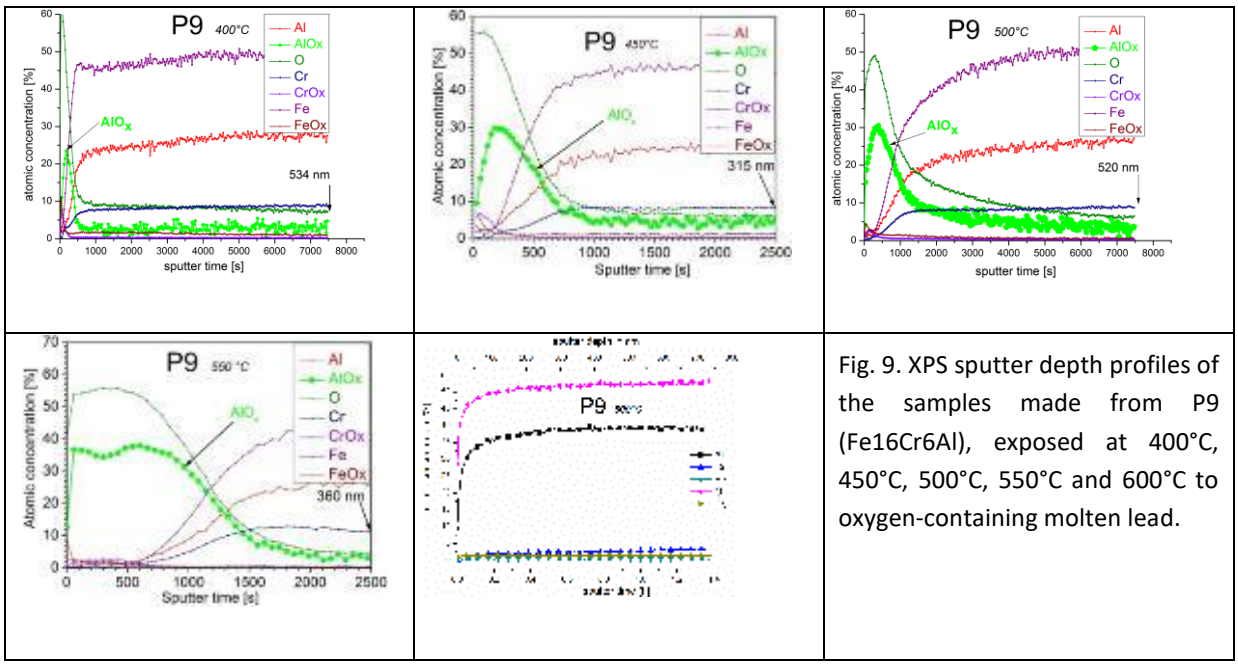

Fig. 9. XPS sputter depth profiles of the samples made from P9 (Fe16Cr6Al), exposed at 400°C, 450°C, 500°C, 550°C and 600°C to oxygen-containing molten lead.

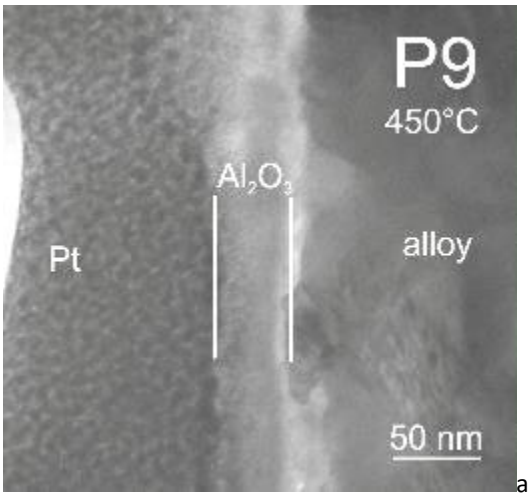

a)

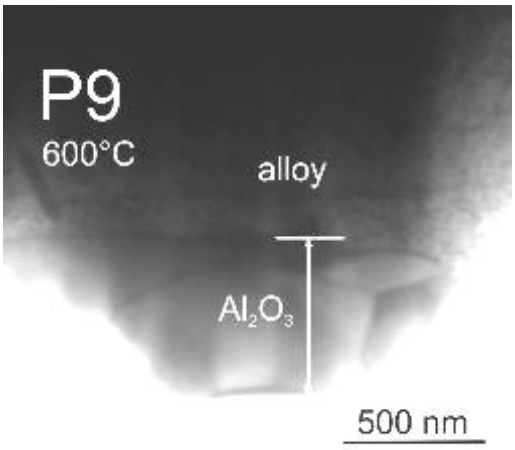

b)

Fig. 10**.** TEM images of the oxide scales grown on P9 samples (Fe-16Cr-6Al) exposed at (a) 450 °C (840 h) and (b) 600 °C (1830 h) in molten lead with 10^{-6} wt.% oxygen. The average scale thicknesses are around 60 nm and 500 nm, respectively.

2.4 Discussion

The experimental results presented in this report concern the surface morphology, composition, structure and thickness of the oxide scales grown on Fe-Cr-Al-based bulk alloys and modified surface layers during their exposure to oxygen-containing molten lead (10^{-6} wt.%) at different temperatures.

Eight bulk alloys (P1-P7 and P10) were protected against dissolution attack during exposure to oxygen-containing molten lead at 400, 450, 500, 550 and 600°C by an iron-based duplex oxide scale (Fe_3O_4 + $Fe(Cr,Al)_2O_4$) with a granular appearance.

Fig. 11 shows the evolution of the $Fe(Cr,Al)_2O_4$ sub-layer thickness over all tested exposure temperatures. It should be mentioned that the magnetite sub-layer spalls off partially or fully either during the experiments or during cleaning procedure and, therefore, only the thickness of the $Fe(Cr,Al)_2O_4$ sub-layer was considered in Fig. 11. The graph also shows the thickness of the $Fe(Cr,Al)_2O_4$ sub-layer, grown on the modified surface layer B2 (450 °C). One can note that the sub-layer thickness increases with temperature. However, for the P5 bulk alloy (Fe-16Cr-4Al), the oxide scale thickness increase with temperature is much lower than in case of the other specimens. Previous studies showed that a concentration of 4 wt.% Al is sufficient, in synergy with the Cr content, to reduce the growth rate of the $Fe(Cr,Al)_2O_4$ oxide scale, with spinel structure, on Al-containing ODS alloys after exposure to flowing LBE [16].

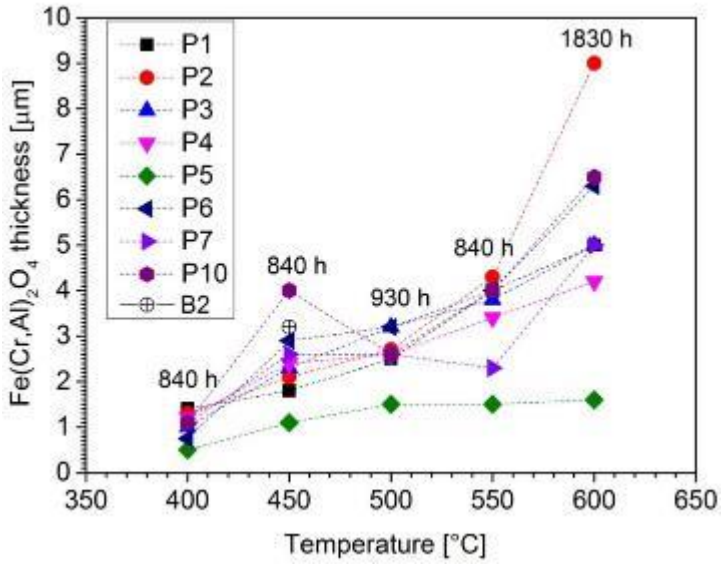

Fig. 11. Thickness of the $Fe(Cr,Al)_2O_4$ sub-layer formed at 400, 450, 500, 550 and 600°C on P1-P7, P10 bulk samples, during exposure to molten lead containing 10^{-6} wt.% oxygen. The graph shows also the thickness of the $Fe(Cr,Al)_2O_4$ sub-layer grown on the B2 modified surface layer after 900h exposure time.

The experiments performed in this study showed that the protective scales grown on P8 (partially) and on P9, P11 and P12 samples, exposed at 400, 450, 500, 550 and 600°C, to oxygen-containing liquid lead were alumina polymorphs κ-Al_2O_3 and θ-Al_2O_3. No area with detached scales was observed and no trace of α - alumina detected. These transient polymorphs are highly protective under the applied experimental conditions.

For the temperature range, oxygen concentration and exposure time considered in the current evaluation, the growth rate of alumina scales was rather low and the thickness could not be evaluated using SEM. However, in case of the P9 sample, the average thickness of the alumina layers was estimated based on (i) a semi-quantitative procedure, applied to the XPS-SDP experimental data and on (ii) TEM evaluation of the samples.

A sharp increase of the alumina scale thickness was observed on the sample exposed to oxygen-containing molten lead at 600°C (Fig. 12a). Besides the higher exposure temperature, two additional factors could be responsible for this behaviour: (i) an exposure time increase and (ii) the formation of θ - alumina polymorph, which was observed only at this temperature and was reported as having a very high growth rate [33].

The growth of the alumina scale on Fe-16Cr-6Al (P9) samples was assumed to follow the parabolic rate law of diffusion-controlled oxidation [34]:

$$d^2 = k_p \cdot t \qquad (1)$$

where d is the average thickness of the oxide scale, k_p the parabolic rate constant (which is a measure for the oxidation rate), and t the oxidation time.

Values of the parabolic rate constants k_p related to P9 samples were calculated for all exposure temperatures and are presented as a function of temperature in the Arrhenius plot of Fig. 12b. Calculated data at 400 °C, 450 °C, 500 °C and 550°C correspond to κ-Al_2O_3 polymorph grown at these temperatures and fit a single regression line. The oxide growth at these temperatures is thermally activated with an activation energy, calculated from the slope of the fitting line, of about 82 kJ/mol. This is lower than the value reported for α–Al_2O_3 (200 kJ/mol, [35]), which is reasonable. At 600°C the

growth rate is much higher than the rate extrapolated from the Arrhenius plot (dot-line). This deviation of the parabolic rate constant, corresponding to the sample exposed to oxygen-containing molten lead at 600°C, can be attributed to the formation of θ-Al_2O_3 that has a higher growth rate than κ-Al_2O_3.

The results allow to estimate the stability domain of alumina formed on Fe-Cr-Al-based alloy system, exposed to molten lead containing 10^{-6} wt.% oxygen, over the 400-600 °C temperature range (Fig. 13, solid symbols).

The P9 (Fe-16Cr-6Al), P11 (Fe-12Cr-8Al) and P12 (Fe-16Cr-8Al) samples are included in the alumina stability domain, while the P8 (Fe-12Cr-7Al) sample was localized on the boundary between the alumina stability domain and the Fe-based oxide domain. The boundary between the two domains shows a clear dependence on Cr concentration: higher Cr content leads to alumina formation at lower Al concentration.

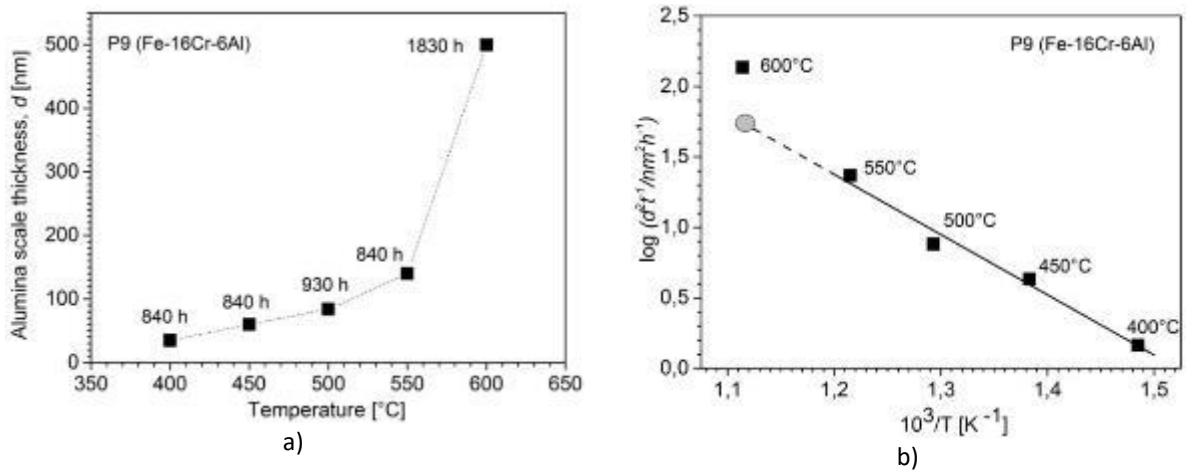

Fig. 12. (a) Thickness of the alumina scale *"d"* grown on P9 bulk alloys (Fe-16Cr-6Al) during exposure in oxygen-containing molten lead (10^{-6} wt.%) at 400°C, 450°C, 500°C, 550°C and 600°C; (b) Arrhenius-plot of oxidation rate constant k_p corresponding to alumina scale on P9 samples versus reciprocal temperature.

The results obtained on bulk model alloys are combined with results obtained on modified surface layers in order to draw a comprehensive picture of the alumina stability domain superimposed onto Fe-Cr-Al ternary diagram. In case of modified Fe-Cr-Al-Y-based surface layers (Table 1), yttrium acts as a reactive element (RE) when exposed to molten, oxygen-containing lead or lead-alloys. It has been experimentally shown that the addition of reactive elements in small quantities (< 1 wt.%) reduces the scale growth rate and improves the scale/substrate adherence [36]. However, only minor or no effect at all is expected on the alumina stability domain since the amount of these elements is not sufficient to change the phase composition significantly. Therefore, data of the modified Fe-Cr-Al-Y-based surface layers are added (open symbols) in the oxide map in Fig. 13.

The samples A1-A4 easily fall within the alumina stability domain determined with the model bulk alloy experiments. B1 and B3 also form stable alumina scales and extend in a reasonable way the stability domain towards lower Cr contents. The B4 sample was identified to show both the Fe-based oxide and the alumina scale over considerable regions, thus marking the transition between the two domains, in agreement with the boundary estimated from the experiments with the model bulk alloys. B2, despite the slightly higher Al content than that of B4, was covered by Fe-based oxide scale. This observation indicates a temperature dependence of the alumina stability domain. It should be taken into account that B2 was exposed at 450 °C, while B4 at 550 °C.

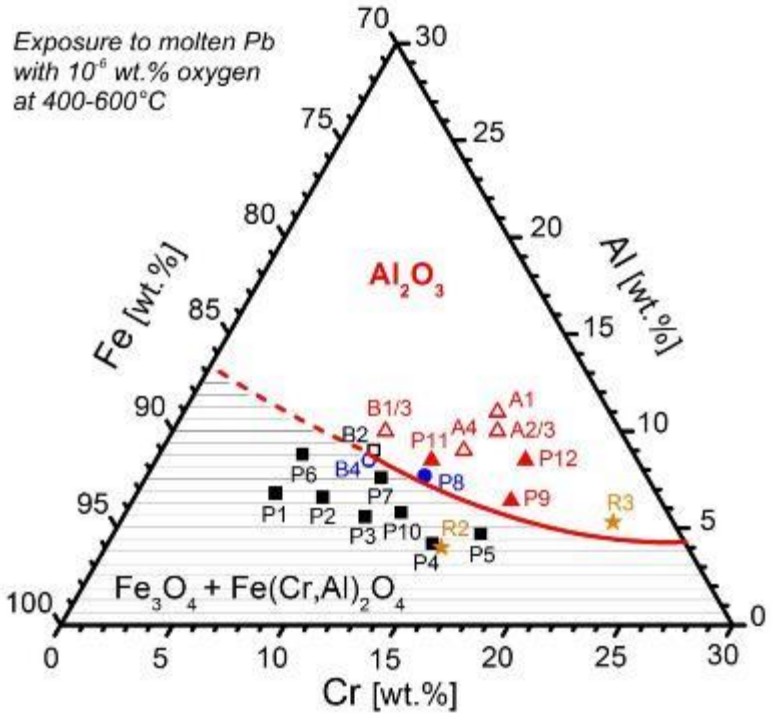

Fig.13. Oxide "map" for the oxidation of Fe-Cr-Al-based bulk alloys and modified surface layers exposed to molten lead containing 10^{-6} wt.% oxygen in the temperature range 400-600 °C (■): alloy sample forming Fe-based oxide scale; (□): modified surface layer sample forming Fe-based oxide scale; (▲): alloy sample forming alumina scale; (Δ): modified surface layer sample forming alumina scale; (●): alloy sample forming both Fe-based oxide and alumina scale; (O): modified surface layer sample forming both Fe-based oxide and alumina scale; (★): other alumina-forming alloys of type Fe-Cr-Al-RE.

Based on the results presented in this report, an experimental criterion was defined concerning the minimum Al concentration (C_{Al}) required to form a slowly growing and protective alumina scale on Fe-Cr-Al-based alloys and on modified surface layers exposed to molten lead containing 10^{-6} wt.% oxygen, in the 400-600°C temperature range, for a chromium content (C_{cr}) in the range 10-25 wt.%:

$$C_{Al} = 15.3 - 0.81\,(C_{Cr}) + 0.0156\,(C_{Cr})^2\ [\text{wt.\%}], \qquad (2)$$

This formula corresponds to the boundary line, which separates the alumina stability domain from the Fe-based oxides stability domain (Fig. 9).

The oxide map in Fig. 13 also shows the additional points "R2" and "R3", which were previously reported [37,38]. The exposure temperatures for these two references were 650-700 °C (R2) and 500-750 °C (R3), both forming stable alumina scales. As for Fe-Cr-Al-based modified surface layers, alumina-forming R2 (ODS) and R3 (Kanthal AF) alloys belong to the Fe-Cr-Al-RE system. The reactive element was hafnium in case of R2 and silicon in case of R3. As can be observed, the point R3 is clearly located within the alumina stability domain. The ODS steel containing 3.8 wt.% Al (corresponding to point R2), exposed at higher temperatures, was also protected by an alumina scale. This indicates a shift of the alumina domain to lower Al concentration in case of Fe-Cr-Al-based alloys exposure at higher temperatures. This result is in accordance with the findings reported in literature for exposures of alumina-forming alloys to oxygen atmosphere at 800 °C [39] and 1000 °C [40].

2.5 Conclusions

This work is a comprehensive report on the stability domains of various oxide phases grown on Fe-Cr-Al-based alloys and modified surface layers, when exposed to oxygen-containing liquid lead.

The main conclusions of this work are:

(1) The stability domain of alumina grown as protective scale on Fe-Cr-Al-based alloys, exposed to oxygen-containing liquid lead in the 400-600°C temperature range, was defined based both on new and on previously reported results. The domain border shifts with higher temperatures to lower aluminium concentration;

(2) An experimental criterion was defined concerning the aluminium and chromium content necessary to form a highly protective Al_2O_3 layer on the surface of Fe-Cr-Al-based alloys and modified surface layers exposed to molten lead with 10^{-6} wt.% oxygen in the 400-600°C temperature range. It was found that higher Cr content leads to alumina formation at lower Al concentration;

3) Outside this alumina stability domain, a concentration of 4 wt.% Al is sufficient, in synergy with 16 wt.% Cr content, to reduce drastically the growth rate of $Fe(Cr,Al)_2O_4$ sub-layer with spinel structure, on Fe-Cr-Al alloys exposed to oxygen-containing molten lead.

(4) Transient aluminas, κ-Al_20_3 and θ-Al_2O_3, were found to be the protective oxide scales grown on Fe-Cr-Al-based alloys with chromium and aluminium contents of 12-16 wt.% and 6-8 wt.%, respectively, at the given temperatures, oxygen concentration in the molten lead and exposure times.

(5) The growth rate of θ-Al_2O_3 formed only at 600°C is much higher than that of κ-Al_20_3 grown during exposure to molten lead with 10^{-6} wt.% oxygen in the 400-550°C temperature range.

References

[1] M. Serban, M. Lewis, C. Marshall, R. Doctor, Energy & Fuels 17 (2003) 705-713.

[2] J. Pacio, Th. Wetzel, Solar Energy 93 (2013) 11-22.

[3] Z. Su'ud, H. Sekimoto, J. Nucl. Sci. Technol. 32 (1995) 834–845.

[4] D. Frazer, E. Stergar, C. Cionea, P. Hosemann, Energy Procedia 49 (2014) 627–636.

[5] R.C. Asher, D. Davies, S.A. Beetham, Corros. Sci., 17 (1977) 545-557.

[6] Handbook on Lead–Bismuth Eutectic Alloy and Lead Properties, Material Compatibility, Thermal–Hydraulics and Technologies, AEN/NEA Nuclear Energy Agency, OECD, Nuclear Science, 2007 (Chapter 4). ISBN 978-92-64-99002-9.

[7] V.S. Rao, J. Lim, I.S. Hwang, L.K. Singhal, Corros. Sci.,63 (2012) 113-118

[8] Y. Kurata, M. Futakawa, S. Saito, J. Nucl. Mater. 343 (2005) 333-340

[9] A.K. Rivai, M. Takahashi, J. Nucl. Mater. 398 (2010) 139–145.

[10] E. Yamaki, K. Ginestar, L. Martinelli, Corros. Sci., 53 (2011) 3075-3085.

[11] J.S. Zhang, Corros. Sci., 51 (2009) 1207-1227.

[12] D. Sapundjiev, S. Van Dyck, W. Bogaerts, Corros. Sci., 48 (2006)

[13] C. Schroer, O. Wedemeyer, J. Novotny, A. Skrypnik, J. Konys, Corros. Sci., 84 (2014) 113-124

[14] H.U. Borgstedt, H. Glasbrenner, Fusion Eng. Des. 27 (1995) 659–662.

[15] M. Kondo, M. Takahashi, J. Nucl. Mater. 356 (2006) 203–212.

[16] P. Hosemann, H.T. Thau, A.L. Johnson, S.A. Maloy, N. Li, J. of Nucl. Mater. 373 (2008) 246-253.

[17] J. Lim, H.O. Nam, I.S. Hwang, J.H. Kim, J. Nucl. Mater. 407 (2010) 205–210.

[18] M. Ph. Short, R. G. Ballinger, Nuclear Technology, 177 (2012) 366-381.

[19] I. Gurrappa, S. Weinbruch, D. Naumenko, W.J. Quadakkers, Materials and Corrosion 51(2000) 224-235.

[20] J. Lim, I.S. Hwang, J.H. Kim, J. Nucl. Mater. 441 (2013) 650-660.

[21] J. Van den Bosch, P. Hosemann, A. Almazouzi, S.A. Maloy J. Nucl. Mater., 398/1 (2010) 116-121.

[22] A. Weisenburger, A. Heinzel, G. Mueller, H. Muscher, A. Rousanov, J. of Nucl. Mater., 376/3 (2008) 274-281.

[23] V. Engelko, G. Mueller, A. Rusanov, V. Markov, K. Tkachenkov, A. Weisenburger, A. Kashtanov, A. Chikiryaka, A. Jianu, J. of Nucl. Mater., 415/3 (2011) 270-275.

[24] P. Hosemann, H.T. Thau, A.L. Johnson, S.A. Maloy, N. Li, Corrosion of ODS steels in lead-bismuth eutectic, J. Nucl. Mater. 373 (2008) 246–253.

[25] S. Takaya, T. Furukawa, M. Inoue, T. Fujisawa, T. Okuda, F. Abe, S. Ohnuki,

A. Kimura, Corrosion resistance of Al-alloying high Cr-ODS steels in stagnant

lead-bismuth, J. Nucl. Mater. 398 (2010) 132–138.

[26] J. Zhang, A review of steel corrosion by liquid lead and lead–bismuth, Corros.

Sci. 51 (2009) 1207–1227.

[27] G. Müller, G. Schumacher, F. Zimmermann, J. Nucl. Mater. 278 (2000) 85–95.

[28] http://www.ips.kit.edu/766.php.

[29] K.L. Parry, A.G. Shard, R.D. Short, R.G. White, J.D. Whittle, A. Wright, Surf Interface Anal 38 (2006) 1497-1504.

[30] J.H. Scofield J. Electron Spectrosc. Relat. Phenom., 8 (1976) 129-137.

[31] S. Tanuma, C.J. Powell, D.R. Penn, Surf Interface Anal 21 (1994) 165-176.

[32] M. Veith, K. Andres, S. Faber, J. Blin, M. Zimmer, Y. Wolf, H. Schnöckel, R. Köppe, R. de Masi, S. Hüfner, The Metastable, Eur. J. Inorg. Chem. 24 (2003) 4387–4393.

[33] H.J Grabke, Oxidation of NiAl and FeAl, Intermetallics 7 (1999) 1153-1158.

[34] S. Canovic, J. Engkvist, F. Liu, H. Lai, H. Gotlind, K. Hellstrom, J.E. Svensson, L.G. Johansson, M. Olsson, M. Halvarsson, J. Electrochem. Soc. 157 (2010) C223–C230.

[35] P. Lours, J. Alexis, G. Bernhart, J. of Mater. Sci. Lett. 17 (1998) 1089-1093.

[36]P. Kofstadt, High temperature corrosion, Elsevier, London-New York, 1988, ISBN 1-85166-154-9.

[37] S. Takaya, T. Furukawa, G. Müller, A. Heinzel, A. Jianu, A. Weisenburger, K. Aoto, M. Inoue, T. Okuda, F. Abe, S. Ohnuki, T. Fujisawa, A. Kimura, J. Nucl. Mater. 428 (2012) 125–130.

[38] M. Del Giacco, A. Weisenburger, A. Jianu, F. Lang, G. Mueller, J. Nucl. Mater. 421 (2012) 39–46.

[39] P. Tomaszewicz, G.R. Wallwork, Oxid. Met. 20 (1983) 75-109.

[40] Z.G. Zhang, X.L. Zhang, L. Sheng, X. Teng, Open Corros. J. 2 (2009) 37-44.

3 Optimizing the Oxidation Properties of FeCrAl Alloys for Liquid Lead Environment – KTH (Kanthal) contribution

Peter Dömstedt, Jesper Ejenstam, Bo Jönsson & Peter Szakalos

Abstract. FeCrAl alloys are proposed candidate materials for liquid lead applications. Chromium is needed to assist the formation of a protective alumina layer, albeit has to be limited to avoid α' precipitation. Reactive elements (RE) improves oxidation properties, but little is known about the RE effects at lower temperatures. An alloy matrix based on Fe-10Cr-4Al (wt. %), with varying Zr, Y and Ti content was exposed to liquid lead up to one year in the temperature interval of 450-550°C. It was found that the formation of protective alumina was dependent on the RE/carbon ratio. All alloys with ratios lower than unity showed poor oxidation properties due to the formation of Cr-carbides in the metal-oxide interface. A sufficiently high amount of Zr and Ti was shown to significantly improve the oxidation properties at both temperatures. The positive effect is related to the suppression of Cr-carbides by addition of stronger carbide formers. In addition, a two new set of alloys were developed based on the results conclusions made from the experiments at 450°C and 550°C and two more tests were made at 650°C and 750°C in liquid lead for up to three months.

Keywords: FeCrAl, Reactive Elements, Cr-carbides, Alumina

3.1 Introduction

FeCrAl alloys have been proposed as a candidate material for use in energy applications, such as lead-cooled fast reactor (LFR) systems and Concentrated Solar Power (CSP) systems, due to their good oxidation properties, which is a result of the formation of an alumina (Al_2O_3) layer on the alloy surfaces. These alloys have historically been used in heating elements and wires at temperatures at around and in excess of 1000 °C. Nevertheless, numerous recent studies have shown that the same alloys also perform well in liquid lead and lead-bismuth eutectic (LBE) in the temperature interval of 400-600 °C [1-9], which is the target temperature interval for future LFR applications cooled by pure lead. However, commercial FeCrAl alloys that contain around 15-20 wt. % Cr, are embrittled due to α-α' phase separation within this temperature range [10-13]. In a theoretical study by the authors, it was shown that a FeCrAl alloy that contains 4 wt. % Al also may contain up to 11 wt. % of Cr to avoid α-α' phase separation down to 328 °C [13]. Recent irradiation experiments carried out in the HFIR reactor at Oak Ridge National Laboratory in the US showed nevertheless that α' clusters are formed even in a Fe-10Cr-5Al (wt. %) alloy at 320 °C, although at such small fractions that the mechanical properties of the alloy was seemingly not impaired [14, 15]. In several studies, various FeCrAl compositions have been tested in lead or LBE, after which critical compositional windows (that indicate the formation of alumina) have been proposed. Weisenburger et al. [7] showed that model FeCrAl alloys' containing ≥ 12.5 wt.% Cr and ≥ 6 wt.% Al were able to form thin protective alumina layers in the temperature interval of 400-600 °C. Another work by Lim et al. [6] showed that a Fe-13Cr-4Al alloy would be able to form protective alumina from 500 °C. However, 12.5-13 wt.% Cr is still too much due to the α-α' embrittlement issue motioned above. An important factor, when dealing with FeCrAl alloys, is the reactive element (RE) addition [16-20]. At high temperatures, additions of *e.g.* Y, Zr, Hf improves the alloys oxidation properties by balancing the outward diffusion of metal ions and the inward diffusion of oxygen, which leads to a balanced oxide growth and thus a reduction of mechanical stresses and/or porosity in the oxide layer. Some RE's, like Y, have shown to improve the oxide adherence during thermal cycling by the formation of oxide pegs that penetrate into the metal bulk. The effects of RE-additions in FeCrAl alloys have not yet been thoroughly investigated at low temperatures (400-600°C). However, in a previous study by Ejenstam et al. [8], the importance of Zr and Ti additions was evident for the long-term (10,000 h) corrosion resistance of Fe-10Cr-6Al alloys in liquid lead at 550°C.

The main purpose of this paper is to design a low Cr (10 wt. %) FeCrAl alloy, which is able to form protective alumina in liquid lead environments by optimizing the RE additions.

3.2 Material and experimental

The experiments are divided into three groups, the exposures at 450°C and 550°C for 1000 and 8760 h respectively, the exposure at 650°C for 1400 h, and an exposure at 750°C for 2000 h. The alloys used in the 450°C and 550°C tests are shown in table 1, and the second generation of alloys, exposed at 650°C, are shown in table 2, and the third generation of alloys, exposed at 750°C, are shown in table 3. See table 4 for a summary of important parameters for all four exposures. All Fe-10Cr-4Al alloys from the 2nd and 3rd generation contain different RE compositions, which due to patenting process will not be displayed in this report.

ALLOYS EXPOSED IN THE 450°C AND 550°C TESTS

TABLE 1. Chemical composition (wt. %) and grain size (GS, in µm) of the 1st generation of alloys in the 450°C and 550°C experiments. Impurity levels of oxygen (<35 ppm), nitrogen (<30 ppm) and sulfur (<50 ppm) are expected in the presented alloys.

								RE			
Alloy	**GS**	**Fe**	**Cr**	**Al**	**Si**	**Mn**	**C**	**Ti**	**Zr**	**Y**	**RE/C (at.%)**
Zr-0.1	75.5	Bal.	10.12	3.98	0.12	0.11	0.04	0.08	0.11	-	0.86
Zr-0.2	40.8	Bal.	10.15	3.95	0.13	0.11	0.03	0.09	0.21	-	1.67
Zr-0.4	26.5	Bal.	10.20	4.06	0.12	0.12	0.03	0.07	0.39	-	2.30
Y-0.02	60.1	Bal.	10.26	4.24	0.07	0.12	0.03	0.07	-	0.02	0.67
Y-0.1	27.7	Bal.	10.21	4.14	0.12	0.13	0.03	0.07	-	0.09	0.99
Y-0.2	22.4	Bal.	10.12	4.05	0.12	0.11	0.03	0.08	-	0.19	1.52

ALLOYS EXPOSED IN THE 650°C TESTS

TABLE 2. Chemical composition (wt. %) of the 2nd generation of alloys, exposed to liquid lead at 650°C for 1400h, including references samples. Impurity levels of oxygen (<35 ppm), nitrogen (<30 ppm) and sulfur (<50 ppm) are expected in the presented alloys. RE-additions not included in the table.

2nd generation of Fe-10Cr-4Al	**Fe**	**Al**	**Cr**	**Ni**	**Mo**	**Mn**	**Si**
3	Bal.	3.98	10.11	-	-	0.01	0.15
10A	Bal.	3.96	10.16	-	-	0.20	0.31
10B	Bal.	3.99	10.18	-	-	0.19	0.30
10C	Bal.	3.98	10.07	-	-	0.12	0.16
Reference alloys							
AISI 316L	Bal.	-	18	14	2.5	2.0	0.75
Kanthal APMT™	Bal.	5.0	21	-	3.0	0.4	0.70

ALLOYS EXPOSED IN THE 750°C TESTS

TABLE 3. Chemical composition (wt. %) of the 3nd generation of alloys, exposed to liquid lead at 650°C for 1400h, including references samples. Impurity levels of oxygen (<35 ppm), nitrogen (<30 ppm) and sulfur (<50 ppm) are expected in the presented alloys. RE-additions not included in the table.

2nd generation of Fe-10Cr-4Al	Fe	Al	Cr	Ni	Mo	Mn	Si
8	Bal.	4.00	9.99	-	-	0.01	0.15
Reference alloys							
AISI 316L	Bal.	-	18	14	2.5	2.0	0.75
Kanthal APMT™	Bal.	5.0	21	-	3.0	0.4	0.70

SAMPLE PREPARATION

The influence of Ti, Zr and Y additions on the oxidation properties of Fe-10Cr-4Al alloys was evaluated in this study. The experimental alloys, with varying RE content, were produced in a vacuum induction furnace. Samples were hot-rolled into 8 × 1 mm strips and homogenized at 1050 °C for 5 minutes after each step. The analyzed chemical compositions, as well as the grain sizes, for all studied alloys, are presented in table 1 for the 450°C and 550°C tests, table 2 for the 650°C and table 3 for the 750°C tests. Coupons measuring 30 × 8 × 1 mm were prepared for the oxidation study. The surfaces were polished to a #800 grit finish using SiC abrasive papers, after which the coupons were sonicated in ethanol and subsequently placed in alumina crucibles filled with 2 mm 99.9 % (metal base) lead shots. The oxidation test was carried out in a tube furnace, inside sealed quartz tubes. The dissolved oxygen content in the liquid lead was controlled by means of a flowing Ar-H_2-H_2O gas mixture. H_2/H_2O ratios of 1.3 and 0.2 were used to achieve a dissolved oxygen concentration of 10^{-7} wt.% in the liquid lead at 550°C and 450°C respectively. The H_2/H_2O ratio was set to 1 for both the 650°C and 750°C tests, corresponding to $5x10^{-7}$ and $2x10^{-6}$ wt. % respectively of dissolved oxygen in the lead. A summary of important parameters for all four experiments is shown in table 4. After the exposures, the samples were air cooled and cleaned from residual lead in an acetic acid and hydrogen peroxide (1:1) solution. Transmission electron microscopy (TEM) samples were prepared through the standard lift-out technique using an FEI quanta 3D field emission scanning electron microscope (FEG-SEM), equipped with a focused ion beam (FIB). The TEM evaluation was carried out using a JEOL JEM-2100F FEG TEM. Energy dispersive spectroscopy (EDS) elemental analysis was made using an Oxford Instruments 80 mm^2 X-Max^N silicon drift detector (SDD). SEM samples were prepared by molding the oxidized sample into a conductive resin followed by fine polishing down to the final 0.25 µm diamond step. A Zeiss Leo 1530 FEG-SEM equipped with an Oxford Instruments 50 mm^2 X-Max SDD EDS were used for general characterization. Thermodynamic modeling was carried out using the TCFE7 and SSOL4 databases and the Thermo-Calc software.

TABLE 4. Summarization of important parameters for all four exposures done in this study.

Expusure	Temperature [°C]	Duration [h]	H_2/H_2O ratio	wt.% O in thePb
1	450	1000	0.2	10^{-7}
2	550	8760	1	10^{-7}
3	650	1400	1	$5x10^{-7}$
4	750	2000	1	$2x10^{-6}$

3.3 Results

450°C AND 550°C TESTS

The results from the 8,760 h oxidation test at 550°C showed clear differences in oxidation properties with respect to the RE additions. The three alloys with an excess of C in relation to RE, Zr-0.1, Y-0.02 and Y-0.1, all formed significant amounts of Cr-rich carbides, presumably $Cr_{23}C_6$ according to the thermodynamic calculations, Fig. 1. Remarkably, nearly all Cr-carbides were formed in contact with the Al-rich oxide at the sample surface, Fig. 2.

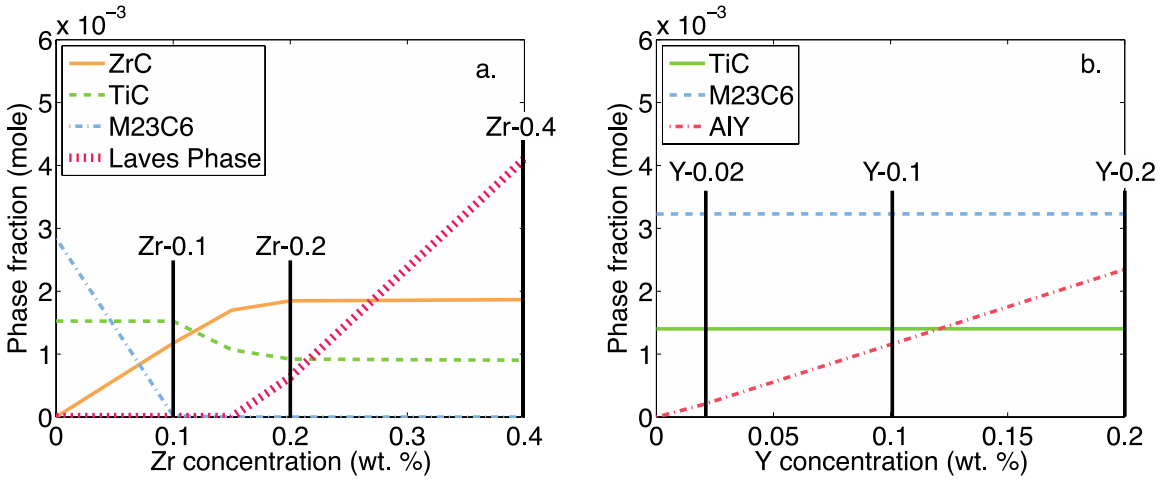

FIGURE 1. Thermodynamic calculations, showing the expected fraction of minor phases (ferrite not shown) at 550°C, for a. Zr concentrations and b. Y concentrations. The vertical lines indicate the studied alloys.

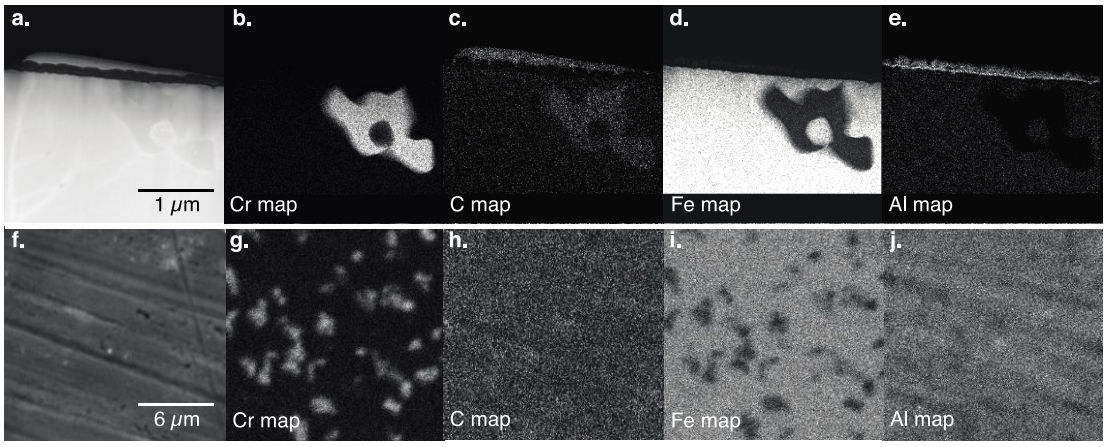

FIGURE 2. Cr-carbides formed under the oxide layer on the Zr-0.1 sample exposed to liquid lead at 550°C for 8,760 h. a. TEM cross-section, b. TEM Cr EDS map, c. TEM C EDS map, d. TEM Fe EDS map, e. TEM Al EDS map, f. SEM micrograph showing a top view of the sample surface, g. SEM Cr EDS map, h. SEM C EDS map, i. SEM Fe EDS map, and j. SEM Al EDS map.

Although $Cr_{23}C_6$ is thermodynamically expected, the C content in the carbides was consequently measured to about 15 at. % using TEM and SEM EDS *i.e.* about 6 at. % lower than expected. The results were confirmed by wavelength dispersive spectroscopy (WDS), which measured the C content to about 14 at. % C. A reference $Cr_{23}C_6$-sample was used

to calibrate the WDS detector prior to the analysis. TEM diffraction pattern analysis could not conclusively differentiate between the two crystallographic space groups, Fm-3m ($M_{23}C_6$) and Fd-3m (M_6C), due to the geometrical similarities. Due to the uncertainties in the identification process, the present Cr-carbides may hence be described as low C surface carbides. The large volume fraction, of such surface carbides in the metal-oxide interface, leads seemingly to a pitting type of accelerated oxidation, displaying inward growing mixed metal oxides measuring up to about 5 µm,3a. In the shorter (1000 h) oxidation test at 450°C, the same three alloys that displayed surface Cr-carbides at 550°C were completely covered with a three-layered oxide structure, consisting of an outward growing Fe_3O_4 layer and an inward growing mixed metal oxide, under which an internal oxidation zone was seen, Fig. 3b. The total depth of the corrosion attacks was measured to 3-4 µm. Two alloys in the study, Zr-0.2 and Y-0.2, contained a minor excess of RE with respect to the C content. While no attacks were found on the Zr-0.2 alloy at 550°C, localized pits were found on the Y-0.2. The thermodynamic prediction indicated formation of a Y-Al intermetallic phase (Fig. 1b.), however, the presence of such a phase could not be confirmed. The absence of C-containing Y-compounds in the thermodynamic database (SSOL 4) made the calculation to propose the formation of $Cr_{23}C_6$ for all Y compositions. The microstructure characterization found µm-sized Y-rich precipitates, which were enriched in C, O, S, and in particular Fe.

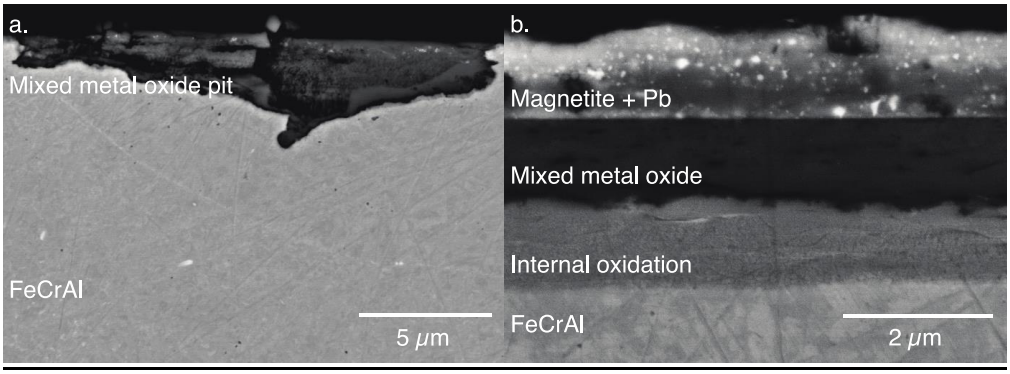

FIGURE 3. SEM cross-section micrographs, showing representative accelerated oxidation attacks at a. 550°C (Zr-0.1) and b. 450°C (Y-0.02).

In the Zr-0.2 sample, high C concentrations were only found in sub-µm sized Ti and Zr-rich precipitates, most likely TiC and ZrC as predicted by the thermodynamic calculations in Fig. 1. A TEM evaluation was carried out to study the surface of the Zr-0.2 sample, and it showed the presence of a thin, approximately 100 nm thick, oxide that had formed during the 8,760 h exposure in liquid lead. The oxide was divided into three layers, an inner layer solely enriched in Al, an outer part rich in Fe and Al, and an intermediate oxide layer rich in Cr, Fig. 4a. The Zr-0.4 alloy contained a large excess of RE compared to C, which also resulted in pitting type oxidation attack. Similar to the Y case, a large excess of Zr is thermodynamically expected to result in the formation of intermetallic phases, such as Laves, Fig. 1a. In the Zr-0.4 sample, Fe and Zr-rich phases measuring up to 2 µm were found throughout the matrix. In addition, the oxide pits on the same alloy were enriched in Zr. At 450°C, the Zr-0.2 alloy again displayed favorable oxidation properties, *i.e.* a protective oxide layer was formed. The thin oxide that formed on its surfaces was investigated by means of TEM and was measured to about 40 nm, Fig. 4b. Similar to the TEM results at 550°C, the oxide formed at 450°C was divided into three zones, with an inner layer enriched in Al, an outer part rich in Fe and Al, and an intermediate Cr-rich layer. Comparable oxidation behavior was observed for Zr-0.4 and Y-0.2 in the 450°C exposure.

Grain sizes of all alloys were evaluated prior to the corrosion tests. The spread between the different alloys were rather large, a difference of about 50 µm was observed for the alloy with largest grains (Zr-0.1) and smallest grains (Y-0.2).

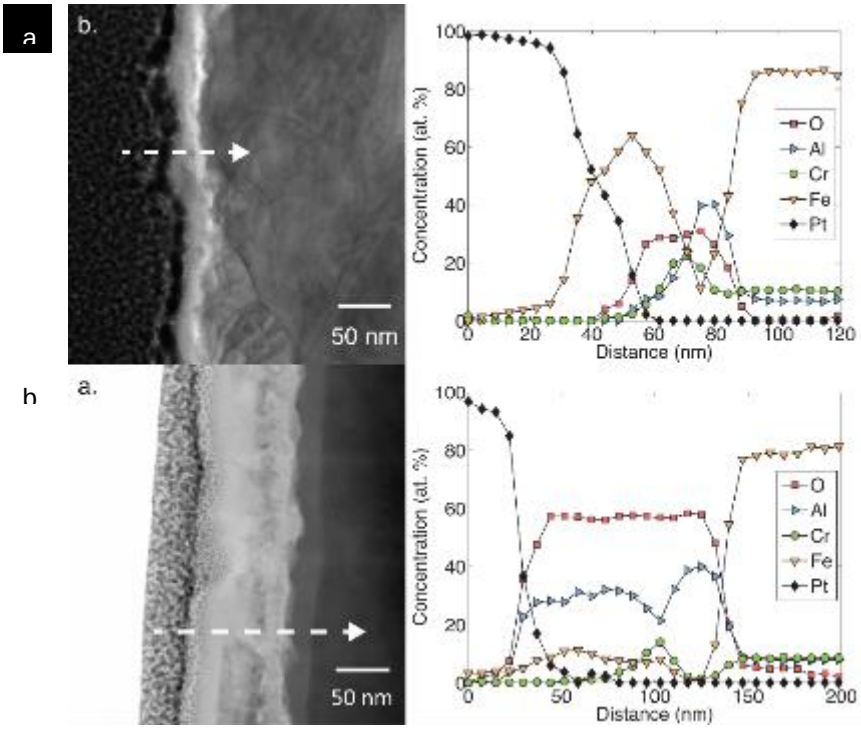

FIGURE 4. TEM BF micrographs showing the alumina layer formed on Zr-0.2 at a. 450°C (1,000 h) and b. 550°C (8,760 h). Corresponding TEM EDS line scans, indicated by dashed arrows in the micrographs, show the chemical composition of the oxides.

650°C TESTS

All 2nd generation of experimental alloys performed very well compared to the stainless steel reference material, AISI 316L. The SEM images in Fig. 5 and 6 shows the large difference between the better experimental alloys, exemplified by alloy 3 (see table 2), and the reference material AISI 316L.

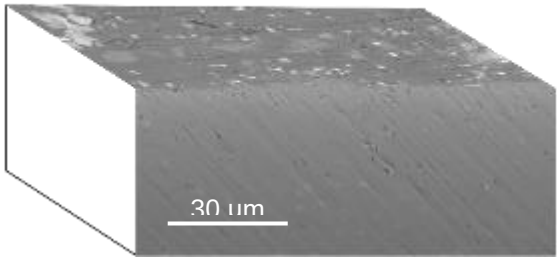

FIGURE 5. SEM-BSE cross section of sample 3 from the second generation of alloys. Thin protective alumina (slightly darker) can be observed in the top part on the micrograph

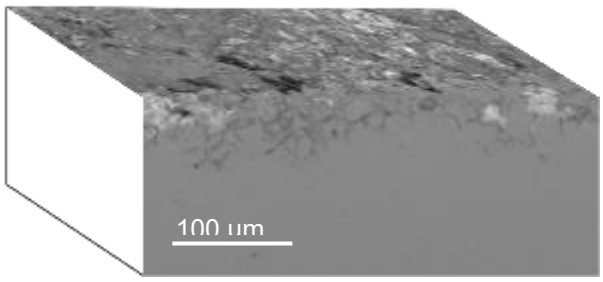

FIGURE 6. SEM –BSE cross section of reference sample AISI 316L. Total attack up to 100 µm.

In Fig. 7, samples 10A, 10B and 10C from table 2 are shown. Sample 10B serves as a reference to the earlier studies made at 450°C and 550°C, and the other two samples have the have the same RE alloying elements, but varying RE/C ratio. Sample 10A have the lowest RE/C value of the three and 10C the highest. 10B have closest RE/C ratio to what was assumed to be optimal from previous studies and showed good results from the experiments. Although sample 10B have suffered from some oxidation attacks at the surface (roughly 20 µm in depth), samples 10A and 10C have attacks covering somewhat larger areas and are slightly deeper (measured up to 40 µm in depth). However, the surface attacks found were relatively minor, and all three alloys showed promising results in exposures.

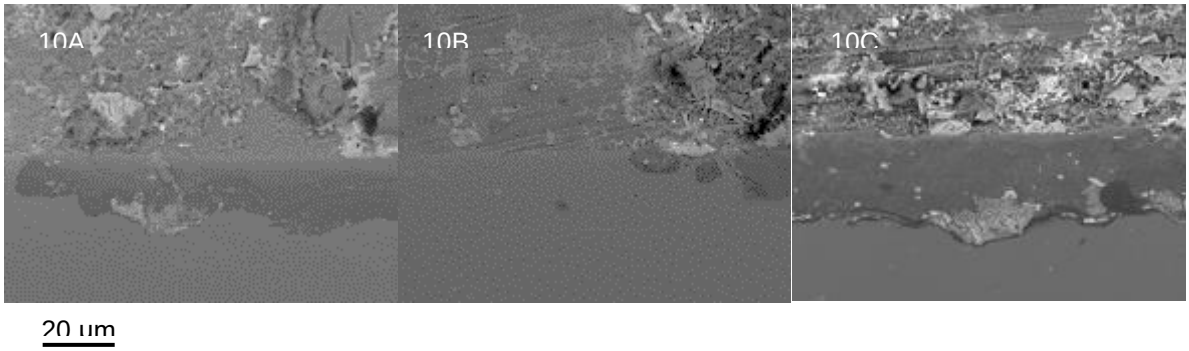

FIGURE 7. *BSE-SEM images of samples 10A, 10B and 10C from the second generation of alloys after exposure to liquid lead at 650°C for 1400h.*

750°C TESTS

In Fig. 8, sample 8 from the 3rd generation of alloys is shown. This sample showed the best result in the 750°C, liquid lead (2000h) test. The upper half of the images (white areas) consists of lead with abrasive particles (black). In between the substrate and lead, an even and consistent protective alumina layer (dark line) can be observed. In Fig. 9, the reference sample Kanthal APMT™ is shown. Comparing Fig. 8 and 9, it is observed that the alumina formed on sample 8 is both thicker and darker. This indicates that the "self-healing" effect of 8 is more efficient at 750°C than for APMT. More oxidation attack was also observed, in greater areas, on the surface of APMT. Thus, it can be concluded that sample 8 has less defects, as well as a more defined and even alumina.

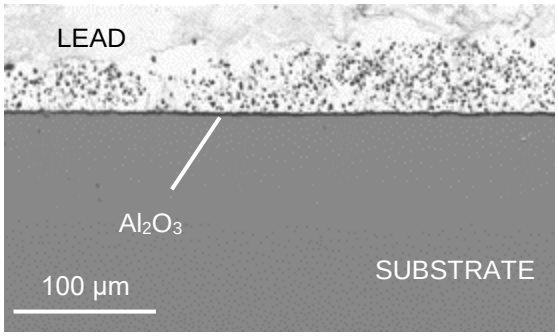

Figure 8. *Sample 8 from the 3rd generation of alloys, Exposure 4, SEM-BSE cross-section. A thin protective alumina (Al_2O_3) (slightly darker) can be observed in the middle of the micrograph.*

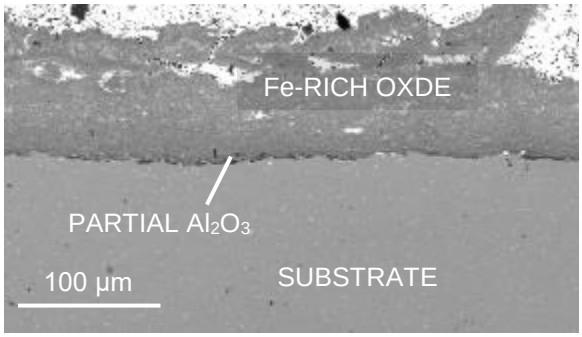

Figure 9. Reference sample Kanthal APMT™, Exposure 4, SEM-BSE cross-section. A partially weak dark alumina-layer can be detected. However, the "self-healing" effect seems to be less efficient compared with sample 8.

Fig. 10 shows one of few defects found on the surface and the EDS analyses from the points marked in the are shown in Table 5. It was unexpected to see such an intact and protective alumina layer for this exposure in lead, as the temperature was relatively high and the exposure time long. Note that the width of the defect is about 100 µm and the depth around 20 µm.

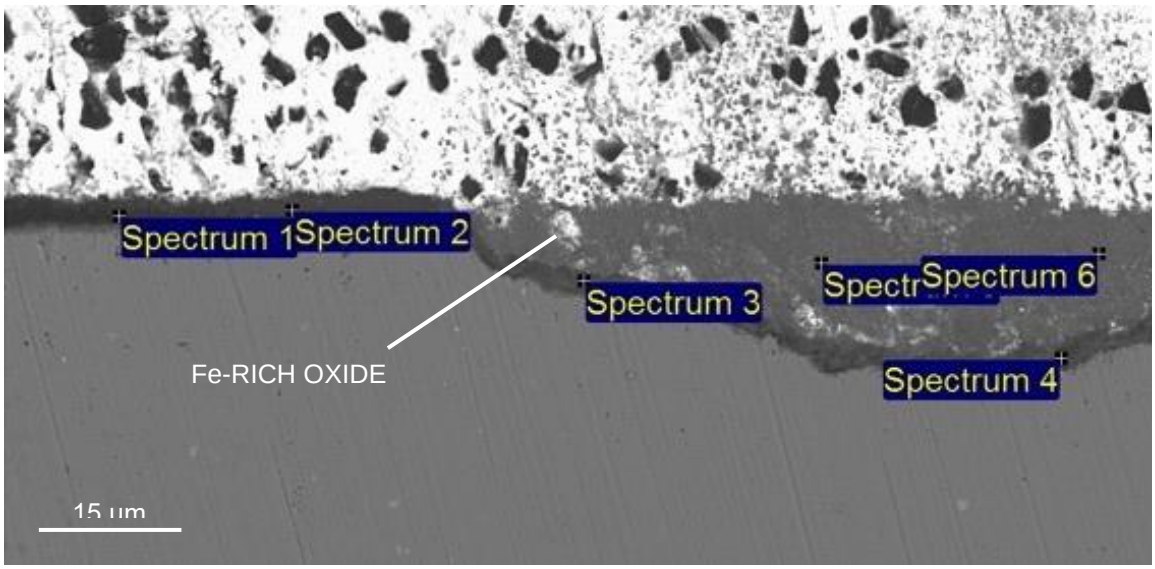

Figure 10. *Sample 8 from 3rd generation of alloys, exposure 4. A dark layer (alumina) has sealed the oxidation attack and prevented further oxidation of the substrate material*

Observing the results from the spectra in table 5, it is seen that the oxidation attack has occurred to the right side of Fig. 10. The oxidation has resulted in an iron rich oxide, which is light grey colour, much like the substrate material. There are some white spot inside this iron rich oxide, which are lead particles that have dissolved down although not managed to penetrate the formed alumina layer. This indicates an efficient "self-healing" effect for this alloy, which will play an important role in long-term exposures.

Spectra 1-4 were taken on the aluminium oxide where 3 and 4 are of a newly formed layer that has prevented further lead penetration. Comparing the compositions from these spectra, the original oxide at the top surface is more Al-rich and is likely of higher Al_2O_3-purity as this layer have had longer time to form than the newly healed alumina layer. It is also worth mentioning that the sample is held in an Al-holder inside the SEM equipment and the observed surface, seen in Fig. 10, is in close contact with this Al-holder. Therefore, it is likely that the Al-contents from this analysis might slightly exceed the true values.

Table 5. *EDS-analyses from Fig. 10. All given in wt. %.*

Spectrum	O	Al	Cr	Fe	Pb
1	45.7	38.9	1.0	9.8	4.6
2	42.5	32.4	0.7	21.1	3.3
3	36.0	18.9	16.5	22.8	5.9
4	34.0	17.9	19.8	26.4	1.9
5	27.8	2.4	16.9	49.0	3.9
6	30.7	3.24	14.0	47.5	4.5

3.4 Discussion

450°C and 550°C tests

The results from this work indicate a clear relation between carbide forming RE additions and the C content of the alloys with respect to the ability to form protective alumina. Alloys having compositions that resulted in surface Cr-carbide formation all displayed reduced oxidation properties. Similar observations were made by Lim et al. [6] when exposing FeCrAl alloys to LBE at 500 °C. In another study, the formation of Cr-rich surface carbides was shown to reduce oxidation properties of FeCrAl alloys, albeit during thermal cycling up to 1200 °C [21]. By balancing the C and RE content, similar to what this work is indicating, the FeCrAl alloy lifetime was shown to increase. However no clear explanation why the carbides precipitate and grow in the metal oxide interface have been presented in literature.

Aluminium suppresses carbide formation and stabilizes graphite. Additionally, Al has been shown to significantly increase the solubility of C in ferritic alloys [22]. Thermodynamically it is expected that the carbon activity in the alloy decrease in the Al-depleted zone that results from the groh of an alumina scale in a hypothetical Fe-10Cr-4Al-0.02C (wt. %) alloy, shown in Fig. 11a. By modeling the Cr-carbide phase fraction as a function of Al content, carbides are expected to precipitate where the Al content is low as the carbon activity gradient flattens with time. In other words, carbon diffuses from the underlying bulk metal to the Al-depleted zone under the alumina scale where Cr-carbides precipitate, Fig. 11b. Moreover, since RE is normally enriched in thermally grown alumina, additional free C may originate from the dissolution of RE-carbides [23-25]. It seems thus likely that the Cr-carbide nucleation and growth is governed by this mechanism, which is schematically shown in Fig. 11c, and it would also explain the unusually large volume fraction of Cr-carbides near the sample surface.

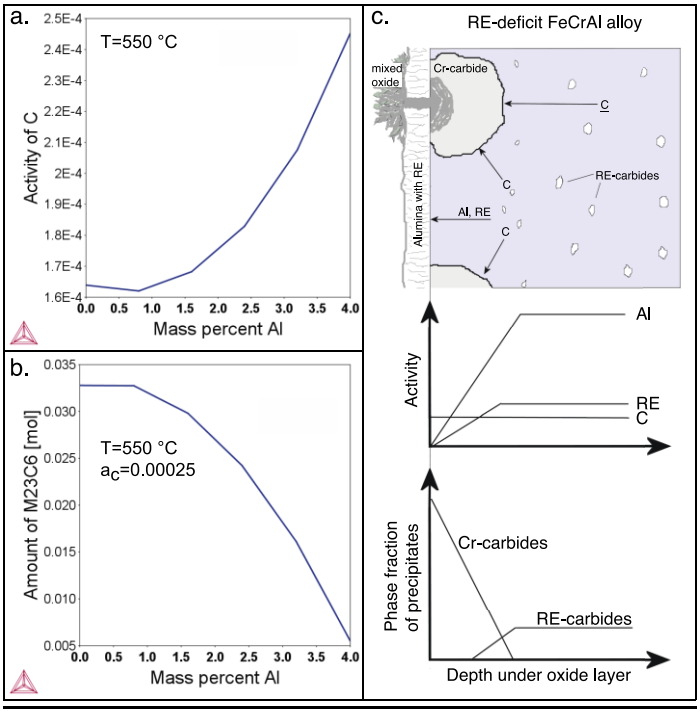

FIGURE 11. a. Thermodynamic modeling (TCFE7) of Fe-10Cr-4Al-0.02C (wt. %) at 550°C showing the carbon activity as function of Al content, mimicking the Al-depleted zone under an alumina scale. b. Showing the amount of M23C6 as function of Al content under a constant carbon activity (a=0,00025). c. Schematic illustration of the proposed mechanism causing Cr-carbide precipitation under the alumina scale in alloys having an excess of C compared to RE.

The type of the Cr-carbides under discussion could not be completely identified in this work. Although the thermodynamic calculations indicated that the carbides should be of $M_{23}C_6$ type, the chemical analysis did not match. The M_6C phase would have matched the measured results better and TEM diffraction was carried out, albeit no

convincing results were achieved. Although the pure Cr_6C exists in theory, the phase is unstable and has not yet been found experimentally [26].

As indicated by the thermodynamic calculations presented in Fig. 1, Zr and Ti forms stable MC-type carbides, whereas no Y-based carbide is predicted. Nevertheless, increasing Y content improved the oxidation properties likely due to the formation of a Y and Fe rich intermetallic compound containing C. In literature, Y_2Fe_{17} have been shown to incorporate C [27], thus increasing the Y content would lead to a reduction of Cr-carbide formation. At 550°C, only the Zr-0.2 showed protective behavior, forming thin alumina, whereas at 450°C, Zr-0.2 alloy, the Zr-0.4 and the Y-0.2 alloy performed in a similar manner. The impact of the excess of Y and Zr did not result in a decrease in oxidation properties at 450°C, which was the case at 550°C. However, the slower kinetics at 450°C in comparison to 550°C as well as a shorter exposure time must be taken into account and may mask the result. Hence, longer oxidation studies should be carried out at 450°C to clarify this. The tested alloys displaying surface Cr-carbide formation at both 450°C and 550°C show corrosion attacks up 5 µm depth. This should be compared to 40-100 nm thin protective alumina scale that formed on the alloys having a balanced RE and C concentrations, *i.e.* where Cr-carbides are thermodynamically suppressed. The crystal structure of the alumina scale was not analyzed. Based on synchrotron x-ray diffraction data in the literature, the Al-rich oxide layer is likely of κ-alumina type [7]. Transient aluminas, like κ-alumina, are normally not considered protective but under presented conditions they seem to be beneficial.

Another factor that influence the oxidation properties is the grain size. Small grains lead to a higher concentration of grain boundaries, which are the primary route for diffusion of metal ions at low temperatures. The spread in grain size between the different alloys were rather large, a difference of about 50 µm was observed for the alloy with largest grains (Zr-0.1) and smallest grains (Y-0.2). In addition, a clear trend was seen where increased Zr and Y content lead to a reduced grain size, which also has been documented in the literature [28]. Regardless of the grain size difference, the influence of a balanced alloy with respect to RE and C was found to be more important for achieving good oxidation properties, *i.e.* formation of alumina on the alloy surfaces.

The general conclusion of this study is that the transition from non-protective mixed metal oxide/Fe_3O_4 layers to protective alumina is possible only if the surface Cr-carbide formation is suppressed by the addition of MC-forming RE additions. Over doping of RE leads to the formation of µm-sized precipitates of intermetallics, likely Laves phase, which seemingly decrease the oxidation resistance of the alloys. Given the presented results, a C and RE free alloy would then perform equally well as a balanced RE/C alloy. However, producing such a C-free alloy is both difficult and expensive. Moreover, precipitation of mono-carbides improves creep strength and RE additions are known to improve the stability of the thermally grown alumina. The combinatory effect of RE and C may thus be utilized when improving both strength and oxidation properties of a FeCrAl alloy.

650°C and 750°C tests

All the 2nd and 3rd generations of alloys were designed to avoid Cr-carbides and have some fundamental differences (lower Cr and Al) from the reference alloys (APMT), it is difficult to evaluate the effect of this factor for the 650°C and 750°C tests. No indications of Cr-carbides were detected by the the SEM-analyses. However, comparing these new alloys with alloys from the previous research, it is clear that the performance has advanced for the better against liquid lead corrosion. Thus, avoiding Cr-carbides is still considered a valid factor to achieve good corrosion resistance.

Many alloys from the 2nd generation showed promising results from the COSTA-experiments in stagnant lead at 650°C. No clear evidence of Cr-carbides was found in any of these experimental alloys. Therefore no evaluation of the Cr-carbide effect on corrosion resistance could be made for these experiments. The alloys 10A, 10B and 10C were designed to evaluate the RE/C-ratio, which by observing the cross-sections of these samples after exposure, showed interesting results. Although all three samples showed good performance in the experimental conditions, sample 10B had smaller and fewer attacks on the surface than the other two. Sample 10B had an RE/C ratio close to that which was argued to be optimal from previous results while 10A had a lower ratio and 10C a higher. This indicates that besides the type and amount of different REs are crucial for the corrosion resistance, the RE/C ratio could also be a major factor.

The 3rd generation of alloys showed surprisingly good performance for the 750°C test in liquid lead. Alloy 8 from the 3rd generation of Fe-10Cr-4Al alloys showed indications of better corrosion resistance than the reference alloy, Kanthal APMT™, which is unexpected considering the low alloying content.

Many of the less well performing alloys from the 3rd generation series had the common factor of having a lower or higher RE/C-ratio than the better performing alloys. This study argued that even though Cr-carbide formation is avoided (by the addition of RE resulting formation of RE-carbides instead), the RE/C-ratio should be close to 2. Even though the

RE content is high enough to suppress Cr-carbide formation, presence of and type of the "free" REs in the matrix seems to be important parameters for the alloy to form a stable and protective alumina scale. On the other hand, an excessive amount of REs can result in too much intermetallic phases, which also can disrupt the corrosion protection if present beneath the surface of the alloy.

Furthermore, this could be an indication that optimization of RE/C-ratio can aid the corrosion resistance towards liquid lead. However, some of the inadequate performing alloys had a RE/C-ratio close to 2, and some of the better performing alloys had different ratios. This speaks for other critical factors that affect the corrosion resistance of the alloys. Examples of such factors are the combination of REs, as well as the contents. Due to on-going patenting process, the specific details of the findings made in this study, related to the RE combinations and compositions, will not be discussed further in this report.

3.5 Conclusions

Formation of alumina layers on Fe-10Cr-4Al-based alloys were investigated in liquid lead at 450°C (1,000 h) and 550°C (8,760 h). Transition from non-protective mixed metal oxide/Fe_3O_4 layers to protective alumina occurs when more stable carbide formers, such as Ti and Zr, suppress Cr-carbide formation. An excess of RE leads to the formation of intermetallic phases, which at 550°C lead to transition from protective alumina back to non-protective mixed metal oxide/Fe_3O_4 layers, despite grain size-reducing effect of high RE content. Cr-carbide formation at the surface were shown to be detrimental to the alloys oxidation properties, especially at 450°C. A thermodynamic explanation for the formation of surface Cr-carbides is proposed, which is based on the changes in C-activity in the Al-depleted zone under the oxide layer. Presented results show that it is possible to form protective alumina layers on ductile FeCrAl alloys, containing as low as 10 wt.% Cr and 4 wt.% Al, given that the RE and C concentrations are strictly controlled and optimized. These results show that it is feasible to design ductile alumina-forming FeCrAl alloys as construction materials in corrosive environments at temperatures as low as 450°C.

Based results and conclusions made from the 450°C and 550°C experiments, a 2nd generation series of allos (see table 2) were developed to avoid Cr-carbide formation and to find an optimal RE-balance. These experimental alloys were exposed to 650°C test in liquid lead for 1400 h (see exposure 3, table 4). From this exposure, following conclusion could be made:

- Low Cr-FeCrAl alloy, with good RE additions, perform better than the reference stainless steels in liquid lead environments.
- For the alloys tested in the liquid lead environment, the concept of optimised RE additions were demonstrated, as well as the concept of RE/C-ratio.
- The temperature used in the liquid lead exposures, 650°C, was not high enough to clearly differentiate between the experimental alloys. In other words, the alloys showed a greater potential than what was expected at the start of the project.

A 3rd generation of alloys (see table 3) were then developed based on the previous results. The aim was to further optimize RE addition and fine balance them, as well as supress Cr-carbide formation. These new experimental alloys were exposed to liquid lead at 750°C for 2000h. After the exposure, following conclusion could be made:

- Some low Cr-FeCrAl alloys from the 3rd generation series performed better than the reference FeCrAl alloys in high temperature lead environments.
- The experimental Fe-10Cr-4Al alloys were designed to supress Cr-carbide formation. Thus, it is difficult to evaluate the effect of this factor for the corrosion resistance. Although, due to the good performance, it could be an indication that Cr-carbide formation should be avoided for increased corrosion resistance.
- The concept of optimising the RE/C-ratio was again indicated to be of importance. However, other factors' relating to REs seems as critical for the corrosion resistance. Due to an on-going patent process, the specific details on the findings made in this study, related to the RE combinations and compositions, will not be discussed further in this report.
- The alloys showed surprisingly good results in exposure of liquid lead at 750°C for 2000h. The exposure temperature would need to be increased further in order truly identify the optimal composition as well as to benchmark these new FeCrAl-alloys.

3.6 Acknowledgements

Sandvik Heating Technology AB is greatly acknowledged for providing model alloys and know-how. The authors are particularly thankful for the kind help provided by F. Rave, D. Chandrasekaran, T. Helander, R. Berglund and P. Byhlin. O. Karlsson (SEM and EBSD) and F. Lindberg (FIB-SEM and TEM), both at Swerea KIMAB, are thanked for helping out with microscopy analyzes. The authors are also grateful for the fruitful input and guidance from Prof. J. Wallenius (Div. Reactor Physics, KTH), adj. Prof. R. Pettersson (Jernkontoret and Div. Surface and Corrosion Science, KTH) and adj. Prof. M. Lundberg (Sandvik Materials Technology AB and Div. Surface and Corrosion Science, KTH).

References

1. R.C. Asher, D. Davies and S.A. Beetham, Corrosion Science **17**, 545 (1977).
2. M. Kondo and M. Takahashi, Journal of Nuclear Materials **356**, 203 (2006).
3. P. Hosemann, H.T. Thau, A.L. Johnson, S.A. Maloy and N. Li, Journal of Nuclear Materials **373**, 246 (2008).
4. J. Lim, H.O. Nam, I.S. Hwang and J.H. Kim, Journal of Nuclear Materials **407**, 205 (2010).
5. M. Del Giacco, A. Weisenburger, A. Jianu, F. Lang and G. Mueller, Journal of Nuclear Materials **421**, 39 (2012).
6. J. Lim, I.S. Hwang and J.H. Kim, Journal of Nuclear Materials **441**, 650°C (2013).
7. A. Weisenburger, A. Jianu, S. Doyle, M. Bruns, R. Fetzer, A. Heinzel, M. DelGiacco, W. An and G. Muller, Journal of Nuclear Materials **437**, 282 (2013).
8. J. Ejenstam, M. Halvarsson, J. Weidow, B. Jonsson and P. Szakalos, Journal of Nuclear Materials **443**, 161 (2013).
9. N.S.C. OECD Nuclear Energy Agency, Handbook on lead-bismuth eutectic alloy and lead properties, materials compatibility, thermal-hydraulics and technologies, 2015 ed., OECD Nuclear Energy Agency no. 7268, 2015
10. J.L. Bartos, *The nature of aging of Fe-Cr-Al-Y alloys at 450°C C*, Technical report No. GEMP 709 (General Electric Company 1969).
11. C. Capdevila, M.K. Miller, K.F. Russell, J. Chao and J.L. Gonzalez-Carrasco, Materials Science and Engineering a-Structural Materials Properties Microstructure and Processing **490**, 277 (2008).
12. S. Kobayashi and T. Takasugi, Scripta Materialia **63**, 1104 (2010).
13. J. Ejenstam, M. Thuvander, P. Olsson, F. Rave and P. Szakalos, Journal of Nuclear Materials **457**, 291 (2015).
14. K.G. Field, X.X. Hu, K.C. Littrell, Y. Yamamoto and L.L. Snead, Journal of Nuclear Materials **465**, 746 (2015).
15. P.D. Edmondson, S.A. Briggs, Y.Yamamoto, R.H. Howard, K. Sridharan, K.A. Terrani and K.G. Field, Scripta Materialia **116**, 112 (2016).
16. H. Hindam and D.P. Whittle, Oxidation of Metals **18**, 245 (1982).
17. J. Stringer, Materials Science and Engineering a-Structural Materials Properties Microstructure and Processing **120**, 129 (1989).
18. F.H. Stott, G.C. Wood and J. Stringer, Oxidation of Metals **44**, 113 (1995).
19. B.A. Pint, Oxidation of Metals **45**, 1 (1996).
20. B.A. Pint, *"Progress in understanding the reactive element effect since the Whittle and Stringer literature review"* in John Stringer Symposium on High Temperature Corrosion, edited by P.F. Tortorelli, I. G. Wright and P.Y. Hou, Proceedings from Materials Solutions Conference, Materials Park, OH, ASM, Indianapolis, IN, 2003, pp 9-19.
21. V. Kochubey, D. Naumenko, E. Wessel, J. Le Coze, L. Singheiser, H. Al-Badairy, G.J. Tatlock and W.J. Quadakkers, Materials Letters **60**, 1654 (2006).
22. W.C. Leslie and G.C. Rauch, Metallurgical Transactions a-Physical Metallurgy and Materials Science **9**, 343 (1978).
23. D. Naumenko, K. V, J. Le-Coze, E. Wessel, L. Singheiser and W.J. Quadakkers, High Temperature Corrosion and Protection of Materials 6, Prt 1 and 2, Proceedings **461-464**, 489 (2004).
24. E. Wessel, V. Kochubey, D. Naumenko, L. Niewolak, L. Singheiser and W.J. Quadakkers, Scripta Materialia **51**, 987 (2004).
25. S.G. Gopalakrishnan, P. Huczkowski, J. Pernpeintner, T. Fend, H. Hattendorf, R. Iskandar, J. Mayer, L. Singheiser and W.J. Quadakkers, Materials at High Temperatures **29**, 249 (2012).
26. C.M. Fang, M.A. van Huis and H.W. Zandbergen, Computational Materials Science **51**, 146 (2012).
27. B. Li, S. Wu, Y. Teng, C. Liu, Y. Yan, Z. Zhao and H. Wu, Acta Metallurgica Sinica **32**, 926 (1996).
28. K.A. Darling, B.K. VanLeeuwen, J.E. Semones, C.C. Koch, R.O. Scattergood, L.J. Kecskes and S.N. Mathaudhu, Materials Science and Engineering a-Structural Materials Properties Microstructure and Processing **528**, 4365 (2011).

4 Effect of alumina coatings on corrosion protection of steels in molten lead – contribution by CNR

E. Vassallo, M. Pedroni, and V. Spampinato, S. M. Deambrosis, E. Miorin, E. Ricci and V. Zin

Abstract

Lead alloys are attractive candidates as coolants for future generation nuclear reactors (fast reactors - FR). Unfortunately, they easily corrode structural steels of reactors. To mitigate this phenomenon, surface protective coatings may be applied. In this study, T91 steel (Cr9Mo1) samples were coated with Aluminum Oxide coatings (Al-O) deposited by Radio Frequency Magnetron Sputtering (RF-MS). The alumina coatings were characterized using SEM–EDS, XRD and tribological techniques. A corrosion test of coated steel samples was performed in stagnant lead at 550°C for 1200 h and none of the samples revealed corrosion signs.

4.1 Introduction

Lead alloys are considered very interesting materials for applications as coolants for next generation nuclear reactors[1]. Indeed, they offer a number of attractive chemical, thermal, physical and nuclear properties such as chemical inertness with air and water, low vapor pressure over the relevant temperature range, high boiling point and high atomic number. However, one of the main concerns with the use of liquid metals is their compatibility with the containment structure. Lead is actually very corrosive to common steels used in nuclear plants. This has been widely recognized as a critical issue to be solved before accepting a general use of lead coolants. Moreover, it is well known that the corrosion behaviour of steels depends on the oxygen concentration in the liquid Pb[2]. Yeliseyeva et al.[3] have determined different interaction modes of steels which change from the dissolution in lead, when the oxygen content in the melt is $Co \leq 10^{-10}$ wt%, to the formation of protective oxide layer on the surface of steel, when the oxygen concentration is approximately between 10^{-6} and 10^{-4} (in wt%), i.e. the so-called " oxygen- added Pb" or " mixed domain"[4]. Under these conditions neither a severe oxidation accompanied by formation of thick multilayer scale, that could inhibit further oxidation and prevent a direct contact between the material and the molten metal, nor the dissolution of steel and intergranular penetration of liquid Pb should occur. This can be attributed to the low oxygen concentrations that may hinder the formation a protective oxide layer. On the other hand, at $Co \geq 10^{-3}$ wt%[5-6], indicating a saturation of molten Pb by oxygen, the formation of multiphase oxide scales[3] can occur, not necessary protective. Therefore, in order to limit the corrosion risk for structural materials the most used protection method up to 500°C, consists in the fine control of oxygen dissolution in Pb and LBE. Indeed, the oxygen content should be high enough to allow a stable oxidation of the structural material, but it should remain below a threshold not to promote the precipitation of lead oxide [2, Chapters 4 and 6]. Surface engineering, and in particular surface alloying and protective coatings, could allow working in a wider range of oxygen potentials. Anyway, although the formation of protective oxide films under "mixed domain" conditions is effective in preserving corrosion resistance in HLMs, austenitic steels suffer from severe corrosion attack in lead, at temperatures above 500°C. Indeed, at high temperature, the formation of a non-protective and non-stable double-layered oxide was observed [2, 7-8]. In addition, ferritic/martensitic steels form thick oxide scales that periodically may spall off plugging the cooling channels[8]. Finally, even when a compact layer of chromium oxide is formed, it was reported to quickly dissolve at about 500°C[9]. For a typical unprotected austenitic steel exposed to liquid lead, the dissolutive process can proceed at the speed of 200 μm/year at 550°C and 10^{-7} wt% oxygen[2]. Therefore, the surface engineering method is studied in order to increase the operating temperatures above 500°C without serious corrosion. Even in this case, the corrosion mitigation strategy involves the growth of a passivating and adherent layer, containing strong oxide-forming elements (e.g. Al, Si)[2, Chapters 4 and 6]. Rivai et al.[10] reported the results observed on the samples of high Cr steels uncoated and coated with Al-Fe layer and subsequently processed under the same operating conditions. A very thin oxide layer was formed on the surface of the coating which was stable at least for 1000 h, protecting the steel from both LBE and lead attack. Similar studies on the effectiveness of the surface treatment of steels with various aluminum alloying techniques have been reported[11-16]. Overlay coatings represent an attractive solution to overcome this problem

in the short-term since there are several well-known technologies industrially used to protect steels. FeAl based films, Si and Al oxides, Cr, Ti, Si and Zr nitrides and carbides have been deposited using different techniques such as Vacuum Plasma Spray (VPS), Chemical Vapor Deposition (CVD) and PVD oxide[2, Chapters 9] and references therein,[17]. However, specific tests in HLMs are still required. Serious consideration must be given not only to microstructural and compositional characteristics that favor corrosion resistance, but also to adhesion, which is equally paramount. Indeed, the areas that are most prone to degradation are located at the interfaces coating/environment and coating/substrate. The sputtering techniques are among the most used since they allow the production of high quality and dense coatings with the ability to adjust the chemical composition in a wide range. Reactive sputtering is carried out in order to deposit compounds (i.e., oxides or nitrides) by introducing into the process chamber a gas or a mixture of gases that reacts with the target material to form a coating of a desired chemical composition. Sputtered[18-21] and reactively sputtered films[22-23] were extensively studied due to their useful properties such as chemical inertness, mechanical strength, hardness. Concerning material selection, in recent years aluminum oxide films received great attention, since, the alumina is a highly insulating material and shows low ion mobility. Therefore, an alumina layer can inhibit a further oxide growth acting as an effective oxygen diffusion barrier. Nowadays, aluminum oxide thin films are widely used in different industrial applications from microelectronic and optical applications to wear and corrosion protection[24-26]. In this research work, alumina-like thin films were deposited in a Radio Frequency Magnetron Sputtering (RF-MS) reactor by sputtering an aluminum target in an oxygen/argon atmosphere. This PVD technology is known to be one of the excellence methods for the production of insulating coatings such as oxides and nitrides[27]. The corrosion resistance was tested by the exposure of bare and coated T91 steel substrates to static molten lead at 550°C for 1200 h.Morphology, chemical composition, crystalline structure, mechanical and tribological properties of films, before and after the molten lead test, were deeply investigated. Scanning Electron Microscopy (SEM) and Energy Dispersive Spectroscopy (EDS) were used to evaluate the surface morphology and to measure the elemental distribution along each films thickness. Wear tests in dry conditions, scratch tests and nanoindentation measurements were carried out, to evaluate the effects of molten lead on the mechanical properties.

4.2 ***Materials and methods***

4.2.1Coatings deposition

T91 steel (nominal composition Cr 8.3, Ni 0.13, Mo 0.95, Mn 0.4, V 0.2, Nb 0.08, Si 0.4, N 0.02, C 0.11, Fe Balance in wt.%) rectangular substrates and specimens were cut to a dimension of approximately 10 mm x 20 mm x 4 mm. Before deposition, the substrates were polished to a 1 µm diamond finish and then cleaned in an ultrasonic bath with acetone, water rinsed and finally dried in nitrogen flux. Al-O coatings were deposited by RF-MS (13.56 MHz), using an Al target (99.99% purity) with 3-in diameter. The substrates were placed onto the grounded sample holder under the RF powered electrode. Prior deposition the chamber was evacuated to a pressure lower than $1x10^{-5}$ Pa and the substrate temperature was monitored by means of a thermocouple placed in contact with the sample. Thin films depositions were carried out at 260°C. Argon (99.999%) as working gas and oxygen (99.999%) as reactive gas were introduced into the chamber through a mass flow controller and the O_2 flow was fixed at 11%. Total gas pressure and total gas flow rate were fixed at 1 Pa and 20 sccm, respectively. The target to substrate distance was kept constant at 45 mm. In Table 1, the main used working parameters for alumina coating deposition are shown.

TABLE I. Working parameters set for Al-O coating deposition.

SUBSTRATE PRETREATMENT	Ultrasound Cleaning	Yes
	Plasma Etching	Yes
FILM DEPOSITION		
	Mean Cathode Power Density (W/cm^2)	2.3
	Pulse Frequency (MHz)	13.56
	Gas	Ar + O_2
	Total Pressure (Pa)	1
	Substrate Bias Voltage (V)	Grounded
	Deposition Temperature (K)	530

4.2.2Corrosion Tests

Corrosion tests in stagnant liquid lead were carried out in the CorAL (**Cor**rosion **A**pparatus for **L**iquid metal) experimental facility[28]. It is characterized by a 25 cm diameter vacuum chamber, which contains a furnace by an alumina case with a Kanthal A1 resistance, which can be heated up to 1030 °C. A K-type thermocouple operates as feedback for the temperature controller, which ensures an accuracy of ±3 K. An Al_2O_3 crucible (20 mm x 30 mm) contains the liquid metal bath. The apparatus is equipped with both a primary vacuum system and with a gas feed to maintain a controlled inert atmosphere inside the experimental chamber. The oxygen partial pressure of the gas above the liquid level is monitored by a solid-state electrode. The sensor is an electrochemical ZrO_2 micro gauge (SETNAG®) with built in Pd/PdO metallic reference. By fluxing the high purity Ar (99.9999 at%), the resulting oxygen partial pressure in the atmosphere surrounding the samples was measured 10^{-2} Pa which corresponds to an oxygen content in the bath of about 10^{-6} wt% .The steel samples (20x12x3mm) are immersed in the lead bath for about 2/3 of their length by the push-pull feedthrough only when both the atmosphere inside the chamber and the desired temperature of the bath are reached. An uncoated T91 sample (as reference) and an Al-O coated substrate have been simultaneously immersed in the lead bath at T= 550°C and maintained under equilibrium conditions for an exposure time of 1200 h. The uncoated T91 sample was previously metallographically polished and ultrasonic cleaned in an ethanol bath. After the required exposure time the samples were pulled out the bath and the apparatus was cooled. The two samples were not chemically etched to remove the residual adherent lead but directly prepared for the microscopic analyses by applying a standard procedure for a cross-section metallographic analysis[(2, Chapters 6, (Par 6.7.3))].

4.2.3Coatings characterizations

Coating thickness was evaluated by means of ball crater micro-abrasion method by a Calotest (CSM Instruments now Anton Paar). ImageJ software[29] was used to carry out image analysis and measure geometrical parameters of obtained tracks. Average coating thickness was calculated from the equation described by Fildes et al.[30]The morphology and microstructure of samples before and after oxidation in molten metal were analyzed by a Sigma Zeiss Field Emission Scanning Electron Microscope (FE-SEM), equipped with an Oxford X-Max energy dispersive spectroscopy (EDS) system. SEM-EDS was also used to assess the elemental distribution along the film thickness. The crystalline phases in the specimens were identified by using X-Ray Diffraction (XRD), with a Philips PW 3710 diffractometer operating in Bragg-Brentano geometry and equipped with a Cu-Kα source (40 kV, 30 mA). Spectra were first evaluated with Match! 2.2.1 software to identify the crystalline phases from the position of the detected peaks. Data were elaborated with Maud 2.46 software[31-32] to measure mean grain size and cell parameters through the iterations of Rietveld method, applied

to peaks broadening and positions[33]. Adhesion was investigated by scratch tests using an UMT-2 tribotester (CETR now Bruker), equipped with a standard Rockwell C diamond indenter (angle 120° and spherical tip radius 200 μm). Measurements were performed in compliance with the European standard UNI EN 1071-3 standard[34] for ceramic materials in Progressive Loading Scratch Test (PLST) mode. The coating/substrate adhesion was quantified through the failure critical load Lc3, at which adhesive failure was initiated due to the coating delamination. Tribological tests to evaluate friction and wear behaviour, were carried out in dry conditions with the UMT-2 tribotester, set for pure sliding contact. *Ball-on-flat* geometry was chosen, in order to achieve a 1 GPa Hertzian contact pressure on coupled surfaces, thanks to a non-conformal contact type. 5 mm diameter alumina balls with hardness in the range 1250-1700 HV were used as counterparts. Wear tests were conducted up to 3500 cycles at a speed of 10 $mm \cdot s^{-1}$ and frequency of 1 Hz.

4.3 Results and discussion

This work is aimed at checking the effectiveness of alumina coatings in the protection against corrosion by molten lead of T91 steel structural elements. The RF-MS technique has been chosen in order to grow a non-conductive material.

4.3.1Corrosion test

The effectiveness of the coatings was tested in an environment simulating the operating conditions for a sufficiently long time to get reliable results. In Figure 1, T91 specimens (uncoated (1a) and with Al-O coating (1b)) are presented after 1200 h testing in molten lead at 550°C. The uncoated substrate is showed in Fig. 1(a) and appeared evidently corroded after the experiment, since a thick non-adherent oxide scale was produced and it diffusely detached from the bulk. On the contrary, from a macroscopic point of view, the Al-O coated sample (Fig. 1(b)) did not seem to have suffered apparent modifications.

FIG. 1. Samples after 1200 h testing in molten lead at 550°C, a) uncoated T91 substrate, b) Al-O coated sample.

4.3.2Scanning Electron Microscopy and Energy Dispersive Spectroscopy

As previously mentioned, all the samples were analyzed just after the extraction from the crucible. None etching treatment was performed to remove possible residual lead. No additional oxide layer was detected above the Al-O coating after the Pb test. Top view SEM images (Fig. 2) of the Al-O sample in the as deposited state and after molten Pb test, did not show any significant changes of the sample surface morphology, except for negligible amounts of residual solidified lead detected just in some restricted areas. Both the samples showed the typical surface morphology of a dense, nanostructured PVD film. It could be deduced that alumina-like deposited coating is only slightly wetted by liquid lead. On the contrary, EDS analyses (Tab. 2) pointed out an oxygen content decrease. Since aluminium has greater

affinity for oxygen than lead, the reason for this oxygen content drop within the coating needs a further investigation. Moreover, considering EDS results after molten Pb test, the Al-O coating is characterized by a slight increase of metallic elements of the substrate (i.e. Fe and Cr). This proves a little diffusivity of these metallic elements trough the coating thickness.

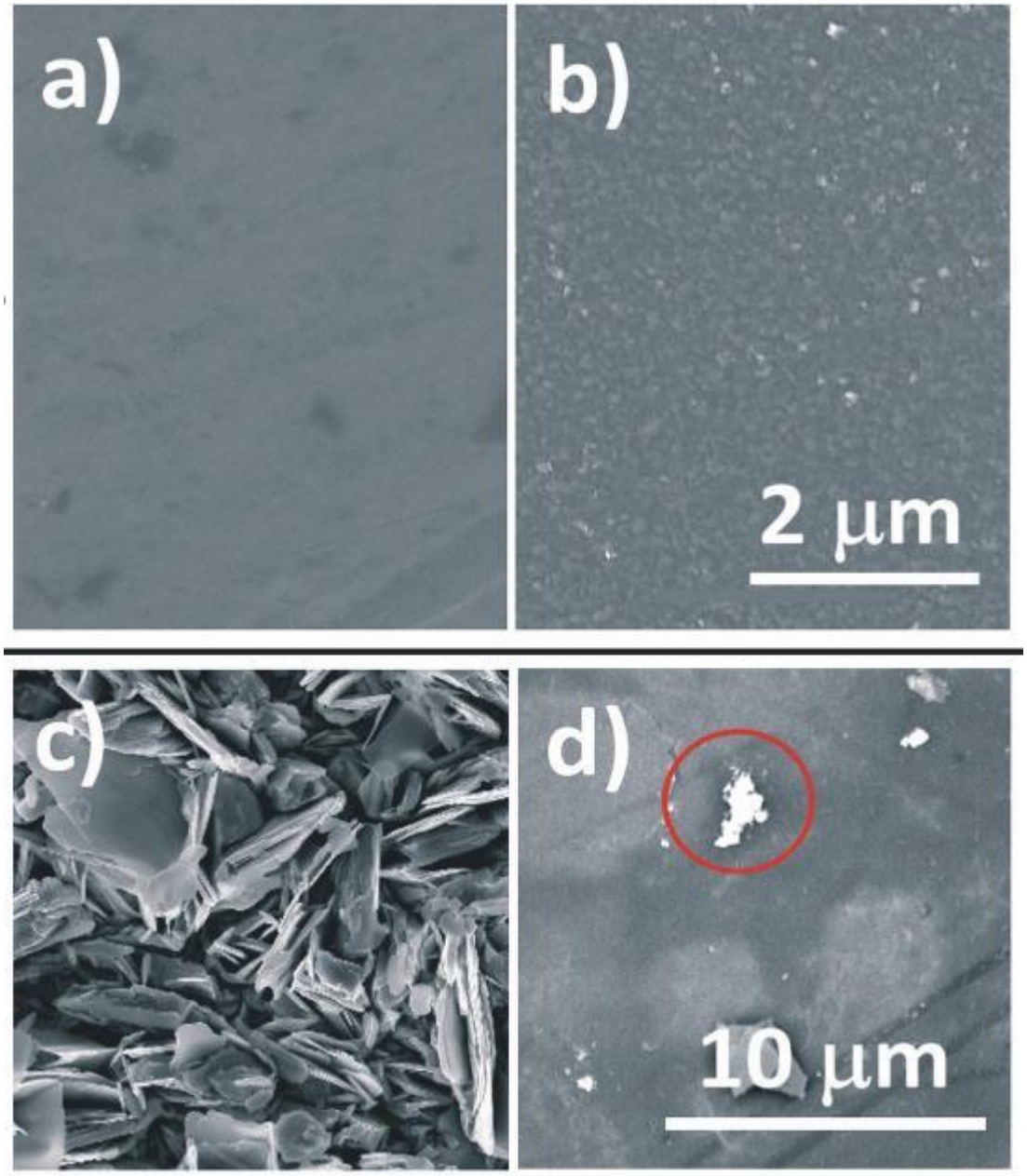

FIG. 2. (Color online) Top view SEM images of T91 substrate (without Al-O coating) before (a) and after (c) molten lead test. SEM images of T91 substrate with Al-O coating before (b) and after (d) molten lead test. In the red circle of (d) picture Pb-rich particles are showed.

TABLE II. EDS analysis of the top surface of the samples.

	As deposited Al-O coating on T91	After molten Pb test
Element	Atomic%	Atomic%
O K	74.0	60.6
Al K	25.0	35.5
Cr K	/	0.4
Fe K	0.8	1.9
Pb M	/	1.4

SEM images and EDS elemental profiles of the sample cross section (Fig. 3) confirmed the Al-O film presence with an uniform distribution of Al and O into the coating. No formation of an oxide scale above the protective coating is detectable. A thickness of 1.5 micron was measured by calotest for as deposited coating. As it can be verified looking at Fig. 3, the coating thickness after molten Pb test did not change. Coating was still intact, adherent and compact. EDS analysis did not show detectable signals of bath elements diffusion through the film towards the steel substrate nor film elements diffusion into the substrate. As a result, T91 was not corroded.

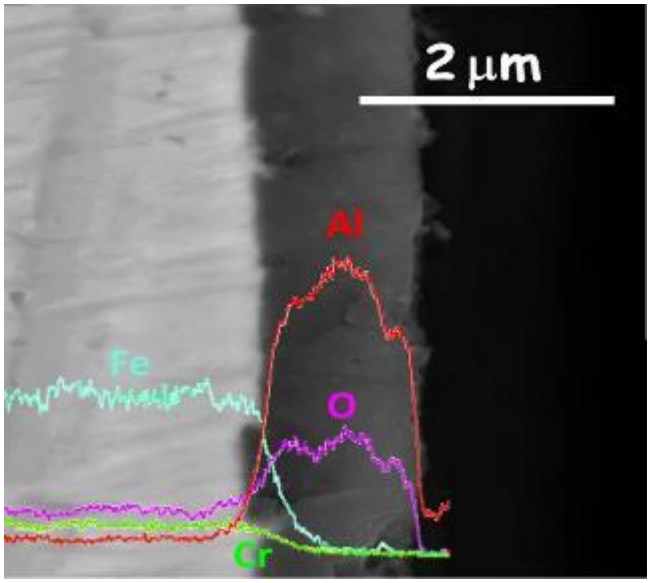

FIG. 3. (Color online) SEM image of the cross section of an Al-O coated sample after exposure test in molten lead. Obtained EDS elemental distribution profiles are visible.

4.3.3X-Ray Diffraction

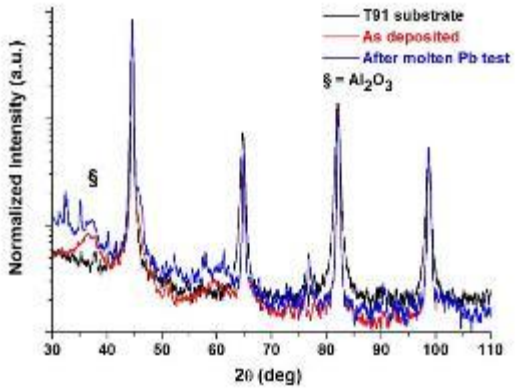

FIG. 4. (Color online) XRD spectra of T91 substrate (black), as deposited coated sample (blue) and after molten Pb test (red). The patterns are shown in logarithmic scale.

XRD structural characterization confirmed that Al-O film was still present after molten Pb test, and its microstructural properties were unchanged (Fig. 4). For Al-O specimens γ-phase alumina is usually expected, when the substrate temperature is around 200°C[35]. Anyway, it was possible to detect just a little crystallized Al_2O_3 phase, presumably monoclinic theta type, for both "as deposited" and "after molten Pb test" samples. The other observed peaks were associated with reflections from the T91[36] substrates.

4.3.4Scratch test

In order to investigate the film/substrate adhesion, scratch tests were performed too. The analyses were carried out by progressive load scratch test (PLST) mode in which the applied normal load increases linearly with time. In Figure 5, the coefficient of friction (COF) variations as a function of the applied normal load (F_Z) are shown. Moreover, the SEM images of the tracks were associated to the experimental curves. As it can be seen for Al-O sample, the failure load (Lc3) decreased after molten Pb test.

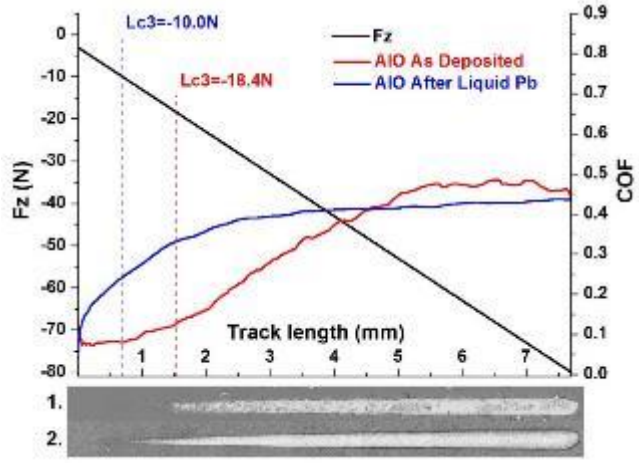

FIG. 5. (Color online) Progressive Load Scratch Test (PLST): applied load (Fz) and coefficient of friction (COF) vs. scratch length for an Al-O sample. The corresponding tracks SEM images are shown: 1 (as deposited) e 2 (after test).

4.3.5Wear

Severe dry wear tests were performed before and after molten Pb test by using an alumina ball as counter - body. For the Al-O sample, after Pb test Coefficient of Friction (COF) increased and coating failed before the “as deposited” one.

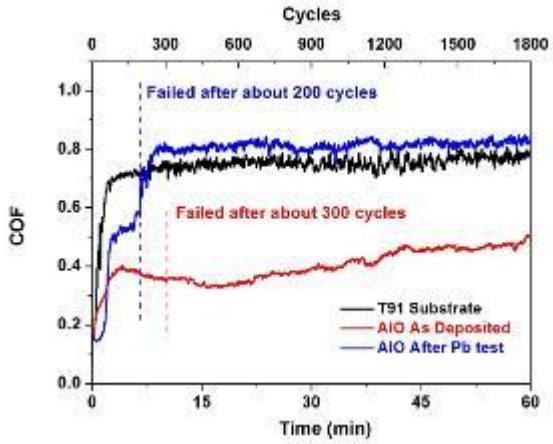

FIG. 6. (Color online) Friction coefficient vs number of cycles-time diagrams of substrate and deposited Al-O coating. As deposited Al-O coating failed after about 300 cycles; molten lead tested Al-O coating failed after about 200 cycles.

4.4 Summary and conclusions

Coating deposition is an effective method to protect structural materials of the next generation nuclear reactors against heavy liquid metal corrosion. Preliminary results showed Al-O can be corrosion resistant against liquid lead. RF-MS technology allowed obtaining dense and high performance coatings. From the experimental results, it emerged that the tribological properties of coatings were affected by the molten lead test. Anyway, this did not seem to correlate with the resistance to corrosion. However, further studies are required to clarify this aspect. Further steps to validate the acceptability of such coatings under relevant conditions for fast reactors are in progress (i.e. a 5000 h medium duration corrosion test).

[1]L. Cinotti, C.F. Smith, H. Sekimoto, L. Mansani, M. Reale, and J.J. Sienicki, J. Nucl. Mater. **415**, 245 (2011)

[2] Nuclear Energy Agency, *Handbook on Lead-bismuth Eutectic Alloy and Properties, Materials Compatibility, Thermal-hydraulics and Technologies*, (NEA. No. 7268, OECD/NEA, Paris, 2015)

[3]O.Yeliseyeva, V.Tsisar, and Z.Zhou, J. Nucl. Mater. **442**, 434 (2013).

[4]M.Roy, L.Martinelli, K.Ginestar, J.Favergeon, and G.Moulin, J. Nucl. Mater. **468**, 153 (2016).

[5]O.I. Yeliseyva, V.P. Tsisar, I. Ivanova, and A.M. Demidik, Powder Metall. Met. Ceram. **47**, 607 (2008).

[6]V.P.Tsisar, Mater. Sci. **44**, 630 (2008).

[7]Y. Kurata, J. Nucl. Mater. **448**, 239 (2014).

[8]A. Weisenburger, A.Jianu, A.Heinzel, J.Konys, H.Steiner, G.Müller, C.Fazio, A.Gessi, S.Babayan, A.Kobzova, L.Martinelli, K.Ginestar, F.Balbaud-Célerier, F.J.Martín-Muñoz, and L.Soler Crespo, J. Nucl. Mater. **415(3)**, 260 (2011).

[9]G. Muller, A. Heinzel, J. Konys, G. Schumacher, A. Weisenburger, F. Zimmermann, V. Engelko, A. Rusanov, and V. Markov, J. Nucl. Mater. **335(2)**, 163 (2004).

[10]A.K. Rivai and M. Takahashi, J. Nucl. Mater. **398(1-3)**, 146 (2010).

[11]G. Müller, G. Schumacher, and F. Zimmermann, J. Nucl. Mater. **278(1)**, 85 (2000).

[12]G. Müller, A. Heinzel, J. Konys, G. Schumacher, A. Weisenburger, F. Zimmermann, V. Engelko, A. Rusanov, and V. Markov, J. Nucl. Mater. **301(1)**, 40 (2002).

[13]A. Heinzel, M. Kondo, and M. Takahashi, J. Nucl. Mater. **350(3)**, 264 (2006)

[14]Y. Kurata, M. Futakawa, and S. Saito, J. Nucl. Mater. **335(3)**, 501 (2004).

[15]F. Garcia Ferré, M. Ormellese, F. Di Fonzo, and M.G. Beghi, Corros. Sci. **77**, 375 (2013).

[16]V. Engelko, G. Mueller, A. Rusanov, V. Markov, K. Tkachenko, A. Weisenburger, A. Kashtanov, A. Chikiryaka, and A. Jianu, J. Nucl. Mater. **415**, 270 (2011).

[17]H. Glasbrenner and F. Groschel, J. Nucl. Mater. **356**, 213 (2006).

[18]T.C. Chou, T.G. Nieh, S.D. McAdmams, and G.M. Pharr: Scripta Metall. Mater. **25**, 2203 (1991).

[19]R. Cremer, K. Reichert, D. Neuschitz, G. Erkens, and T. Leyendercher, Surf. Coat. Tech. **163**, 157 (2003).

[20]O. Kyrylov, R. Cremer, and D. Neuschutz, Surf. Coat. Tech. **163**, 203 (2003)

[21]G. Erkens, Surf. Coat. Tech. **201**, 4806 (2007).

[22]S.M. Rossnagel et al., *Handbook of Plasma Processing Technology* (Noyes Publication, New Jersey, USA, p.233, 1990).

[23]M. Ohring, *Materials Science of Thin Films* (Academic Press, San Diego, CA, p.126, 1992).

[24]M. Schneider, W.D. Sproul, A.A. Voevodin, and A. Matthews, J. Vac. Sci. Technol. A **15**, 1084 (1997).

[25]Th. Roth, K.H. Kloos, and E. Broszeit, Thin Solid Films, **153**, 123 (1987).

[26]T. Hubert, S. Svoboda, and B. Oertel, Surf Coat Tech., **201**, 487 (2006)

[27]K S Sree Harsha, *Principles of Physical Vapor Deposition of Thin Films* (First Edition, Oxford, Elsevier, ISBN: 978-0-08-044699-8, 2006).

[28]F. Di Grabriele, S. Amore, C. Scaiola, E. Arato, D. Giuranno, and R. Novakovic, Nucl. Eng. Des. **280**, 69 (2014).

[29]W. Rasband, *Image J 1.48v*, National Institute of Health, USA. http://imagej.nih.gov/ij

[30]J.M. Fildes, S.J. Meyers, R. Kilaparti, E. Schlepp, Wear **274**, 414 (2012).

[31]L. Lutterotti, D. Chateigner, S. Ferrari, and J. Ricote, Thin Solid Films **450,** 34 (2004).

[32]L. Lutterotti, Nucl. Instrum. Methods. B **268**, 334 (2010).

[33]R. A. Young, *The Rietveld Method* (International Union of Crystallography, Oxford University Press, 1993).

[34] European standard UNI, EN 1071-3, *Advanced technical ceramics – Methods of test for ceramic coatings – Part 3: Determination of adhesion and other mechanical failure modes by a scratch test* (2005).

[35]O. Zywitzki, G.Hoetzsch, F.Fietzke, and K.Goedicke, Surf. Coat. Tech. **82(1-2)**, 169 (1996).

[36]G. Liu, Caifu Wang Fei Yu, and Jihong Tian, Oxid. Met. **81**, 383 (2014).

5 Tensile tests in liquid PbBi – CVR, CNR contribution

F. Di Gabriele, M. Chocholousek, Z. Spirit, J. Prehradna, Lucia Rozumova, E. Ricci, E. Miorin, S.M. Deambrosis

5.1 Experimental

T91 Coated with TiAlN

The material used was a ferritic-martensitic steel T91 (Grade 91 Class 2 / S50460), according to the ASTM A387-Ec99 standard. The steel was made in the form of plate by Industeel, Arcelor group, hot-rolled and thermally treated: normalization was carried out at 1050°C for 15 minutes and then water cooled to room temperature; annealing at 770°C for 45 minutes and slowly cooled in air. The composition is listed in Table 1 as provided by the producer.

Table 1 –Composition of the steel T91

Fe	C	Cr	Mo	Mn	Si	Ni	V	Cu	Nb	P	Al	Ti	S	N
Bal.	0.102	8.895	0.889	0.401	0.235	0.121	0.202	0.080	0.079	0.019	0.010	0.004	0.0007	0.048

Tensile specimens were manufactured in the L direction (dimensions in Fig.1)

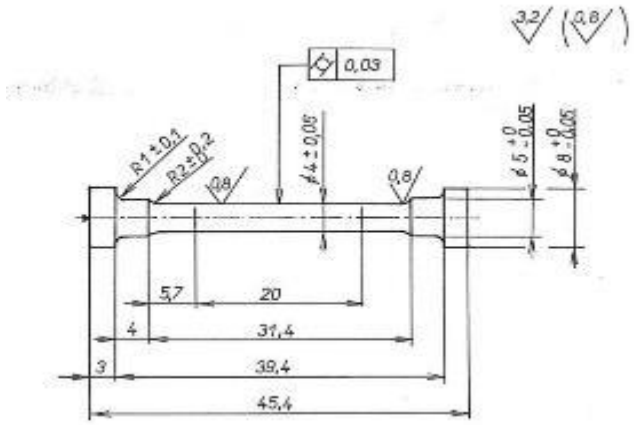

Figure 1 - Dimensions of tensile specimen

Coatings

TiAlN coatings were deposited on T91 tensile specimens using a proper combination of reactive HiPIMS (High Power Impulse Magnetron Sputtering) and pulsed-DCMS (Direct Current Magnetron Sputtering technologies).

A brief introduction to sputtering deposition

Diode sputtering

The substrate to be coated is placed in a vacuum chamber containing Argon and a negative charge is applied to a target source material causing the plasma to glow.

Free electrons flow from the negatively charged target source material in the plasma environment, colliding with the outer electronic shell of the Argon gas atoms driving these electrons off due to their like charge. The inert gas atoms become positively charged ions attracted to the negatively charged target material at a very high velocity that “Sputters off” atomic size particles from the target source material due to the momentum of the collisions. These particles cross the vacuum deposition chamber of the sputter coater and are deposited as a thin film of material on the surface of the substrate to be coated.

In summary, *diode sputtering* is the process of removing surface atoms from a target by ion bombardment. The liberated surface atoms can move to the surface to be coated (the substrate) and may condense there to form a solid film (Figure 2).

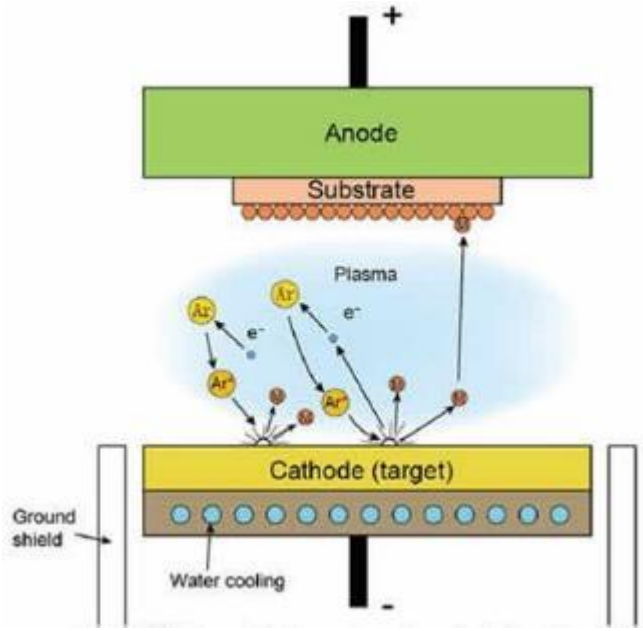

Figure 2 - In a DC diode sputtering system, Argon is ionized by a strong potential difference, and these ions are accelerated to a target. After impact, target atoms are released and travel to the substrate, where they form the film.

Magnetron sputtering and its upgrades

An effective way to enhance diode sputtering process is to use a *magnetron sputtering system*. The magnetron discharge is a magnetically enhanced glow discharge. Thanks to the magnetic field, electrons can travel a much longer path in the same general space in front of the target than without the magnets. This tends to generate a stable plasma with high density of ions. More ions mean more ejected atoms from the target and, therefore, an increased efficiency of the sputtering process.

The majority of coatings needed for applications are compound films, which are produced when a reactive gas is added to the process gas (*reactive Magnetron Sputtering*). When reactive gas is present, a big issue is arcing on the target, which leads to the ejection of microscopic detrimental target debris (macroparticles). Among the measures to suppress arcing, it is possible to operate the magnetron in a pulsed mode (*reactive pulsed-DCMS*): the applied voltage is switched on and off at a medium frequency in the range 10–350 kHz. Pulsed sputtering is used to reduce the propensity to arcing because the arc onset is usually delayed relative to the application of a voltage.

While it is known that ion assistance to film growth can greatly alter the microstructure and associated film properties, sputtered atoms are generally neutral (as opposed to ionized) and therefore cannot be influenced by electric and magnetic fields. A first step to utilizing the magnetron plasma for film growth assistance was made by unbalancing the magnetron. The ions in this approach were ions of the processing gas, usually argon, and of the reactive gas, if present, but not ions of the target material. High Power Impulse Magnetron Sputtering (HiPIMS) was conceived to also produce ions of film-forming target material. When film-forming ions are available, the substrate-film interface and the film interface microstructure can be more efficiently influenced by substrate biasing, and magnetic fields can be used to better transport fluxes to the substrate. Ionization of the target atoms is accomplished by applying the discharge power in pulses such that the current is allowed to rise much above the average, often about 2 orders of magnitude above what the magnetron manufacturer specifies for the DCMS mode of operation. With respect to conventional magnetron sputtering techniques, HiPIMS plasma conditions greatly enhance the flux of energetic ionized species towards the growing film, allowing smoother and denser films to be deposited on complex-shaped substrates. In addition, by tuning the HiPIMS process parameters, novel structures and an increased ratio of hardness to elastic modulus can be achieved. Moreover, the highly ionized conditions in HiPIMS are also well suited for a material pretreatment aimed at the removal of the natural oxide layer that exists on most materials and at adhesion improving.

5.1.1 Deposition conditions

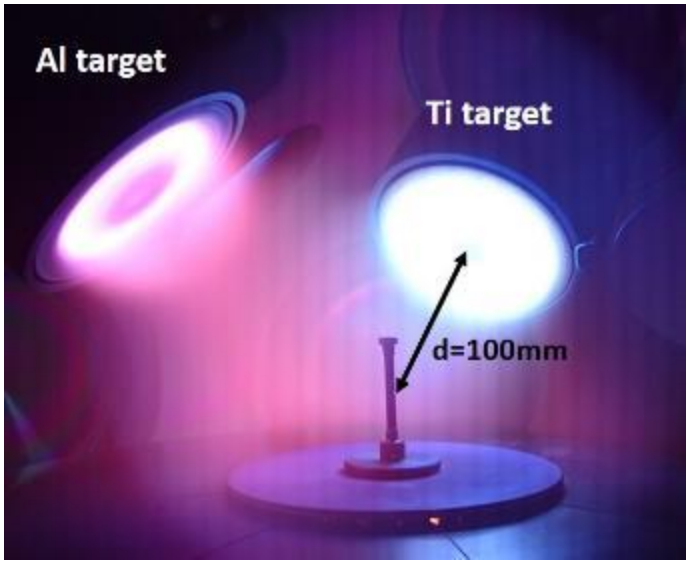

Figure 3 – A tensile specimen during TiAlN sputtering deposition.

Based on preliminary results, all the TiAl nitride coatings were deposited using two sets of optimized working parameters (shown in Table 2). The depositions were performed in a turbo-molecular pumped high-vacuum spherical chamber, which was preliminarily evacuated to a base pressure lower than $1x10^{-7}$ mbar. The inert gas (Ar, 99.9997% purity) and reactive gas (N, 99.998% purity) were introduced through dedicated mass flow controllers so that the chosen pressure and mixture of the sputtering gases were attained (Gas=Ar+N_2 (10%), p(mbar)=$7.7x10^{-3}$). A Ti target (4 inches in diameter, 6 mm thick, and 99.9% purity) was mounted on a lightly unbalanced magnetron cathode, driven by a HiPIMS power supply (TRUMPF-Hüttinger, True Plasma High Pulse 4002). An Al target (4 inches in diameter, 6 mm thick, and 99.9% purity) was mounted on a lightly unbalanced magnetron cathode, driven by a pulsed-DCMS power supply (TRUMPF-Hüttinger, True Plasma pulsed generator mod TP DC 4001).For the substrate biasing, an 18 kW special unit model 3018 HBP (TRUMPF-Hüttinger) specifically designed for HiPIMS was employed. The substrates were placed 100 mm below the cathode (Figure 3) and were heated up to 300°C prior to the deposition. Temperature was maintained throughout the process by *ad hoc* heaters and thermocouple monitoring. Tensile specimens were located in the vacuum chamber using a specially designed mounting (Figure 3). Deposition conditions are summarized in Table 2.

Table 2 - HiPIMS working parameters set for TiAlN film depositions.

Sample	Etching	HiPIMS	Pulsed-DCMS	Bias Voltage V_{low}-V_{high} (V)
i01	V(V)=1200 $P_{Ti\ target}$(W)=100 t(min)=15	P(W)=800 V(V)=460 f(Hz)=500 Pulse length(μs)=100 Dep. t(min)=300	P (W)=400 V (V)=285 f (kHz)=10 Dep. t(min)=300	75-135
i02 (notch)				
i03 (notch)				95-170
i04				

First, substrate surface was plasma etched in an attempt to positively affect film/substrate interface (i.e. adhesion). Using HiPIMS, target metal ions bombard the substrate leading to removal of contaminants, formation of intermixing zones, and the growth of crystalline metallic interlayers, which could increase the coating/substrate adhesion. Anyway, several critical factors were identified: 1) the ability to form interlayers and intermixing zones depends on the second ionization energy of the metal used for the HiPIMS pretreatment; 2) the intermixing zone importance is not clear; 3) a good adhesion is not solely determined by the presence of an interlayer; 4) it is essential to consider the nature of bonding role; etc..[1] In view of the above, the plasma etching step was carried out maintaining the Ti target at a low average power (100 W) and applying a 1200 V bias voltage to the sample holder. In these conditions, it could be assumed

[1] K. D. Bakoglidis, S. Schmidt, G. Greczynski, L. Hultman, Improved adhesion of carbon nitride coatings on steel substrates using metal HiPIMS pretreatments, Surface and Coatings Technology 302 (2016) 454–462.

that the ions reaching the substrate were predominantly Ar ions, since the fraction of ionized metal flux depends on applied power[2].

For each sample, we achieved a multilayer structure varying the applied bias voltage between a low value (V_{low} for 5 minutes) and a high value (V_{high} for 25 minutes) until the deposition end. Moreover, we modified the bias voltage range: V_{low}-V_{high}=75-135 V for i01 and i02, 95-170 V for i03 and i04 to improve density (i.e. corrosion resistance).

Surface before test

After a soft mechanical polishing (not in the notch!), T91 samples were thoroughly cleaned before depositions. Tensile specimen surface finish was not ideal (metal processing traces were clearly visible) but, for these early tests, it could be accepted. Moreover, just before the actual deposition, a 15 minutes plasma etching was performed. Many detrimental macroparticles are visible: they are due to the numerous arcs recorded during all depositions. These droplets represent weaknesses of the protective coating since they can act as trigger for cracks.

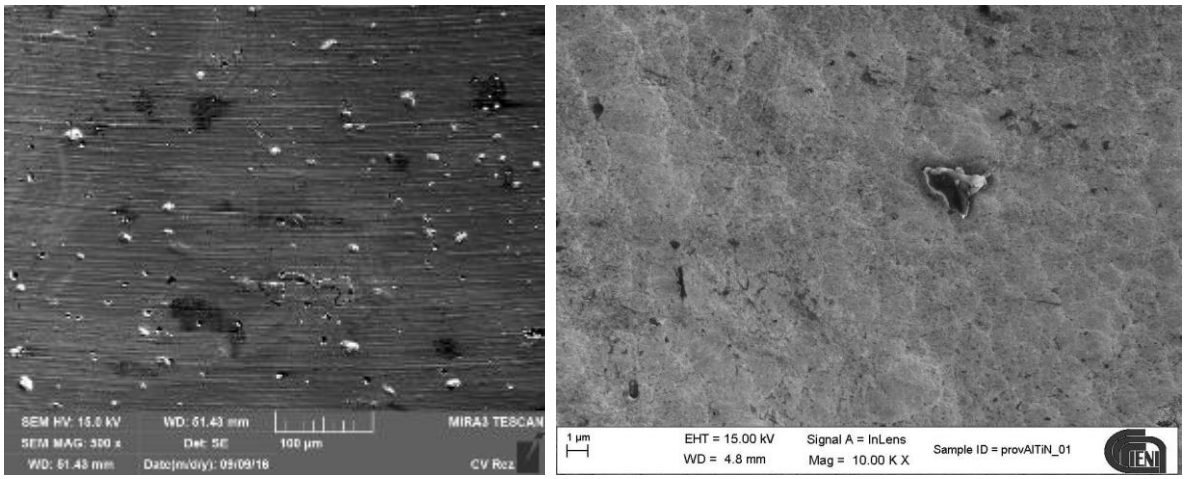

Figure 4 – SEM images of the coating surface on smooth specimens before exposure to PbBi

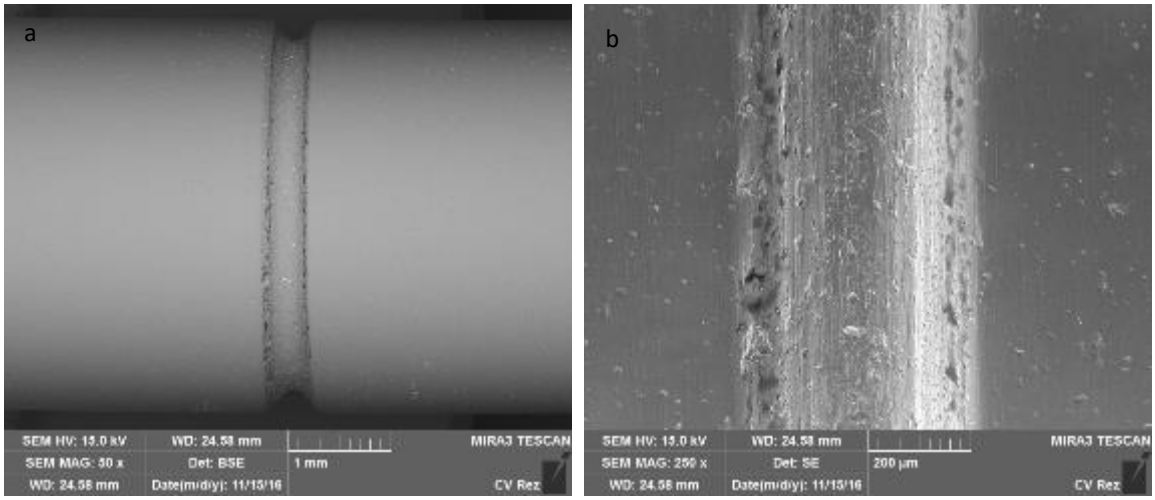

[2] A.P. Ehiasarian, J.G. Wen, I. Petrov, Interface microstructure engineering by high power impulse magnetron sputtering for the enhancement of adhesion, J. Appl. Phys., 101 (2007) 0–10.

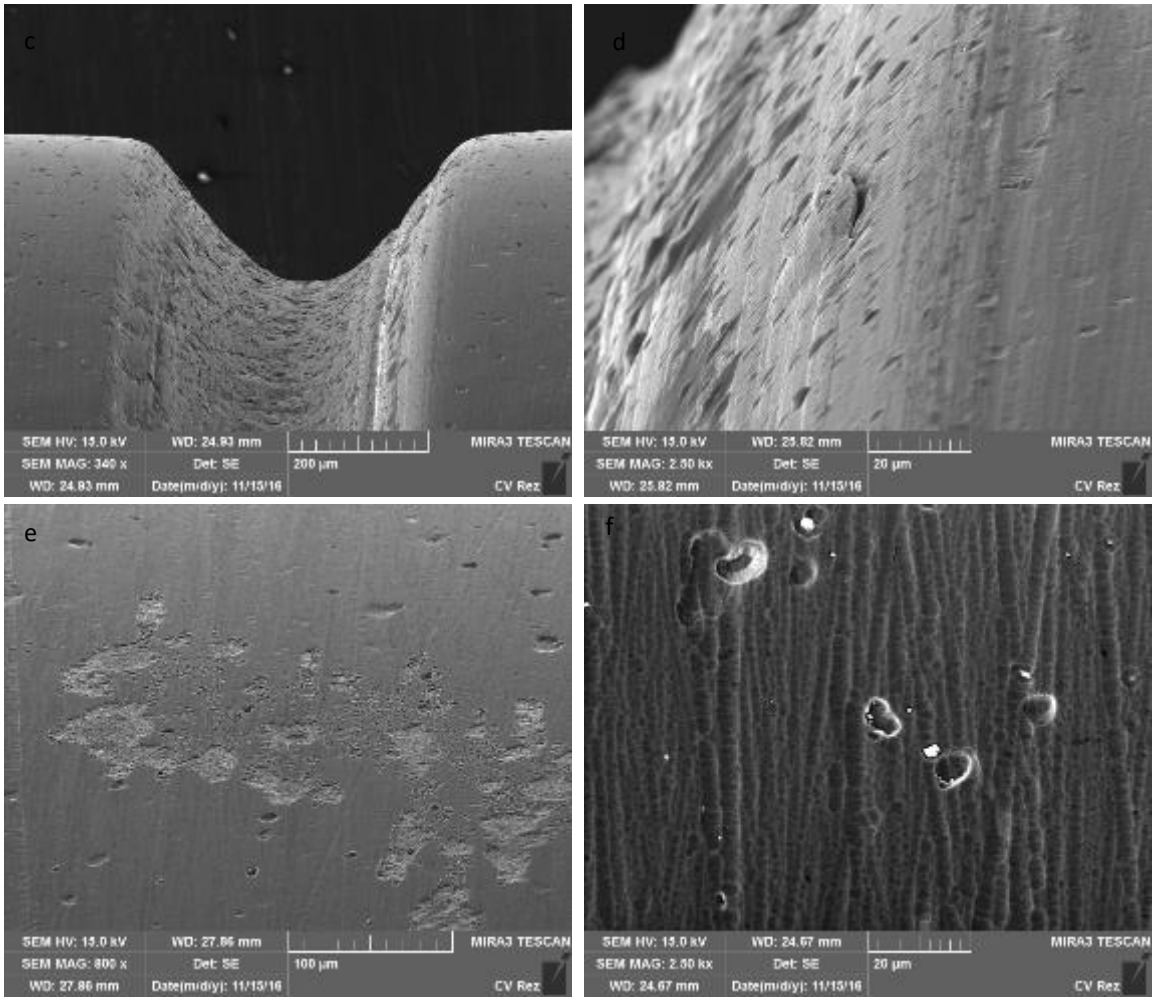

Figure 5 – SEM surface observations of notched tensile i02 specimen. a) general view of the notch; b-c) general feature of the notch; d) detail at the edge of the notch; e-f) smooth surface out of notch with superficial defects

Table 3. is listing the average composition of the coatings for each specimen.

Table 3 – Average composition values of coatings

Sample	Ti/(Ti+Al) x 100 [%] Average value
AlTiN_01	43 ± 1
AlTiN_02 (notched)	48.5 ± 0.3
AlTiN_03 (notched)	41.0 ± 0.8
AlTiN_04	54.6 ± 0.2

5.2 Mechanical testing

Tensile tests were carried out in PbBi, at 550°C, in the CALLISTO cell. CALLISTO is a tank containing liquid PbBi built on a Zwick/Roell Electromechanical Creep Testing machine, Kappa 50DS. CALLISTO is based on the 2-tank concepts, where the first tank is for the preparation of the liquid metal (oxygen dosing). The liquid is then transferred to the second tank, containing holders and specimens. Table 4 summarise the experimental parameters and the last column shows the time that the specimens is immersed in the PbBi before starting loading.

5.3 Microscopy

Specimens after test were observed with two scanning electron microscopes (SEM), VEGA TS 5130 XM and LYRA3 GMU by Tescan Inc with associated EDS detector for chemical analyses. The cross sections of 1 tensile (i01) and 1 notched (i02) specimen were produced in order to examine the coating adherence and more in detail its interface with the PbBi.

Table 4 – Test Matrix for AlTiN coated T91 in PbBi at 550°C

Spec	T	O	Strain rate	Environment	t before test
	°C	Wt%	s^{-1}		h
i01	550	8^-10	10^{-4}	PbBi	24
i02 (notch)	560	9^-12			24
i03 (notch)	557	3^-8			386
i04	550				72

5.4 Results

Smooth tensile specimens

Specimens were loaded up to the UTS point of the material. The stress-strain curves are represented in Figure 6 for the smooth specimens.

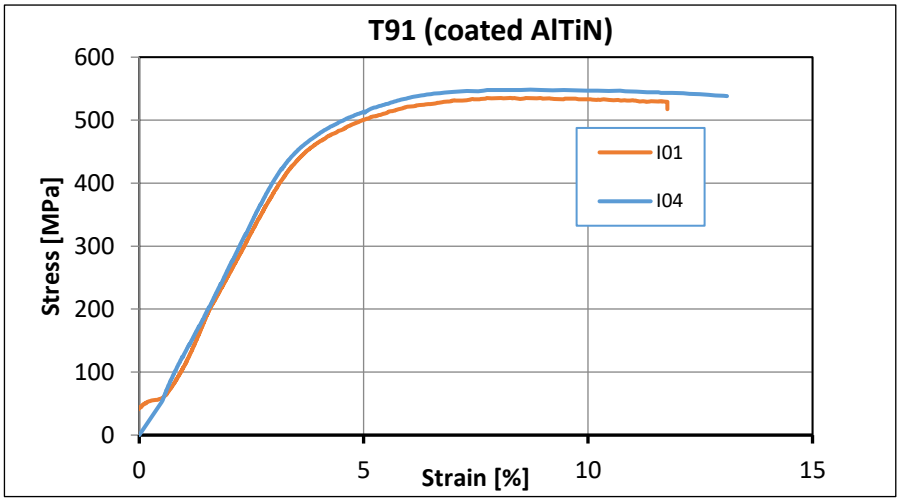

Figure 6 – Stress-strain curves for smooth tensile specimens tested at 550°C in PbBi

5.4.1 Specimen i01

5.4.1.1 Surface after test

From SEM observation of the surface after loading, cracks were observed over all the surface for a length of 26mm. Fig.7b shows the rhomboidal path of slip lines with cracks crossing over all the specimen surface. These were mainly filled with PbBi (Fig.7.g). Besides the rhomboidal cracking, also many cracks perpendicular to the loading direction were observed (Fig7c-g)

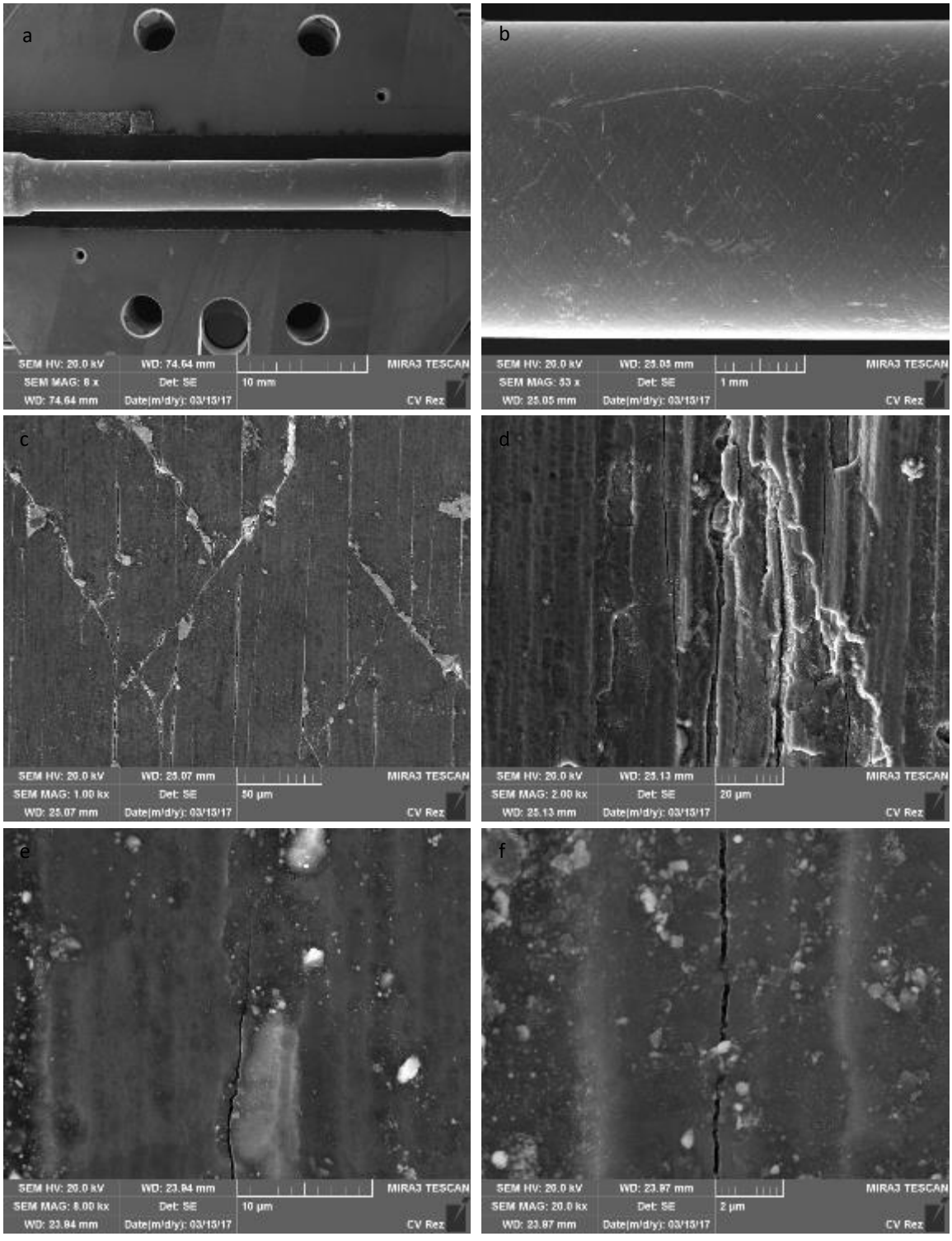
a
SEM HV: 20.0 kV
WD: 74.64 mm
MIRA3 TESCAN
SEM MAG: 8 x
Det: SE
10 mm
WD: 74.64 mm
Date(m/d/y): 03/15/17
CV Rez
b
SEM HV: 20.0 kV
WD: 25.05 mm
MIRA3 TESCAN
SEM MAG: 53 x
Det: SE
1 mm
WD: 25.05 mm
Date(m/d/y): 03/15/17
CV Rez
c
SEM HV: 20.0 kV
WD: 25.07 mm
MIRA3 TESCAN
SEM MAG: 1.00 kx
Det: SE
50 µm
WD: 25.07 mm
Date(m/d/y): 03/15/17
CV Rez
d
SEM HV: 20.0 kV
WD: 25.13 mm
MIRA3 TESCAN
SEM MAG: 2.00 kx
Det: SE
20 µm
WD: 25.13 mm
Date(m/d/y): 03/15/17
CV Rez
e
SEM HV: 20.0 kV
WD: 23.84 mm
MIRA3 TESCAN
SEM MAG: 8.00 kx
Det: SE
10 µm
WD: 23.84 mm
Date(m/d/y): 03/15/17
CV Rez
f
SEM HV: 20.0 kV
WD: 23.87 mm
MIRA3 TESCAN
SEM MAG: 20.0 kx
Det: SE
2 µm
WD: 23.87 mm
Date(m/d/y): 03/15/17
CV Rez

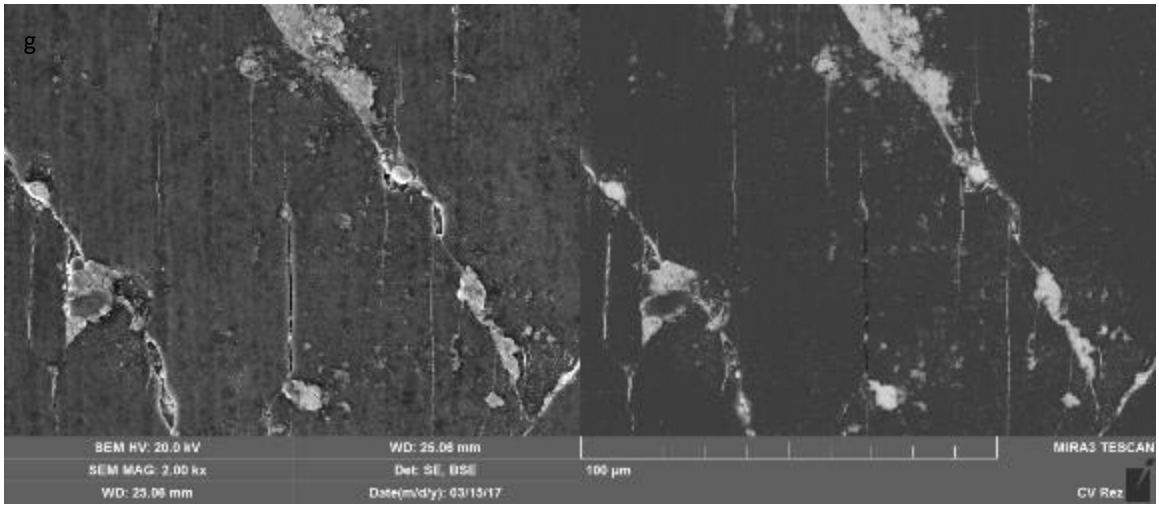

Figure 7 – SEM surface observations of tensile i01 specimen. a) general view; b) general feature of cracking; c-f) details of surface cracks; g) SE and BSE image of cracks highlighting the presence of PbBi inside the large cracks

5.4.1.2 Cross section after test

The cross section of the specimen was observed to characterize the cracks, adherence of coating and its composition. For all the length of the specimen, cracks were observed only in the coating and not in the steel. In particular, the coating stayed adherent to the surface of the steel and no detachment was observed. Figure 8 illustrates the various features of cracks. The BSE mode highlighted different layers inside the coating (Fig.8c-f) which were afterwards confirmed by EDS analyses to have a different composition.

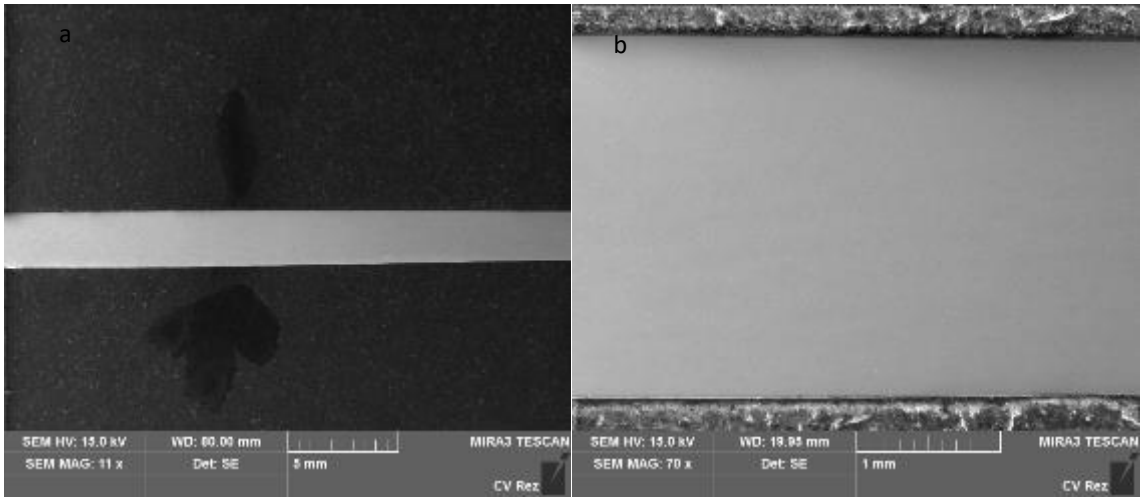

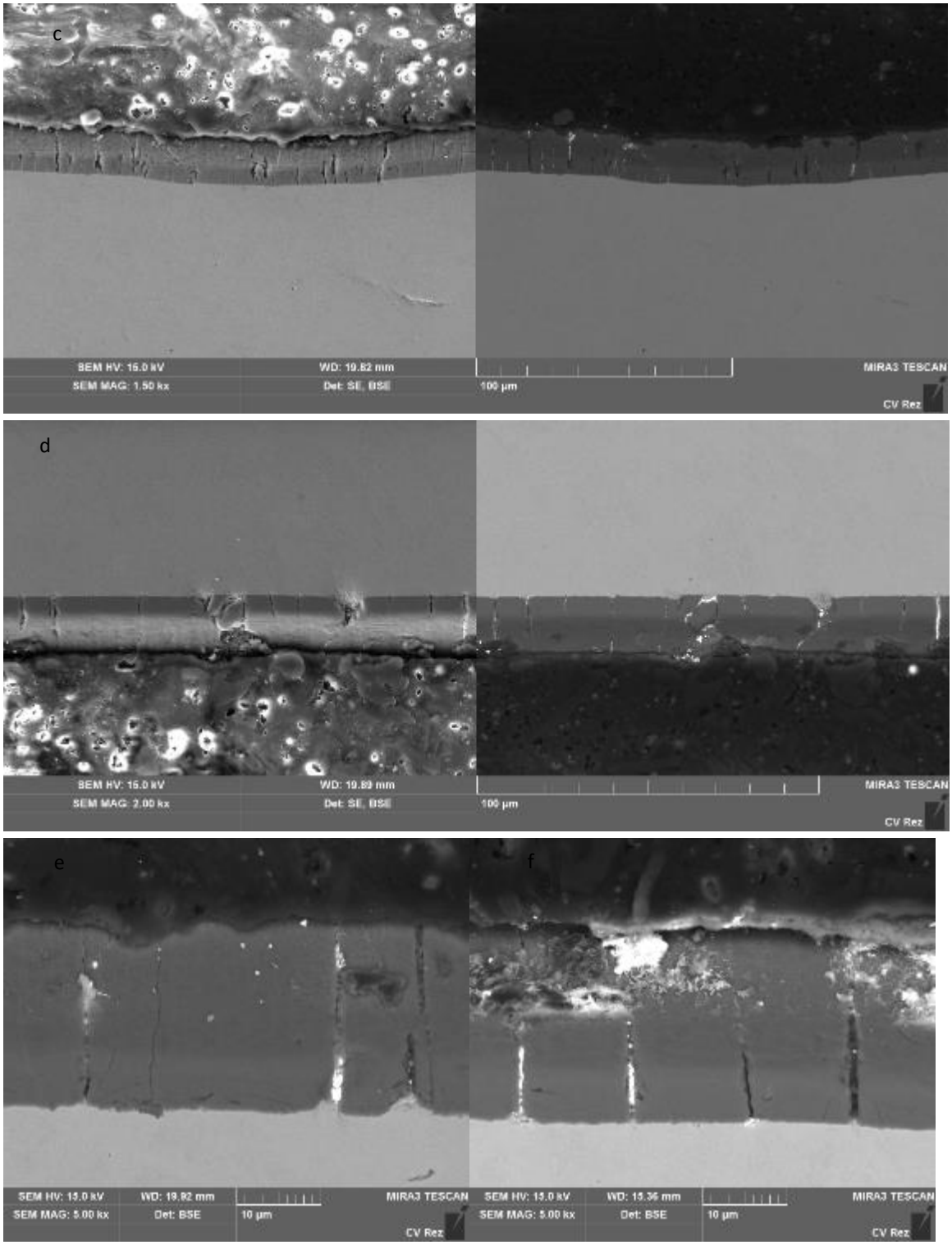

Figure 8 – SEM cross section of specimen i01. a-b) general overview; c) detail of cracks in the central zone (SE and BSE in parallel); d) details of cracks from the opposite side (SE and BSE in parallel); e) detail of cracks containing PbBi; f) detail of cracks and damaged coating

EDX analyses

CRACKED OXIDE

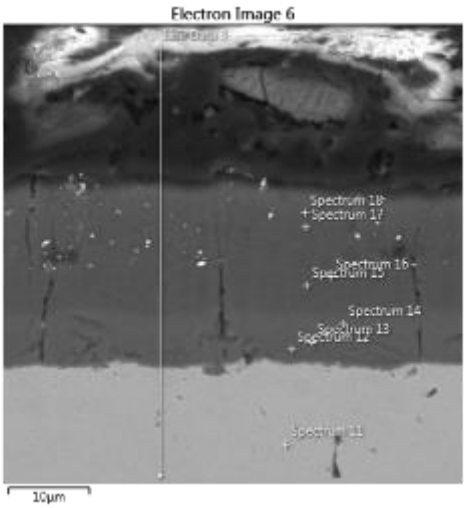

Figure 9 – SEM image with localization of spot analyses

Table 5 – Spot quantitative analyses, wt%, as referred in Figure 9.

points	Fe	Cr	Al	Ti	N	Si	Mn	S	Mo	V	O
11	81.7	8.3				2.2	0.4	0.2			
12	76.3	8.0	4.2	3.4		0.5			0.3	0.2	
13	63.5	6.7	7.8	6.3	8.3	0.3	0.3		0.7	0.2	
14	46.5	3.4	17.2	16.0	14.5			0.1			
15	15.8	2.0	26.7	34.1	20.8						
16	7.3	0.9	28.0	40.3	22.1						
17	0.8		28.3	44.3	14.0						3.0
18	0.8		22.6	45.4	17.2			0.1		0.4	

CRACK-FREE OXIDE

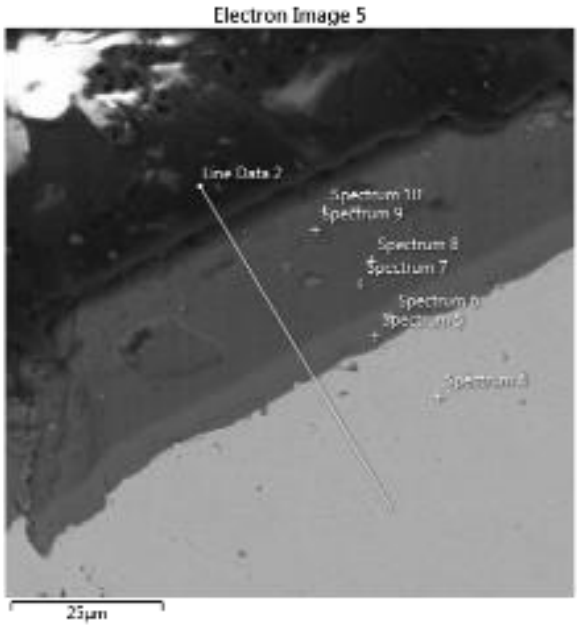

Figure 10 – SEM image with localization of spot analyses

Table 6 – Spot quantitative analyses, wt%, as referred in Figure 10.

Points	Fe	Cr	Al	Ti	N	Si	Mn	S	Mo	V	O
4	83.5	8.0						0.3	0.9		
5	84.7	8.6					0.3	0.3		0.2	
6	83.0	8.3	0.1				0.3	0.3	0.5		
7	23.7	2.8	22.8	23.0	21.0						
8		1.4	20.0	34.3	21.3						
9			32.0	40.6	19.8						
10	0.8		33.4	46.2	18.8						

5.4.2 Specimen i04

5.4.2.1 Surface after test

The other smooth tensile specimen showed similar features (Fig.11), with abundant cracking along slip planes directions (Fig.11b), as well as perpendicular to loading (Fig.11c). Details of small areas where the coating was detached were observed (Fig.11d).

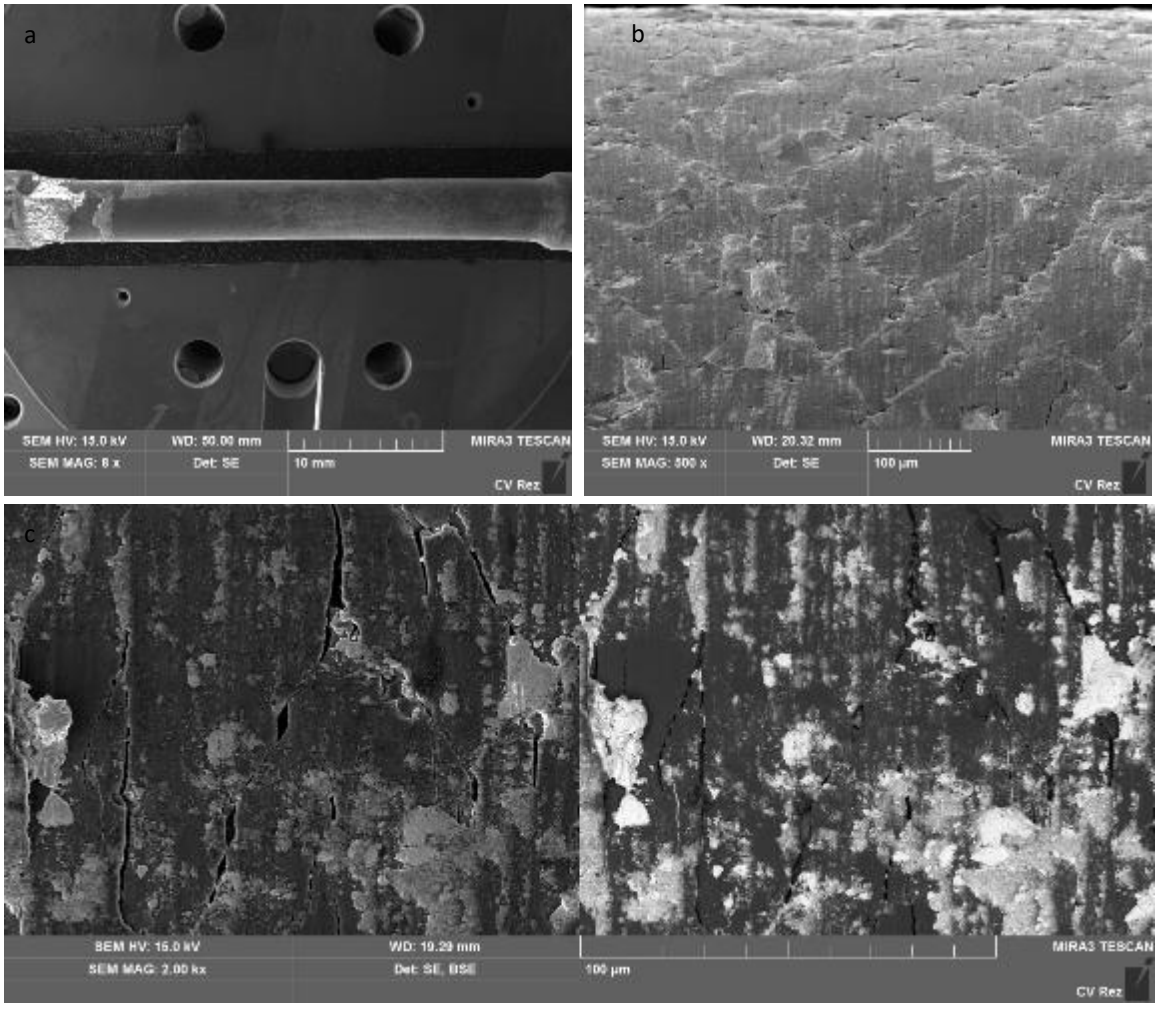

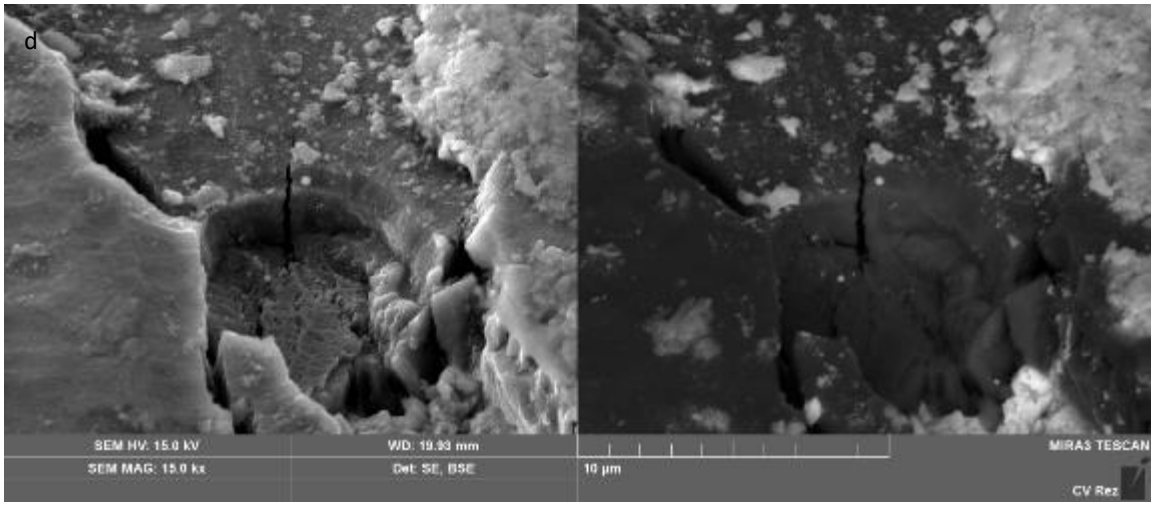

Figure 11 – SEM surface observations of tensile i04 specimen. a) General view; b) general feature of cracking; c) SE and BSE parallel images with details of surface cracks; d) SE and BSE parallel images with detail of detached coating

However this specimen was loaded at higher strain compared to the previous one (blue line in Figure 6) and this was evident in the appearance of the cross section (Fig.12). In the necking, cracks were fully developed (though only in the coating) and due to the high temperature and low amount of oxygen dissolved in the liquid metal, penetration of PbBi occurred.

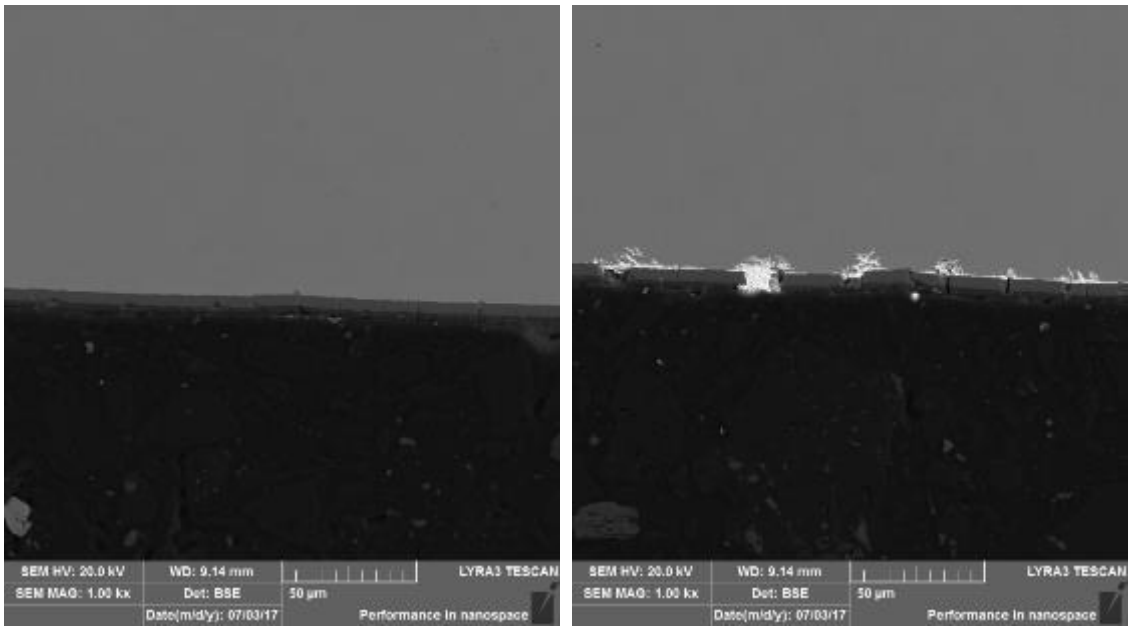

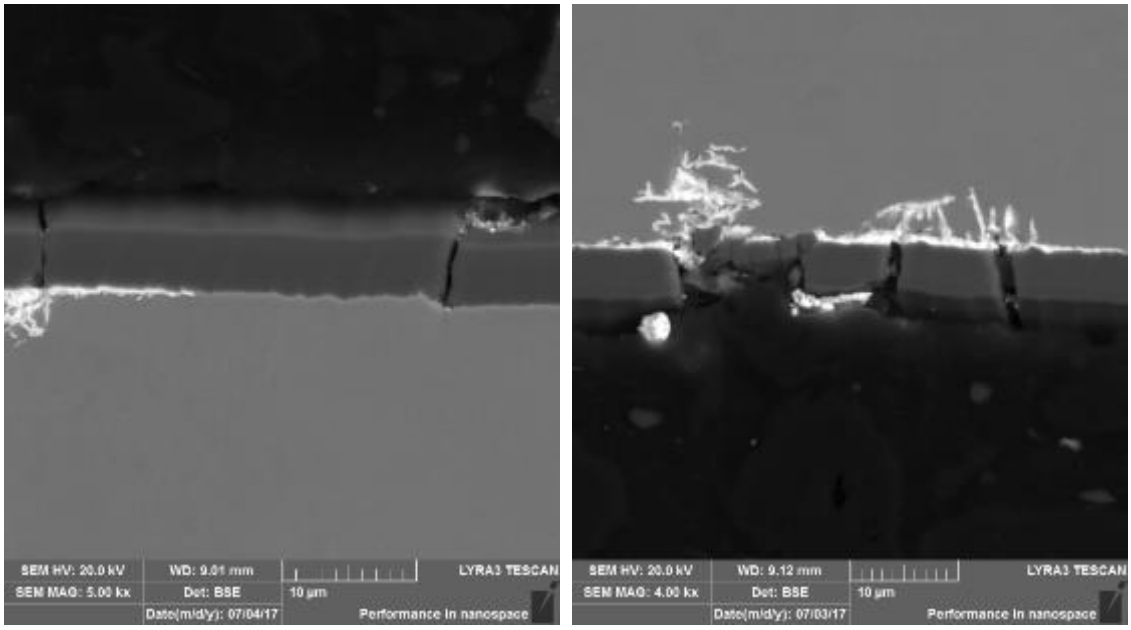

Figure 12– SEM cross section of specimen i04. a) general view; b) detail of cracks in the central zone; c) details of cracks; d) detail of cracks with underneath PbBi

Notched tensile specimens

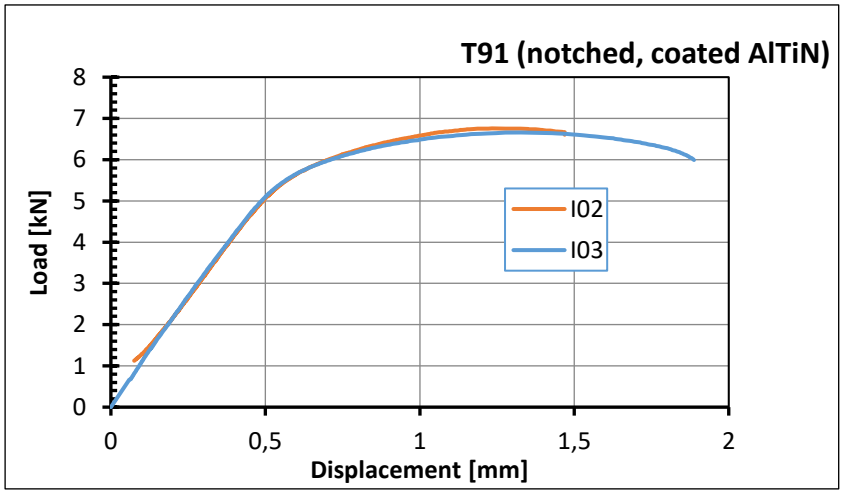

Figure 13 – Load-displacement curves for notched tensile specimens tested at 550°C in PbBi

5.4.3 Specimen i02

5.4.3.1 Surface after test

SEM observations were focused on the notched area, where the main damage occurred. From the surface observation (Fig.14) it was possible to see how cracking initiated at the coating and into the steel (Fig. 14c-f). Factors affecting heavily the performance of the coating in this area were:

-the initial coating deposition was not uniform, as the surface finish was relatively rough at the notch, due to machining (not grinding as for the smooth surface);

-the higher stress concentration at the root of the notch.

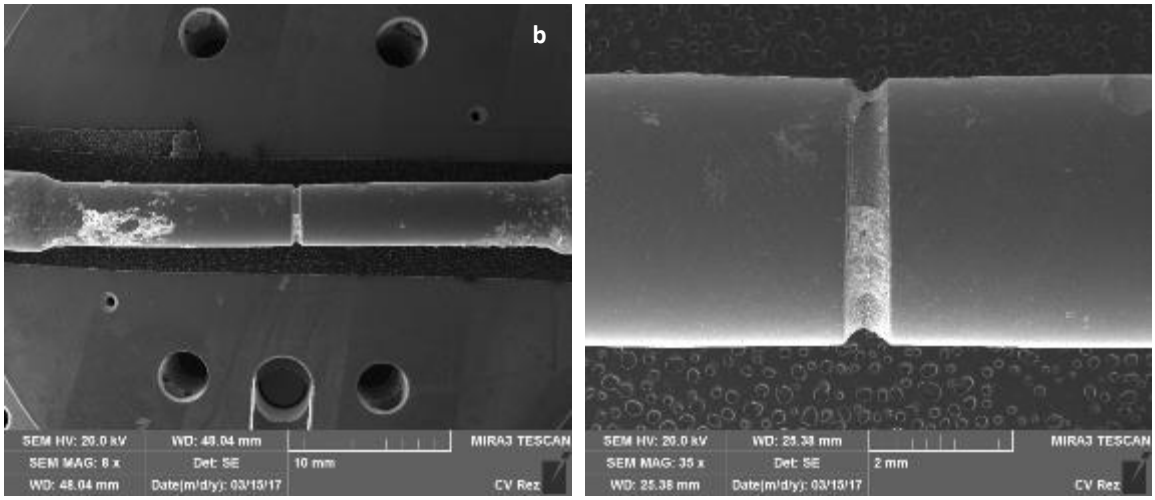

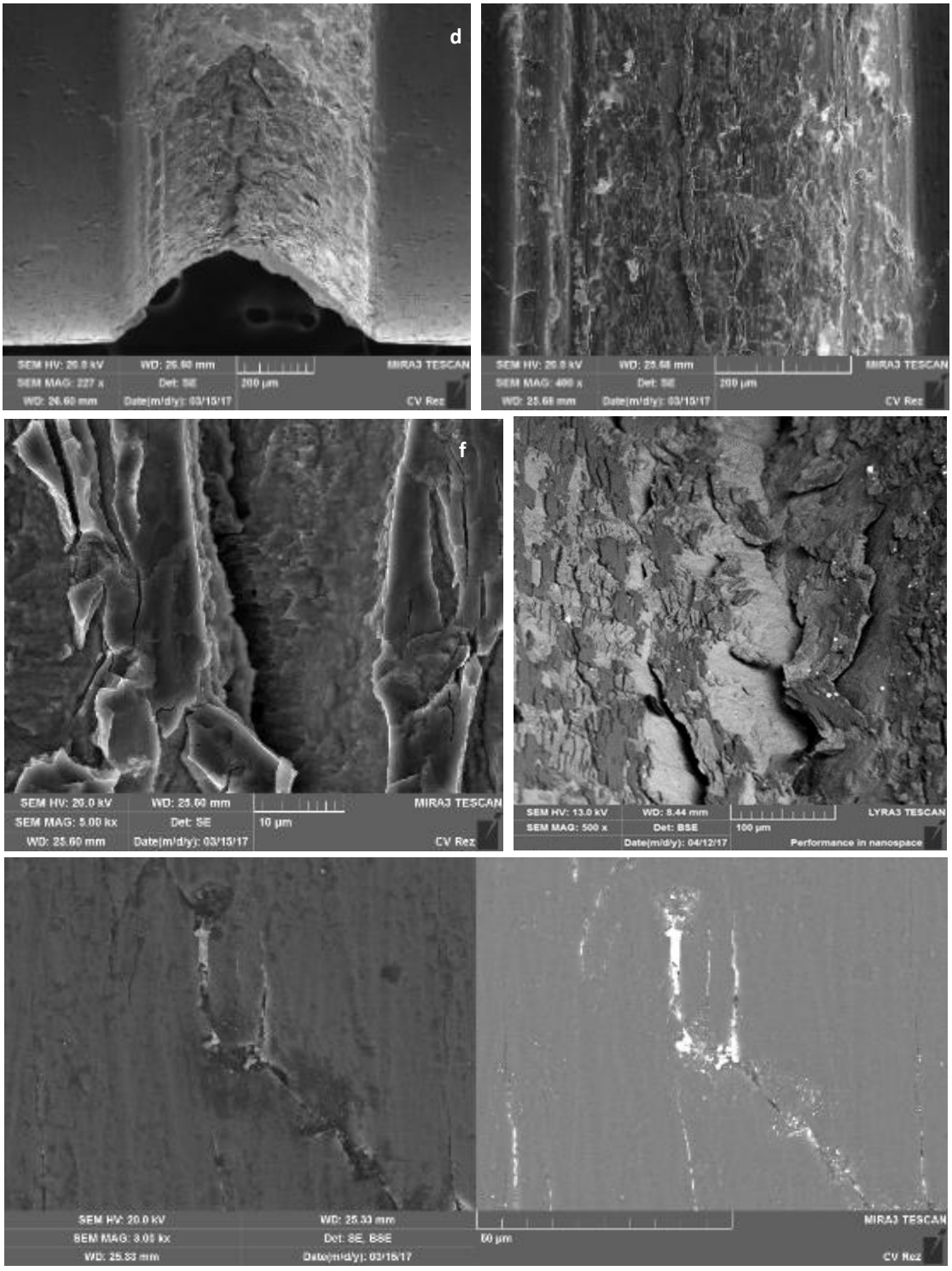

Figure 13 – SEM images of the specimen i02 notched after loading in PbBi at 550°C. a-b) General overview; c d) detail of notch; e) detail of crack in SE mode; f) detail of crack in BSE mode; g) SE and BSE parallel images with detail of cracks on the smooth surface.

On the smooth surfaces the cracking in rhomboidal patterns occurred as for specimens i01

5.4.3.2 Cross-section after test

The non-homogeneous nature of the coating on the notch was clearly observed from the cross section examination (Fig. 14b). One main crack was observed to grow into the steel (Fig. 14c-d) and in the surrounding areas the coating was heavily damaged (Fig15 g-h). Along the smooth surface the coating was also affected (Fig. 15 e-f).

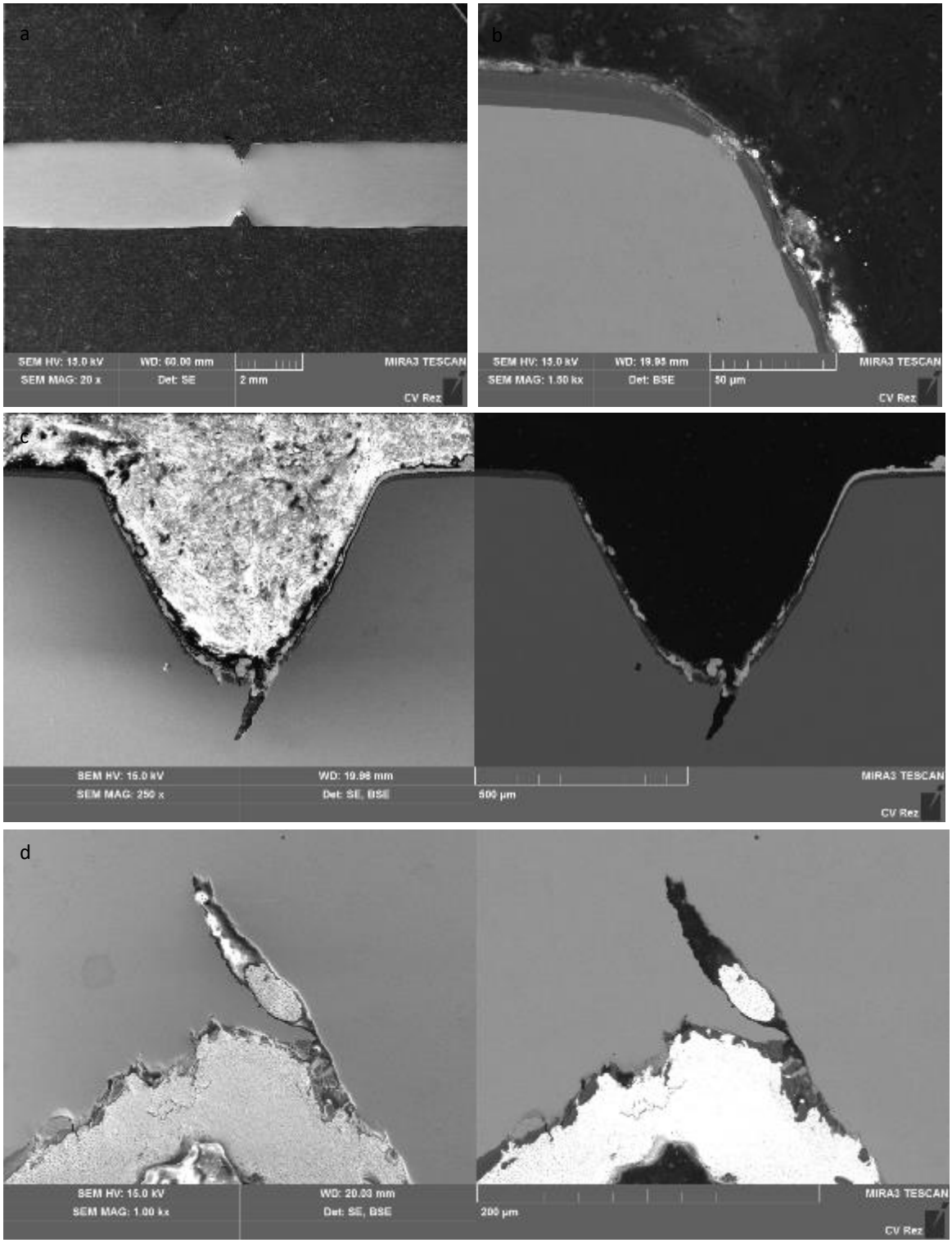
a
SEM HV: 15.0 kV
WD: 60.00 mm
MIRA3 TESCAN
SEM MAG: 20 x
Det: SE
2 mm
CV Rez
b
SEM HV: 15.0 kV
WD: 19.95 mm
MIRA3 TESCAN
SEM MAG: 1.50 kx
Det: BSE
50 µm
CV Rez
c
SEM HV: 15.0 kV
WD: 19.98 mm
MIRA3 TESCAN
SEM MAG: 250 x
Det: SE, BSE
500 µm
CV Rez
d
SEM HV: 15.0 kV
WD: 20.03 mm
MIRA3 TESCAN
SEM MAG: 1.00 kx
Det: SE, BSE
200 µm
CV Rez

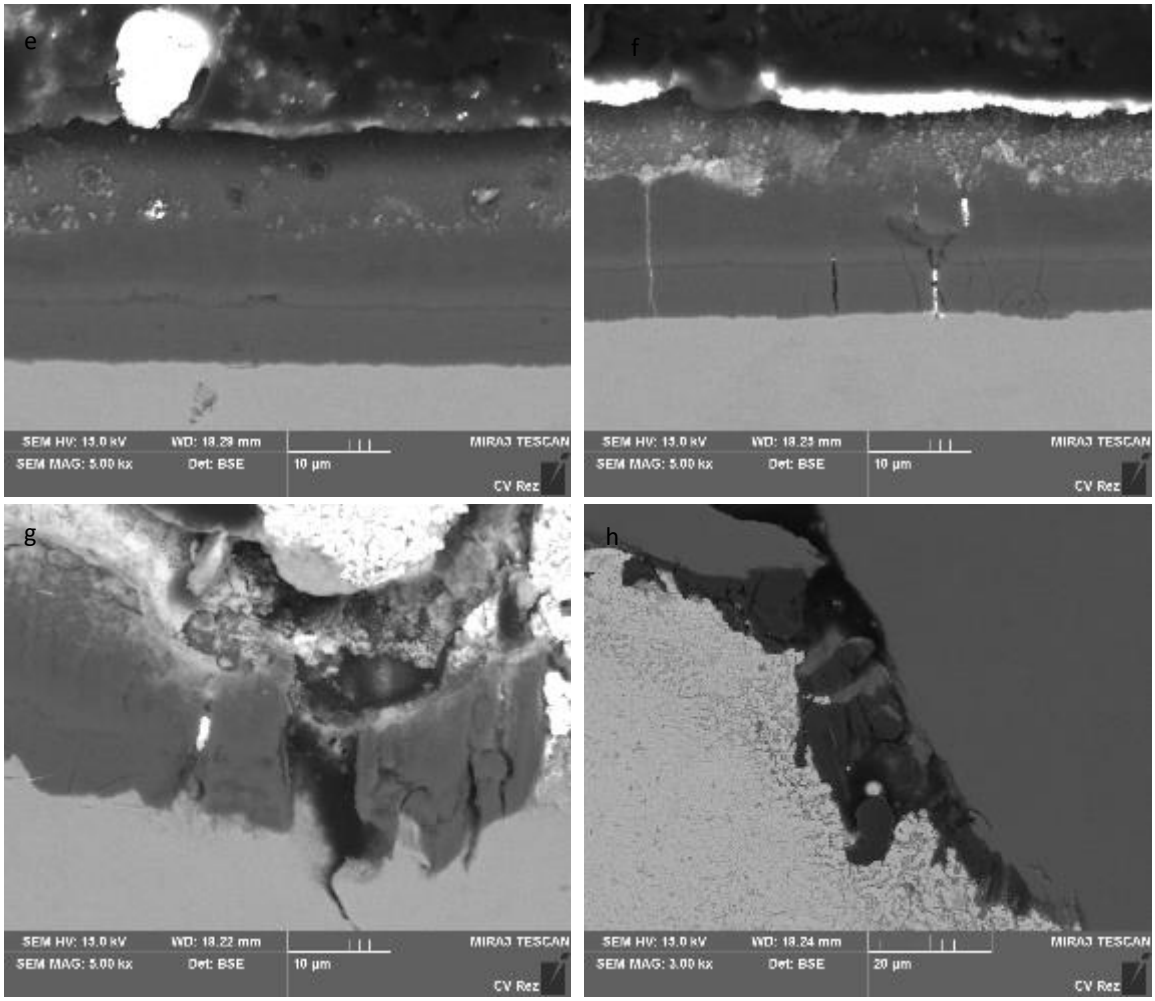

Figure 15 – SEM images of the notched specimen i02 after loading in PbBi at 550C. a) General overview; b) detail of the edge with not uniform coating; c) SE and BSE parallel images of the notch; d) SE and BSE parallel images with detail of the crack; e) coating on the smooth surface without defects; f) coating on the smooth surface with cracks; g-h) details of damaged coating in the notched area.

EDS analyses

CRACK-FREE OXIDE

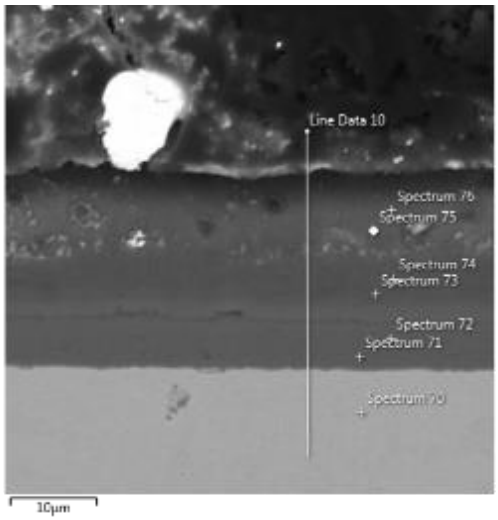

Figure 16 - SEM image with localization of spot analyses

Table 7 – Spot quantitative analyses, wt%, as referred in Figure 16.

Points	Fe	Cr	Al	Ti	N	Si	Mn	S	Mo	V	O	Pb
70	84.8	8.7					0.4	0.3	0.9	0.2		
71	84.4	8.9		0.2		0.3	0.4		0.9	0.3		
72	78.4	8.3	3.3	3.1		0.2	0.4			0.2	1.7	
73	34.8	4.0	20.2	22.2	18.1				0.5			
74	23.2	2.7	23.7	28.6	21.2		0.2			0.2		
75	1.0		27.5	50.5	20.6							
76	0.8		20.1	43.7	19.2							2.2

CRACKED OXIDE

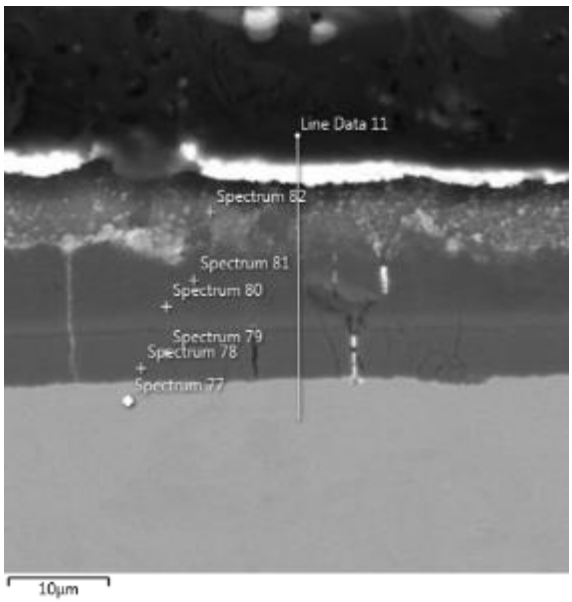

Figure 17 - SEM image with localization of spot analyses

Table 8 – Spot quantitative analyses, wt%, as referred in Figure 17.

Points	Fe	Cr	Al	Ti	N	Si	Mn	S	Mo	V	Pb
77	86.0	8.7				0.3	0.5	0.2			
78	85.5	8.5		0.1		0.3	0.4		0.8	0.2	
79	84.1	8.6	0.5	0.6		0.3	0.5		0.9	0.2	
80	43.8	4.9	14.8	15.8	15.4	0.1			0.4		
81	28.3	3.3	21.9	26.9	19.5						
82	0.9		23.0	49.1	19.5					0.4	1.3

NOTCH

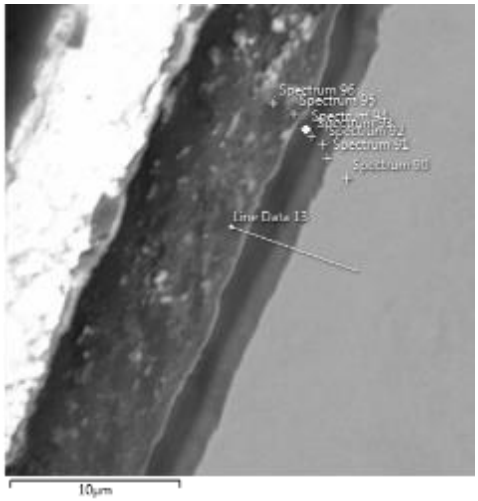

Figure 18 - SEM image with localization of spot analyses

Table 9 – Spot quantitative analyses, wt%, as referred in Figure 18.

Points	Fe	Cr	Al	Ti	N	Si	Mn	Mo	V	O
90	84.6	8.8				0.3	0.3	0.9	0.2	
91	84.7	8.6		0.2		0.3	0.4	0.8	0.2	
92	85.2	8.7		0.2		0.3	0.4		0.2	
93	84.2	8.3		0.4	0.3	0.3	0.5	0.9	0.2	
94	81.0	8.3	1.1	2.0	0.7	0.3		0.9		0.8
95	61.1	6.5	5.7	10.7	9.6	0.2	0.4	0.6		
96	38.7	4.7	10.4	23.3	17.6					

i03

Surface after test had very similar features as for i02, with the coating cracked in the smooth area and coating + substrate cracked at the notch (Fig.19).

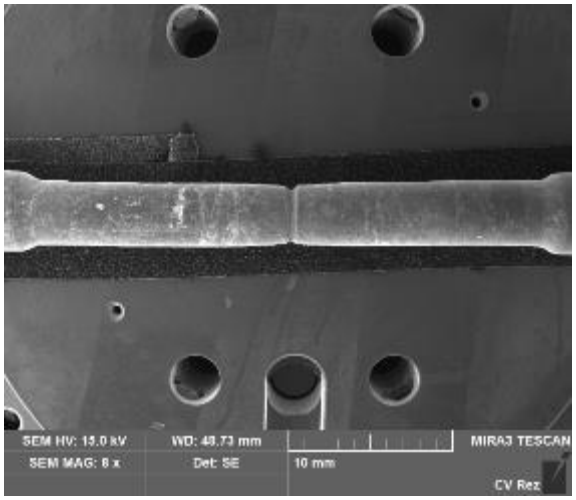

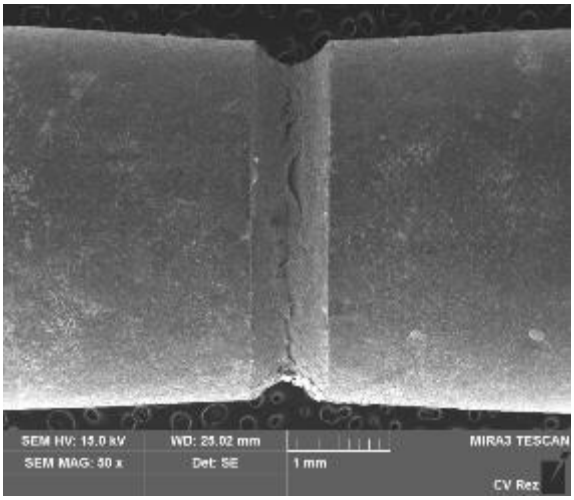

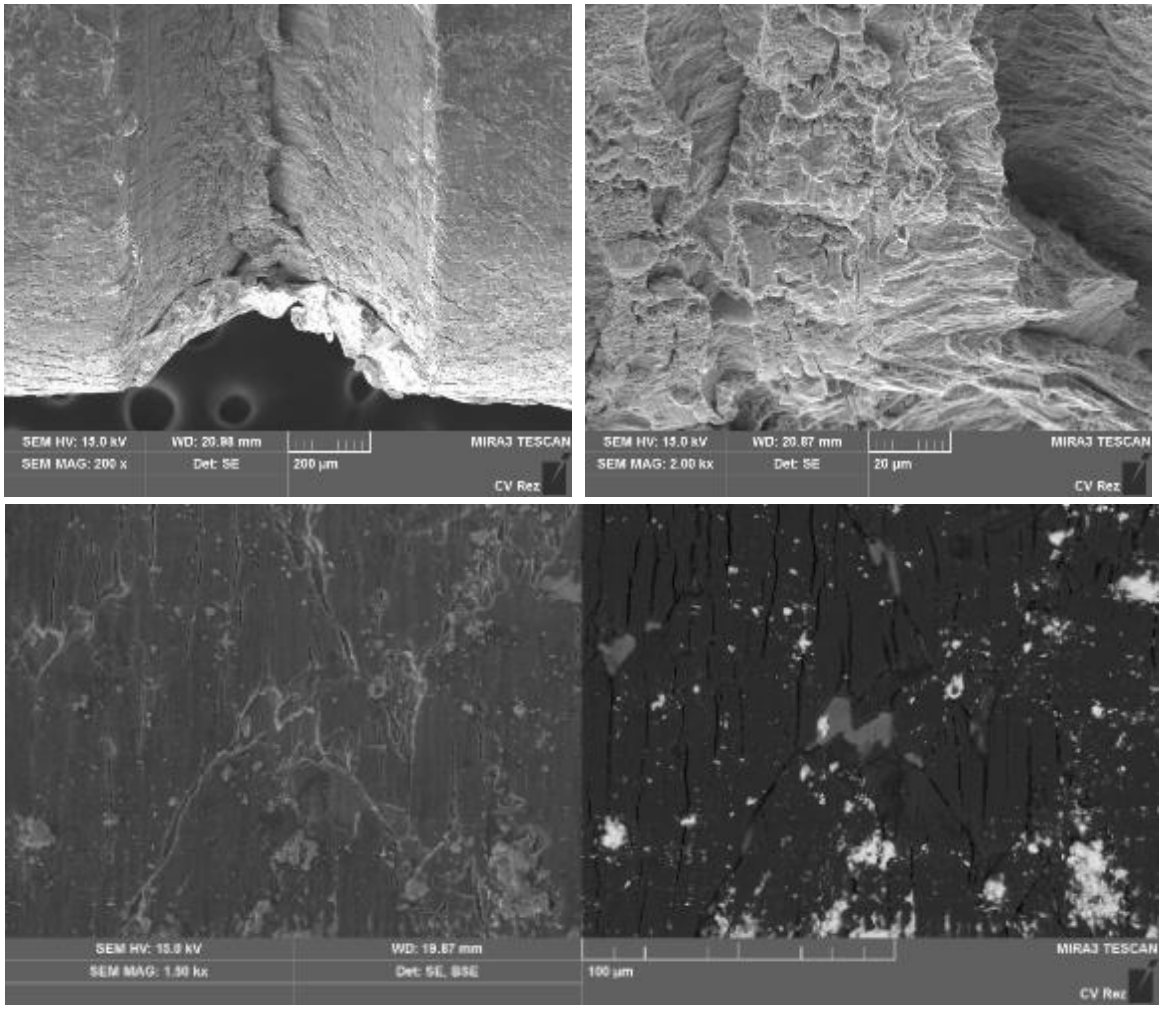

Figure 19 – SEM images of the surface of the notched specimen i03 after loading in PbBi at 550C. a) General view; b-c) details of damaged notch; d) detail of crack at the notch; e) SE and BSE parallel images of cracks on the smooth surface of the specimen.

In a similar way, it was shown (Fig.20) as the behavior of the coating was the same also from the cross-section examination. On the smooth surface the cracks were limited to the coating and there was no detachment of the coating.

On the notch, the coating was more damaged, in localized areas delaminated and there was cracking of the T91 substrate.

EDS analyses also confirmed the same features as highlighted for the previous specimen.

It has to be highlighted that this specimen was in the PbBi, before loading, for a much longer time (386h, see Tab.4). This time in the PbBi, at 550°C did not affect the coating at all. From the chemical point of view it showed high stability and no tendency to react with the liquid metal.

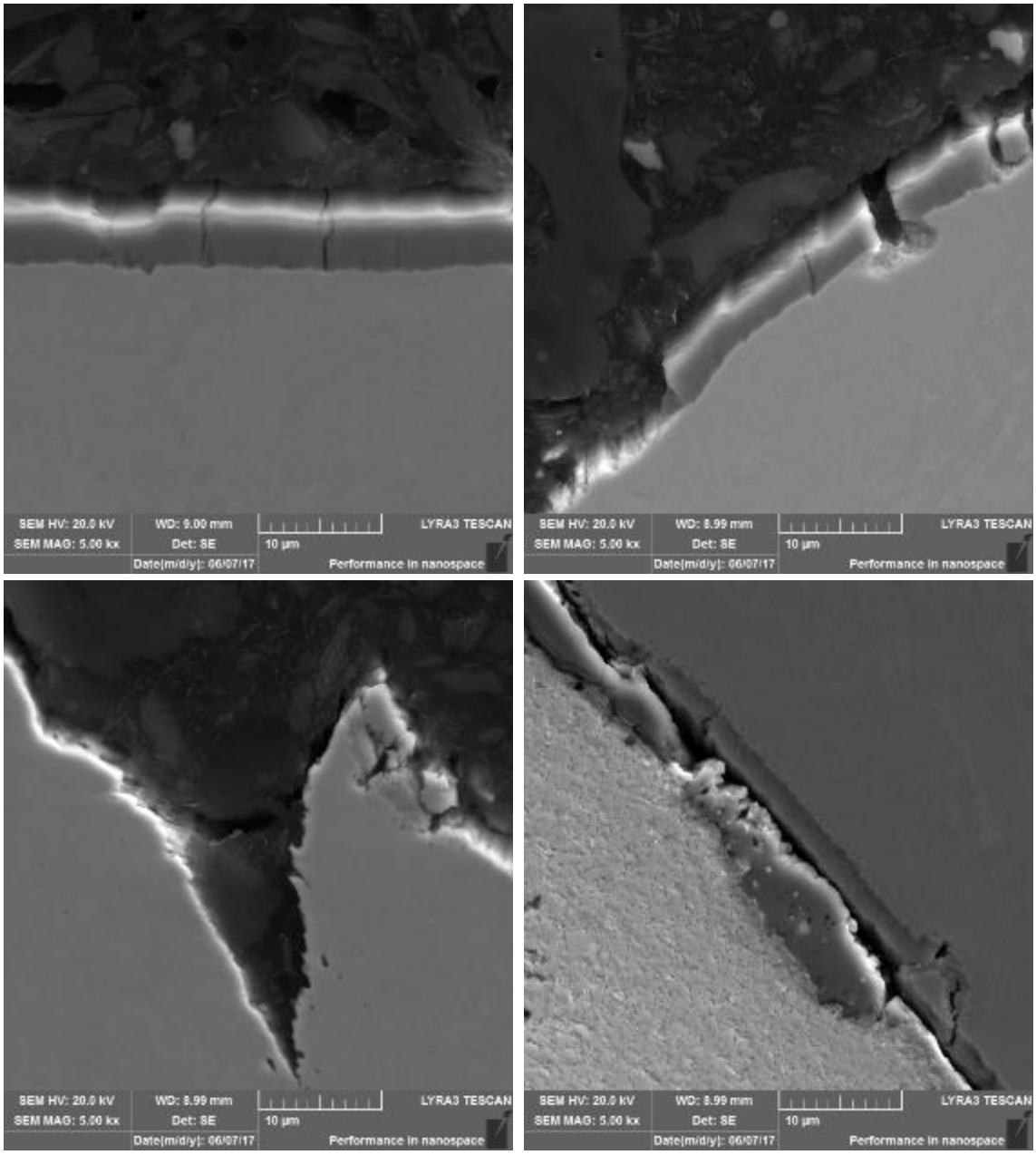

Figure 20 – SEM images of the cross section of the notched specimen i03 after loading in PbBi at 550C. a) Coating on the smooth surface; b) coating on the notch surface; c) crack in the notch; d) coating delamination from the notch.

5.5 Summary

-coating thickness up to 15µm

-Coating cracking along the full specimen length but not detaching from substrate on the smooth surfaces

-no oxygen detected in the coating. The oxygen content in the PbBi was too low to induce oxide formations. However, the coating did not have any interaction with the environment (no chemical degradation).

-cracking of steel at the notch: higher localized stresses and multiaxial load

-tests with lower oxygen content terminated earlier: the system was set to stop automatically after 10% decrease from the UTS. For both specimens (i01 and i02) a sudden decrease of the load appeared and the tests was interrupted. While for i02 could be the crack initiation, for i01 there was no apparent reason (no anomalies observed in the specimen)

-due to the good mechanical properties of the substrate, even at 550°C, the loads applied were very high (up to 550MPa), which is well above the loads that would be applied in operational conditions. It would be important, in a future development, to study the AlTiN coating in more conservative conditions (lower stress level).

6 Experimental 316L surface alloyed – CVR, KIT

6.1 316L – surface alloyed

FeCrAl coating was manufactured on austenitic 316L steel (Tab. 9 composition from DEMETRA batch). The 2 tensile specimens were manufactured in the L direction (Fig.1) and were round tensile specimens with a 4mm diameter and 20mm gauge length.

Table 9 –Composition of the steel 316L

Fe	C	Cr	Mo	Mn	Si	Ni	V	Cu	P	Al	Ti	S	N
Bal.	0.02	16.73	2.05	1.81	0.67	9.97	0.07	0.23	0.03	0.02	0.006	0.003	0.03

Tensile specimens were manufactured in the L direction (dimensions in Fig.21)

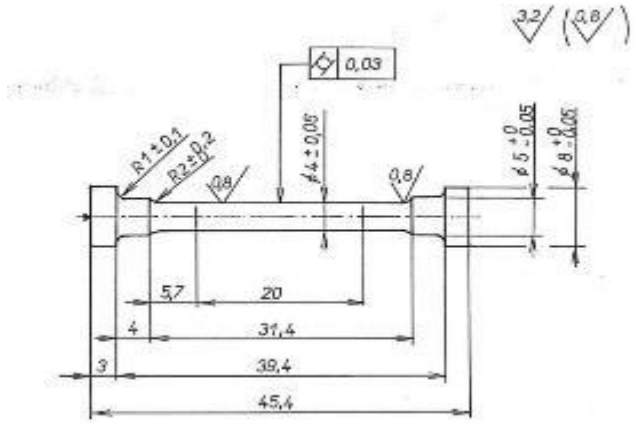

Figure 21 - Dimensions of tensile specimen

6.1.1 Coating and surface alloy process

FeCrAl coating was applied using the E-beam PVD device at KIT. The coating was deposited using a target of FeCrAl with an Al concentration of 8wt% and Cr of 12wt% with additions of Y below 0.5 wt%. The deposited layer had a thickness of 8 µm and were applied using a deposition rate of about 5nm/sec. During the coating the specimen was rotated with a rotation speed of about 60rpm. The so coated tensile specimen was transferred to the GESA facility (see section 2 of this report) and their surface alloyed applying a pulse of 40µs each 90°. A surface inspection using the SEM/EDX revealed the existence of a FeCrAl layer on top of the sample after the 1st pulse. To smooth and homogenous the surface layer a second serous of pulses (again each 90°) with shorter pulse length (less energy) was applied. However, after these the previous existing FeCrAl layer was not really measureable applying SEM/EDX from the surface. Due to lack of time and samples no further specimens could be prepared and therefore the ones with none optimized surface alloying were used for the tests at CVR. Finally one can conclude that the results reflect the behaviour of 316L steel at such test more that of a FeCrAl surface alloyed 316L.

6.1.2 Mechanical testing

Tensile tests were carried out in PbBi, at 550°C, in the CALLISTO cell. CALLISTO is a tank containing liquid PbBi built on a Zwick/Roell Electromechanical Creep Testing machine, Kappa 50DS. CALLISTO is based on the 2-tank concepts, where the first tank is for the preparation of the liquid metal (oxygen dosing). The liquid is then transferred to the second tank, containing holders and specimens. Table 10 summaries the test matrix with experimental parameters.

Table 10 – Test Matrix

Spec	T [°C]	O [Wt%]	Strain rate [s^{-1}]		Max load [MPa]	Environment	Time in PbBi before loading [h]
1	550	10^{-7}	10^{-6}		160	PbBi	46
2		10^{-7}			233		23

6.1.3 Microscopy

Specimens were examined before and after test with a scanning electron microscopes (SEM), MIRA3 GMU by Tescan Inc with associated EDS detector for chemical analyses. Due to the limited amount of specimens, before tests only the surface of the specimen was observed. After test, surface and cross-section were examined for both specimens.

6.2 Results

6.2.1 Specimen before exposure

From SEM observation of the surface after coating (Fig. 22) it was observed a uniform and rather smooth surface (Fig. 2.a and b). The wavy appearance along the length of the specimen is most likely connected with the E-beam melting and surface alloying of the coating.

Detailed observation of the surface revealed localized features, such as superficial cracks (opened grain boundaries due to the rapid cooling after E-beam treatment) along lines of grain boundaries (Fig. 2.c). Moreover, closer to the side of the specimen (not the central part), superficial bubbles were observed, as an integral part of the coating (Fig. 2.d).

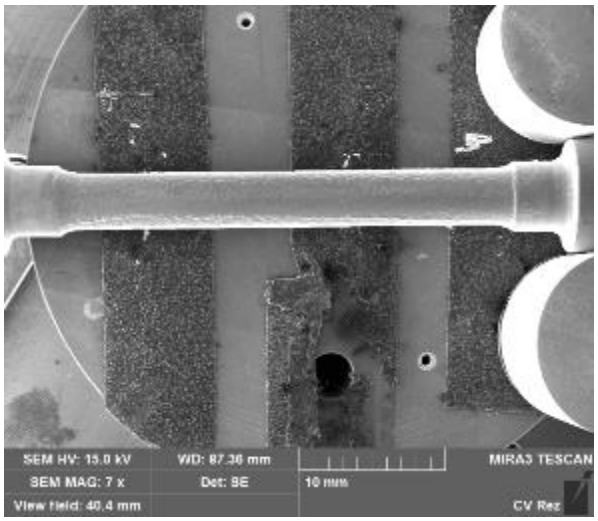

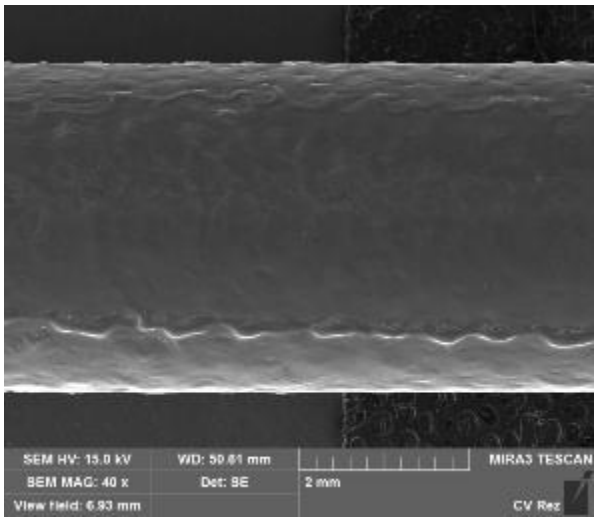

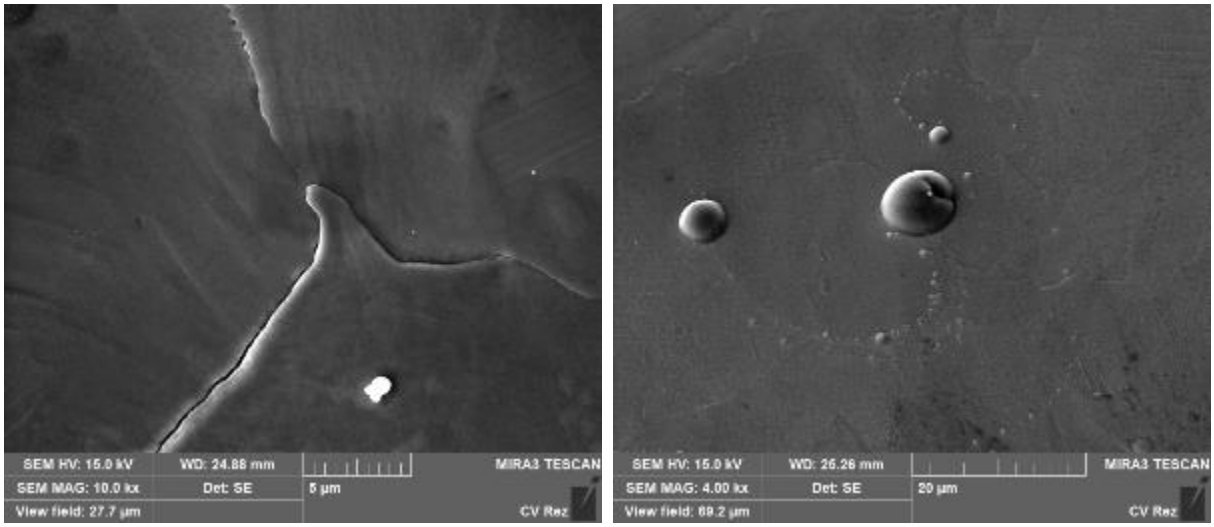

Figure 22 – SEM images of the FeCrAl-surface alloyed surface. a) general view of the specimen; b) detail of the surface in the central part of the specimen; c) localized cracks on the surface; d) bubbles on the surface. The surface does not contain due the non optimized treatment any Al that can serve as reservoir for the formation of a protective scale

6.2.2 Mechanical Tests

Specimens were loaded up to different levels, just above the YS point of the substrate material. The stress-displacement curves are represented in Figure 3. The curves are in agreement with the behavior of the austenitic steel 316L at 550°C, with the Yield stress at about 150Mpa. The max UTS would be located at about 350Mpa and 11mm displacement, which was decided to be a level of plastic deformation beyond the application of the alloy and the coating itself. Therefore, tests were interrupted at lower levels of deformation (crosshead displacement 0.5mm, *blue line*, and 1.5mm, *orange line*).

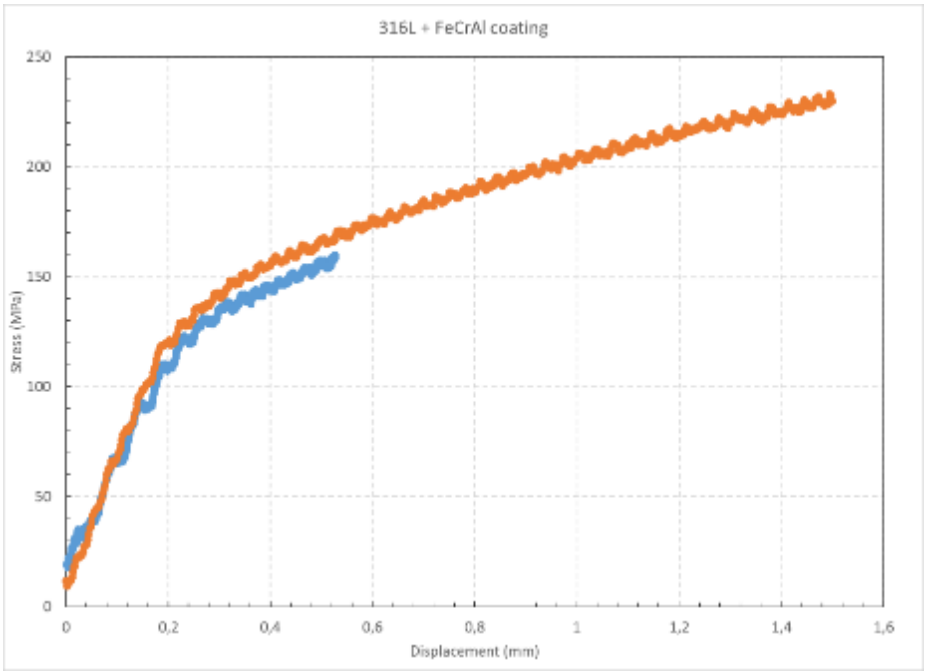

Figure 23 – Stress-strain curves for FeCrAl-coated 316L steel tested at 550°C in PbBi for specimen 1 (blue line) and 2 (orange line).

6.2.2.1 Specimen 1

Specimen 1 was loaded up to 160MPa (slightly above the YS). After test the surface of the specimen was almost entirely covered with PbBi (Fig. 24) and it was not possible to observe the surface of the specimen. In order to prevent any influence of the chemical solution normally used for removing the PbBi on the metallic surface, the PbBi was not removed and the specimen was embedded in resin for the cross-section examination.

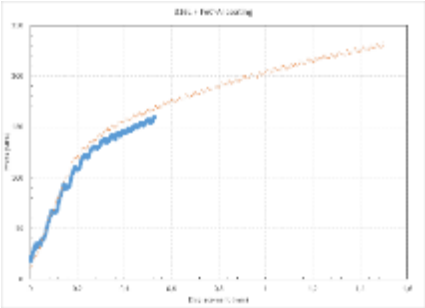

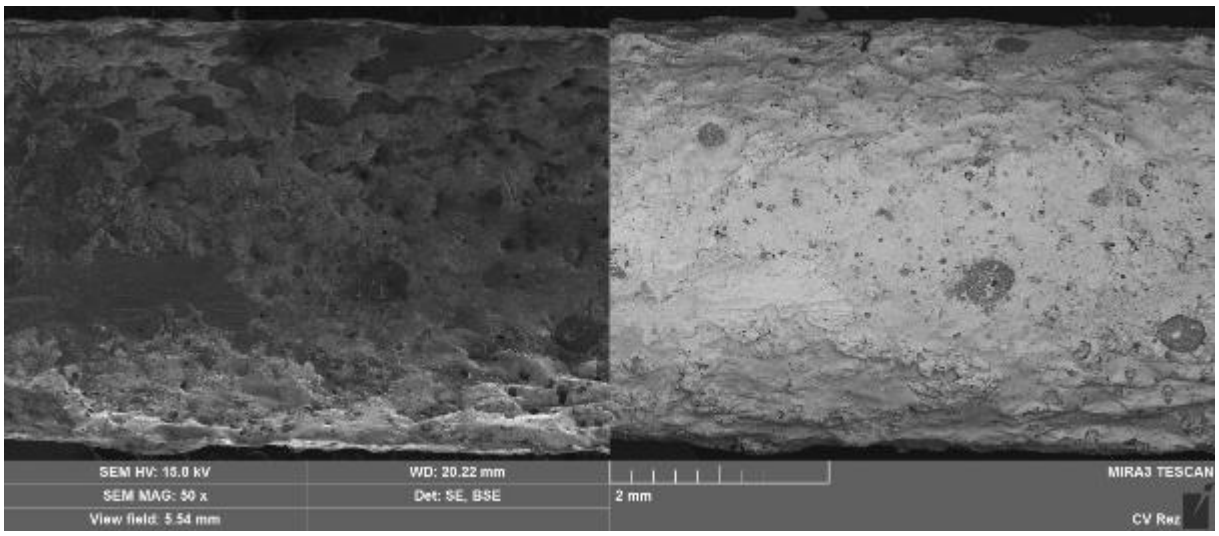

Figure 24 – SEM image (SE vs BSE) of specimen 1 surface tested at 550°C in PbBi

Examination of the cross section revealed that in the central area of the specimen there was formation of superficial cracks (Fig. 25) up to 20μm deep. A continuous oxide layer was observed over all the surface of the specimen and EDS analyses revealed that it was an Fe-Cr- rich oxide (Fig. 26, Tab.11). The oxide cracked in a few locations and PbBi penetration was observed. Although the steel has a Ni content of 9.7wt% (spot 174) all the analyses inside the crack and near the surface showed a marked decrease of the Ni content. This results highlighted that the outer diffusion of Ni occurred. At 550°C this is a very fast process and the inner penetration of PbBi is favoured.

Ni depletion in the surface area might also induce ferritisation of the alloy and thus cracking may be favoured. Based on the present results is not possible though to verify this condition.

There was no Al detected in the surface layer, nor in the outer oxide.

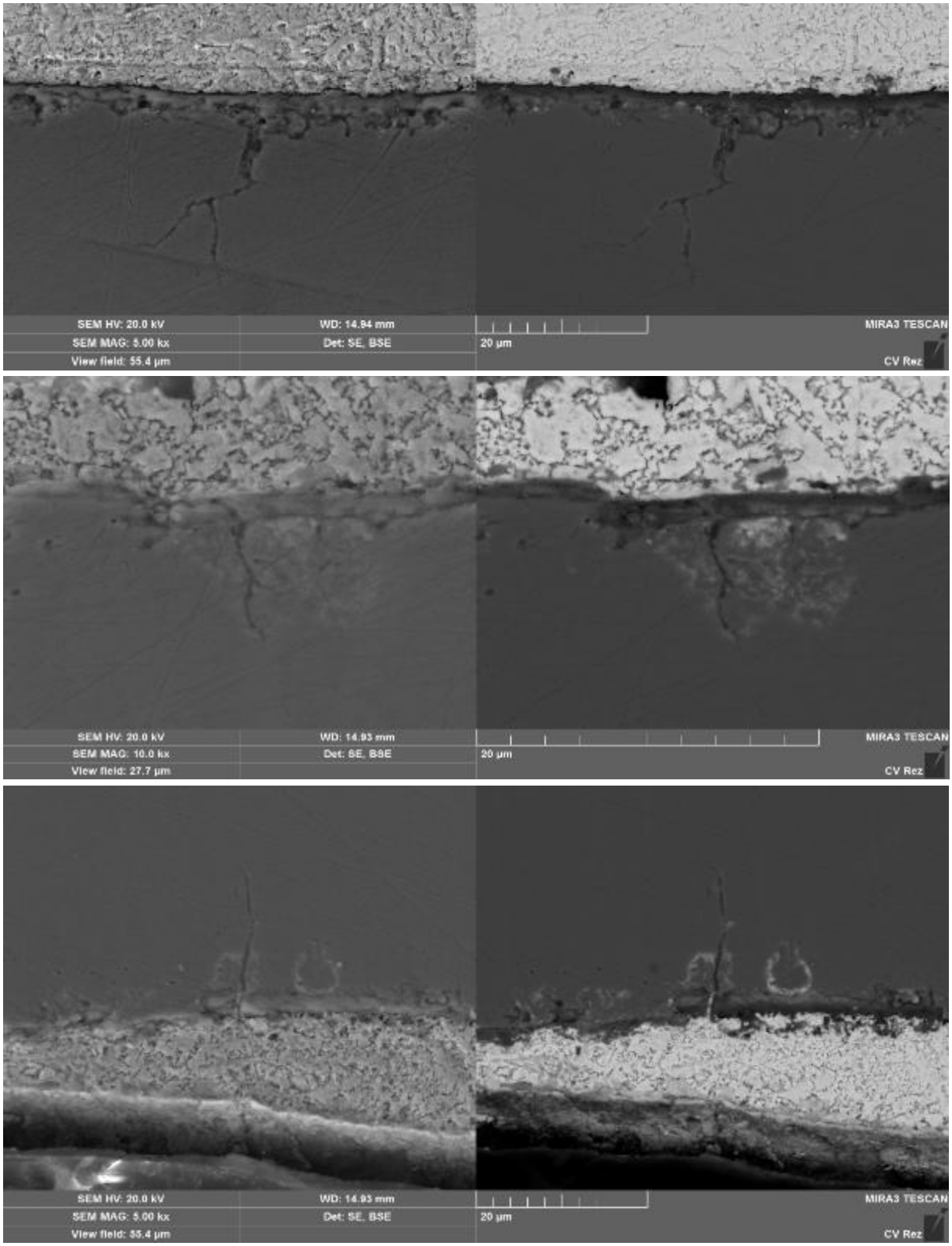

Figure 25 – SEM images (SE vs BSE) of specimen 1 cross-section, after loading at 550°C in PbBi. Cracks on both sides and PbBi penetration

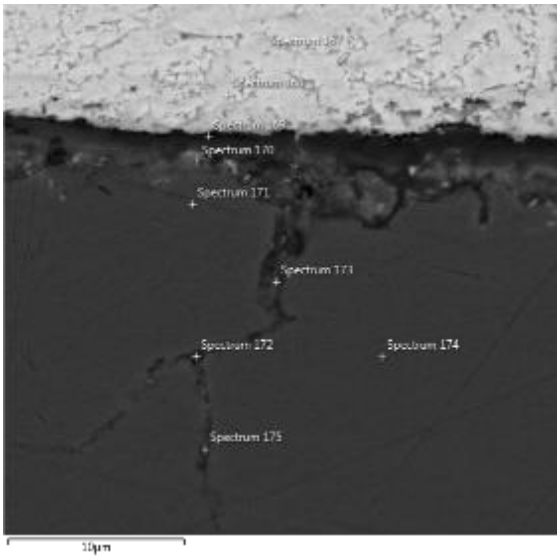

Figure 6 – SEM image of crack with location of spot analyses

Table 11 – Spot quantitative analyses corresponding to Figure 6, wt%

Spot n.	Fe	Cr	Ni	Mn	Mo	Si	V	O	Pb	Bi
169	37.6	25.4	1.0	2.9	2.3	0.6	0.1	9.8	7.5	12.7
170	29.0	18.9	1.0	1.4	1.8	0.7	0.1	18.3	14.8	14.0
171	68.7	17.1	9.4	1.8	2.0	0.6	0.1		0.3	
172	58.3	22.1	4.2	2.0		0.7	0.1	8.7	3.9	
173	66.3	16.5	7.3	1.5	2.0	0.6	0.1	3.7	0.9	1.0
174	68.7	17.3	9.6	1.8	2.0	0.6	0.1			
175	63.6	18.3	5.2	1.9	2.0	0.6	0.1	5.4	1.2	1.6

6.2.2.2 Specimen 2

Specimen 2 was loaded up to 233MPa (above the YS). After test the surface of the specimen was almost entirely covered with PbBi and there were a few visible areas (Fig. 27) were cracks were observed.

EDS analyses of these surfaces (Tab.4) confirmed the enrichment in Fe and Cr, associated to O. Minimal amount of Ni were detected. No Al was measured on the surface.

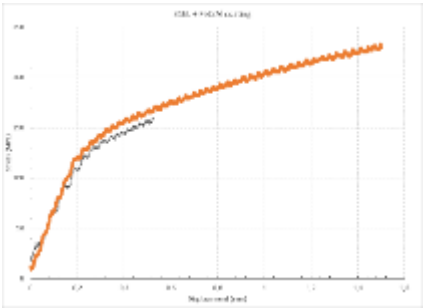

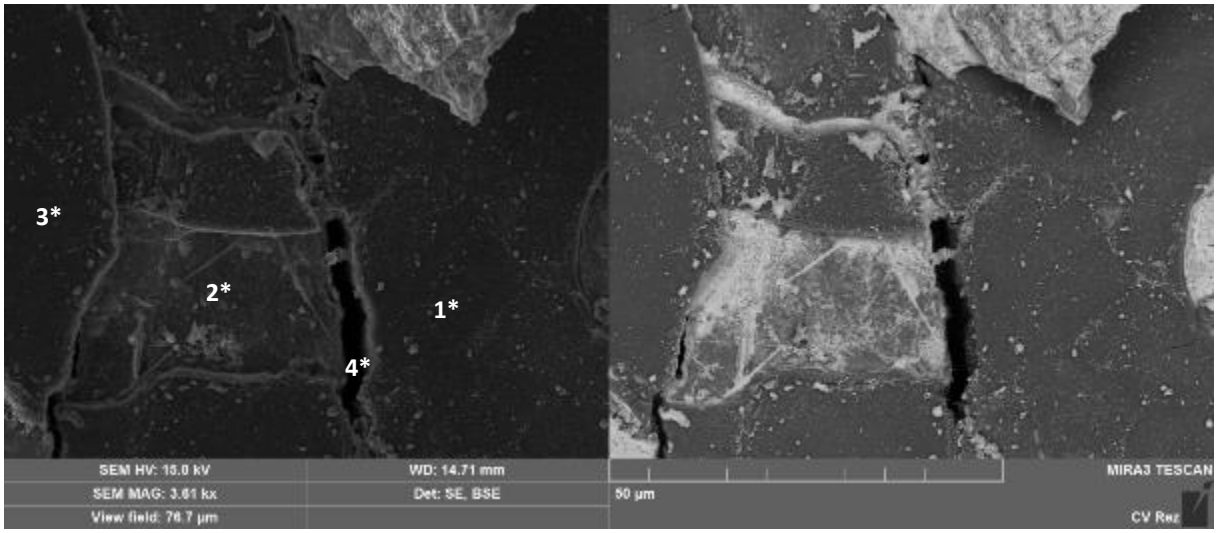

Figure 27 – SEM image (SE vs BSE) of specimen surface, with location of spot analyses (left-hand side)

Table 3 – Spot quantitative analyses corresponding to Figure 27, wt%

Spot n.	Fe	Cr	Ni	O	Si	Mn	Mo	Bi	Pb
1	27.8	26.8	0.9	25.2	0.9	3.7	2.8	5.4	6.4
2	37.6	5.5	0.6	7.3	0.5	0.6		33.5	14.5
3	30.9	23.8	1.3	25.3	0.9	2.6	2.6	4.8	7.7
4	16.1	20.7	0.8	19.7	0.5	4.1		15.9	22.2

Examination of the cross section (Fig.28) highlighted the presence of more cracks and deeper inside the specimen (up to 35µm). The cracks are mainly perpendicular to the surface and loading direction.

The oxide layer (Cr-Fe-based) is well visible in all the surface, but it is also detached in those locations were the cracks started and the PbBi is penetrating the alloy.

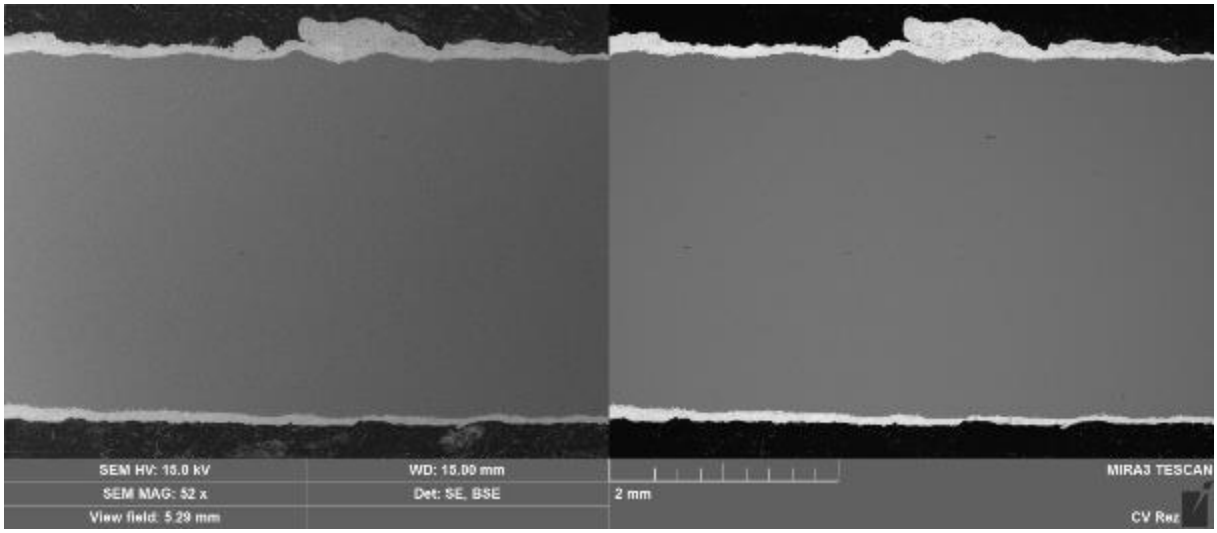

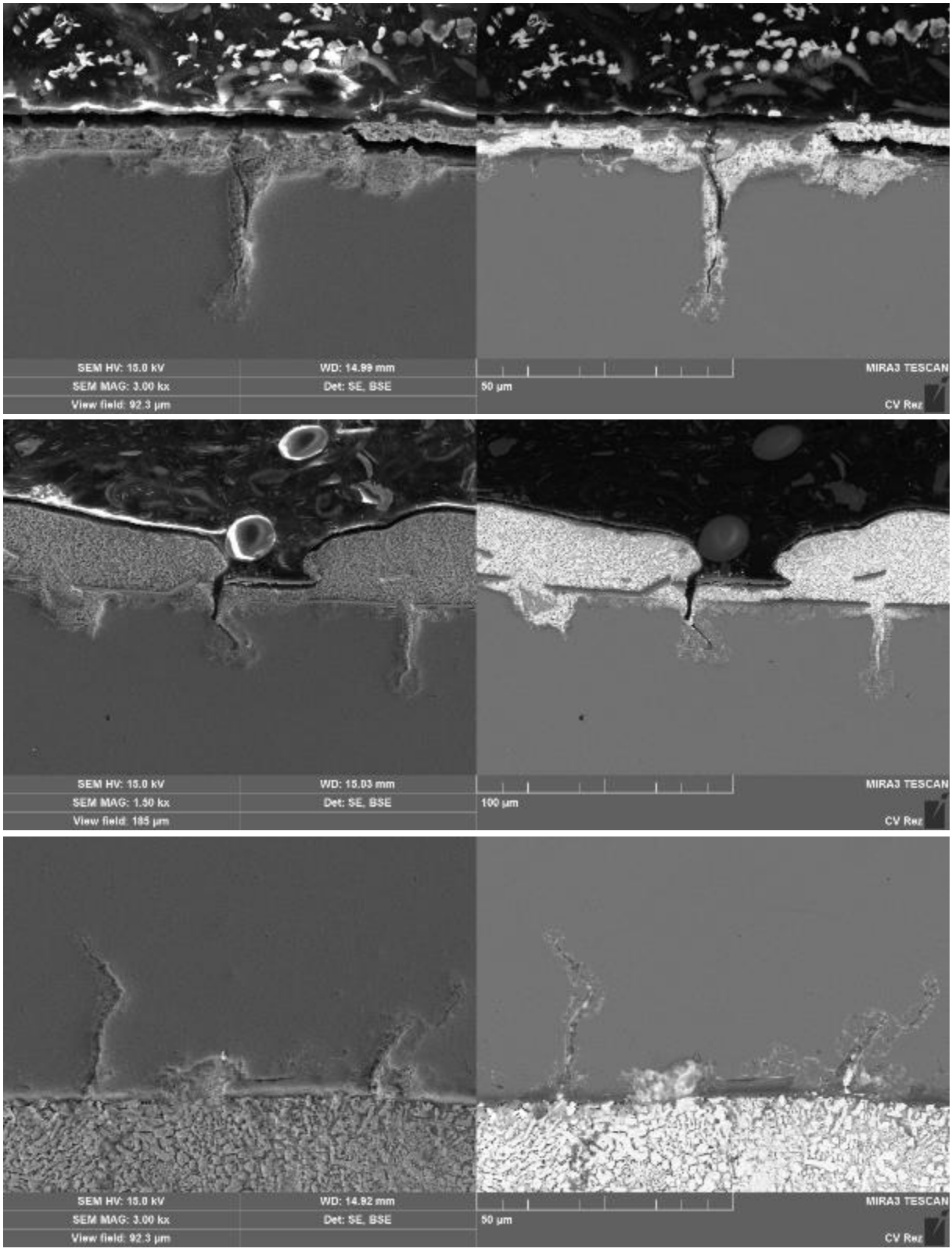

Figure 28 – SEM image (SE vs BSE) of specimen cross section highlighting the outer oxide layer, the cracks and the inner penetration of PbBi.

Quantitative spots and qualitative line scans (Fig.29) analyses were carried out in those locations and confirmed the enrichment of Fe and Cr at the surface combined with O and a gradual depletion of Ni starting from about 10µm from the surface. This depletion seem related to the presence of the coating, mixing with the substrate. No Al was detected.

The Ni depletion

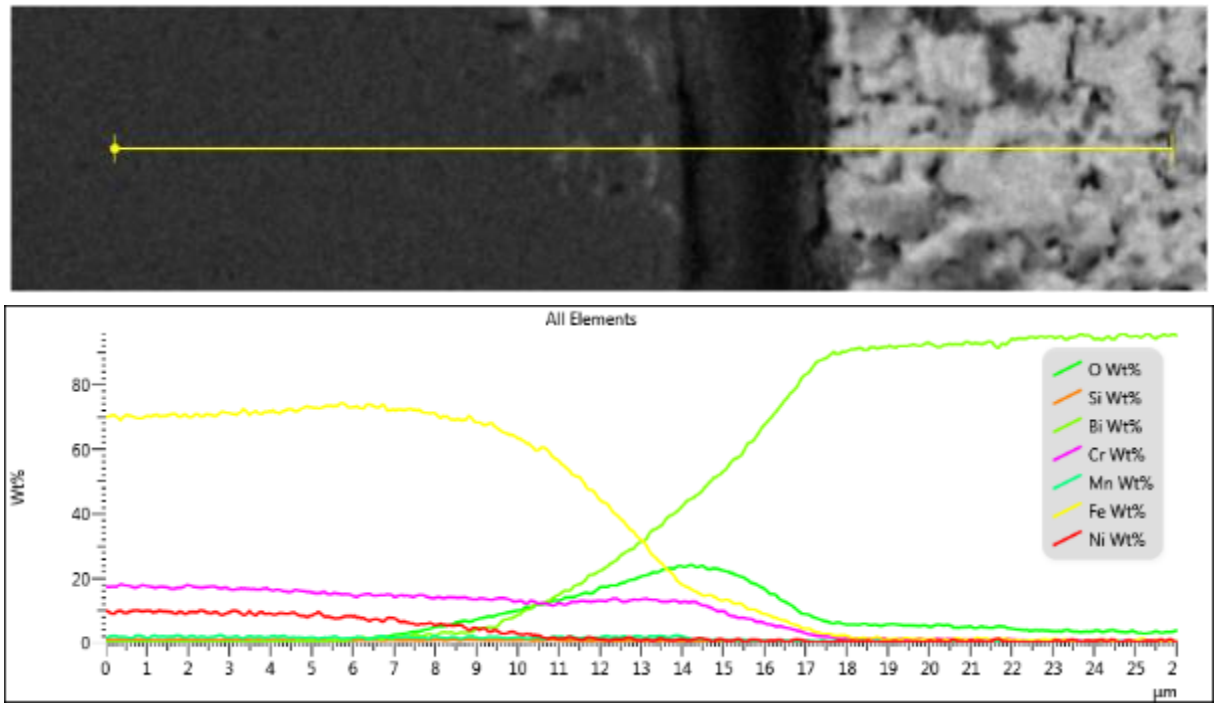

Figure 29 – EDS qualitative line scan on the surface of specimen 2

6.3 Summary

- Austenitic 316L was coated with a FeCrAl coating and surface alloyed
- After surface alloying no Al was detected applying SEM/EDX from the surface
- 2 round tensile specimens were coated and tested in PbBi at 550°C.
- The 2 specimens were loaded up to 2 different stress levels, above the Yield Stress of the 316L.
- The surface of the as-received coating was very smooth, with localised irregularities (small cracks and bubbles).
- After loading it was shown that both specimens reacted to the environment:
  - Lack of Al and consequently Al_2O_3
  - Formation of a Fe-Cr-rich oxide
  - Ni depletion (possible due to missing FeCrAl layer - most likely removed by 2nd GESA pulse)
  - Localised PbBi penetration and cracking
- The Fe-Cr-rich oxide, up to 3mm thick, was locally damaged and spalled off.

7 Tensile tests with FeCrAl alloy – CVR, KTH

7.1 Experimental

7.1.1 Material and Specimens

The alloy studied was cast in a vacuum furnace located at the R&D center at Sandvik Heating Technology AB (former Kanthal AB) in Hallstahammar, Sweden. Upon finishing the melting of the batch, the alloy's chemical composition is analyzed using inductively coupled plasma optical emission spectroscopy (ICP-OES) and combustion analysis (Tab.1). The material was hot rolled.

Table 6 – Alloy composition, wt%

Fe	Cr	Al	Si	Mn	C	Ti	Zr
Bal	10.15	3.95	0.13	0.11	0.03	0.09	0.21

The batch procured (LS4735) for mechanical testing was a 15x3x170 mm flat bar. From this bar were produced 2 flat tensile specimens (Fig.1).

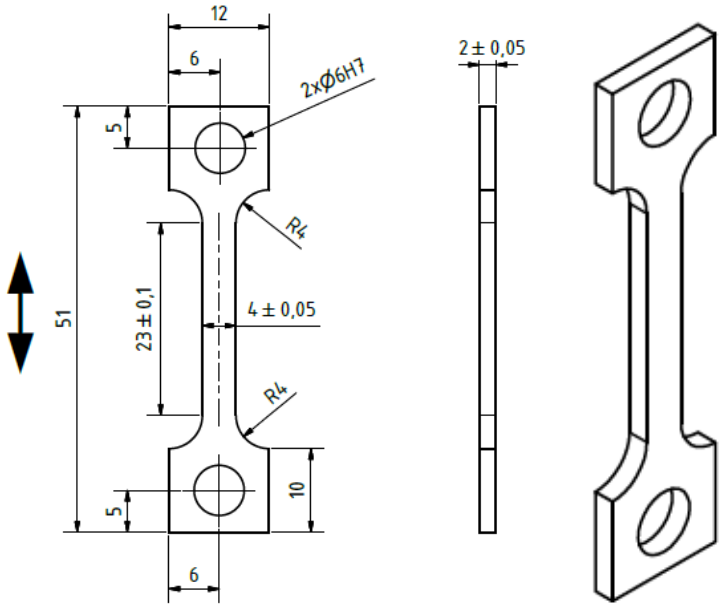

Figure 12 – Flat tensile specimen

Mechanical testing

The 2 tensile specimens (Fig.1) were loaded in PbBi at 550°C. The detailed test matrix is in Table 2. Tests were performed in CALLISTO, a cell that was especially designed and manufactured for mechanical testing with heavy liquid metals (HLM). The cell was mounted on a Zwick/Roell Electromechanical Creep Testing machine, Kappa 50DS. CALLISTO works on the 2-tank concept: 1st tank for liquid conditioning (reduction of oxygen content from saturation to the desired value) and the 2nd tank for mechanical testing. Both tanks are provide with oxygen sensors based on the ref. Bi/Bi_2O_3.

Table 7 – Test Matrix

Spec.	T	Environ.	Oxygen	Strain rate	t* before	t test
	°C		wt%	s^{-1}	h	h
F1	550	PbBi	10^-8	10^-4	64	1.5
F2			10^-8	10^-4	12	1.8

*time before start loading, when the specimen is already at temperature in PbBi and the O is being regulated.

7.2 RESULTS

Tensile tests

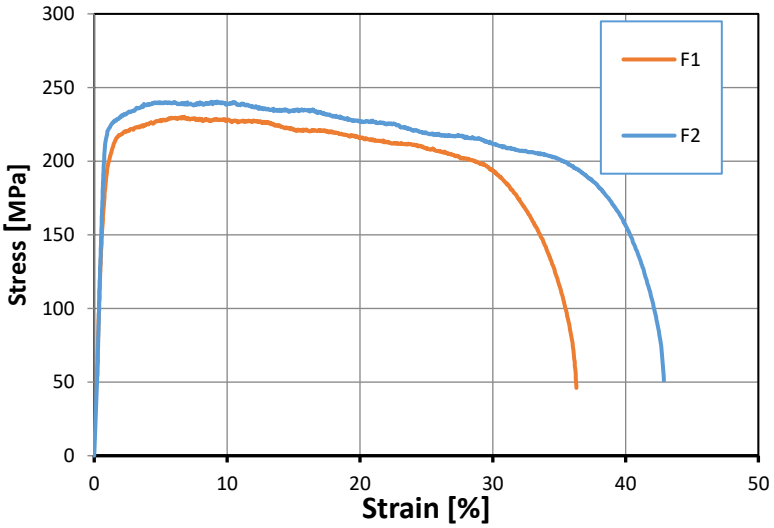

Figure 2 – Stress-strain curve for the 2 specimens F1 and F2, tested in PbBi at 550°C.

Stress-strain curves (Fig.2) shows a similar trend for both specimens in the elastic regime, although F1 afterwards showed lower UTS and shorter elongation to rupture. The main difference between the 2 specimens is only in the time they were immersed in PbBi before the loading period. F1 was for 64h at 550°C in PbBi and if this could have an impact on the specimen performance cannot be assessed at this stage. More material would be required in order to confirm the effect of pre-exposure.

Table 3 – Summary of mechanical properties of the FeCrAl alloy in PbBi at 550°C

Specimen	YS [MPa]	UTS [MPa]	ε_{rup} %
F1	216	230	36.3
F2	218	240	42.9

7.2.1Fractography

F1

Examination of the fracture surface after test was carried out by SEM. The examination revealed a fully ductile fracture (Fig.3) with elongated dimples (Fig.3.e and f).

Observation of the flat surface (Fig. 3.b and c) also confirmed the ductile character of the fracture, with heavy plastic deformation. In particular, on the surface (Fig.3b) were observed large area were there was material loss (lighter parts highlighted by the blue lines). These features are presented below in more detail in Figure 5.

Figure 3.d highlights an anomalous part of the fracture surface, where it is evident the influence of the laminated structure (hot rolling) on the fracture mode. This is also visible below, in Figure 8, from the cross-section observations.

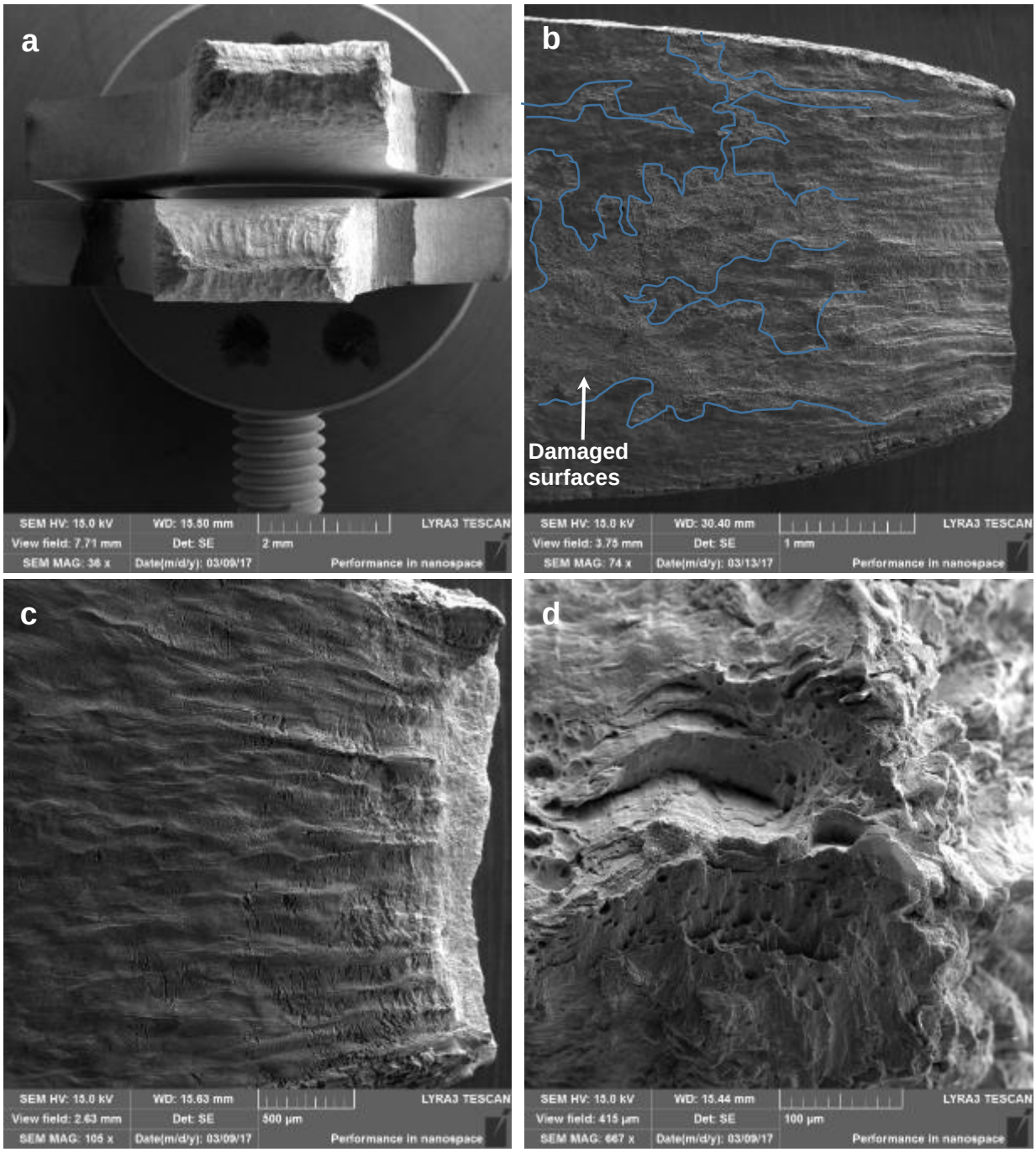

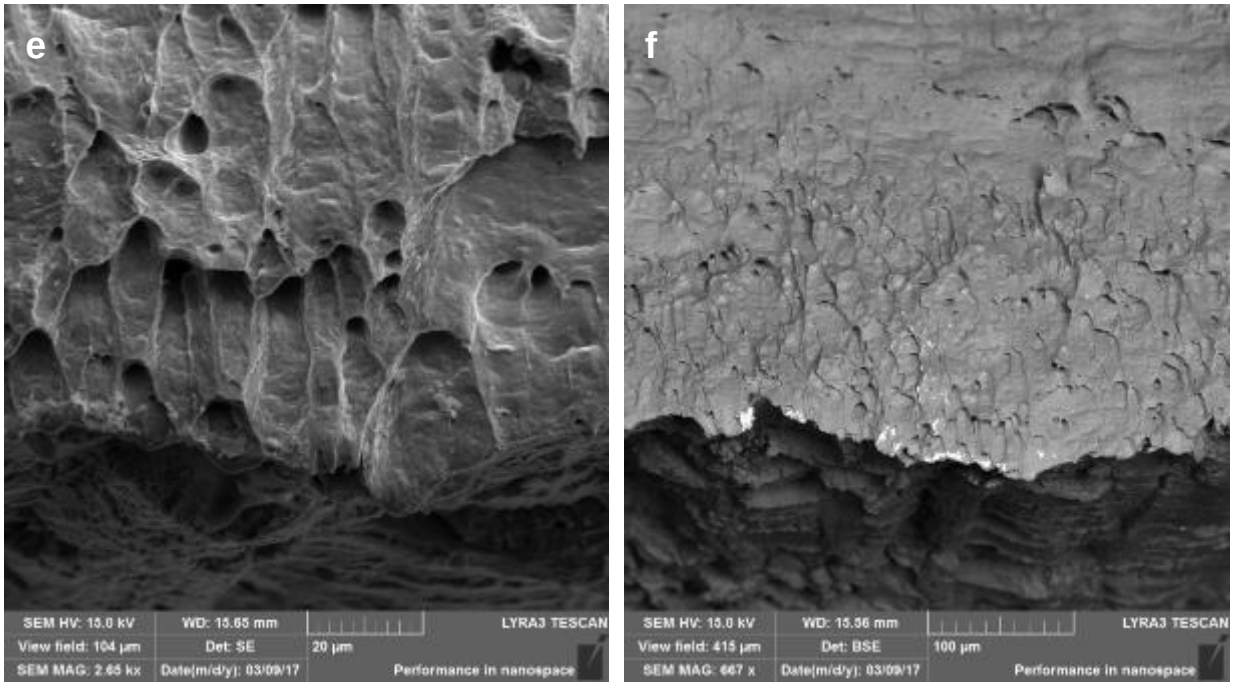

Figure 3 – a) SEM images of the fracture surfaces from both halves of the specimen; b) 1st flat surface after loading; c) 2nd flat surface after loading; d) detail at the edge of the fracture surface; e) detail of the ductile dimples in the fracture surface; f) BSE image of the dimpled fracture surface.

In more detail, the cracks on the plastically deformed area (necking) were studied (Fig. 4). These appeared to be all cracks developing perpendicular to the loading direction. In particular, they did not grow perpendicular to the specimen surface, but in a ductile way the followed the direction of slip plans and are inclined in respect to the flat, original surface.

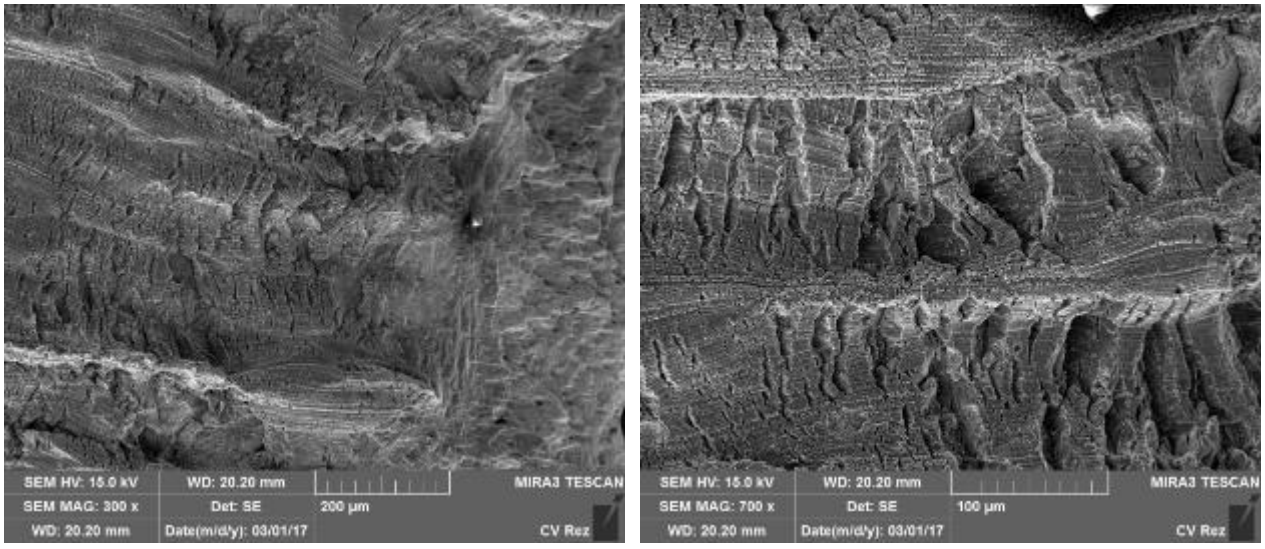

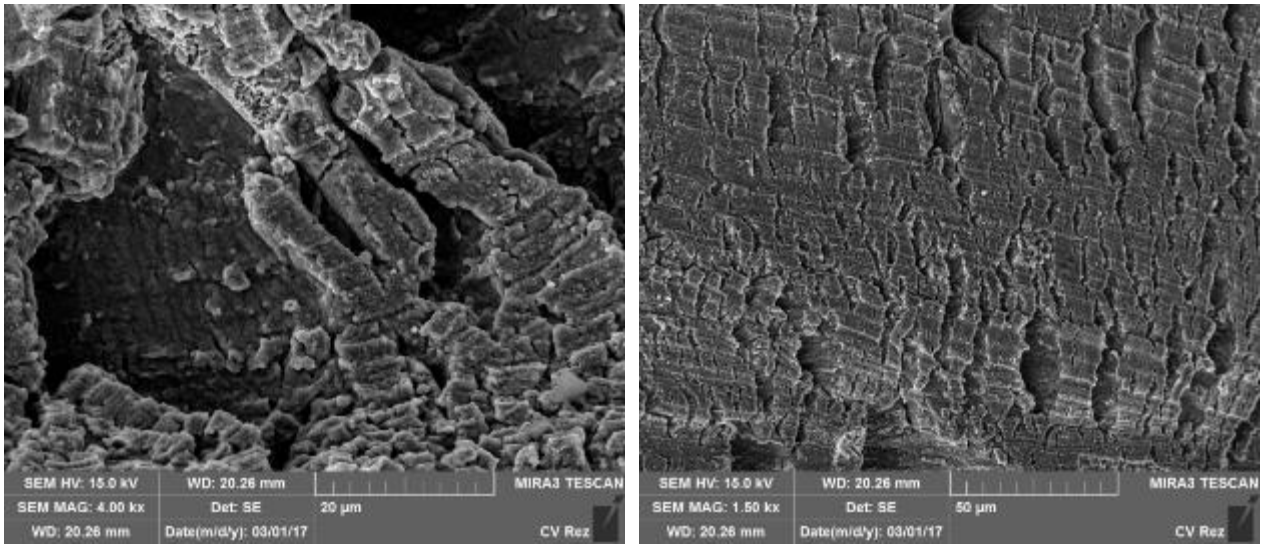

Figure 4 – SEM images of the cracks in the necking area (highest plastic deformation)

As already reported above, material loss occurred on large area of the specimen surface (Fig.5). This was most probably due to the very low oxygen content of oxygen in the environment, which might have prevented the formation of a protective alumina scale. The spongy appearance from the top view was then observed from the cross-section (Fig.8) as a very rough profile. It has to be mentioned that the specimens were treated with a chemical solution in order to remove the residual PbBi and this would have also removed all the material that was no longer attached to the surface (this is the reason for the clean crater appearance.

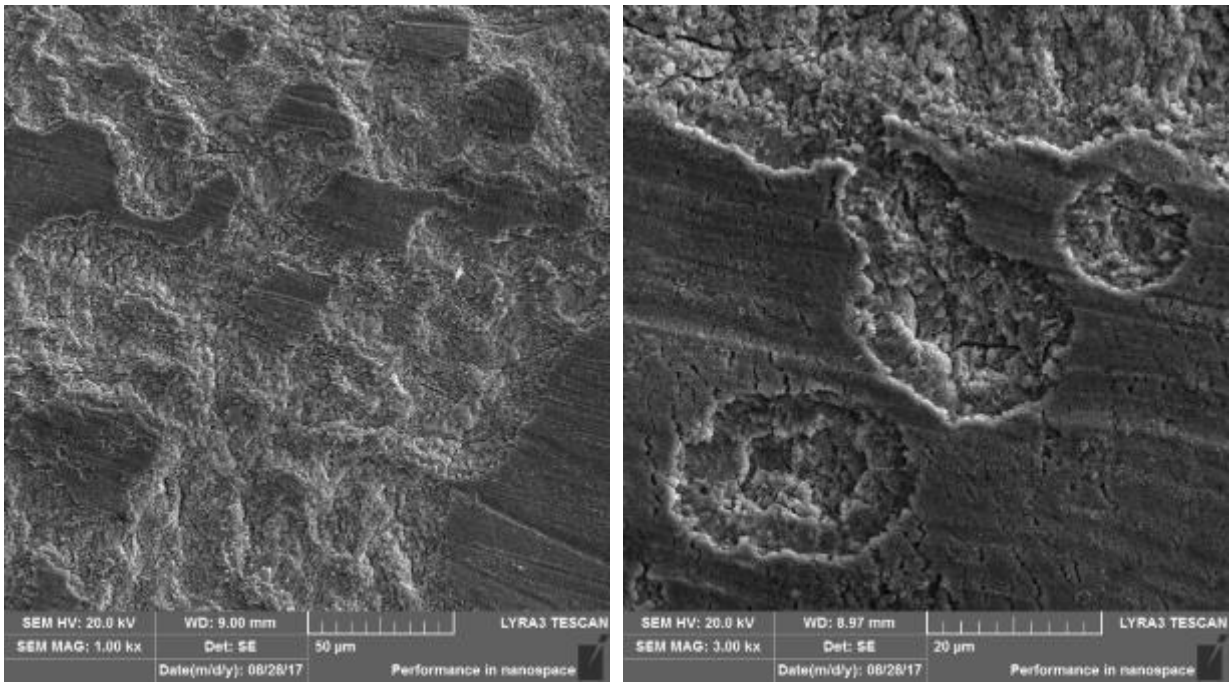

Figure 5 – SEM images of the damage occurred on the flat (lowest deformation) surfaces. a) Spongy surface after localised damage; b) detail of the localised damage.

F2

Examination of the fracture surface confirmed the ductile character of the fracture also for this specimen (Fig.6). Also in this case, beside the ductile dimples, cracking on preferential plates was observed (Fig.6.c and d) in the direction of the hot rolling.

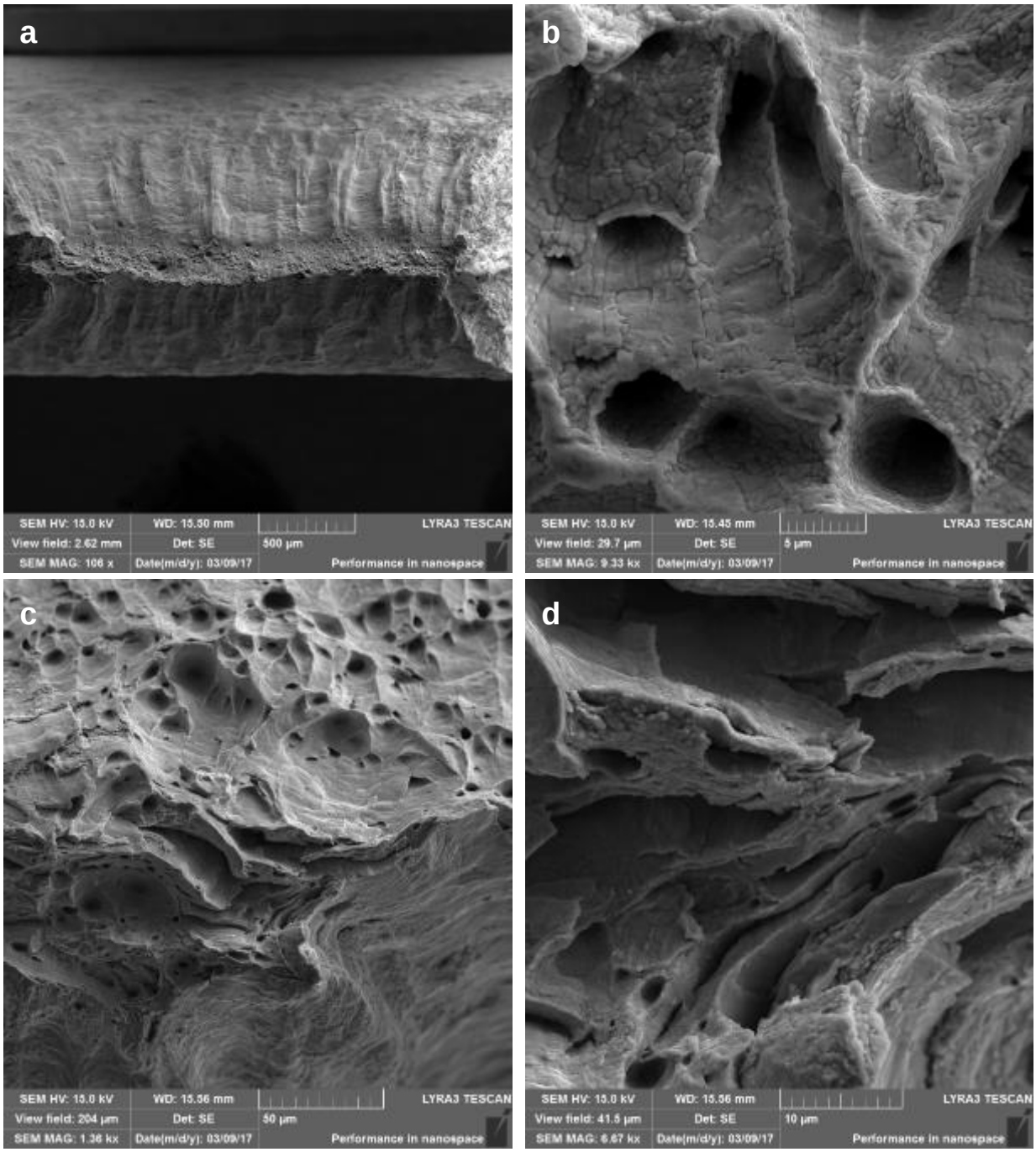

Figure 6 – a) SEM images of the fracture surface; b) detail of the ductile dimples; c) fracture surface with mixed fracture mode; d) detail of "delamination"

Also the surface of this specimen suffered material loss (Fig.7). In particular it was observed as the damaged surface was a preferential site for crack initiation

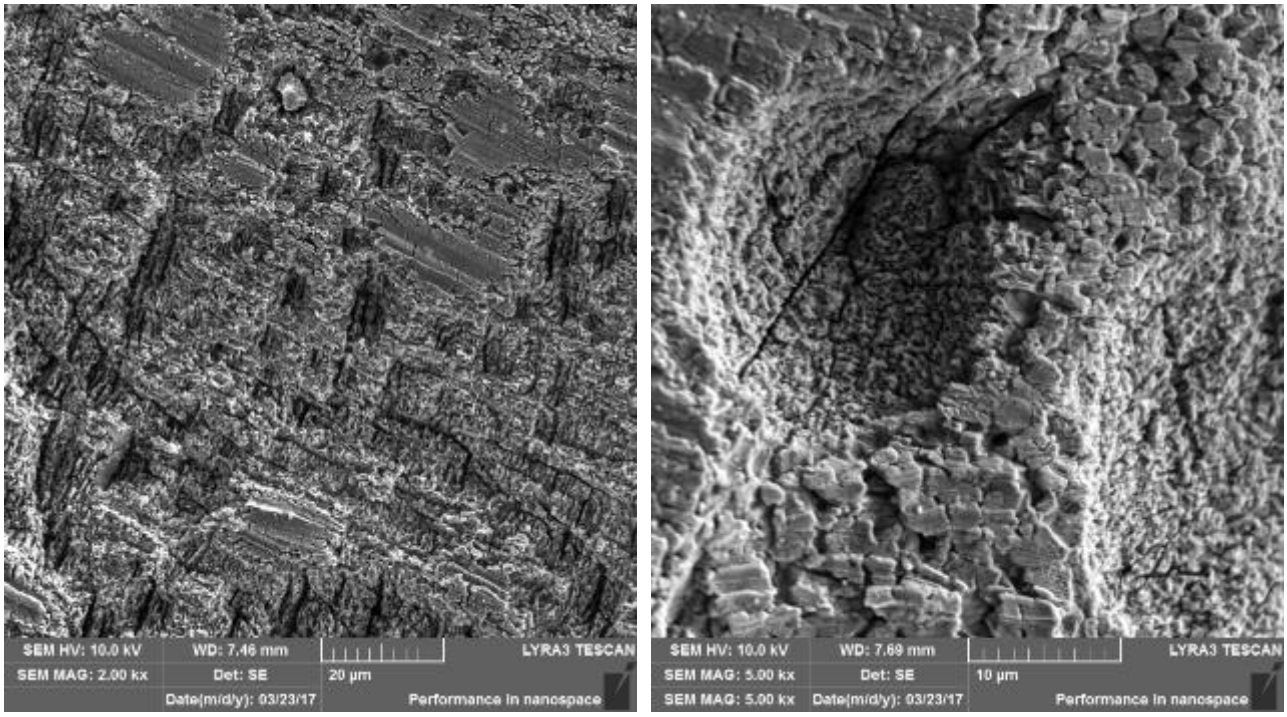

Figure 7 – SEM images of the damage occurred on the flat (lowest deformation) surfaces. a) Spongy surface after localised damage; b) detail of the localised damage

Examination of the cross-section (Fig.8) confirmed the marked plastic deformation (Fig.8.a) creating the angular ending of the fracture surface. Figure 8.b and c also show the relationship between the hot rolling direction and the features of the fracture, where the material has plates-like thin layers. The elongated openings in Figure 8.c might be corresponding to cracks developing not only along the rolling direction but also transversal to the specimens.

Figures 8.d-f show details of the damaged surface with a spongy appearance from the top. The cross section highlighted their morphology, showing the presence of a preferential attack along small preferential sites/lines (up to 2□m deep inside the material) which are not correspondent to grain boundaries. The characteristics of these features were specified by EDS analyses, where there was measured only a slight depletion of Fe at the surface layer (Fig. 9 and Tab.4) confirmed both by spot and line scans.

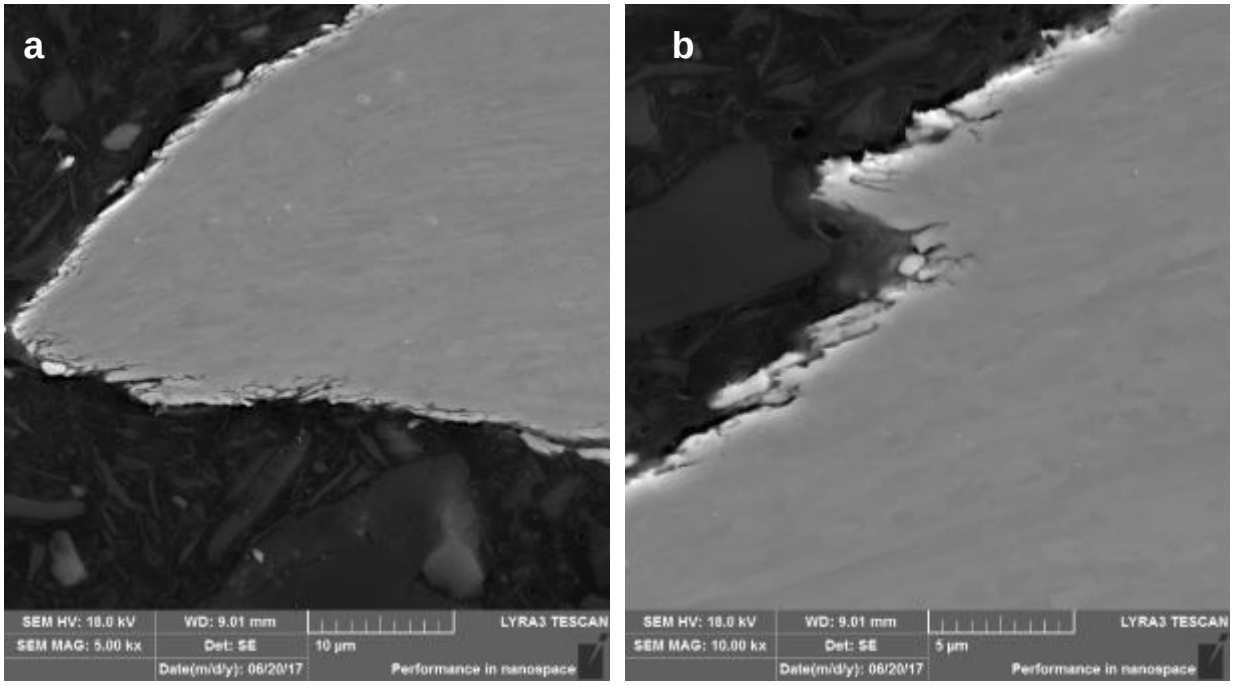

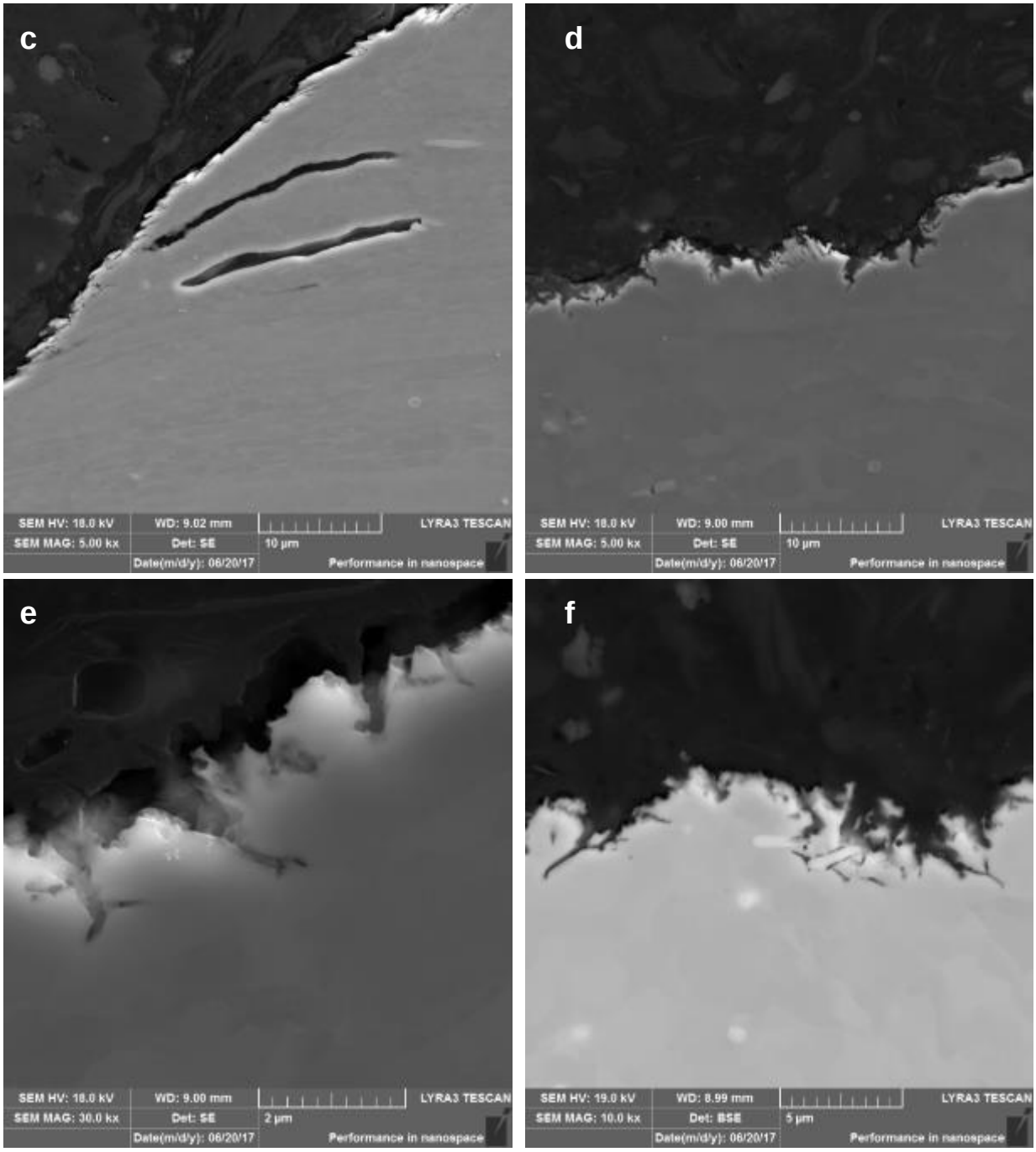

Figure 8 – SEM images of the cross section,

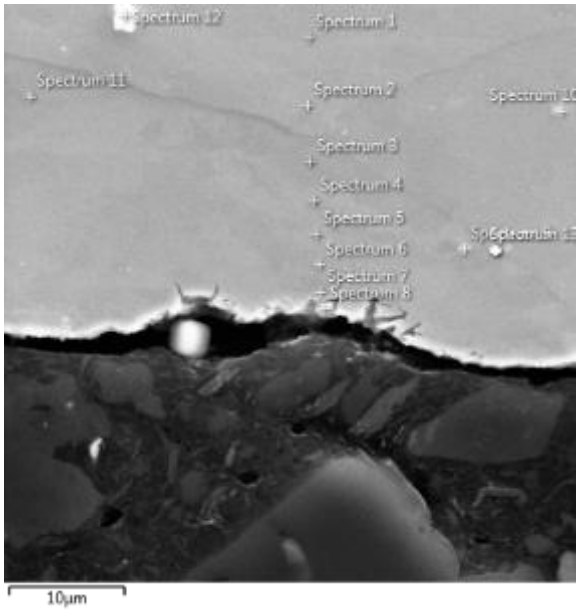

Figure 8 – SEM images of the cross section with location of spot analyses reported in Table 4

Table 4 –Spot quantitative analyses located in Figure 8, wt%

Spot n.	Fe	Cr	Al	Si	Ti	Zr	Pb/Bi	C	O
8	72.1	8.4	3.2	0.2		0.2	1.6	12.8	1.3
7	81.6	9.7	3.8	0.2				4.7	
6	81.7	9.8	3.9	0.2				4.4	
5	81.0	10.0	4.0	0.2	0.1			4.7	
4	81.4	9.9	3.9	0.2				4.7	
3	81.4	10.0	3.9	0.2				4.5	
2	81.8	10.0	3.8	0.2				4.1	
1	80.8	9.5	3.9	0.2		0.2		4.5	

7.3 Summary

-With the FeCrAl bar provided by KTH 2 flat tensile specimens were manufactured.
-They were both tested at 550°C in PbBi with low oxygen content.
-For both specimens the fracture was fully ductile.
-Beside ductile dimples, there were plate-like features that were connected with the specific fracture along the hot rolling direction.
-There is no comparison with air, to be able to observe differences in the behaviour of the alloy. More material will be needed for further investigation.
-The surface of the specimens, where no cracks were detected, showed initiation of degradation. It is not possible at this stage to ascertain which are the causes of the loss of material.

8 Tensile test of Al_2O_3 coated 316Lsteel – ENEA and CVR

M. Utili, C. Mingazzini, F. Di Gabriele, M. Chocholousek, Z. Spirit

8.1 Introduction

The current design of the lead cooled ALFRED reactor foresees operating the reactor with an oxygen content well below the saturation limit at the coldest temperature of the coolant (400°C) to prevent the risk of lead oxide precipitation. This option exposes the steels to severe corrosion/dissolution issues in the regions of the reactor operating at temperatures above 450 °C. In order to protect the steel of main structures, a series of surface engineering processes and coating deposition have been considered up to now. One important constraint of the candidate techniques is that deposition processes have to be carried out without significant heating of the substrate, in order to avoid microstructural modification and degradation of the steel substrates and their performances under neutron irradiation. This is true in particular in the case of reactor vessel which is never replaced during the lifetime of the reactor and where lead can be locally heated up to 450° C, in proximity of the output of the mechanical pumps and before its entrance into the steam generator. Detonation spray is very promising for the application, since high precision control of the layer thickness is not required and the technique is suitable for treating large surfaces. In addition it ensures good adhesive strength, low porosity and surface coating with compressive residual stresses.

Tensile specimens were received from CVR-REZ in order to manufacture coating by detonation spray. With the aim to optimize the adhesion of coating on material before to perform the coating on tensile samples several tests on fake samples were performed.

The procedure adopted and activities performed in order to optimize the Al-base coating on T91 and 15-15Ti is described.

8.2 Detonation Spray Technique

D-gun spray process is a thermal spray coating process, which gives an extremely good adhesive strength, low porosity and coating surface with compressive residual stresses.

A precisely measured quantity of the combustion mixture, consisting of oxygen and acetylene, is fed through a tubular barrel closed at one end. Simultaneously, a predetermined quantity of the coating powder is fed into the combustion chamber, Figure 1.

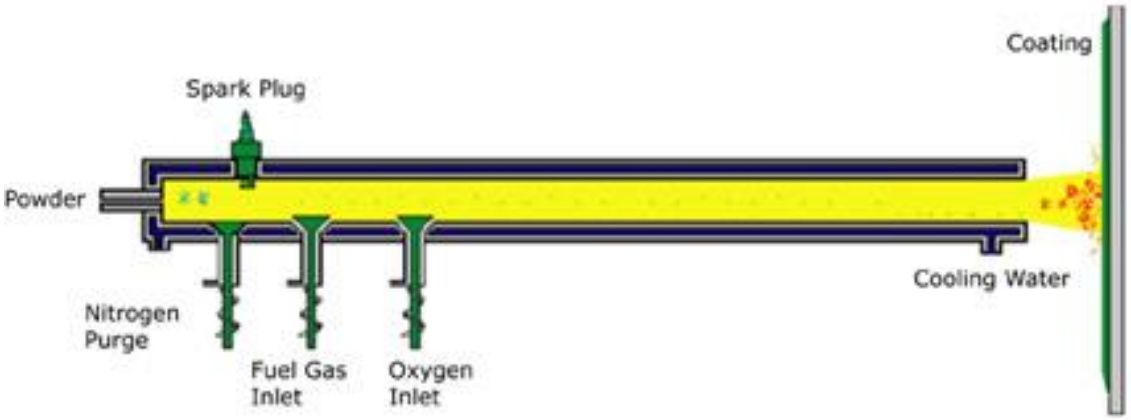

Figure 1 Layout Detonation technique

The gas mixture inside the chamber is ignited by a simple spark plug. The combustion of the gas mixture generates high pressure shock waves (detonation wave), which then propagate through the gas stream.

The hot gases generated in the detonation chamber travel down the barrel at a high velocity and in the process heat the particles to a plasticizing stage with velocity of 1200m/sec.

Detonation spray installed at ENEA Brasimone is shown in Figure 2.

Figure 2 Picture of Detonation Spray installed at ENEA Brasimone

Detonation spraying was conducted using a Computer-Controlled Detonation Spraying facility CCDS 2000 (STPC, Siberia). The explosive charge was kept within 50-70% of the barrel volume and different O_2/C_2H_2 ratios and nitrogen as a carrier gas. The alumina powders (Sulzer Metco 105NS) were deposited on AISI 304 steel and T91 substrates. The coatings were characterised using XRD and SEM-EDS investigations. Surface pretreatments effects on adhesion were also studied.

The samples holder is constituted by mandrel installed on a sled in order to allow the translation and rotation of the sample controlled by CCDS software, Figure 3. A laser pointer installed on the gun allows the identification of the surface to be coated.

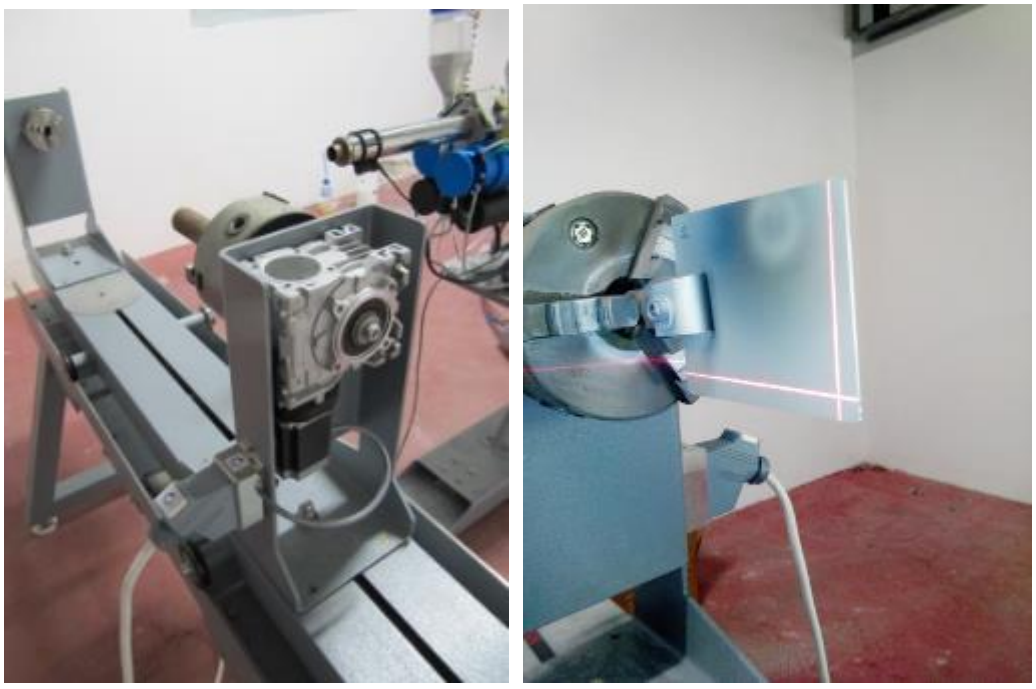

Figure 3 Picture of samples holder.

The coating can be performed on:

- Plates with maximum size up to 590x590mm.
- Cylinder with maximum length: 1,000mm, maximum diameter 590mm and min diameter 4-5mm.

The substrate had to be mechanically sanded before spraying, in order to reach a good adhesion of the layer.

ENEA will carry out experiments with detonation spray method for the deposition of alumina coatings. The substrate selected for the characterization of the coating is T91 martensitic steel and austenitic steel.

The procedure to be adopted to manufacture the coating has to be optimize. The relevant parameters that impact on developed coating are:

- The ratio of combustion gases
- Temperature of the hot gas stream can go up to 4000°C, therefore the distance between barrel and substrate change the energy of the powder that impact on the substrate and the superficial tension generated between coating and substrate
- Frequency
- Powder particle size
- Carrier gas flow rate
- Detonation spraying cycle: that can be repeated at the rate of 1-10 shots per second
- Number fo Layer
- Preparation of the substrate.

The different parameters were combined in order to obtain the best superficial coating in terms of uniform deposition, low porosity, low residual stress that can generate detachment during thermal cycle of materials.

8.3 Optimisation process

During the optimisation procedure AISI 304 steel was used as substrate. The first parameter that was analysed and fixed was the grain size of the powders. The roughness of the substrate was increased with sandblasting process.

8.3.1 Granumelotry

The grain size tested are:

- Al_2O_3 powder with 30 µm grain size
- Al_2O_3 powder with 40 µm grain size
- Al_2O_3 powder with 50 µm grain size

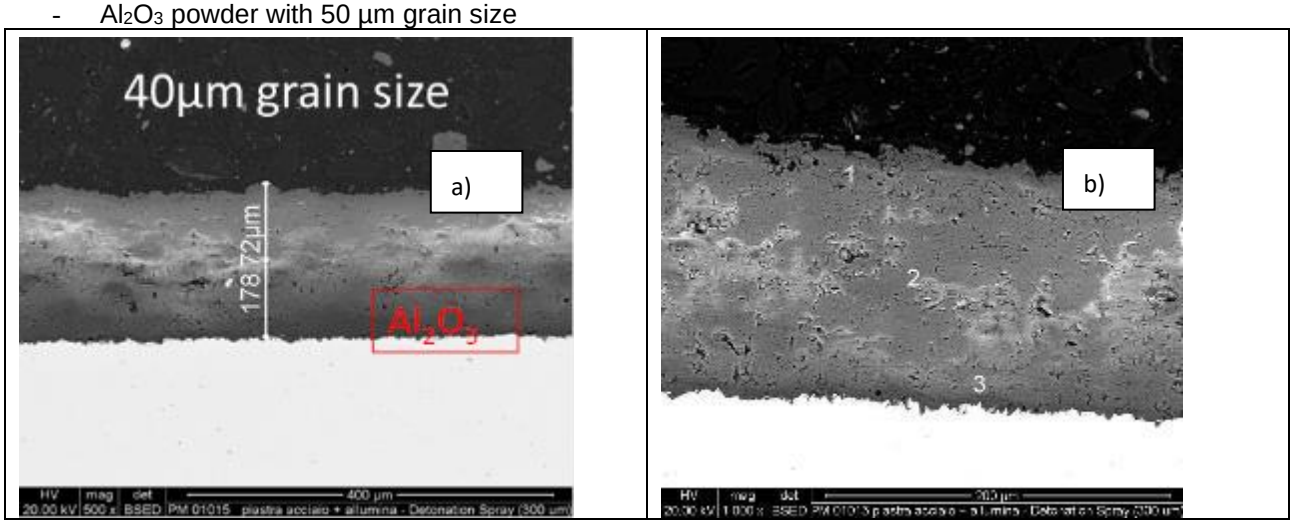

Figure 4 Al_2O_3 coating on 15-15Ti with different powder size: a) 250 µm b) 280 µm c-d) 300 µm.

The thickness of the coating is in the range between 160-200 µm, the 40 µm granulometry appears to give the best compactness, adhesion to substrate and homogeneous deposition, even if some closed porosities can be detected, Figure 3. The EDX analysis performed on 40 µm granulometry Al_2O_3 coating in figure 4-b shows

the chemical composition in the external, bulk and at the coating interface with substrate, Figure 5. No inclusions and no impurities could be observed.

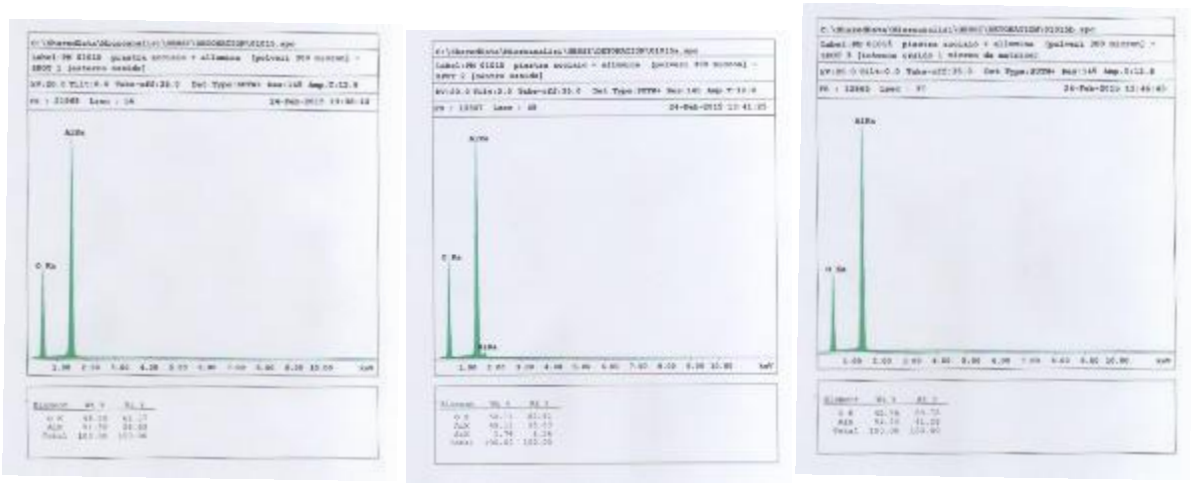

Figure 5 EDX analysis performed on Al2O3 coating with 40 µm: a) coating external part b) bulk of the coating coating c) interface substrate coating.

8.3.2 Identification of operative parameters

In order to reduce porosities inside the coating and the strength between coating and substrate when the component is heated up to 500°C due to different thermal deformation of coating and substrate, a parametric analysis was performed changing the thickness of the coating (number of layer), stoichiometry of the process and the distance between gun and substrate.

The substrate coated are:

- Plates up to 100mmmx100mm
- Tensile specimens with diameter of 4mm

The thickness of the coating manufacture on plates was change between 1 layer (8 µm) and 15 layer (~ 120 µm).

8.4 Microstructural analysis of optimised coating on AISI 304 Plate

8.4.1 SEM and EDX

A set of plates in AISI 304 was coated, the parameters investigated is the ration between layer deposition and thickness of the coating. The thickness analysed was in the range between 10 and 250 µm. Figure 7 shows the coating manufacture with 5 and 15 layers. The lower thickness that guarantees a good adhesion of the coating to the substrate, is 4-5 layers, Figure 7.

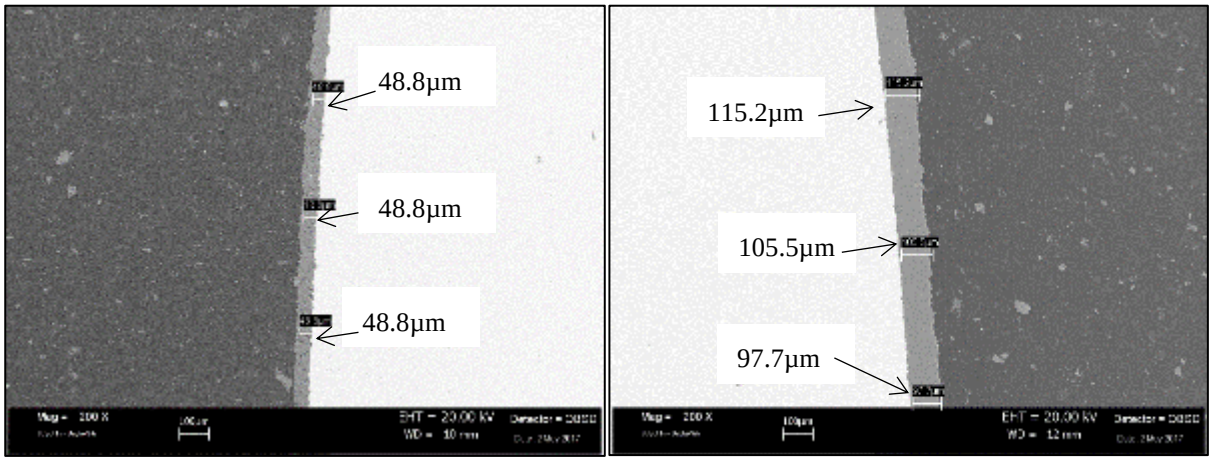

Figure 6 SEM analysis on Al_2O_3 coating with 5 layer 40-50µm on the left and 15layers (100-120µm).

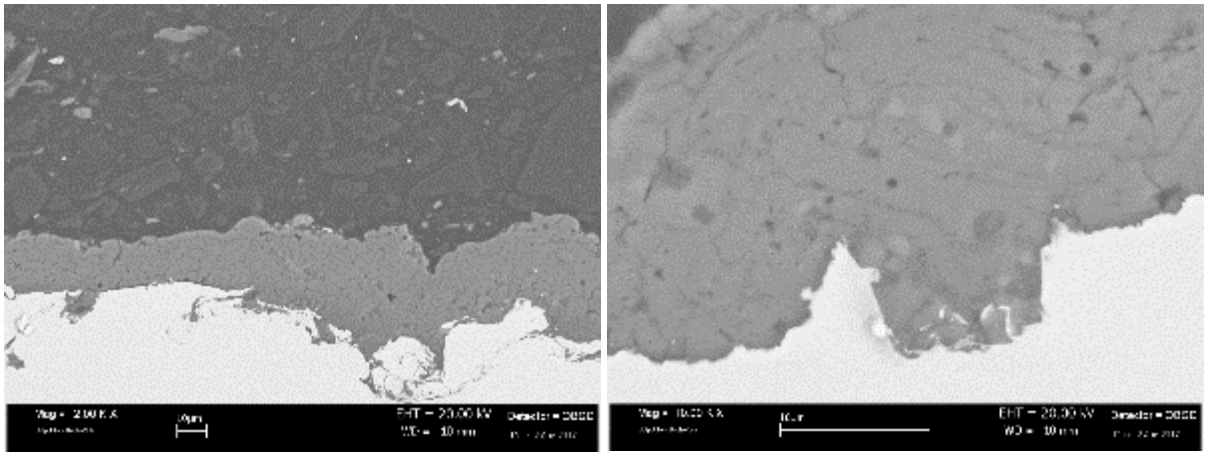

Figure 7 SEM analysis on Al_2O_3 coating with 5 layers.

Generally the quality of the coatings produce keeping the sample at 200mm from the gun is quite good (no inclusions, no pores, no delaminations). Instead, at 100 mm distance, some delaminations from the metallic substrate were observed (at 10'000x), Figure 8

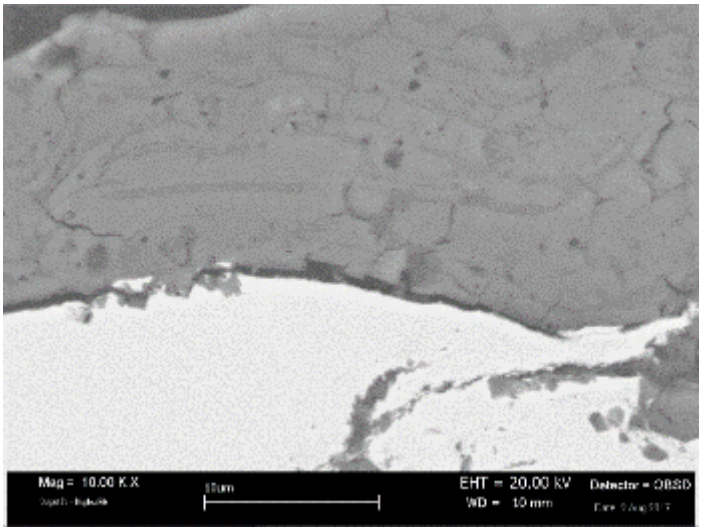

Figure 8 SEM analysis of 5layers, Al_2O_3 coating, 100mm distance between gun and substrate.

8.4.2 Ultrasounds non- destructive tests

ENEA laboratory devoted to US-NDT performed analysis at 15 MHz, in Pulse-Echo mode, on AISI 304 substrate coated with Al_2O_3 by detonation gun, immersing the sample in water for coupling, employing a 1" probe and a XY step of 0.25mm. Digitalization was achieved using a USPC7100 SERIES and a devoted software, Figure 9. No pores were detected, nor delaminations, Figure 10.

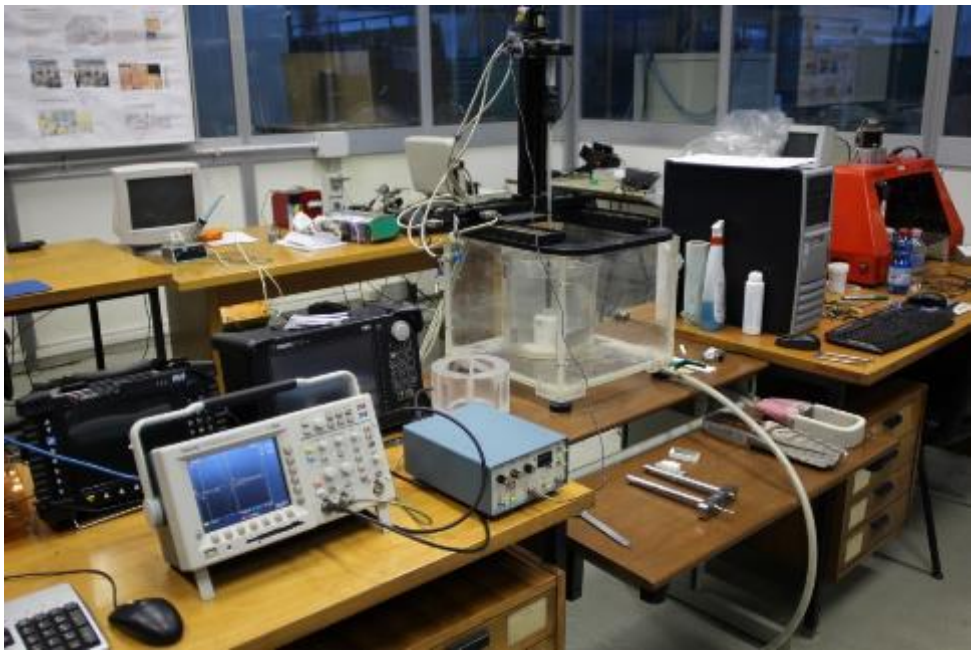

Figure 9 Ultrasound machine, USPC7100 SERIES.

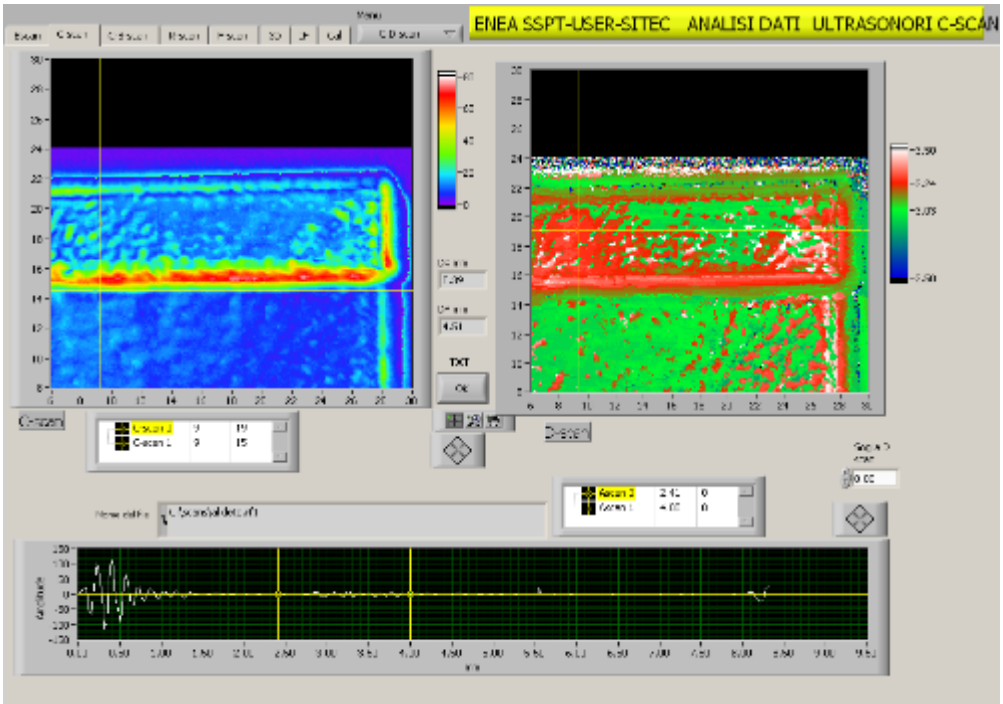

Figure 10 Ultrasound analysis on Al_2O_3 coating on AISI 304 substrate.

8.4.3 Microtomography

An attempt was made to study the internal structure of the Al_2O_3 coating by high resolution X-ray Computed Tomogrphy (u-CT). The scanner was a GE Phoenix nanotom equipped with a 180 kV/15 W nanofocus tube, Figure 11.

Figure 11 X-ray High resolution Computed Tomography system General Electric Phoenix Nanotom S.

The magnification was 25 x, corresponding to a voxel size, i.e. spatial resolution, of 2 um. The scan time was about 4.5 h and each recorded image was the average of 7 acquired one, in order to improve the signal to noise ratio. Despite all this, the result was unsatisfactory because of the noise, Figure 12. The reason is that to get that geometric magnification, the detector must be located away from the X-ray source, heavily weakening the recorded signal.

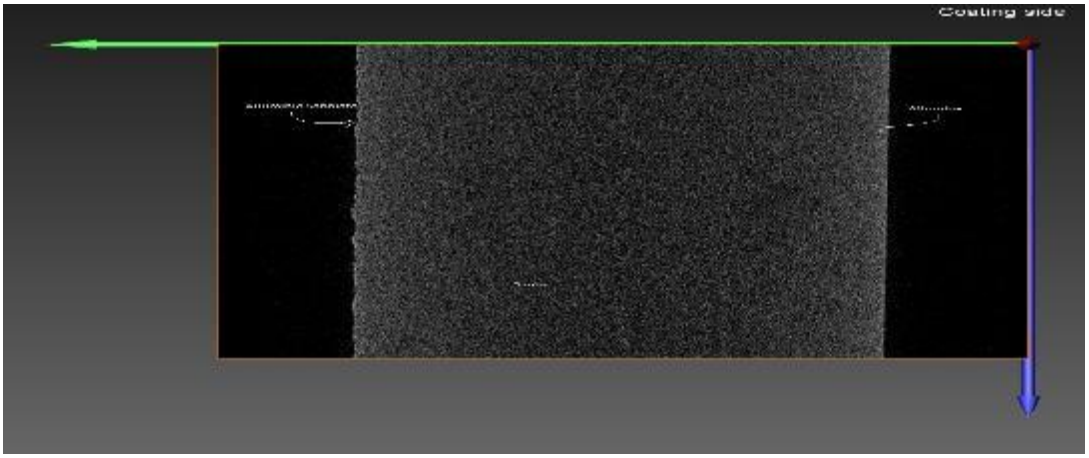

Figure 12 X-ray Tomography of Al_2O_3 coating by detonation spray.

To overcome this limitation, next attempts will be performed by using an ad hoc rotating sample holder made by additive manufacturing, Figure 13. This will allow both the sample and the detector to be closer to the source, retaining high resolution without penalizing the signal.

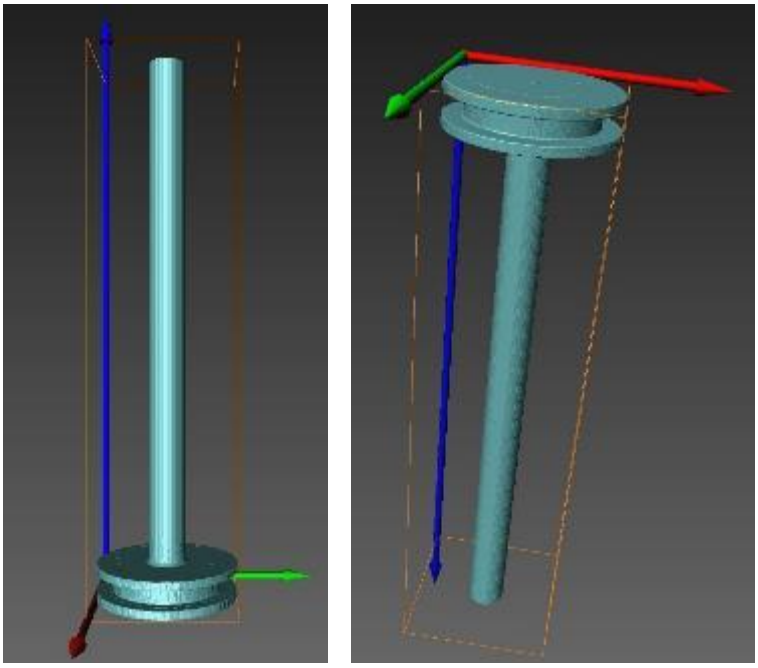

Figure 13 X-ray Tomogrphy rotating sample holder.

8.5 Tensile Tests

8.5.1 Specimens

In order to characterise the thermo-mechanical behaviour of Al2O3 coating obtained by detonation spray in the relevant environment of Lead Fast Reactor, two experimental campaigns were planned at CVR and RATEN. Tensile Test were be performed in Lead bismuth at 500°C on tensile specimens manufactured in 316L. The size of the specimens (Figure 14 and Figure 15) are:

- Length: 40mm
- Diameter: 4mm

The 2 tensile specimens were manufactured in the L direction Figure 14.

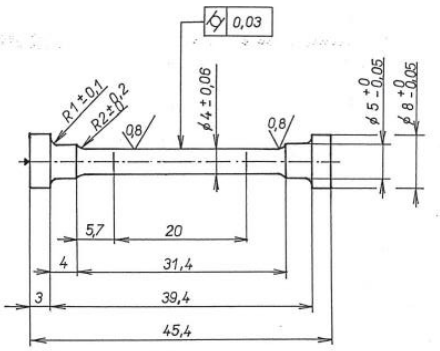

Figure 14 Technical drawing of the round tensile specimen

Taking into account that the minimum diameter of tube that can be coated by detonation gun is 4mm it was necessary to optimise the techniques in order to reduce the stress generated between coating and substrate.

Figure 14 Tensile Sample to be coated.

In Figure 15 it is shown first coating produced on the tensile specimens after tensile test at 500°C in Argon, the thickness of Al_2O_3 coating was 100 µm.

Figure 15 Tensile Sample coated Al2O3 - 10 layer, tested at 500°C in Argon.

Due to small diameter of the sample the techniques was optimized in order to evaluate the minimum thickness of the coating with uniform deposition on rod and low brittleness.

The strength generated between coating and substrate due to thermal expansion is reduced with low thickness. The minimum thickness in order to obtain a homogeneous and uniform coating is 5 layers (30-40µm), **Erreur ! Source du renvoi introuvable.**.

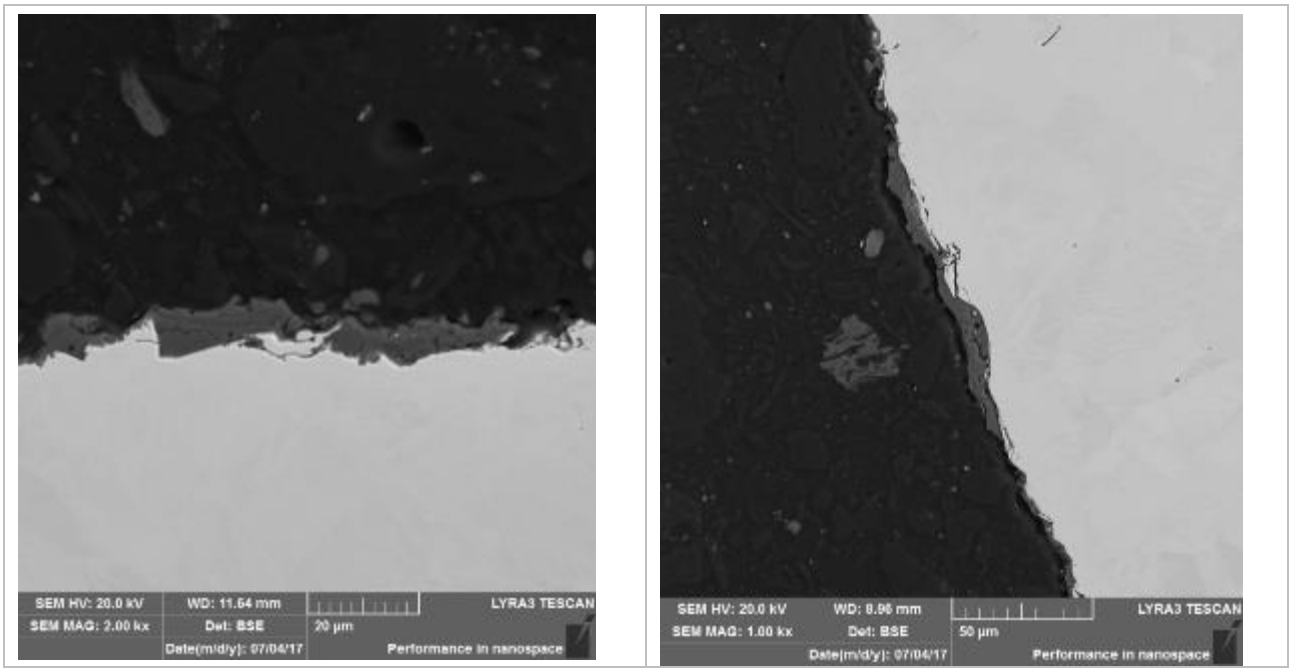

Figure 16 Tensile Sample coated Al_2O_3 - 3 layers (20µm), tested at 500°C in Argon.

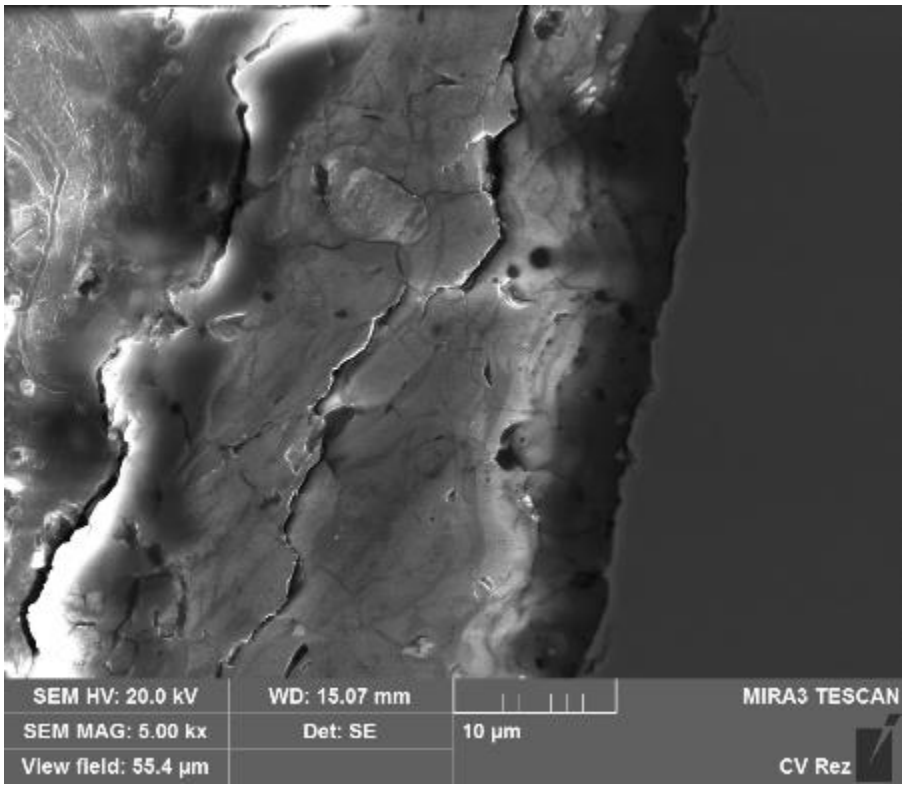

Figure 17 Tensile Sample coated Al2O3 - 5 layers (40µm), tested at 500°C in Argon.

Mechanical Testing

Tensile tests were carried out in PbBi, at 550°C, in the CALLISTO cell. CALLISTO is a tank containing liquid PbBi built on a Zwick/Roell Electromechanical Creep Testing machine, Kappa 50DS. CALLISTO is based on the 2-tank concepts, where the first tank is for the preparation of the liquid metal (oxygen dosing). The liquid is then transferred to the second tank, containing holders and specimens. Table 1 summarise the experimental parameters and the last column shows the time that the specimens is immersed in the PbBi before starting loading.

Table 1 – Test Matrix

Spec	T	O	Strain rate	Environment
	°C	Wt%	s^{-1}	
1	550		10^{-6}	Air
2		10^{-13}		PbBi

8.5.2 Microstructural analysis

One coated specimen was used for metallography study, in order to observe its surface and cross-section characteristics. EDS chemical analyses confirmed that the composition of the coating is purely Al and O (Fig. 19).

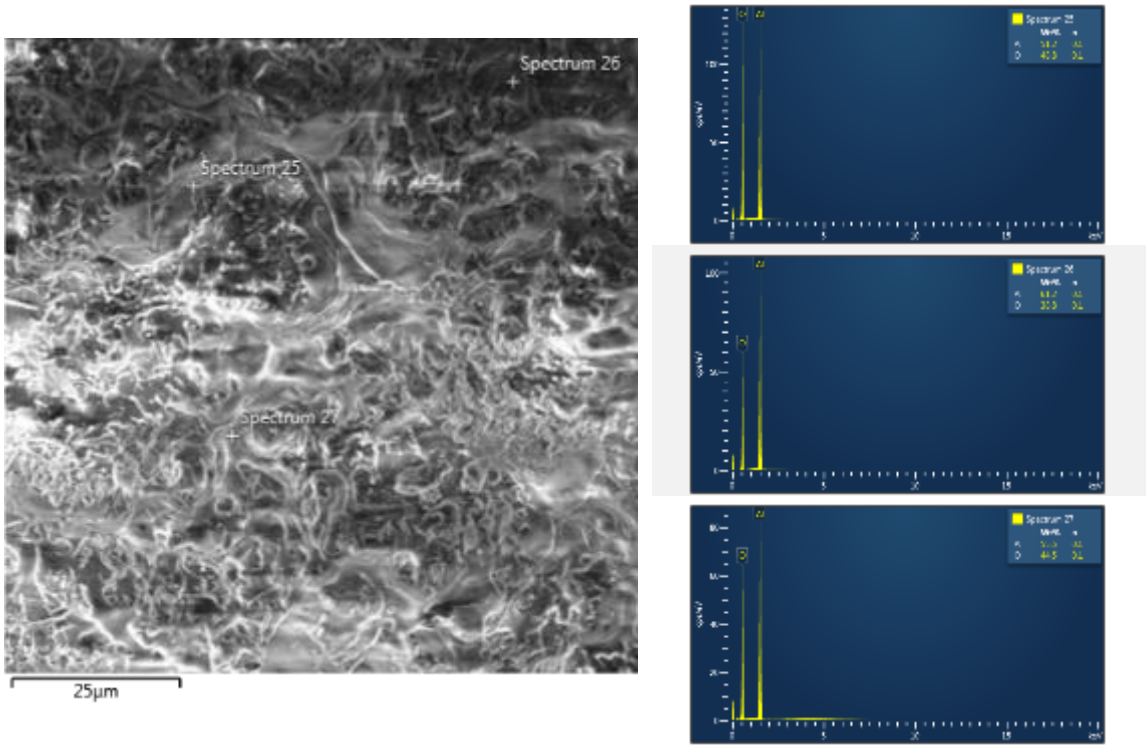

Figure 19 SEM images of the coating surface and EDS quantitative spot analyses

Detailed observation of the surface (Fig. 20) highlighted the rough morphology of the coating (Fig. 20a), typical of sprayed powders. In detail (Fig. 20b) the plastically deformed outer splat had the appearance of partially melted particles glued to the surface of the layer deposited underneath. Moreover, due to the brittle nature of the Al_2O_3, superficial cracks were observed over all the surface (Fig. 20c).

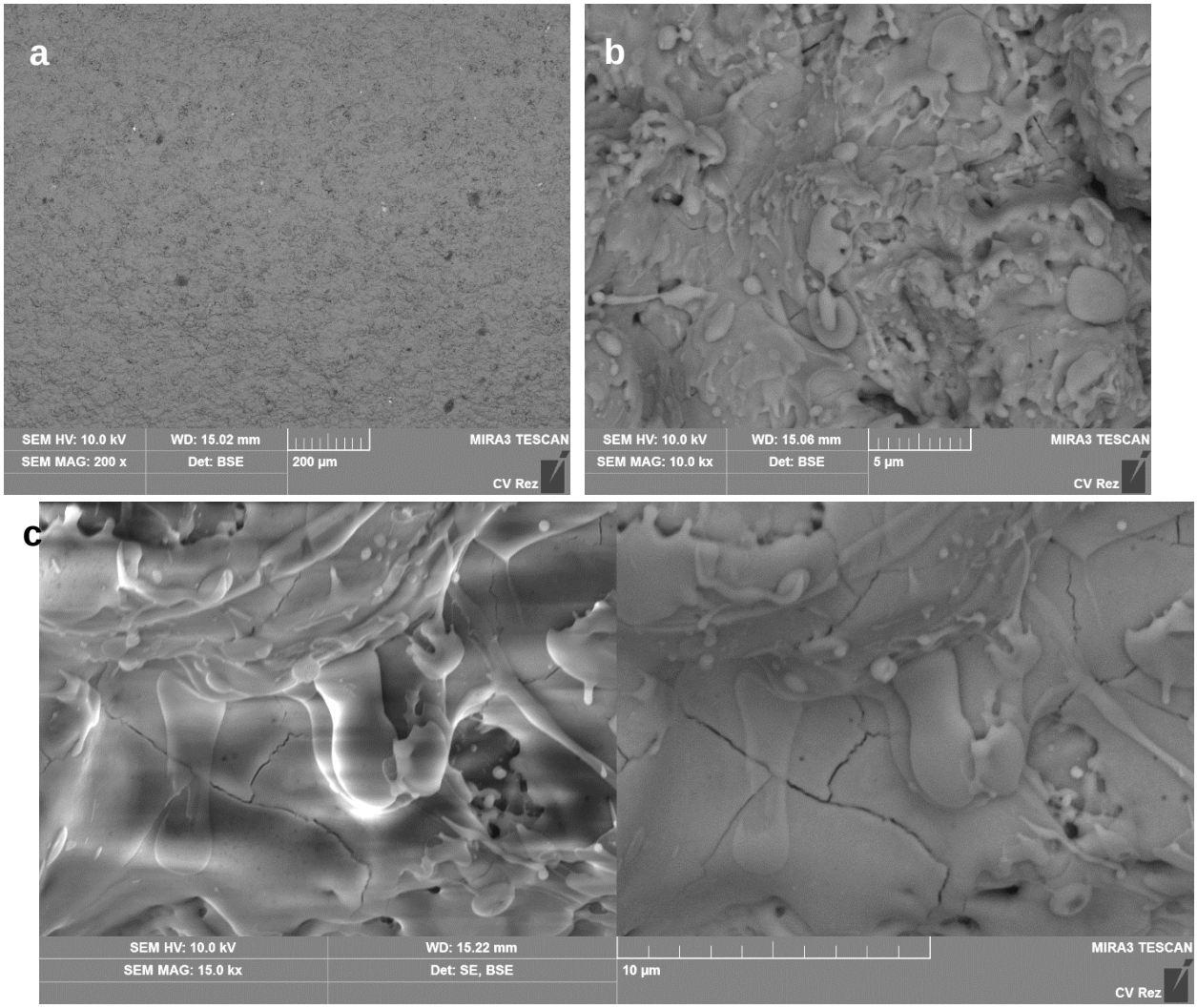

Figure 20 SEM images of the coating surface. a) general view; b) details of particles glued to the surface; c) SE vs BSE image of superficial cracks.

From the examination of the cross-section (Fig. 21), it was measured an average coating thickness of about 30□m. The BSE examination highlighted the irregular morphology of the coating as well as its uniform composition. The coating had many cracks and pores. In several areas there was detachment from the substrate. However, due to the extremely brittle nature of the coating these effects could be produced during the deposition as well as during the mechanical polishing of the specimen. At this stage is not possible to define the role of neither of them and the state observed in this study is what is considered the initial state of the specimen before exposure and loading in environment.

By EDS analyses it was confirmed that the composition of the coating is purely Al_2O_3.

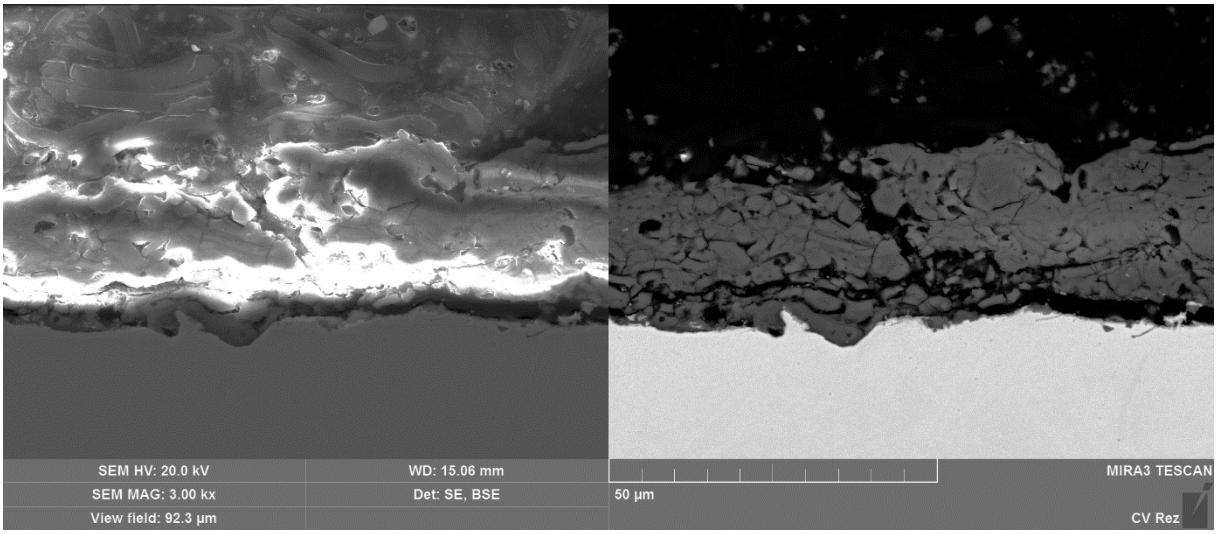

Figure 21 SEM images of the coating cross section. SE vs BSE images highlighting the morphology (SE) and the uniform composition (BSE).

8.5.3Tensile Tests

The specimen in air was loaded up to the UTS point of the material, as a reference test. The stress-displacement curves are represented in Figure 18. However, because the substrate, 316L, has such a long plastic deformation up to the UTS (11mm displacement), it was decided to load the specimen in PbBi up to the Yield stress of the material at 550°C.

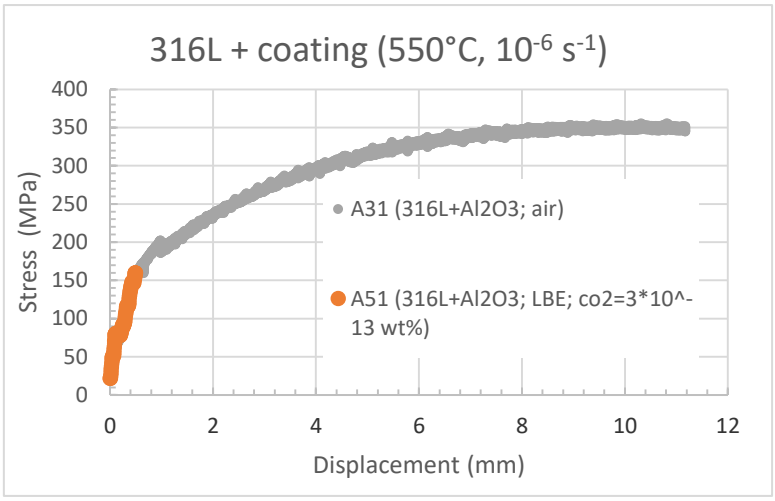

Figure 18 Stress-strain curves for the 2 specimens 316L+Al2O3 coating loaded in air (grey) and PbBi (orange).

Metallography

Specimen in Air

Examination of the surface after testing revealed an unchanged morpgology (Fig. 23). Several superficial cracks were observed as in the oryginal surface after deposition (Fig. 20c).

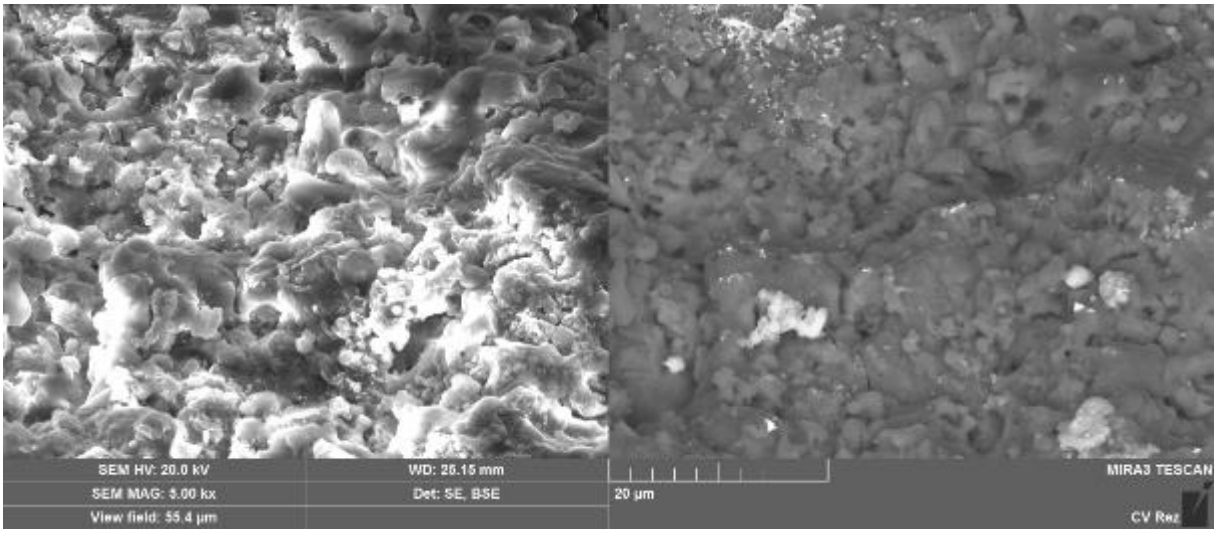

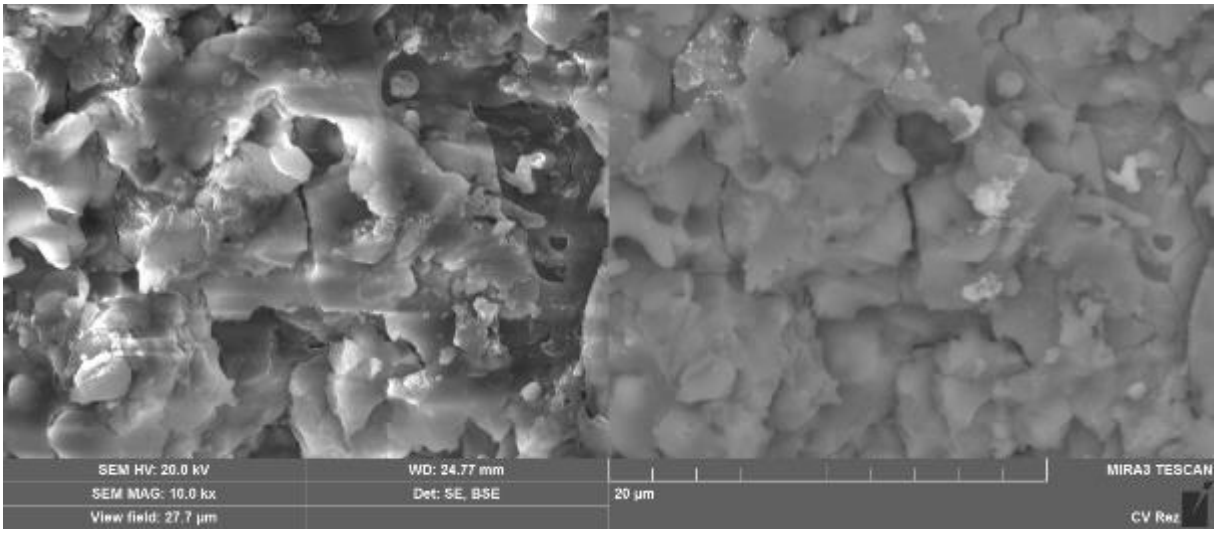

Figure 23 SEM images of the surface of the specimen loaded in air.

Examination of the cross section (Fig. 24) also confirmed the unchanged morphology of the coating. The adhesion was still good and there was limited loss of material (Al_2O_3), where in loalised areas outer parts of the coating was detached.

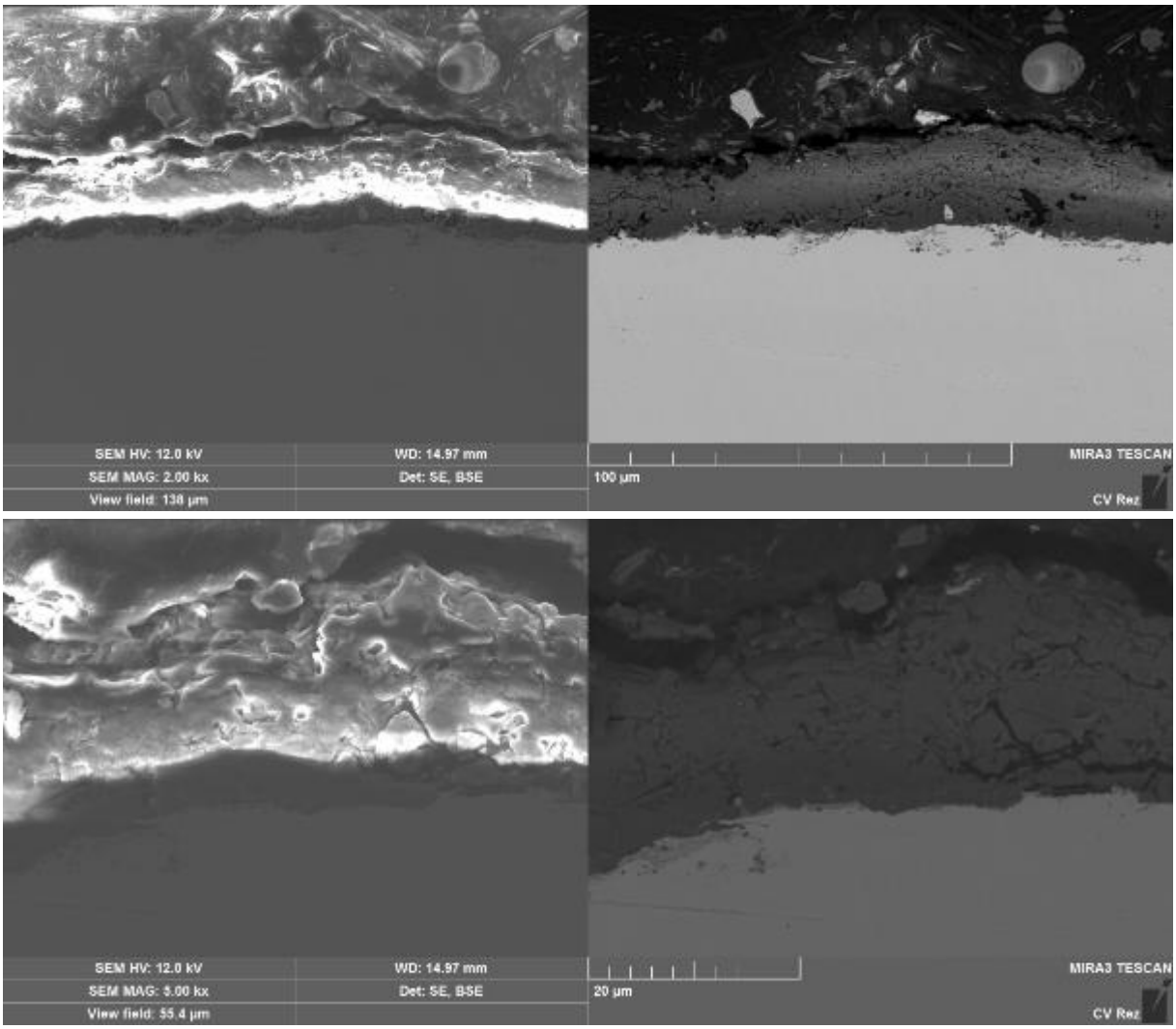

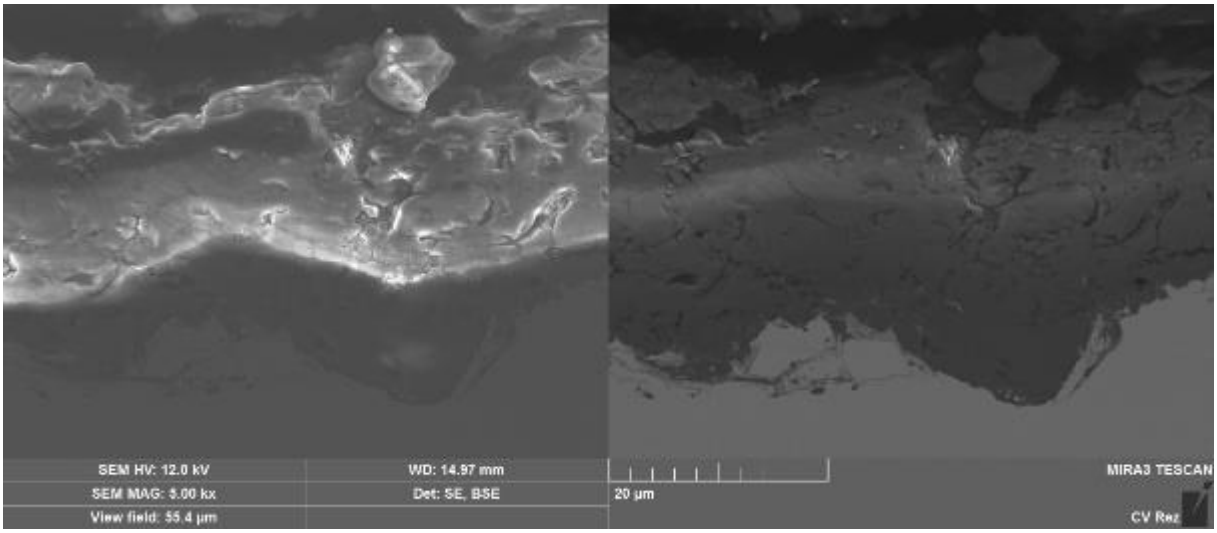

Figure 24 SEM images of the cross-section of the specimen loaded in air.

Chemical analyses of the cross section, at the interface 316L / Al_2O_3 (Fig. 25) confirmed the marked change in composition and no intermediate compound was formed at the interface. The coating at 550°C was very stable and no chemical reactions occurred.

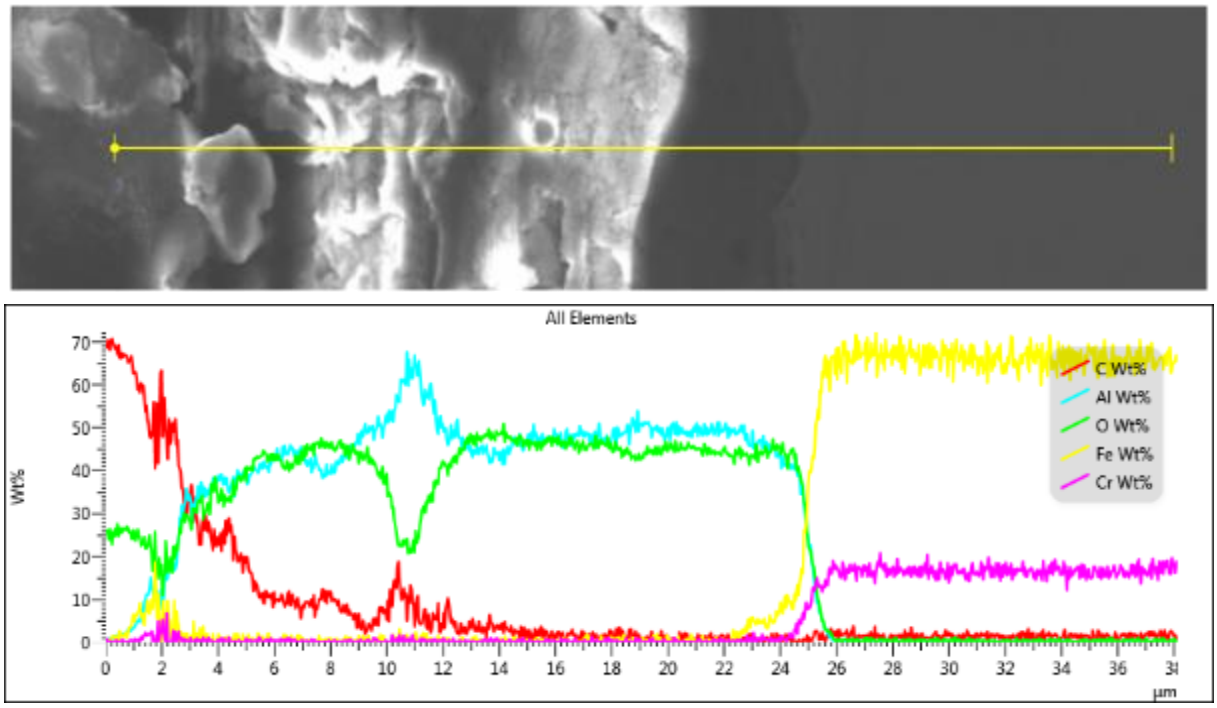

Figure 25 SEM image with associated EDS qualitative line scan highlighting the change on chemical elements.

Specimen in PbBi

On the surface of the specimen, after testing in PbBi, there were large areas covered with PbBi (Fig. 26a). The PbBi was not removed and only the uncovered surfaces were examined (Fig. 26b). Mainly, it is visible how the PbBi is not adherent to the Al_2O_3, there is no wettability and the little spheres are the evidence. Most probably the PbBi remains trapped and attached mechanically to the surface, due to its high roughness.

Little superficial cracks were still observed, but they did not increase in number or size after loading compared to the oryginal surface after deposition.

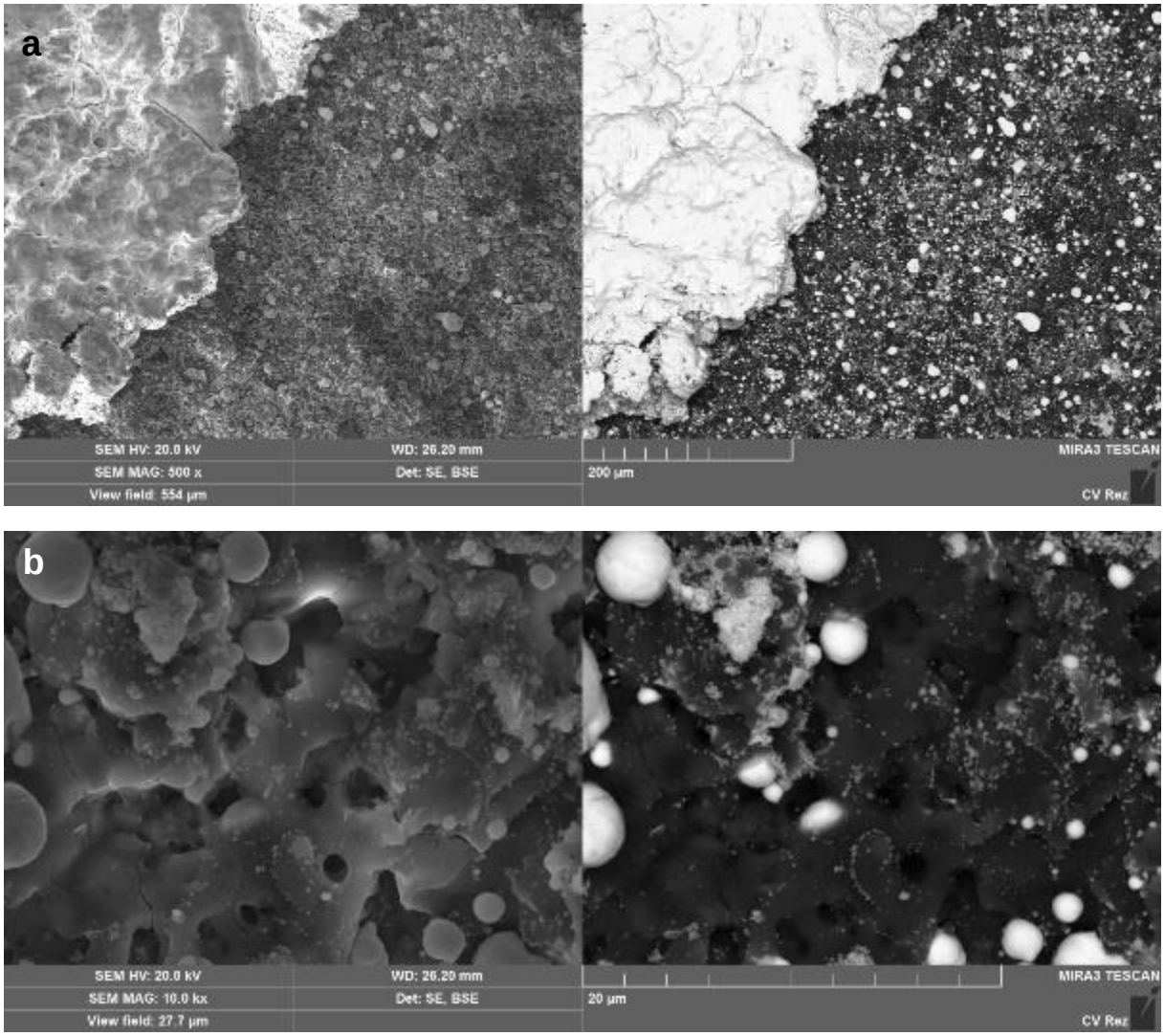

Figure 26 SEM images (SE vs BSE) of the surface of the specimen loaded in PbBi.

Examination of the cross-section (Fig. 27) showed that the coating remained adherent to the substrate. There were localised area where the outer part of the coating was removed, but the PbBi did not reach the substrate, because the adherence of the first splat to the substrate was not affected by the loading.

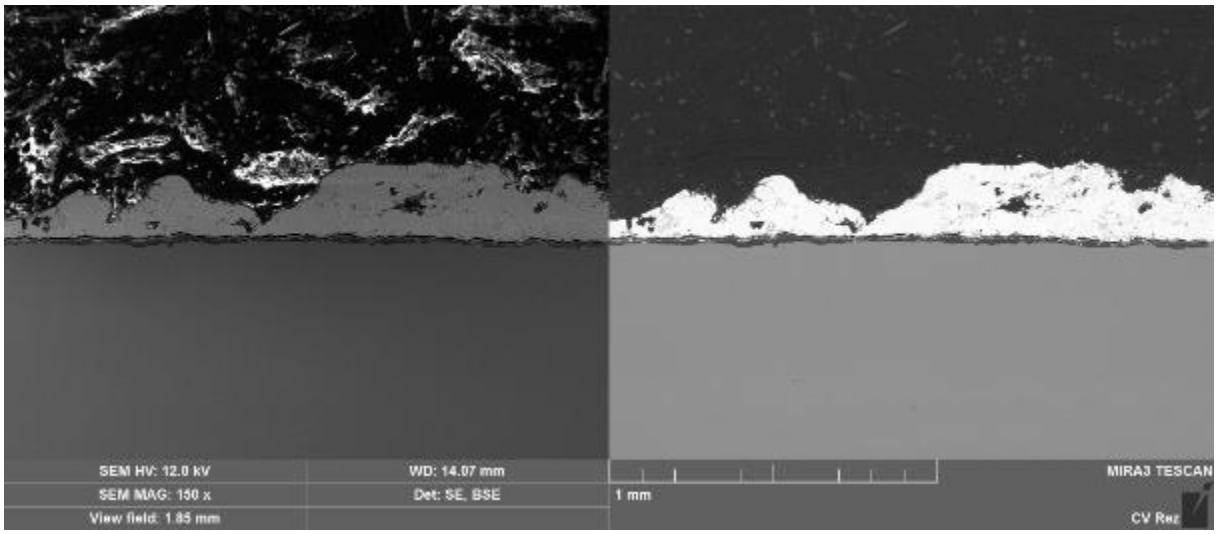

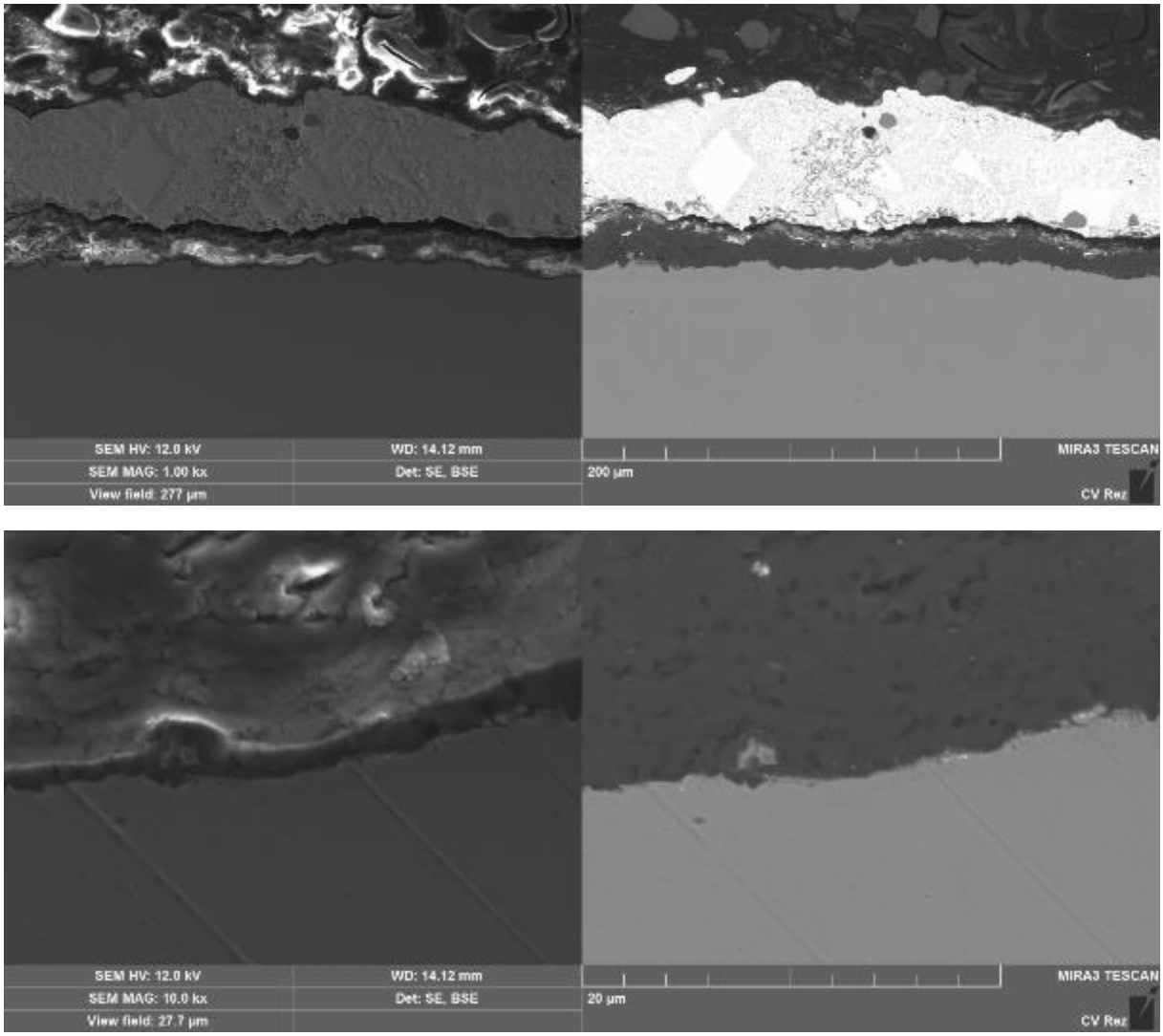

Figure 23 SEM images (SE vs BSE) of the cross-section of the specimen loaded in PbBi.

Chemical analyses of the cross section, at the interface 316L / Al_2O_3 (Fig. 24) confirmed the marked change in composition and no intermediate compound was formed at the interface. The coating at 550°C was very stable and no chemical reactions occurred.

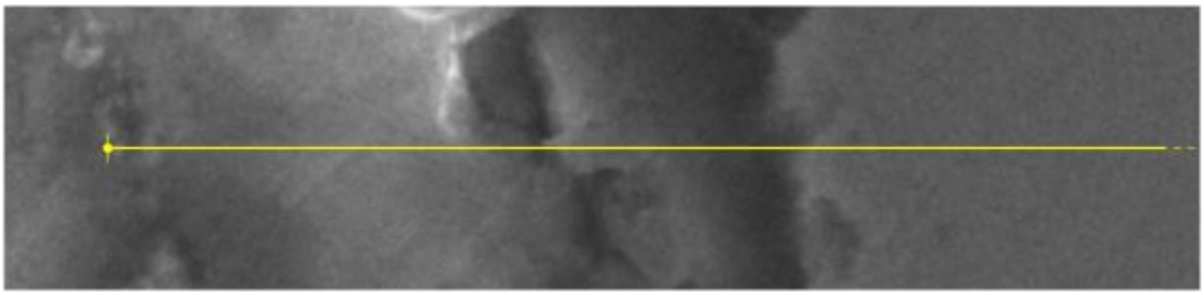

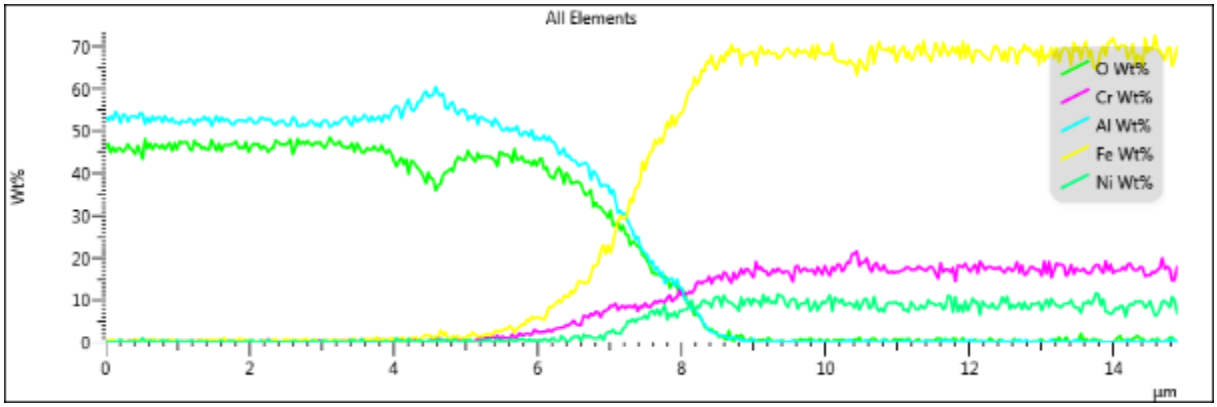

Figure 24 SEM image with associated EDS qualitative line scan highlighting the change on chemical elements.

8.6 Corrosion Test

A plate of 304 coated with 50 µm of Al_2O_3 bty detonation spray was characterised in Lead 480°C with oxygen control (10^{-8}%wt) for 190h. The ageing test in liquid lead at of alumina coated does not show any signs of corrosion Figure 18. Mainly, it is visible how the Pb, as the PbBi, is not adherent to the Al_2O_3, there is no wettability. No cracks can be obserd on the surface of the coating.

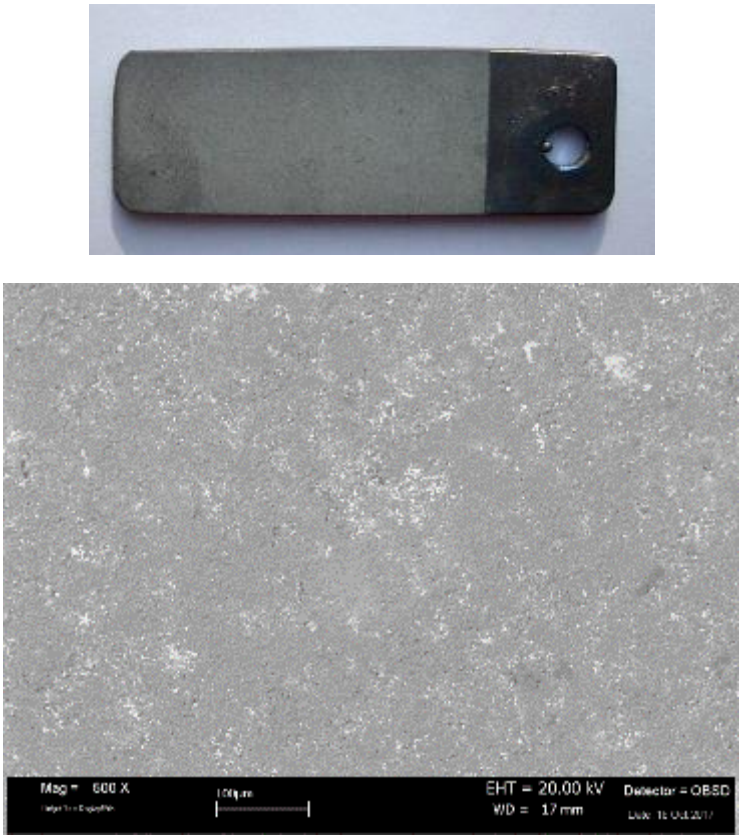

Figure 18 Ageing test of Al2O3 coating in Lead at 480°C.

Examination of the cross-section (Figure 19) showed that the coating remained adherent to the substrate. No corrosion, detachment or cracks can be observed. The Pb did not reach the substrate.

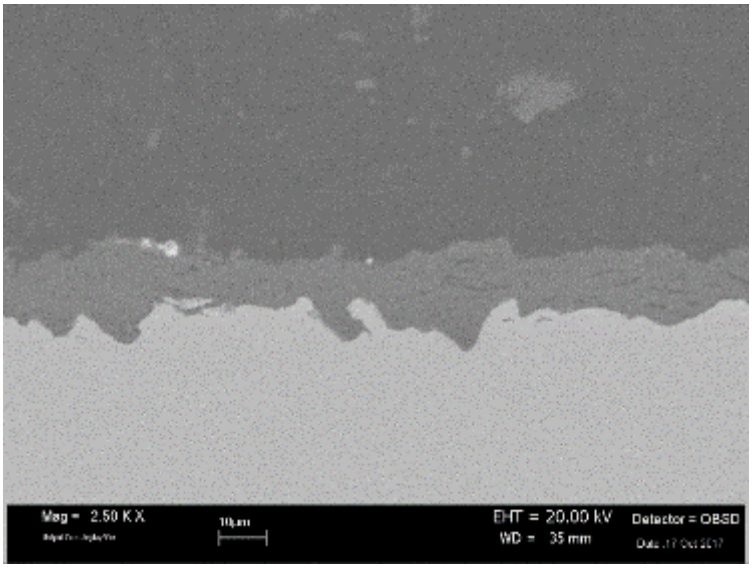

Figure 19 SEM images of the cross-section of the specimen exposed in Lead at 480°C.

8.7 Conclusions

The coating manufactured with detonation spray techniques was optimized in order to reduce delamination, porosities and cracks. Tensile test in Lead bismuth was performed in order to characterise the mechancial proprieties at relevant temperature (550°C). The coating in inert atmoshere and in liquid metal was very stable and no chemical reactions occurred. No cracks can be obsrved after tensile tests. Preliminary corrosion test in Lead at 550°C with oxygen control (10-8%wt) showed no penetration of Lead throught the coating, the coating remained adherent to the substrate.

The techniques has to be optimized as function of the component to be applied. The preliminary results confirm applicability of this techniques for the components likes pump impeller, grids, etc. of liquid metal reactor.

9 Slow strain tensile test of surface alloyed T91 – contribution by RATEN ICN

V. Radu, V. Ionescu

9.1 Introduction

In contact with the liquid metal, the mechanical integrity of the structural materials could be affected. Compatibility of the candidate structural materials with the liquid lead is known to be one of the critical issues in developing of the LFR reactors. Therefore an important aspect is the selection of structural materials to operate properly in the liquid lead environment.

Some important mechanical properties to be known in liquid lead are:

- Stress- Strain behaviour (constitutive equation, tensile properties - $\sigma_{0.2}$, UTS, etc.);
- Fatigue Properties (S-N life time);
- Fracture Mechanics Properties (Fracture Toughness - K_{IC} or J_{IC}, J-R curve);
- Creep Behaviour (secondary creep equation);
- Creep-Fatigue properties.

9.2 Set-up the experimental facility (LILETIN) for the mechanical testing in the liquid lead environment

The experimental facility, called **LILETIN (Li**quid **LE**ad **T**esting **IN**stallation), has been set up at RATEN ICN. It allows performing the experimental tensile tests in the liquid lead environment. At this early stage, the LILETIN facility is able to perform tensile tests in a liquid metal crucible configuration, with temperatures up to 450^{o} C in static lead conditions, but without any oxygen monitoring system.

The global view LILETIN facility, which was set-up in the Instron tensile system, is given by Figure 1. Its main parts are*:*

- the heating system;
- the crucible for molten lead, the sample fixing assembly;
- the pooling road and,
- the Instron tensile tests system*.*

Figure1. Experimental facility for material tensile testing
in the liquid lead environment

Heating system

The heating system is intended for heavy liquid metal (Pb) melting and keeping it at the preset temperature (Figure 2). It consists of a furnace, thermocouples, thermo-regulator and thermal insulation. In this furnace is inserted the crucible for molten lead.

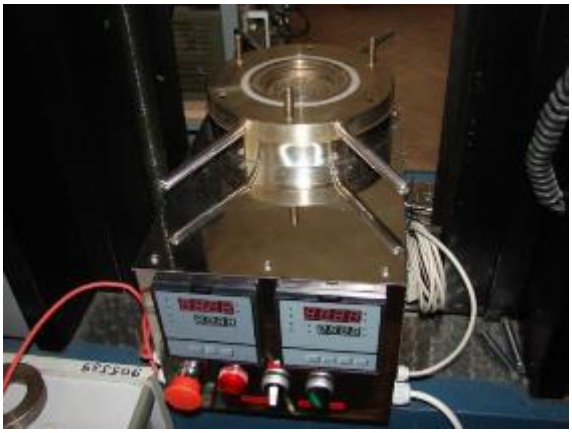

Figure 2. The heating system

The Crucible for Molten Lead

The crucible (showed from both sides in Figure 3) may contain the amount of maximum 0.9 litre lead.

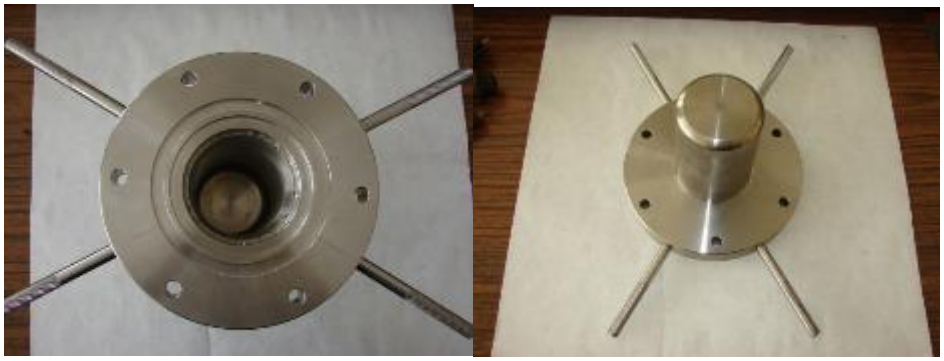

Figure 3 Crucible for Molten Lead (showed from both sides)

Pull grips

The device for catching of samples (pull grips) is displayed in Figure 4, with specimen for testing.

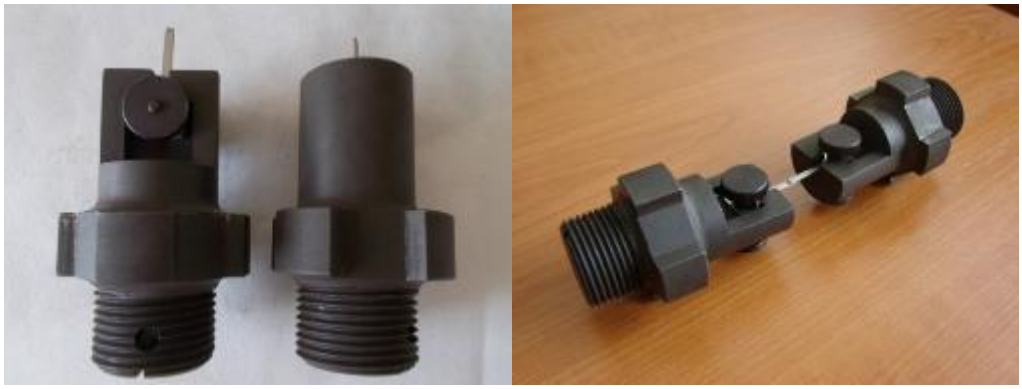

Figure 4. Pull grips for mechanical testing

Tension Specimen Type

Small size plate samples for mechanical testing are used (Figure 5).

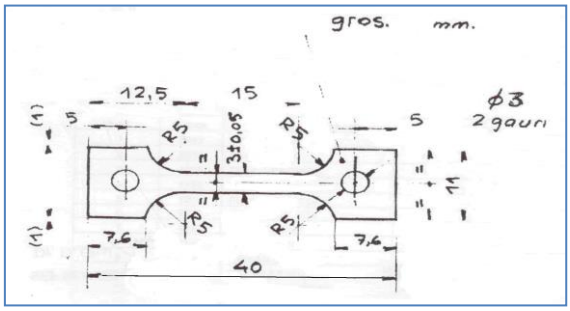

Figure 5. Sketch of the small plate specimen for mechanical testing

In resume, the main design features of the LILETIN facility are:

- Testing temperature: 400 – 600^{0}C;
- Static liquid lead environment;
- Inert gas interface (argon);
- Temperature monitoring;
- Crucible bulk: max 0,9 liters;
- Oxide vapor-tight packing;
- Without oxygen monitoring system.

9.3 The steps of the testing procedure

In order to examine the effect of FeAlCr coating on the mechanical properties of T91 steel tested in the liquid lead environment, the specimens are tested under tensile loading at a constant strain rate of $5 \cdot 10^{-5}$ s^{-1}. The slow strain rate during tensile tests was performed in liquid lead, in static conditions at constant temperature of 450ºC, and without oxygen monitoring system. Small size plate T91 steel tensile specimens were tensile tested by the Instron testing machine software according to ASTM E8. The test scope is to obtain the load-displacement diagram tests of **T91 steel** plate specimens in molten.

The steps of testing procedure are:

- The tensile specimen is attached in the pulling grips and it is bring up in the *sample fixing assembly*. Then, the upper grip is screwed tot he *pooling road*;

- The thermo-regulator of the heating system is set for melting the lead from the crucible. It started and the lead is heated up to 480°C. The crucible is closed;
- The level of the liquid metal has to be between a low level and high level indicator, so that it is sufficiently high to submerge the entire sample. When the lead temperature reaches this temperature, the *sample fixing assembly* with the specimen is inserted in the lead. The *sample fixing assembly is fitted on the* tensile machine mobile beam;
- The thermal transfer between liquid metal and the *sample fixing assembly* takes place so that the lead temperature reaches a temperature below melting temperature. Therefore it is necessary to wait until the temperature reaches again a value above melting temperature;
- By means of the small steps the *sample fixing assembly* is inserted in the lead up to is achieved the link-up with crucible furnace assembly;
- Then, the upper head of the *pooling road* is caught to the tensile machine fix point and the lower grip is fixed in lower side of the *sample fixing assembly*;
- Once the thermal transfer is completed the temperature is set to the desired testing temperature (450^{o}C). When the liquid metal temperature is stabilized, the test can be started;
- The temperature is kept at the preset temperature (450^{o}C) during the time test;
- After the sample is broken, the *sample fixing assembly is uncoupled to the crucible and then it is get out from liquid lead. The both sides of broken sample are cut out and then these are analyzed.* The assembly is cooled down to room temperature and the liquid metal is kept into crucible.

Notes:

- The tensile testing in the liquid metal environment inside of this experimental facility is based on the ASTM standard E 8M requirements. However, this standard does not include any liquid metal environment and therefore does not strictly apply to tensile testing in liquid metal environment;
- No additional extensometer or visual observation of the deformation can be used due to the opaque and conducting nature of the liquid lead.

After the test data are analysed, one half of the specimen is cleaned in a solution of acetic acid, hydrogen peroxide and ethanol in a ratio of 1:1:1 to allow analysis of the fracture surface by the SEM.

Tensile results as function of displacement are presented as tensile curves. Then one can determine the tensile properties of the FeCrAl coated T91 steel in liquid lead testing environments like as: the yield stress, the ultimate tensile strength. Moreover, the optical and SEM analyses of tested specimen could provide supplementary information about the coated specimen behaviour in liquid lead under tensile loading.

9.4 Results

The tests in liquid lead has been performed on the 5 tensile specimens of the FeCrAl coated and partially surface alloyed T91 steel (Figure 6). All specimens were coated with FeCrAl using a modified LPPS procedure (Sulzer) and one side of it was treated applying a GESA pulse (see section 2) resulting in a surface alloyed layer. The specimens are on one side just coated and on the other side surface alloyed with FeCrAl.

Figure 6. Specimen #5 of coated T91 steel for tensile test

The steps of testing procedure were mentioned in chapter 2, and during the tensile test the temperature was kept around 450 ºC (Figure 7).

Figure 7. Temperature monitored during tensile test in liquid lead

After tests the specimens were extracted from the crucible and the aspect of few specimens are shown in Figure 8.

Upper head

Specimen #3

Specimen #2

Figure 8. Aspect of specimens extracted from the testing crucible

During the tests it was recorded the stress-strain curves, and these could be seen in the Figure 9, where some parameters are presented. One may see that curves are very close each to other, and allow extracting the mechanical properties. However, the “S shapes” of curves, are related on the “accommodation” of the loading assembly during increasing of the tensile applied force, and seems to be a quite “intrinsic” feature of the test. Therefore from the parameter values given by the machine processing software only UTS are trustworthy. Thus, Young modulus (E) values are not valid, but from the aspect of stress-strain curves the yield stress (elastic limit) of the FeCrAl coated T91 steel specimens tested in liquid lead environment at 450 °C could be estimate approximately $\sigma_{0.2}$ = 430 MPa.

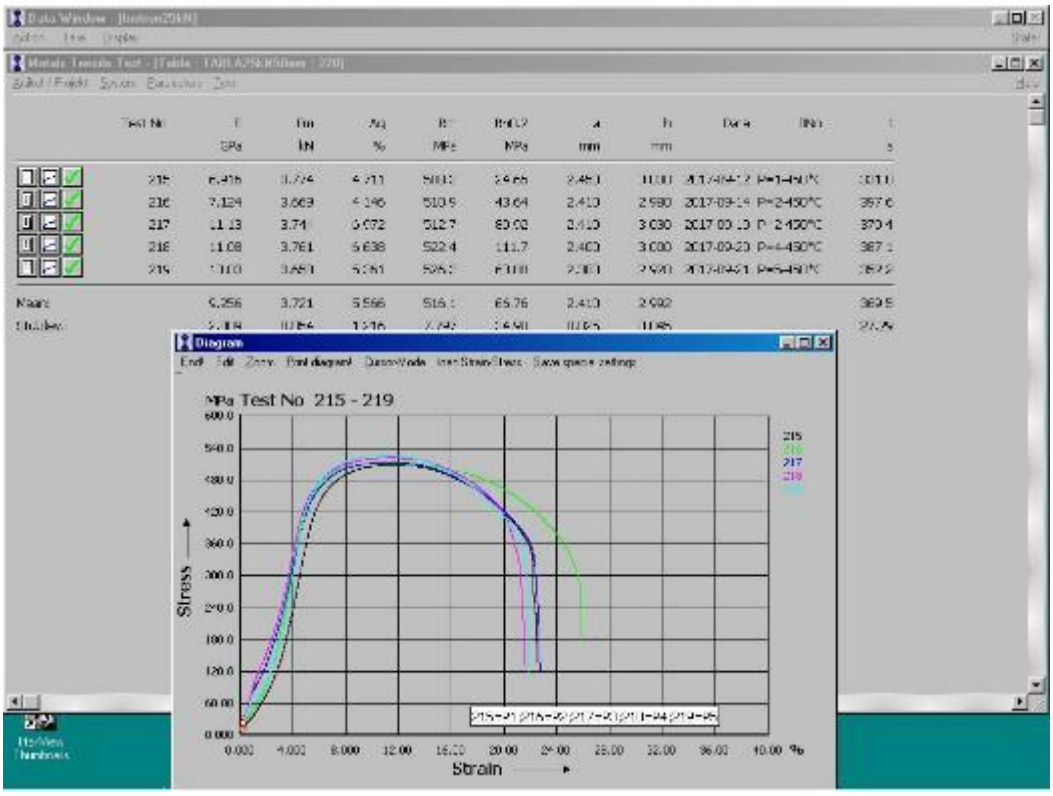

Figure 9. The stress-strain tensile curves for the FeCrAl coated T91 steel specimens

To conclude, for the UTS of the FeCrAl coated T91 steel specimens tested in the liquid lead environment at 450 °C is UTS= 516.1 MPa, with standard deviation of 7.8 MPa.

The coating layer seems to be adherent quite, and a metallographic examination is given in Figure 10.

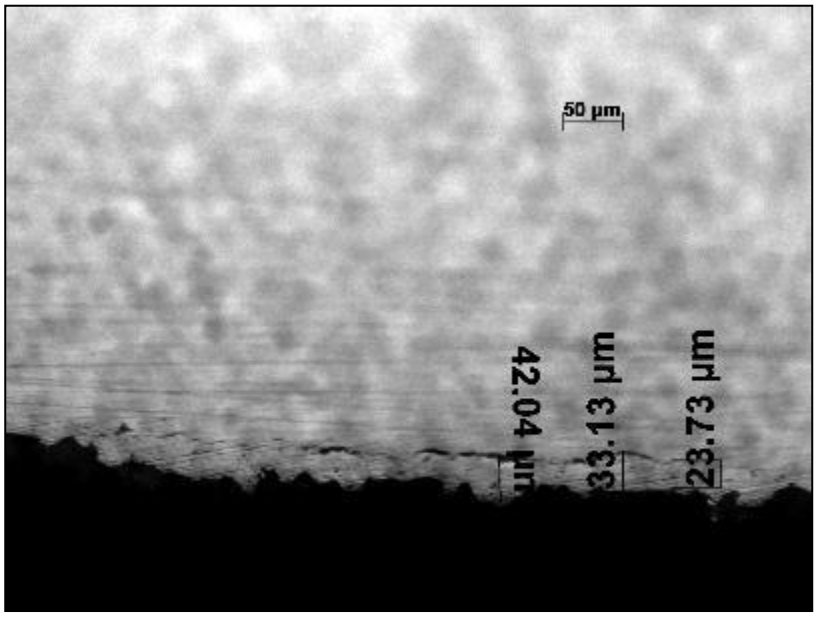

Figure 10. Metallographic aspect of coating layer

From the measurements, one may see that the layer thickness is in the range 24-42 micrometers, with a slight unevenness.

SEM aspects of the fracture surfaces are shown in Figures 11 (specimen #2) and 12 (specimen #3).

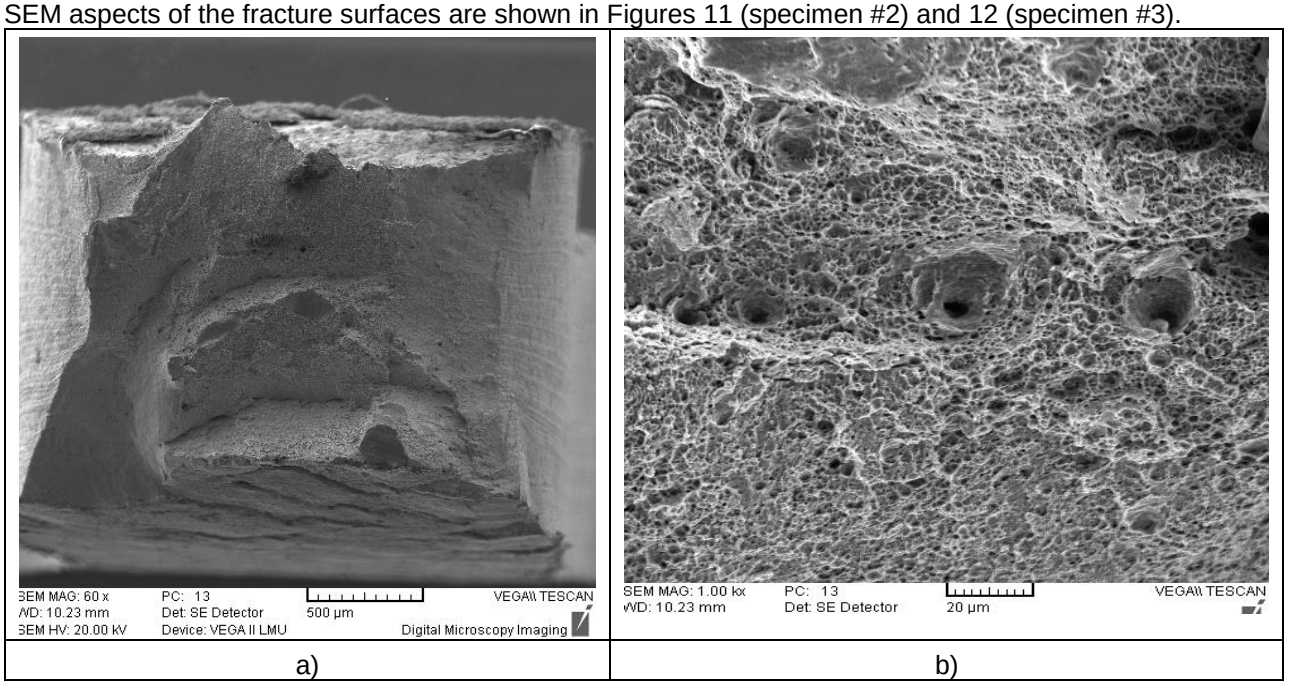

a) b)

Figure 11. SEM aspects of tested specimen #2: a)fracture surface (x60), b) base material (x1000)

SEM pictures highlight the ductile behaviour of the fracture for base material in Figure 11 a) and with typical voids as in Figure 11 b). Also, it can be seen that for large deformation close to breaking, the coating that was not surface alloyed in addition is exfoliated, and released from the base material. The same considerations are supported by the examination of Figure 12. Comparing both side of the specimen (Fig. 12 upper and lower side) one can clearly distinguish between the only coated and the surface alloyed parts of the specimen. The surface alloyed parts due not exfoliate to that extent like the just coated ones.

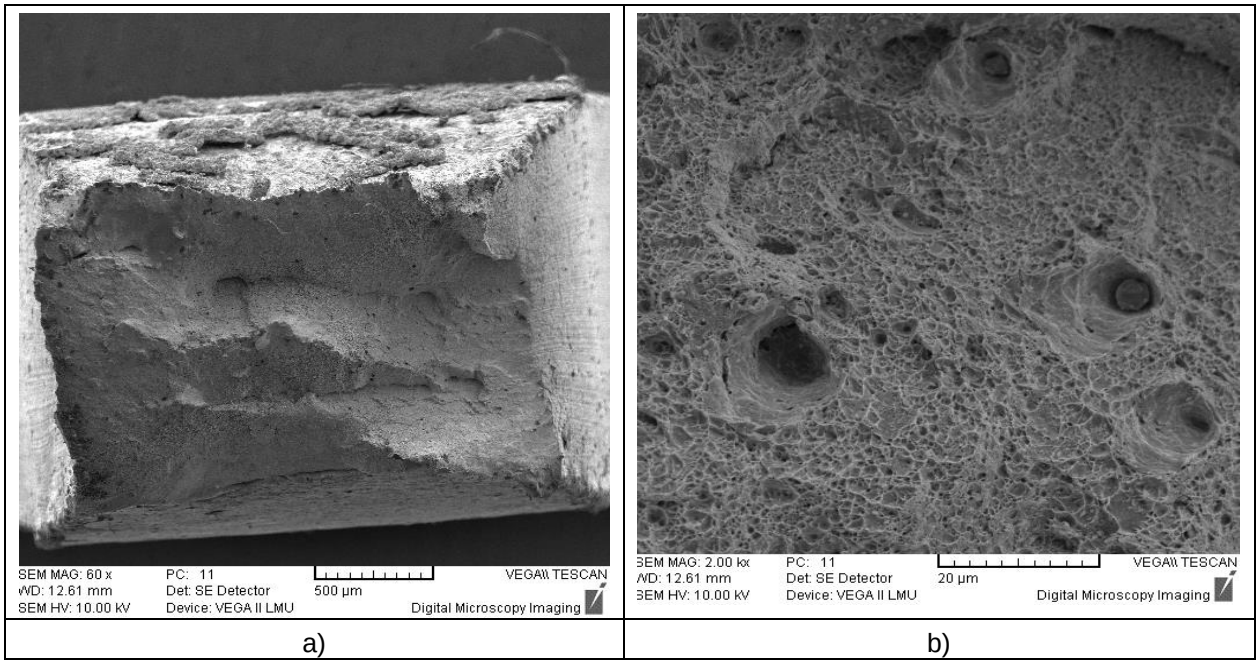

Figure 12. SEM aspects of tested specimen #3: a) fracture surface (x60), b) base material (x2000)

9.5 Conclusions

The experimental facility, called **LILETIN (Li**quid **LE**ad **T**esting **IN**stallation), which has been set up at RATEN ICN, allows performing the experimental tensile tests in the liquid lead environment. At this early stage, the LILETIN facility is able to perform tensile tests in a liquid metal crucible configuration, with temperatures up to 450º C in static lead conditions, but without any oxygen monitoring system.

Few conclusions from works performed on the FeCrAl coated T91 steel specimens tested in the liquid lead environment at 450 ºC:

- In order to examine the effect of FeAlCr coating on the mechanical properties of T91 steel tested in the liquid lead environment, the specimens are tested under tensile loading at a constant strain rate of $5 \cdot 10^{-5}$ s^{-1};
- From the parameter values given by the machine processing software only UTS are trustworthy; the Young modulus (E) values are not valid, and from the aspect of stress-strain curves the yield stress (elastic limit) of the FeCrAl coated T91 steel specimens tested in liquid lead environment at 450 ºC could be estimate approximately $\sigma_{0.2}$ = 430 MPa;
- UTS of the FeCrAl coated T91 steel specimens tested in the liquid lead environment at 450 ºC is UTS= 516.1 MPa, with standard deviation of 7.8 MPa;
- From metallographic measurements, the layer thickness is in the range 24-42 micrometers, with a slight unevenness;
- SEM pictures highlight the ductile behaviour of the fracture for base material and for the large deformation close to breaking, the only coated layer (one sied was surface alloyed only), is exfoliated, and release from the base material.

10 Slow strain tensile test of Al_2O_3 coated (using detonation gun) 316L specimens – contribution by RATEN ICN - ENEA

10.1 Set-up the experimental facility (LILETIN) for the mechanical testing in the liquid lead environment

The experimental facility, called **LILETIN (Li**quid **LE**ad **T**esting **IN**stallation), has been set up at RATEN ICN. It allows performing the experimental tensile tests in the liquid lead environment. At this early stage, the LILETIN facility is able to perform tensile tests in a liquid metal crucible configuration, with temperatures up to 450^{o} C in static lead conditions, but without any oxygen monitoring system.

The global view LILETIN facility, which was set-up in the Instron tensile system, is given by Figure 1. Its main parts are*:*

- the heating system;
- the crucible for molten lead, the sample fixing assembly;
- the pooling road and,
- the Instron tensile tests system*.*

Figure1. Experimental facility for material tensile testing in the liquid lead environment

Heating system

The heating system is intended for heavy liquid metal (Pb) melting and keeping it at the preset temperature (Figure 2). It consists of a furnace, thermocouples, thermo-regulator and thermal insulation. In this furnace is inserted the crucible for molten lead.

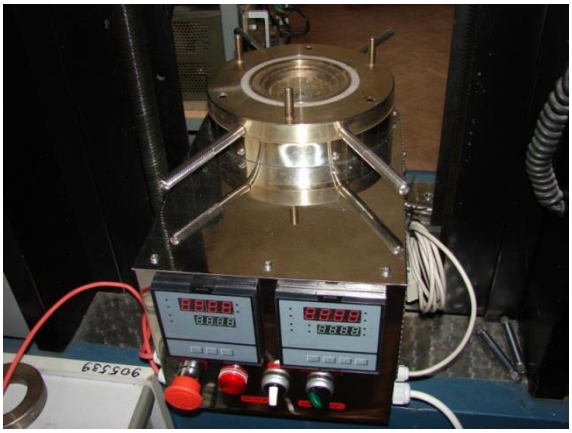

Figure 2. The heating system

The Crucible for Molten Lead

The crucible (showed from both sides in Figure 3) may contain the amount of maximum 0.9 litre lead.

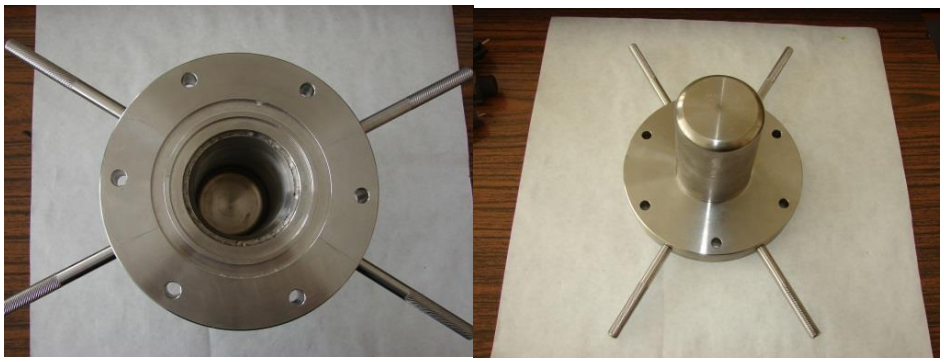

Figure 3 Crucible for Molten Lead (showed from both sides)

Pull grips

The device for catching of samples (pull grips) is displayed in Figure 4, with specimen for testing.

Figure 4. Pull grips for mechanical testing

Tension Specimen Type

Small size round bar samples for mechanical testing are used (Figures 5).

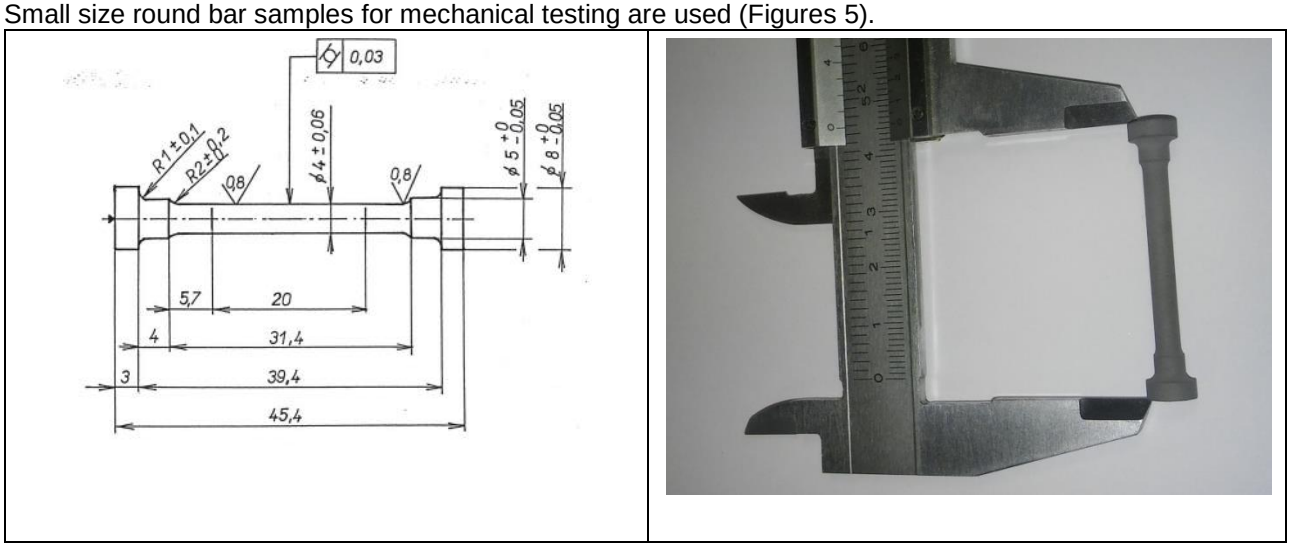

Figure 5. Sketch of the round specimen for mechanical testing

In resume, the main design features of the LILETIN facility are:

- Testing temperature: 400 – 600^{0}C;
- Static liquid lead environment;
- Inert gas interface (argon);
- Temperature monitoring;
- Crucible bulk: max 0,9 liters;
- Oxide vapor-tight packing;
- Without oxygen monitoring system.

10.2 The steps of the testing procedure

In order to examine the mechanical properties of 316 L steel coated bars tested in the liquid lead environment, the specimens were tested under tensile loading at a constant strain rate of $5 \cdot 10^{-5}$ s^{-1}. The slow strain rate during tensile tests was performed in liquid lead, in static conditions at constant temperature of 450ºC, and without oxygen monitoring system. The tensile specimens were tensile tested by the Instron testing machine software according to ASTM E8. The test scope is to obtain the load-displacement diagrams of specimens in molten lead.

The steps of testing procedure are:

- The tensile specimen is attached in the pulling grips and it is bring up in the *sample fixing assembly*. Then, the upper grip is screwed tot he *pooling road*;
- The thermo-regulator of the heating system is set for melting the lead from the crucible. It started and the lead is heated up to 480°C. The crucible is closed;
- The level of the liquid metal has to be between a low level and high level indicator, so that it is sufficiently high to submerge the entire sample. When the lead temperature reaches this temperature, the *sample fixing assembly* with the specimen is inserted in the lead. The *sample fixing assembly is fitted on the* tensile machine mobile beam;
- The thermal transfer between liquid metal and the *sample fixing assembly* takes place so that the lead temperature reaches a temperature below melting temperature. Therefore it is necessary to wait until the temperature reaches again a value above melting temperature;
- By means of the small steps the *sample fixing assembly* is inserted in the lead up to is achieved the link-up with crucible furnace assembly;
- Then, the upper head of the *pooling road* is caught to the tensile machine fix point and the lower grip is fixed in lower side of the *sample fixing assembly*;

- Once the thermal transfer is completed the temperature is set to the desired testing temperature (450°C). When the liquid metal temperature is stabilized, the test can be started;
- The temperature is kept at the preset temperature (450°C) during the time test;
- After the sample is broken, the *sample fixing assembly is uncoupled to the crucible and then it is get out from liquid lead. The both sides of broken sample are cut out and then these are analyzed.* The assembly is cooled down to room temperature and the liquid metal is kept into crucible.

  Notes:
- The tensile testing in the liquid metal environment inside of this experimental facility is based on the ASTM standard E 8M requirements. However, this standard does not include any liquid metal environment and therefore does not strictly apply to tensile testing in liquid metal environment;
- No additional extensometer or visual observation of the deformation can be used due to the opaque and conducting nature of the liquid lead.

After the test data are analysed, one half of the specimen is cleaned in a solution of acetic acid, hydrogen peroxide and ethanol in a ratio of 1:1:1 to allow analysis of the fracture surface by the SEM.

Tensile results as function of displacement are presented as tensile curves. Then one can determine the tensile properties of the coated 316L specimen in liquid lead testing environments like as: the yield stress, the ultimate tensile strength. Moreover, the optical and SEM analyses of tested specimen could provide supplementary information about the coated specimen behaviour in liquid lead under tensile loading.

10.3 Results

The tests in liquid lead has been performed on the 5 tensile coated specimens received from ENEA (Figure 6).

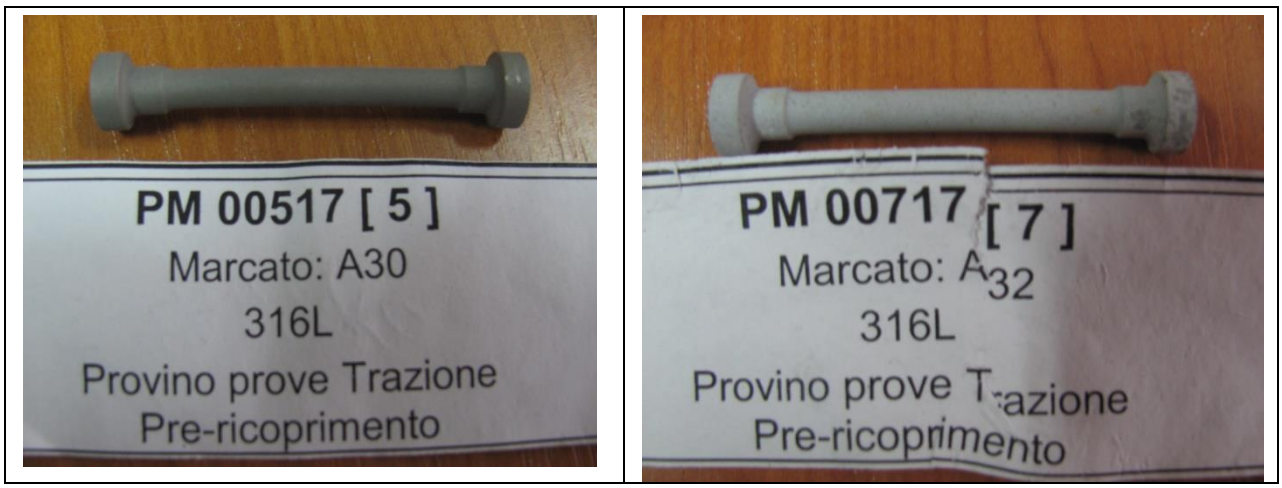

Figure 6. Coated specimens for tensile test

The steps of testing procedure were mentioned in chapter 2, and during the tensile test the temperature was kept around 450 °C (Figure 7).

Figure 7. Temperature monitored during tensile test in liquid lead

After tests the specimens were extracted from the crucible and the aspect of few specimens are shown in Figure 8.

Figure 8. Aspect of specimen extracted from the testing crucible

During the tests it was recorded the stress-strain curves, and these could be seen in the Figure 9, where some parameters are presented. One may see that curves are very close each to other, and allow extracting the mechanical properties. However, the “S shapes” of curves, are related on the “accommodation” of the loading assembly during increasing of the tensile applied force, and seems to be a quite “intrinsic” feature of the test. Therefore from the parameter values given by the machine processing software only UTS are trustworthy. To conclude, for the UTS of the coated steel specimens tested in the liquid lead environment at 450 ^{o}C is UTS= 421.5 MPa.

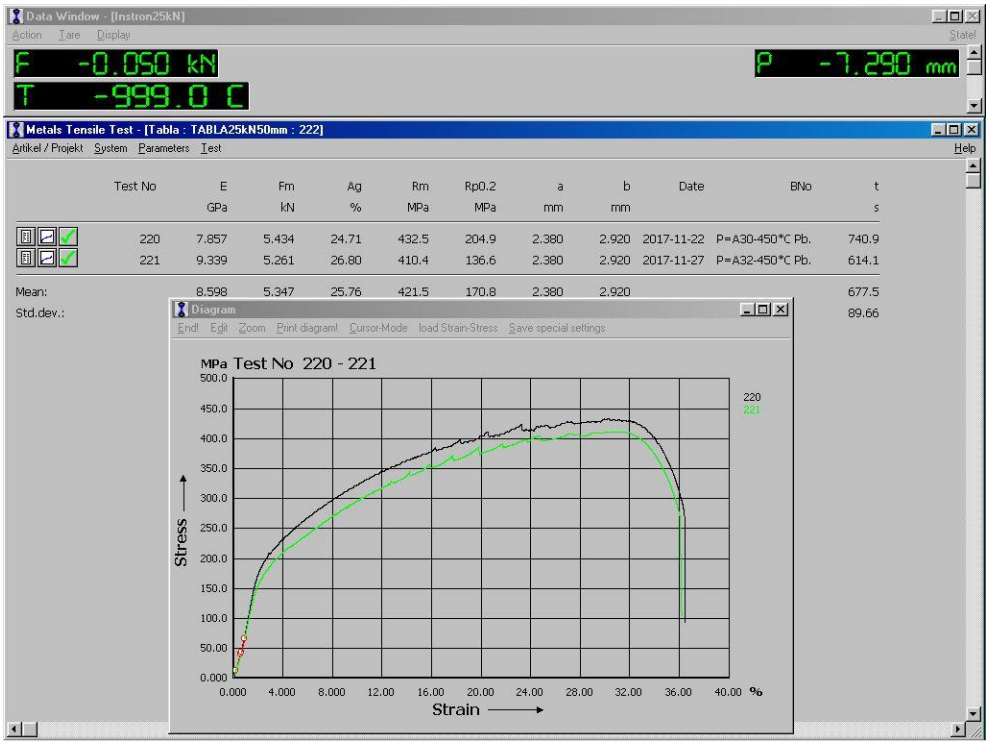

Figure 9. The stress-strain tensile curves for the coated 316L specimens

The coating layer seems to be adherent quite, SEM aspects of the fracture surfaces are shown in Figures 10, revealing the ductile features.

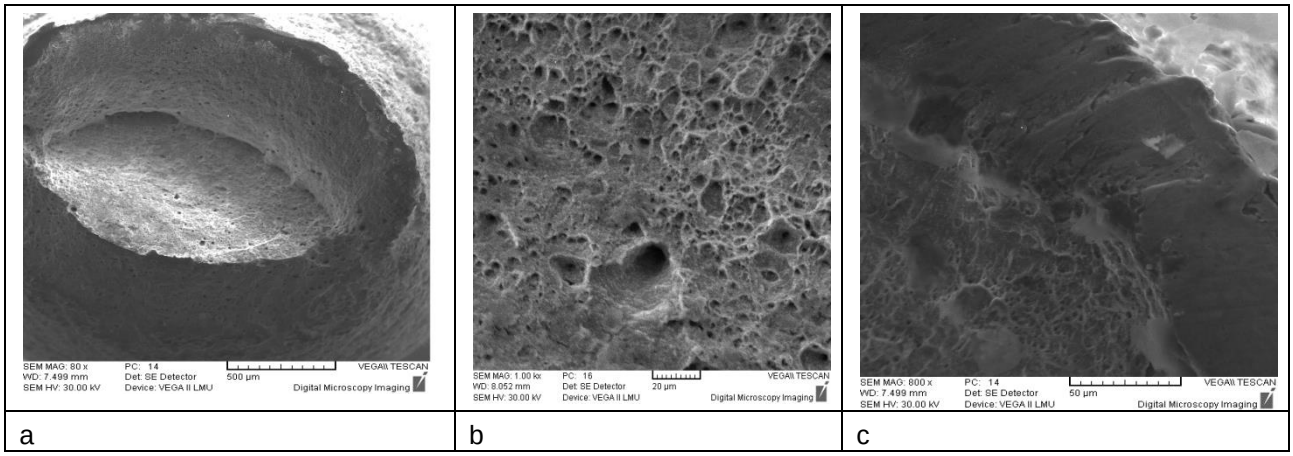

Figure 10. SEM aspects of tested specimen: a) fracture surface (x80), b) base material (x1000), c) the coating layer (x800)

SEM pictures highlight the ductile behaviour of the fracture for base material in Figure 10 a) and with typical voids as in Figure 10 b) and adhesive coating layer Figure 10 c).

10.4 Conclusions

The experimental facility, called **LILETIN (Li**quid **LE**ad **T**esting **IN**stallation), which has been set up at RATEN ICN, allows performing the experimental tensile tests in the liquid lead environment. At this early stage, the LILETIN facility is able to perform tensile tests in a liquid metal crucible configuration, with temperatures up to 450^{o} C in static lead conditions, but without any oxygen monitoring system.

Few conclusions from works performed on the 316 L coated steel specimens tested in the liquid lead environment at 450 ^{o}C:

- In order to examine the effect of coating on the mechanical properties of specimens steel tested in the liquid lead environment, the specimens are tested under tensile loading at a constant strain rate of $5 \cdot 10^{-5}$ s^{-1};
- From the parameter values given by the machine processing software only UTS are trustworthy; the Young modulus (E) values are not valid, and from the aspect of stress-strain curves the UTS = 421.5 MPa;
- SEM pictures highlight the ductile behaviour of the fracture for base material and for the large deformation close to breaking, the layer is still adherent to the base material.

11 Ion irradiation of FeCrAl alloys – HZDR contribution

C. Heintze, S. Akhmadaliev, E. Altstadt

11.1 Experiment

Bulk Fe-XCr-4Al-0.2Zr (X = 9, 10, 11, 12wt%) alloys and Fe-16Cr-8Al were provided by KTH and KIT, respectively. The compositions are summarized in

Table 8. All samples exhibit a ferritic microstructure (Figure 13) with equiaxed grains of a size in the order of 100 µm. Detailed grain sizes are given in

Table 9. The Fe-Cr-Al-Zr alloys exhibited Zr-rich inclusions of about 1 µm size. Fe-16Cr-8Al exhibits a subgrain structure and alumina inclusions of about 1-2 µm size.

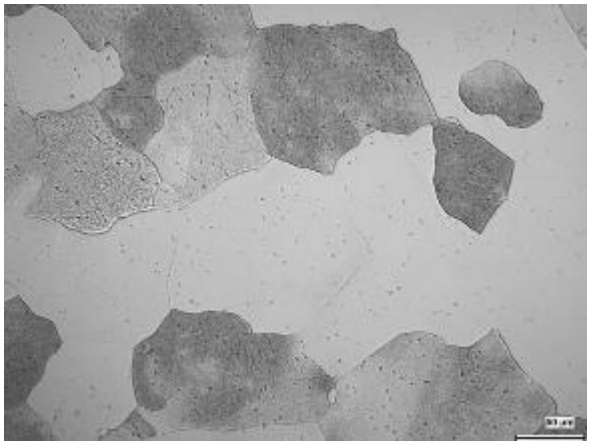

(a)

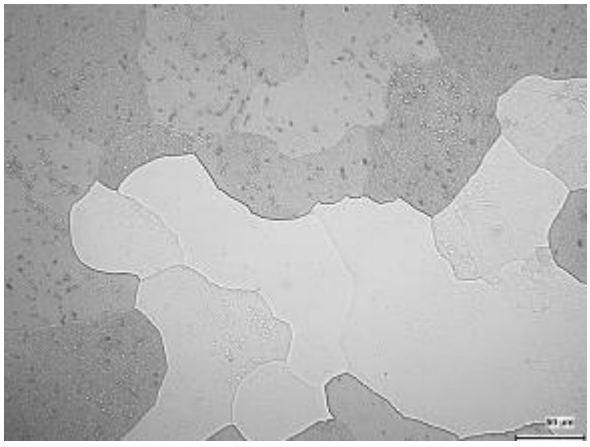

(b)

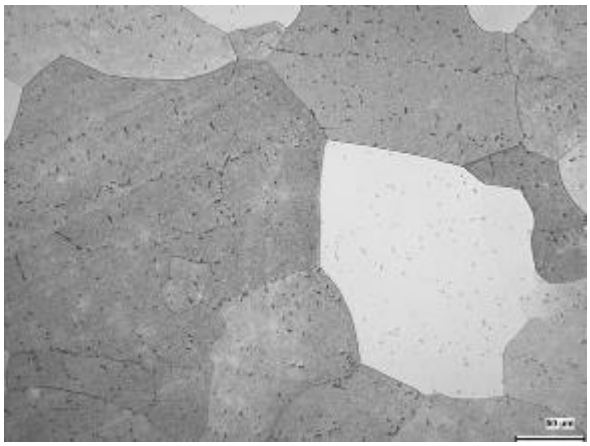

(c)

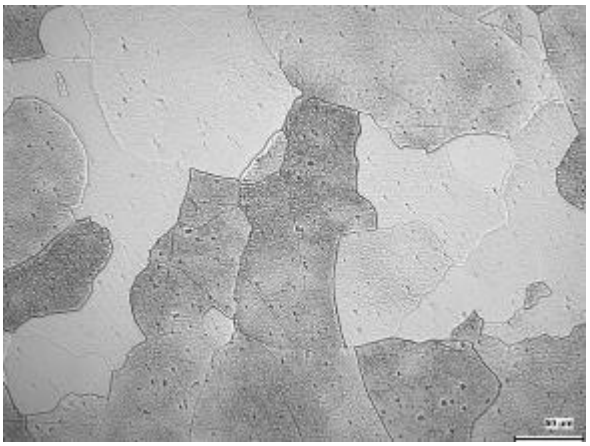

(d)

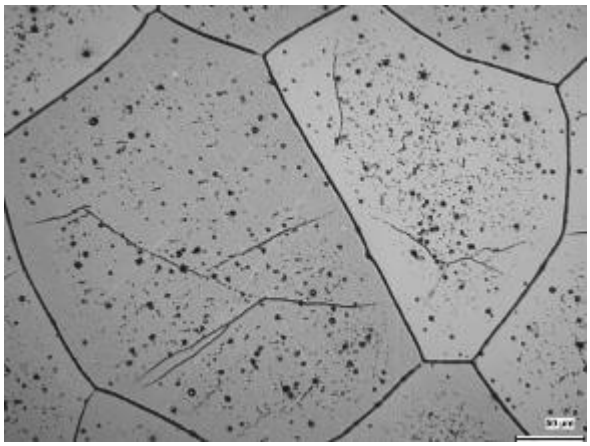

Figure 13: Optical micrographs of the microstructure of the Fe-Cr-Al-(Zr) alloys

(a) Fe-9Cr-4Al

(b) Fe-10Cr-4Al

(c) Fe-11Cr-4Al

(d) Fe-12Cr-4Al

(e) Fe-16Cr-8Al

←(e)

Table 8: Alloy composition (wt%) (ICP-OES if not indicated otherwise)

Alloy	Sample ID	Cr	Al	Zr	Others
Fe-9Cr-4Al	LS4736	8.97	4.01	0.21	according to specifications: Si < 0.1 wt% Mn < 0.1 wt% C < 0.03 wt.%
Fe-10Cr-4Al	LS4735	10.03	3.99	0.20	
Fe-11Cr-4Al	LS4737	10.89	4.01	0.21	
Fe-12Cr-4Al	LS4738	12.04	4.00	0.20	
Fe-16Cr-8Al*	K16	16	8	0	

* nominal composition

Table 9: Grain size

Alloy	Average grain diameter (µm)	ASTM grain size
Fe-9Cr-4Al	113	3.6
Fe-10Cr-4Al	138	3.0
Fe-11Cr-4Al	179	2.3
Fe-12Cr-4Al	127	3.3
Fe-16Cr-8Al	261	1.2

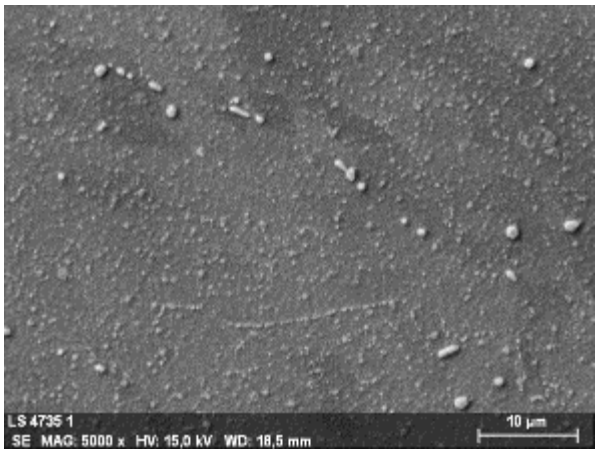

(a)

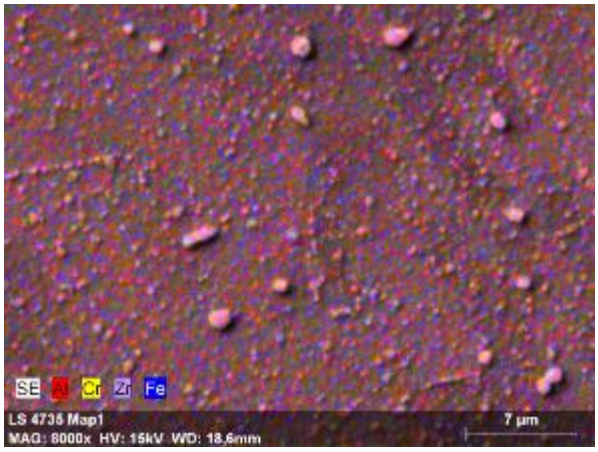

(b)

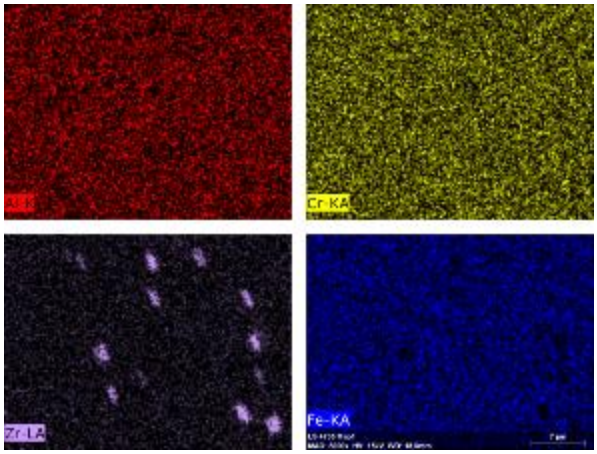

(c)

Figure 14: SEM (SE) image of Fe-10Cr-4Al (a) as well as SEM-EDS overlay image (b) and individual EDS maps(c) of a subsection of image (a)

Samples of 1 mm thickness were cut by wire erosion and mechanically ground and polished. The samples were ion-irradiated at the Ion Beam Centre (IBC) at HZDR with 5 MeV Fe^{2+} ions at two temperatures to a nominal damage of 0.5 dpa at 500 nm depth. The irradiation parameters are summarized in Table 10. The resulting dpa-profile, as shown in Figure 15, was calculated by means of the binary collision code SRIM (SRIM 2008-04) setting the displacement energy to 40 eV and following the recommendations by Stoller [1]. The samples were fixed on a heating target. The temperature was controlled by means of a thermocouple fixed at the back of the sample. To ensure a homogeneous exposure over the whole samples area, the beam was raster scanned over an area of 70 x 70 mm with slightly differing scanning frequencies in the order of 1 kHz.

Table 10: Ion irradiation conditions

No.	Ion	Energy (keV)	Fluence (1/cm^2)	Duration (min)	Temperature (°C)
(1)	Fe^{2+}	5000	$1.33x10^{15}$	200	300
(2)	Fe^{2+}	5000	$1.33x10^{15}$	190	450

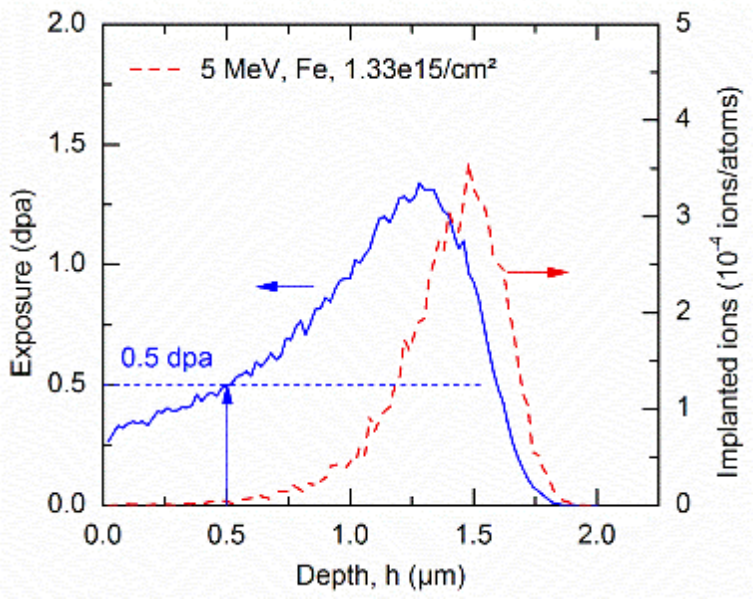

Figure 15: Ion implantation profile and damage distribution in terms of dpa

The samples were characterized by means of nanoindentation testing along with their respective unirradiated references. The tests were performed at HZDR utilizing a Universal Nanomechanical Tester (UNAT) equipped with a Berkovich indenter. Calibrations of the indenter area function and the instrument stiffness were based on measurements on two reference materials (fused silica, sapphire) with known elastic modulus. The quasi continuous stiffness measurement (QCSM) method was applied, where the load is superimposed with a sinusoidal oscillation at discrete loads. This method allows the contact stiffness to be calculated along the loading curve and the full loading curve to be exploited to calculate the indentation hardness (H_{IT}) as a function of contact depth (h_c). The tests were performed with a maximum load of 50 mN with a corresponding contact depth of about 800 to 1000 nm. More than 30 indents per material and condition were performed. Zero point and thermal drift correction were applied to each individual curve. Thereafter, an average curve was calculated and analysed using the method described by Oliver and Pharr [2]. The hardness value at a reference depth of 200 nm was chosen as the hardness representative for the irradiated layer and to calculate the irradiation-induced hardness change. A linear superposition of the initial hardness and the hardness contribution by the irradiation-induced defects is assumed. Moreover, it is assumed that the indentation size effect (ISE) does not significantly change with irradiation.

11.2 Results

The indentation hardness was measured as a function of contact depth for all alloys and ion irradiation conditions including the respective unirradiated reference samples. The indentation hardness as a function of contact depth is shown in Figure 16 for Fe-12Cr-4Al-0.2Zr in unirradiated condition and after ion irradiation at 300°C and 450°C by way of an example representative for the whole set of measurements. For the unirradiated samples the indentation hardness shows only a very weak indentation size effect, i.e. the measured hardness only slightly increases with decreasing contact depth, except for depths below about 100 nm, where artefacts related to tip rounding and/or surface preparation cannot be neglected.

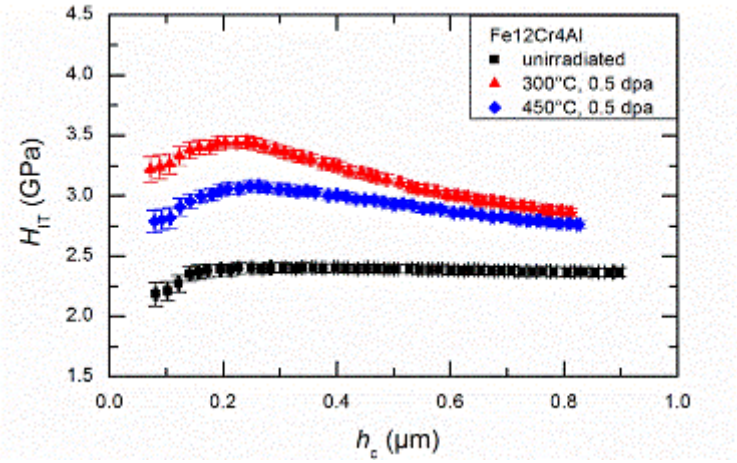

Figure 16: Indentation hardness vs. contact depth for un- and ion-irradiated (300°C/0.5dpa, 450°C/0.5dpa) Fe-12Cr-4Al-0.2Zr

For the ion-irradiated samples a higher indentation hardness with a maximum at about 200 nm contact depth is observed which is related to the irradiation-induced hardening of the ion-irradiated layer. The decrease of indentation hardness with increasing contact depth beyond the maximum is dominated by the increasing contribution of the softer unirradiated substrate. The decrease of the indentation hardness with decreasing contact depth for depths smaller than about 200 nm is attributed to the graded dpa-profile.

In the following only the irradiation-induced hardness change with respect to the unirradiated reference is considered. A reference depth of 200 nm was selected to calculate the hardness difference, which is close to the maximum indentation hardness for most irradiated conditions and ensures negligible substrate effect. A summary of the results is presented in Figure 17 as a function of Cr and Al content.

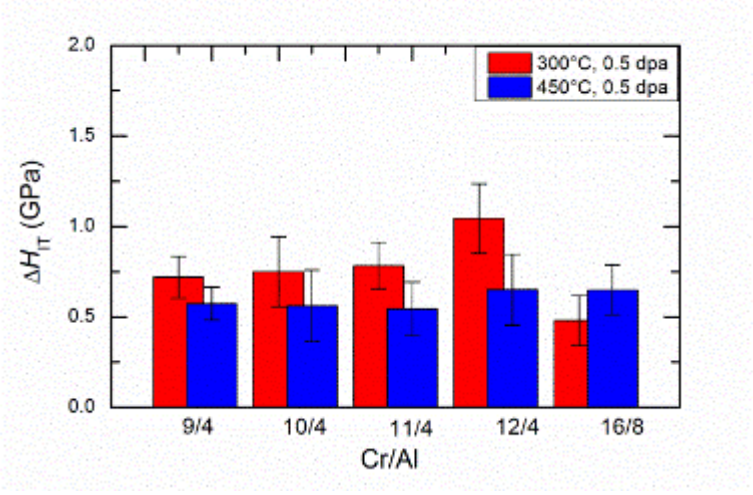

Figure 17: Hardness increase at 200 nm contact depth for Fe-Cr-Al(-Zr) alloys with different Cr and Al contents ion-irradiated at 300°C and 450°C

Significant irradiation-induced hardening is observed for all alloys and conditions. Hardening tends to be higher at 300°C with exception of Fe-16Cr-8Al. At 300°C irradiation hardening is similar for Cr contents of 11%Cr or less. Higher hardening is observed for the 12%Cr alloy. Lowest hardening is observed in Fe-16Cr-8Al. At 450°C the observed hardening is similar for all alloys irrespective of the Cr and/or Fe content.

Discussion

From previous work on ion-irradiated as well as neutron-irradiated Fe-Cr alloys [3–6] and from an ion irradiation experiment performed on a set of Fe-Cr alloys (5-14 wt%Cr) in the framework of this project (WP2) using the same ion irradiation conditions as in the present experiment it is known that the irradiation hardening in Fe-Cr is mediated by the formation of dislocation loops, α'-phase precipitates as well as solute/impurity clusters such as NiSiP(Cr)-clusters. It is hypothesised that the same defects also dominate hardening in Fe-Cr-Al under the given conditions.

Significant irradiation-induced hardening is observed for all alloys at 300°C. According to the binary Fe-Cr phase diagram, at this temperature all Cr contents considered here fall within the miscibility gap indicating that α'-phase precipitation can occur at this temperature. The equilibrium volume fraction increases with Cr content. As the hardening contribution is proportional to the square root of the volume fraction, this would result in an increase of the irradiation-induced hardening by α'-phase precipitates with increasing Cr content. Indeed, α'-phase precipitation and a yield strength increment increasing with Cr content was reported by Field et al. at a slightly higher temperature of 382°C in Fe-Cr-Al alloys (10-18wt% Cr, 2.9-4.8wt% Al) neutron-irradiated up to 1.8 dpa [11]. Based on a dispersed barrier hardening model Field et al. concluded that the observed hardening was dominated by α'-phase precipitation. However, this is not reflected in the irradiation-induced hardness change observed in the present experiment. In fact, an increase in hardening is observed at 12%Cr, while it is roughly constant below. The lowest hardening, though, is observed in Fe-16Cr-8Al despite of the even higher Cr content. Potential reasons include the following issues or a combination thereof:

1) Suppression of α'-phase precipitation under ion-irradiation conditions
2) Suppression of α'-phase precipitation due to an increase in the Cr solubility limit by Al addition
3) Overcompensation by other hardening contributions (i.e. loops, impurity clusters) or softening due to recovery of pre-existing dislocations

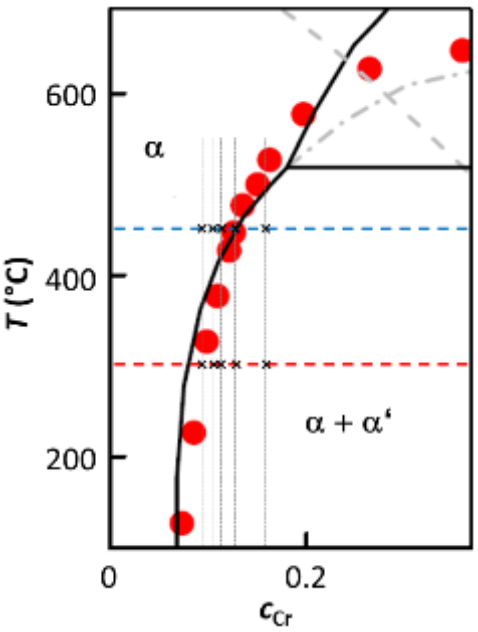

Figure 18: Binary Fe-Cr phase diagram [7,8], conditions analysed within this work marked with black crosses

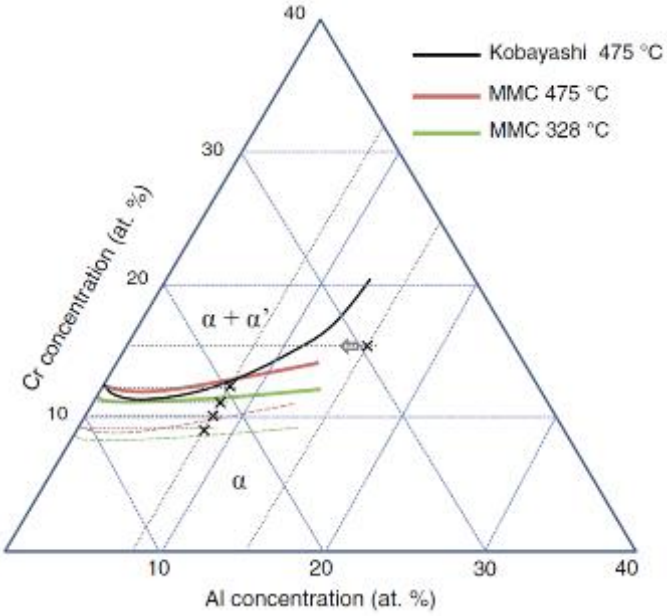

Figure 19: Ternary Fe-Cr-Al phase diagram [9,10], conditions analysed within this work marked with black crosses

Atom probe tomography results obtained by Pareige et al. on Fe-Cr alloys irradiated at 300°C to a similar dose with neutrons and ions suggested that the formation of α'-phase is suppressed or retarded under ion irradiation [5]. The observation was later attributed to the effect of implanted interstitials [12]. This mechanism would be more prominent for the multi-step irradiations with Fe ions of multiple energies those results were based on than for the single-step irradiations performed in the present experiment. Indeed, α'-phase precipitation was observed in Fe-15at%Cr single-step irradiated with 2 MeV Fe ions at 300°C [12]. It was show that the suppression of α'-phase was not complete and limited to the region close to the implantation peak. The damage levels considered were comparable to the present experiment (about 0.5–1 dpa). Therefore, it is taken as a given that α'-phase precipitation can occur under the present ion irradiation conditions. A dependence of the extend of the suppression on the Cr content cannot be excluded, however, it is considered to be of minor importance.

The effect of Al on α'-phase mediated hardening after thermal annealing for 1000 h was studied by Kobayashi et al. [9]. Based on their results, the authors suggested an increase of the Cr solubility limit with the addition of Al. Their results were qualitatively confirmed by Ejenstam et al. [10] by means of Metropolis Monte Carlo simulation. The ternary Fe-Cr-Al phase diagram taken from [10] including the boundaries of the miscibility gap based on the two works described above [9,10] and with the conditions analysed within the present work marked is shown in Figure 19. The predicted lack of α'-phase for the Fe-Cr-4Al-0.2Zr alloys with less than 12wt% Cr (green solid line for 328°C) would explain the step-shaped appearance of the hardening as a function of Cr contents ≤ 12%Cr. However, it is ruled out as an explanation

taking into account the above mentioned experimental results on neutron-irradiated Fe-Cr-Al of similar Al contents. Therefore, a monotonously increasing contribution of α'-phase would be expected. In fact, a continuous hardening would be supported by the error bars for Cr contents ≤ 12%Cr. Still, the effect of Al on the solubility limit is considered to be the main reason for the lower hardening observed for Fe-16Cr-8Al where the Cr content is factor of 2 higher. Although, the matrix concentration of Al is expected to be lower than the nominal concentration due to the presence of the alumina inclusions.

The effect of Cr on the nucleation and growth of dislocation loops and the resulting hardening contribution do not provide sufficient reasoning for the differences or lack thereof observed in the set of alloys. Bergner et al. reported the variation of the contribution related to loops to be small for Cr contents relevant for this work in material neutron irradiated to 0.6 dpa at 300°C [4]. Field et al. reported the loop contribution to monotonously increase with Cr content (10-18wt%) in materials neutron-irradiated at 382°C to 1.8 dpa, but this increase was small compared to the increase of the contribution of α'-phase [11].

Contributions of impurities to the total hardening cannot be excluded. From previous works it is known that impurity clusters can extensively contribute to the observed hardening. However, their contribution, either direct in terms of solute/impurity clusters or indirect by affecting loop nucleation and growth, does not explain differences within the set of Fe-Cr-Al-Zr alloys as they were produced using the same base materials and fabrication route. However, it may contribute to the difference observed between the Fe-Cr-Al-Zr alloys and the Fe-16Cr-8Al alloy. Hardening observed in Fe-9Cr-4Al is slightly higher than in pure binary Fe9Cr (0.23 ± 0.1GPa), however, it is in reasonable agreement with the hardening observed in a commercially pure Fe9Cr alloy (0.47 ± 0.15 GPa). Both alloys were irradiated and tested under the same conditions in the framework of WP2. As in terms of impurities the alloys used here are more comparable to the commercially pure alloy, we conclude that Al does not significantly alter the irradiation response for Cr contents, where α' precipitation does not play a dominating role (about 9%Cr or less).

Significant hardening is observed for all alloys at 450°C. It is very similar irrespective of the Cr and Al content. Considering both the binary Fe-Cr and the ternary Fe-Cr-Al phase diagram it can be concluded, that α'-phase precipitation does not play a role at this temperature, which is supported by the lack of difference in the observed hardening. The observed hardening is tentatively attributed to the combined effect of impurity clusters and dislocation loops.

Further clarification of the individual hardening contributions requires characterization of the irradiation-induced microstructure by means of TEM and APT and considering the structure-property relation e.g. based on a dispersed barrier hardening model.

11.3 Summary and conclusions

Significant hardening is observed for all alloys at 300°C and 450°C. The combined effects of the Al mediated shift of the Cr solubility limit and potentially Cr content dependent partial suppressing of α'-phase precipitation by the implanted ions are considered as the main reasons for the variation of hardening observed for the different alloys. A significant contribution of impurity clusters to the observed hardening is expected.

Acknowledgement

The use of HZDR Ion Beam Center facilities and the support by its staff is gratefully acknowledged. We kindly thank M. Rossner, M. Houska and J. Pietzsch for sample preparation and G. Müller for the SEM analyses.

11.4 References

[1] R.E. Stoller, M.B. Toloczko, G.S. Was, A.G. Certain, S. Dwaraknath, F.A. Garner, Nucl. Instrum. Methods Phys. Res. Sect. B Beam Interact. Mater. At. 310 (2013) 75–80.

[2] W.C. Oliver, G.M. Pharr, J. Mater. Res. 7 (1992) 1564–1583.

[3] C. Heintze, F. Bergner, A. Ulbricht, H. Eckerlebe, J. Nucl. Mater. 409 (2011) 106–111.

[4] F. Bergner, C. Pareige, M. Hernández-Mayoral, L. Malerba, C. Heintze, J. Nucl. Mater. 448 (2014) 96–102.

[5] C. Pareige, V. Kuksenko, P. Pareige, J. Nucl. Mater. 456 (2015) 471–476.

[6] M. Hernández-Mayoral, C. Heintze, E. Oñorbe, J. Nucl. Mater. 474 (2016) 88–98.

[7] G. Bonny, D. Terentyev, L. Malerba, J. Phase Equilibria Diffus. 31 (2010) 439–444.

[8] F. Soisson, T. Jourdan, Acta Mater. 103 (2016) 870–881.

[9] S. Kobayashi, T. Takasugi, Scr. Mater. 63 (2010) 1104–1107.

[10] J. Ejenstam, M. Thuvander, P. Olsson, F. Rave, P. Szakalos, J. Nucl. Mater. 457 (2015) 291–297.

[11] K.G. Field, X. Hu, K.C. Littrell, Y. Yamamoto, L.L. Snead, J. Nucl. Mater. 465 (2015) 746–755.

[12] O. Tissot, C. Pareige, E. Meslin, B. Décamps, J. Henry, Mater. Res. Lett. (2016) 1–7.

12 Evaluation of the stability FeCrAlY coating under irradiation – contribution by PSI

Lijuan Cui and Yong Dai

EXECUTIVE SUMMARY

The FeCrAlY coating using the GESA (surface alloying using pulsed electron bean) technique developed at Karlsruhe Institute of Technology (KIT) has demonstrated a good resistance to LBE corrosion. In order to apply this coating to ADS or LFR, the stability of the coating under irradiation has to be investigated. The irradiation-induced embrittlement could degrade the stability of the coating. This issue has been studied at the Paul Scherrer Institut (PSI) using the LiSoR facility, where a specimen was irradiated with 72 MeV protons in contact with flowing LBE. The results demonstrated that the FeCrAlY coating on T91 steel showed evident irradiation-induced hardening and embrittlement effect after irradiation at 2.5 dpa in the temperature range of 300-400°C. In this project, the microstructure of the FeCrAlY coating before and after irradiation has been investigated.

The microstructure of the FeCrAlY coating was investigated by means of transmission electron microscopy (TEM), coupled with the high angle annular dark field (HAADF) technique to analyze the precipitate structure. The focused ion beam (FIB) technique was used to prepare TEM samples from the cross section of the coating layer. Samples in conditions of unirradiated and after irradiation at 2.5 dpa at 300-400°C were investigated. The results show that, as compared to normal ferritic/martensitic (FM) steels, the special microstructural feature of the FeCrAlY coating is its precipitate structure. The precipitates were seen in different shapes and enriched with Al, Y, Cr and O. While $M_{23}C_6$ type precipitates normally observed in tempered FM steels were not detected. Al enriched precipitates should be Al-oxides, in either spherical or faceted shape with sizes of few tens to few hundreds of nanometers, were detected throughout the coating layer. Y enriched ones should be either Y-oxides or sometimes pure Y particles. They are in spherical shape slightly smaller than the Al oxides and also distributed throughout the whole coating layer. The Cr enriched precipitates, not with O, are mostly in elongated shape of few hundreds nanometers length and observed everywhere in the coating layer. The Al and Y enriched precipitates are largely combined together, partially with the Cr enriched ones. The shape and chemical composition of the precipitates changed with depth from surface in the coating layer. In the region close to the surface, the Al and Y oxides are spherical, while the Cr enriched ones are elongated. In the middle region of the coating, the Al oxides are mostly in faceted shape. The elongated Cr enriched precipitates become much shorter. In the region close to the T91 matrix, the precipitate structure looks similar to that in the region close to surface. The depth dependence of the precipitate structure might be associated with the local cooling rate during the solidification of the coating layer in the GESA treatment. The regions close to either surface or the T91 matrix should be with a higher cooling rate than the middle region. But, the mechanisms for forming such a structure are not clear.

No convinced irradiation effects on the precipitate structure could be identified due to the inhomogeneity of the precipitate structure. The irradiated induced hardening and embrittlement of the coating layer should be mainly attributed to the defect structures (nanometer-sized defect clusters and/or dislocation loops) as normally observed in FM steels in such irradiation conditions, which were not successfully observed in the FIB'ed samples.

12.1 Introduction

It is well known that liquid lead-bismuth eutectic (LBE) can introduce a significant corrosion effect to FM steels [1]. Surface protection with coatings is considered to be necessary for steels applied in the future accelerator driven systems (ADS) for nuclear waste transmutation and lead-cooled fast reactors (LFR). Among various coatings, the FeCrAlY coating using the GESA (surface alloying using pulsed electron bean) technique [2] developed at Karlsruhe Institute of Technology (KIT) showed good resistance to LBE corrosion. The behaviors of this coating under stress in contact with flowing LBE have been studied by different authors (e.g. [3]). The results show that stability of this coating is good under rather high stresses. However, in order to apply this coating to ADS or LFR, the stability of the coating under irradiation has to be investigated, because irradiation may introduce severe embrittlement depending on irradiation temperature. The irradiation-induced embrittlement could degrade the stability of the coating. In the Euratom FP6 VELLA (Virtual European Lead Laboratory) project [4], studies on this issue were carried out at the Paul Scherrer Institut (PSI), Switzerland using the so-called LiSoR facility [5], which was a LBE loop installed at the 72 MeV Injector-I proton beam line. The results demonstrated that the FeCrAlY coating on T91 steel showed evident irradiation-induced embrittlement effect after irradiation at 2.5 dpa in the temperature range of 300-400°C [6]. In this project, the microstructure of the FeCrAlY coating before and after irradiation has been investigated to improve the understanding of the coating material and its behavior after irradiation.

12.2 Experimental

12.2.1 Material and specimens

The irradiation of the FeCrAlY coating was performed in the 6th LiSoR experiment (LiSoR-6). The test section of LiSoR-6 consisted of two components: a tube of 1 mm wall thickness and a tensile specimen of 1 mm thickness. The dimensions of the tube and the tensile specimen are shown in Figure 1. Both the tube and the tensile specimen were made of martensitic steel T91. One of the major surfaces of the tensile specimen was firstly coated with FeCrAlY (14-16 wt.-% Cr, 6-8 wt.-% Al, 0.5 wt.-% Y and <0.012 wt.-% Ni and Co) using the plasma spray technique and then treated with the GESA technique which delivered surface alloying in a depth of 20-30 □m. Due to high internal stress induced during the surface alloying process, the specimen was slightly distorted after the single-side coating. To reduce the internal stress, the specimen was stress-relieved at 450°C for 4 hours. However, the specimen was still slightly bent after the treatment. The appearance of the tube and the tensile specimen before irradiation is shown in Figure 2.

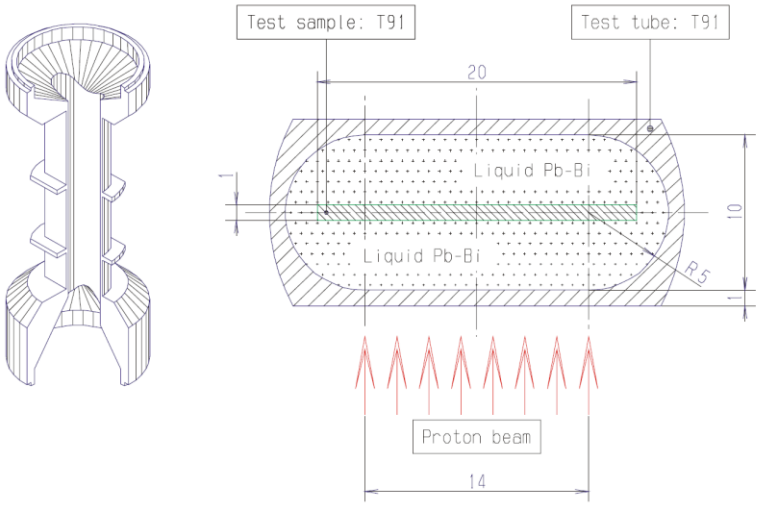

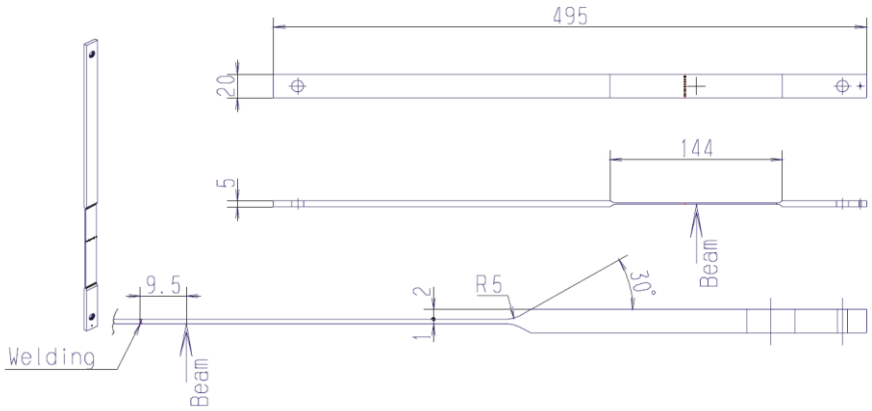

Figure 1: Sketches showing the dimensions of the tube (upper) and the tensile specimen (lower).

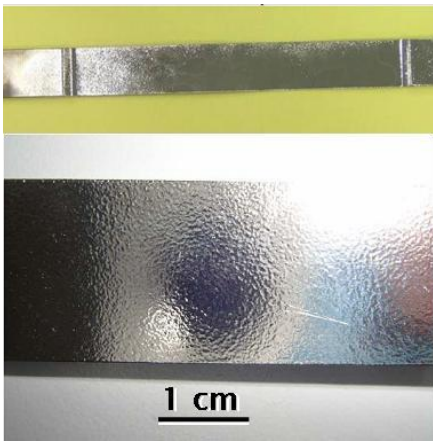

Figure 2: The single-side FeCrAlY-coated tensile specimen.

12.2.2 Irradiation

LiSoR-6 was irradiated with 72 MeV protons at a beam current of 25-28 □A. The proton beam had a Gaussian profile of 1.2 mm sigma and was wobbled over an area of about 0.8×1.4 cm^2. The wobbling frequency was 14.3 Hz in the direction perpendicular to the major axis of the tensile specimen and 2.38 Hz in the direction along the major axis [7]. A total proton charge of 21.6 mAh was received. The irradiation dose was calculated using the MCNP code. The maximum dose of the specimen is 2.5 dpa.
The tensile specimen was positioned in the center of the tube and mechanically loaded to a tension stress of 200 MPa. Inside the tube the LBE had a mean velocity of about 1 m/s. The temperature of the inlet LBE flow was kept at about 300°C. The calculated surface temperature in the irradiation area of the tensile specimen was up to about 405°C. No clear surface damage could be detected after irradiation [6].

12.2.3 Mechanical test

The irradiation-induced hardening effects were investigated by conducting nano-indentation measurement on the cross-section of a sample with an irradiated zone (0.48 dpa) in the mid part and unirradiated areas at the ends. Whereas the behaviors of the coatings under deformation were studied by performing a series of SEM observations in the course

of bending the samples to various surface strain values between 0.7% to 9% for most of the tested samples and up to 16% for an unirradiated sample [6].

The results showed that the hardness of the coating layer is higher than the T91 steel. After irradiation the hardness increased in the coating layer, but slightly less than that of in the T91 steel matrix.

The SEM observations demonstrated that the cracks formed on the surface of an irradiated coating specimen were much larger but fewer than that of an unirradiated coating specimen. The interface between the coating layer and the T91 steel matrix is a strong barrier to the propagation of the cracks.

These tests indicated evident irradiation-induced hardening and embrittlement effects of the FeCrAlY coating.

12.2.4 TEM sample preparation

In order to conduct TEM (transmission electron microscopy) observation on the microstructure of the coating layer, lamella samples were fabricated by using a Zeizz NVision Focused Ion Beam (FIB) machine. Lamellas were extracted from an area at 2.5 dpa irradiation dose and an area without irradiation. In order to reduce the damage induced by FIB process, 1 keV / 80 pA ion beam was used at the final polishing step. However, it was found out that the surface damage could not be well removed. Therefore, the irradiation-induced defect structures (nanometer-sized defect clusters and/or dislocation loops) were not successfully observed.

12.2.5 TEM observation

The TEM observation was conducted on the lamellas without or with further treatment, flash-polishing after FIB'ing. Most of the observations were performed by using Jeol 2010 TEM at PSI operated at 200 keV, while the chemical element mapping was done by using the HAADF (High angle Annular Dark Field) technique available at the FEI-Talos TEM at ETH-Zürich. The observation was focused on the precipitate structure of the coating layer.

12.3 Results and discussion

12.3.1 grain structure in the coating

The grain structure can be observed during FIB'ing process imaged with the ion beam. Figure 3 presents a view of the cross section of the FeCrAlY coating during fabricating a lamella. It can be seen that the grain structure in the coating layer is different from that normally observed in martensitic steels. The grains are slightly elongated with a major axis perpendicular to the surface. Therefore, the grain boundaries are also in the direction roughly perpendicular to the surface. The insert on the right side of the figure depicts qualitatively the concentration distribution of elements Fe, Cr, Al and Y obtained by using EDX line-scan along the depth direction. It indicates clearly a boundary between the coating layer and the T91 steel matrix.

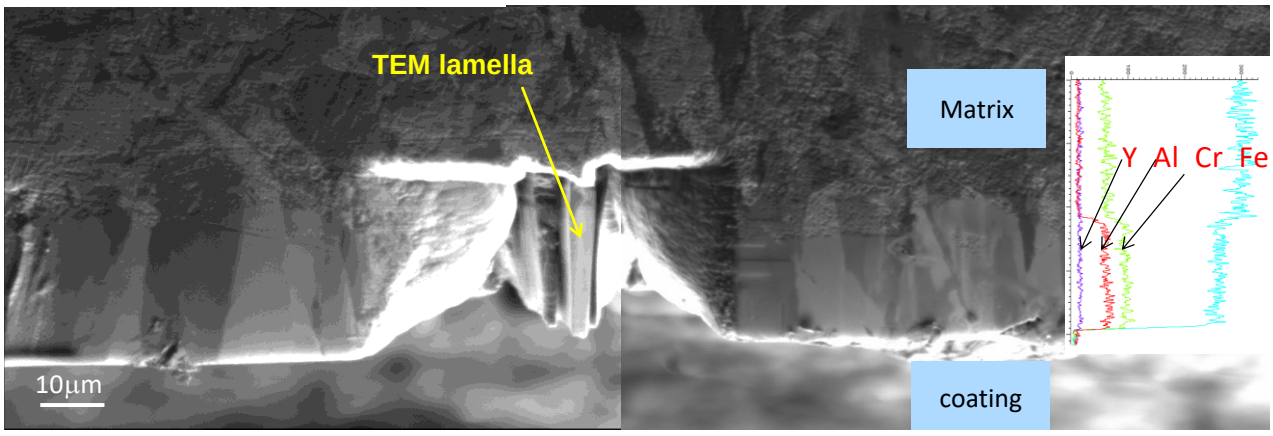

Figure 3: A view of the cross section of the FeCrAlY coating during fabricating a lamella

12.3.2 Precipitate structure in the coating

The main microstructural feature of the FeCrAlY coating is the precipitate structure. The TEM observation shows that there are several types of precipitates. They can be distinguished from their shapes and chemical compositions. The precipitates in the coating layer do not have notable changes after irradiation. The distribution of the precipitates depends on the depth in the coating layer.

Figure 4 presents an example showing an overview of a lamella sample after FIB'ing, SEM image a) and TEM image b) acquired by the HAADF (High angle Annular Dark Field) technique in the area indicated in a). Observations and element analyses were performed in the different areas as such 1-3 in the figure.

The shapes of the precipitates can be divided into three types, as shown in Figures 5. The first type is spherical shape inhomogeneous distributed from the surface of the coating layer to the T91 steel matrix with different chemical compositions. The size of these spherical precipitates varies from few tens to about two hundred nanometers. The second type is faceted precipitates. They are formed in small clusters sometimes around spherical precipitates or independent. Their size is smaller than that of the spherical one. The third type is elongated ones of about hundreds of nanometers length.

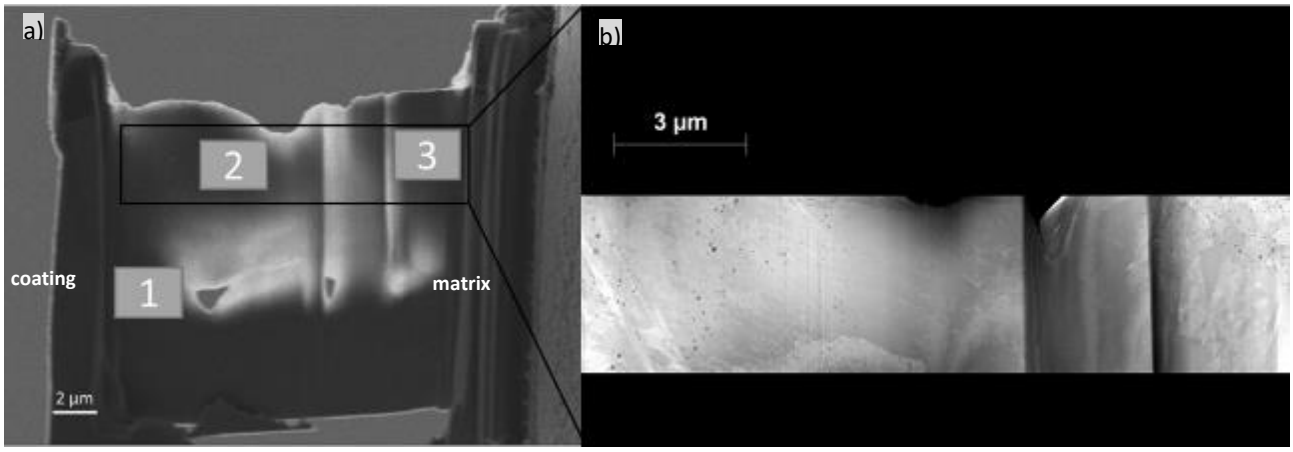

Figure 4: Image a), an overview of STEM mapping areas in the TEM lamella. Image b), at a lager magnification of the area indicated in a) acquired by the HAADF (High angle Annular Dark Field) technique.

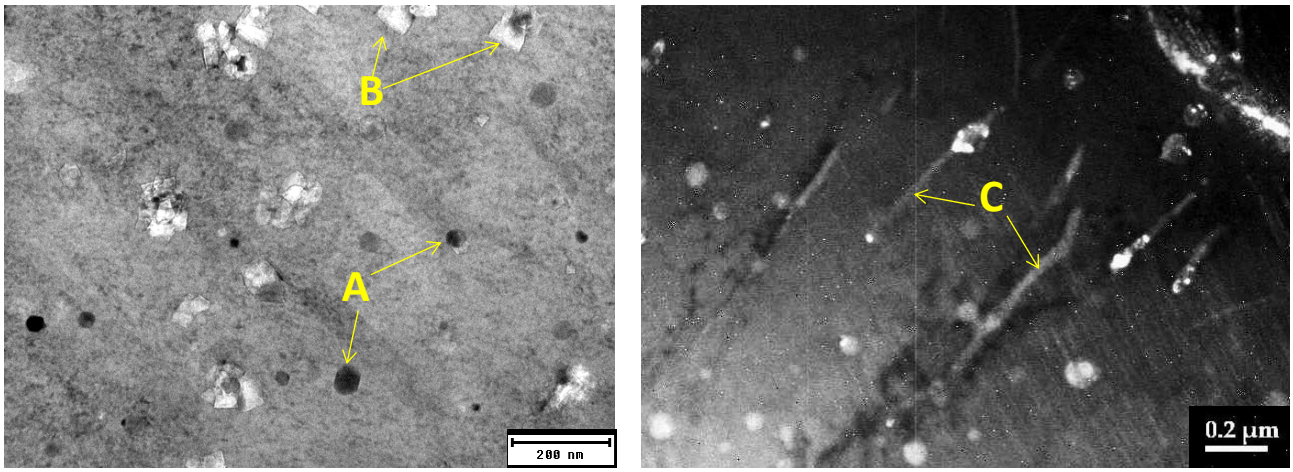

Figure 5: TEM graphs showing the precipitate in the FeCrAlY coating layer.

The precipitates can be also divided into three types from their composition, which enrich with Al, Y and Cr. All Y enriched precipitates are spherical type, but for Al or Cr enriched precipitates have various forms. The shape of Al enriched precipitates related to the depth of the coating could be spherical or faceted. The Cr enriched precipitates can be either spherical or elongated shapes which depended on the depth. The Al enriched precipitates are also enriched with O and expected to be Al-oxide particles. The Y enriched precipitates are mostly enriched with O and expected to be Y-oxide particles.

The distribution of precipitates changes with the depth from the coating surface to T91 matrix. Hereby an illustration is given for an un-irradiated sample. HAADF-STEM images and element EDX maps were obtained in Areas 1-3, at depths of about 3-6µm, 6-9µm and 17-20µm from the surface, respectively, as shown in Figure 4.

Close to the surface, in Area 1, the precipitates appeared to be two shapes, spherical shape enriched with Al, Y and O, and elongated shape enriched with Cr. The Al, Y and O maps show that all the spherical precipitates are mostly Al-oxide. Some of them contain also Y. Whereas the Cr map indicates that the Cr enriched precipitates are not oxide. It seems that the Y enriched precipitates are always combined with the Al oxide, or in other word, some Al-oxides contain Y. The Cr enriched precipitates sometimes also combine with the Al/Y oxides.

A grain boundary was seen in this area. But, nothing special was detected at the grain boundary.

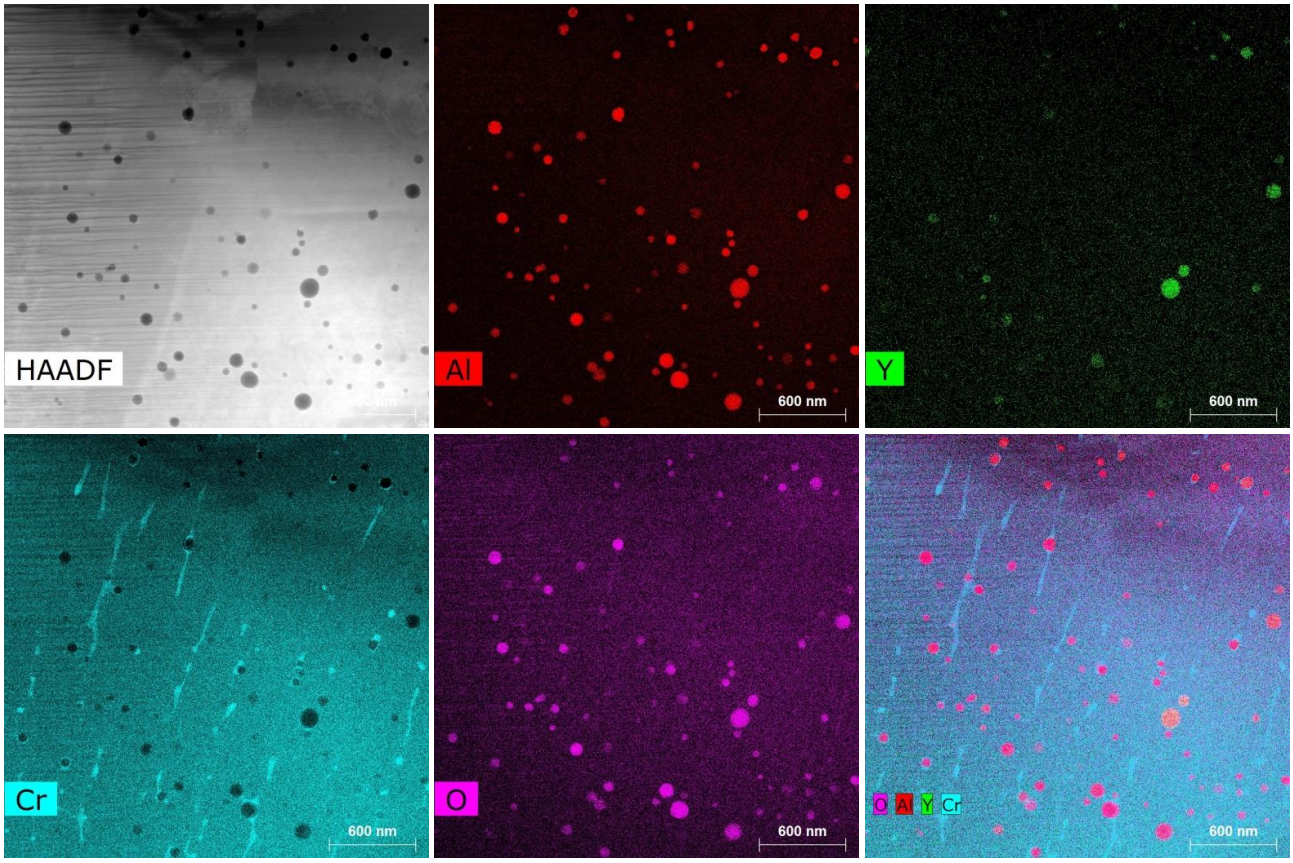

Figure 6: HAADF-STEM image and element maps acquired from Area 1 in Figure 4, in a depth of 3-6 µm from surface. Most of the precipitates are spherical enriched with Al, Y and O. Many of them combined with Cr enriched precipitates.

In Area 2, about 6-9µm from the surface and close to the middle the coating, some faceted precipitates were observed and most the Cr enriched precipitates appeared to be spherical shape instead of elongated shape, as shown in Figure 7. Compared to Area 1 (Figure 6), in Area 2 there are less precipitates enriched in both Al and Y. Although most of them may still be oxides, some are purely enriched with Y (most-left ones in the Y map). The distribution of the Al and Y enriched precipitates is inhomogeneous.

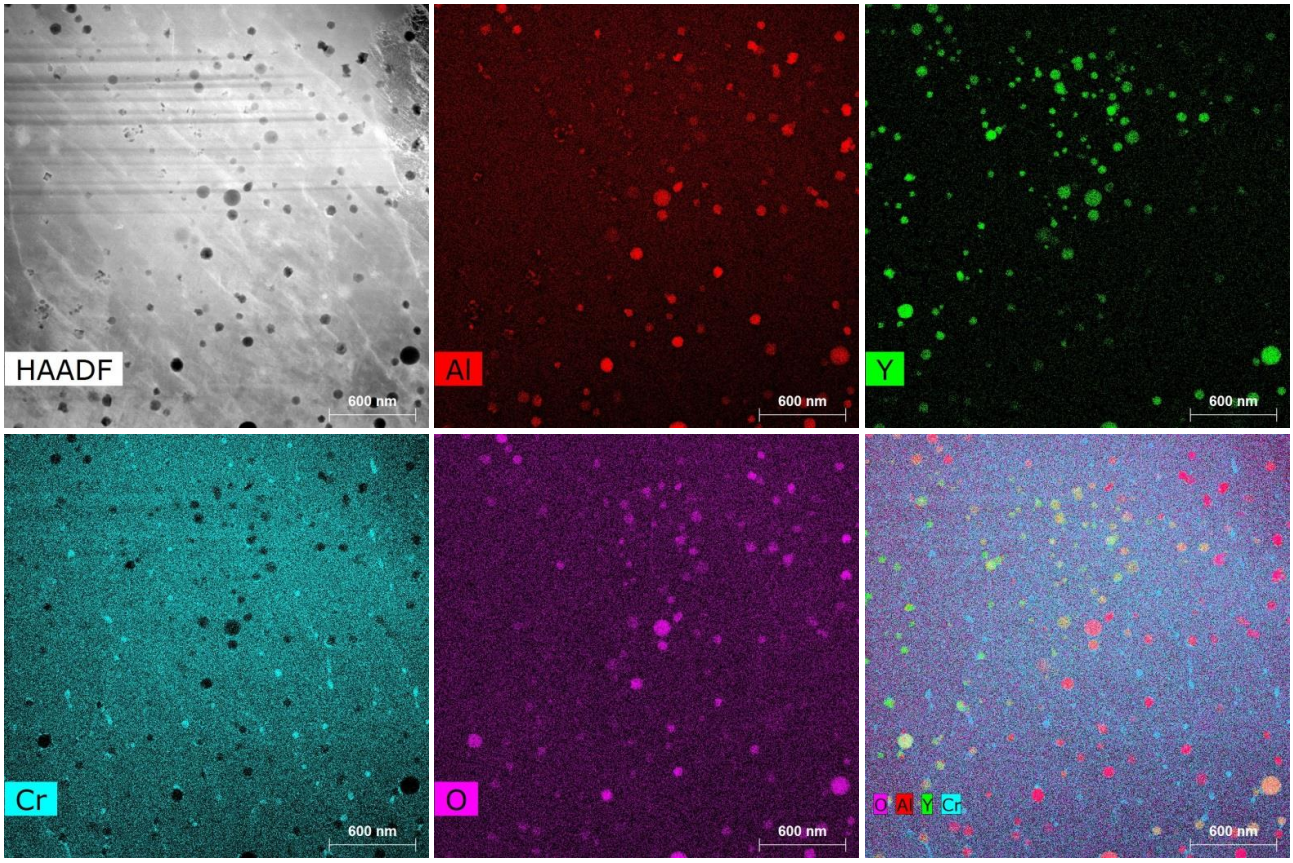

Figure 7: HAADF-STEM image and element maps acquired from Area 2 in Figure 4, in a depth of 6-9µm.

In the area close to the T91 matrix, Area 3 in Figure 4, faceted shapes precipitates enriched with Al are in a large proportion. Elongated Cr precipitates appeared again, mostly combined with the spherical ones. The precipitate structure looks rather similar to that in Area 1.

The depth dependence of the precipitate structure might be associated with the local cooling rate during the solidification of the coating layer in the GESA treatment. The regions close to either surface or the T91 matrix should be a higher cooling rate than the middle region. But, the mechanisms for forming such a structure are not clear.

In Figure 9 two images of the same area were obtained from two orientations in order to identify the exactly form of this type of precipitates. In image a) the shape appeared to be needles. After tilting about 20 degrees they appeared to be slabs as shown in image b). So, they should be thin plates.

No notable changes of the precipitates could be detected in the irradiated sample as compared to the unirradiated one. As shown in Figure 10, image a) is from Area 3 of the unirradiated sample (Figure 4), while image b) is from an area of the irradiated sample in a similar depth of 12-15µm from the surface. Although the precipitate structure in the two images looks different, it is not clear if this is due to irradiation, considering the inhomogeneity of the precipitate structure as depicted above. It is convinced that the precipitates are still in crystalline structure after irradiation. No amorphization of precipitates was detected.

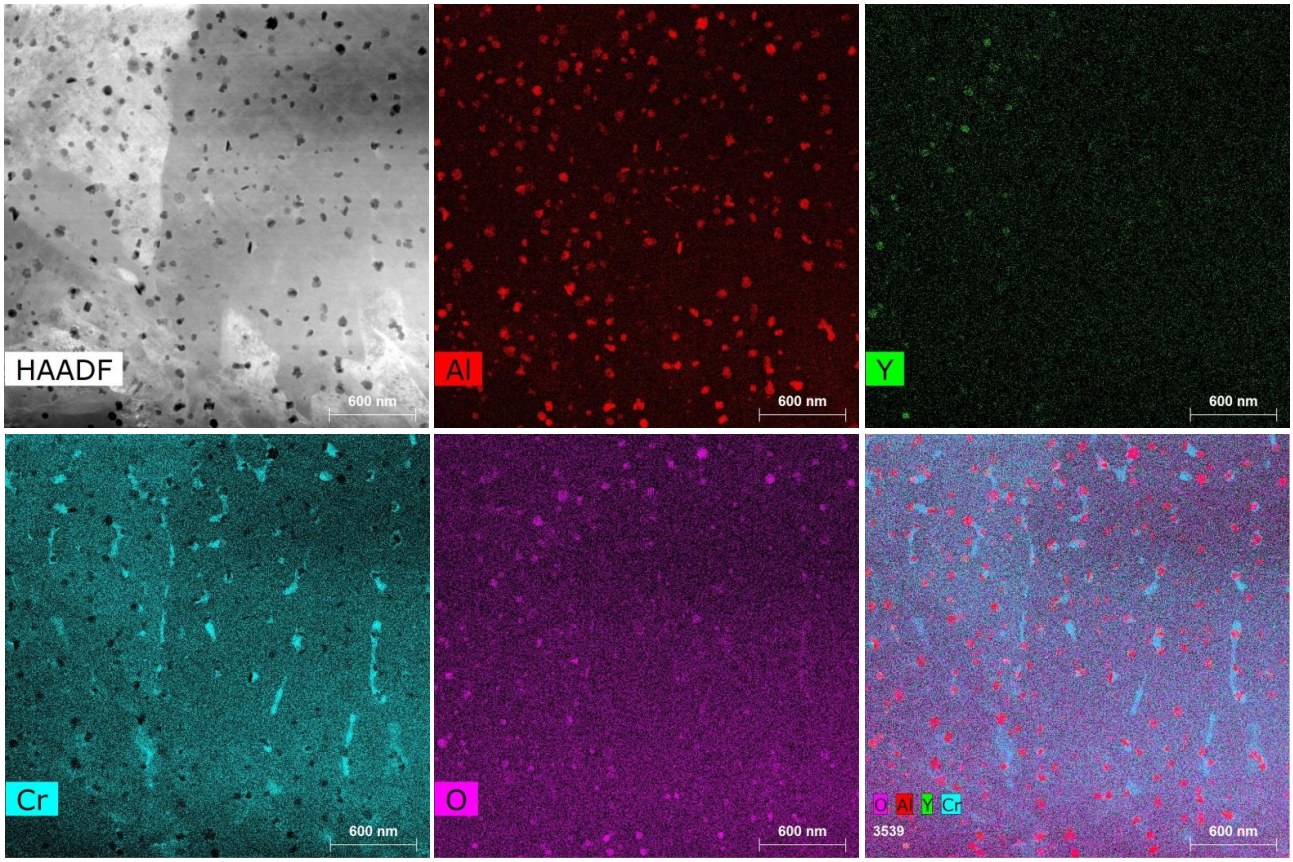

Figure 8: HAADF-STEM image and element maps acquired from Area 3 in Figure 4, in a depth of 17-20µm.

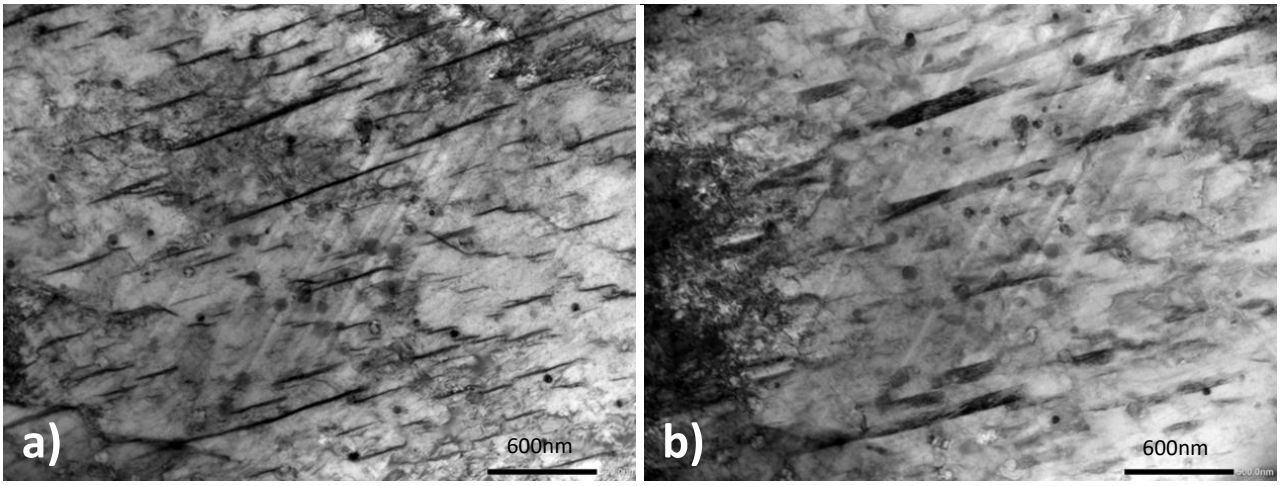

Figure 9: The shape of elongated Cr enriched precipitates viewed from two directions in the unirradiated sample.

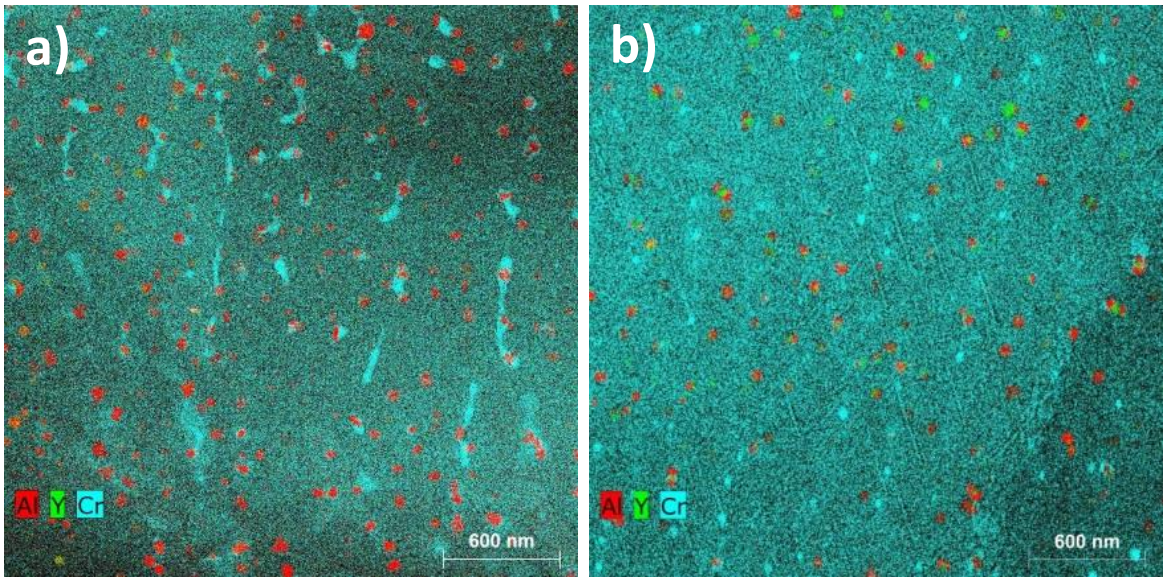

Figure 10: Image a) is from the unirradiated sample in a depth of 17-20 µm (Area 3 in Fugure 4); Image b) is from an area of the irradiated sample in a depth of 12-15 µm.

12.4 Conclusions

The microstructure of the FeCrAlY coating was investigated in conditions of unirradiated and after irradiation at 2.5 dpa at 300-400°C by using FIB lamella samples. The following conclusions can be drawn from the results.

- The main microstructural feature of the FeCrAlY coating is the precipitate structure.
- Precipitates were in different shapes and enriched with Al, Y, Cr and O.
- The shape and chemical composition of the precipitates change with the depth from the surface.
- The distribution of the precipitates is not homogenous in density in the coating layer.
- No convinced irradiation effects on the precipitate structure could be identified due to the inhomogeneity of the precipitate structure.

12.5 References

[1] Chapter 6 of "*Handbook on Lead-bismuth Eutectic Alloy and Lead Properties, Materials Compatibility, Thermal-hydraulics and Technologies"*, OECD 2007, NEA No. 6195, ISBN 978-92-64-99002-9.

[2] G. Müller, G. Schumacher, D. Strauss, *Oxide scale growth on MCrAlY coatings after pulsed electron beam treatment*, Surface and Coatings Technology 108-109 (1998) 43.

[3] A. Weisenburger, A. Heinzel, G. Müller, H. Muscher, A. Rousanov, *T91 cladding tubes with and without modified FeCrAlY coatings exposed in LBE at different flow, stress and temperature conditions* , J. Nucl. Mater. 376 (2008) 274.

[4] The webpage of the VELLA project: http://192.107.58.30/index.html.

[5] T. Kirchner, Y. Bortoli, A. Cadiou, Y. Foucher, J.S. Stuzmann, T. Auger, Y. Dai, S. Dementjev, K. Geissmann, H. Glasbrenner, F. Groeschel, F. Heinrich, K. Kohlik, G. von Holzen, Ch. Perret and D. Viol, *LiSoR, a liquid metal loop for material investigation under irradiation*, J. Nucl. Mater. 318 (2003) 70.

[6] Y. Dai, V. Boutellier, D. Gavillet, H. Glasbrenner, A. Weisenburger, W. Wagner, *FeCrAlY and TiN coatings on T91 steel after irradiation with 72 MeV protons in flowing LBE*, Journal of Nuclear Materials 431 (2012) 66–76.

[7] H. Glasbrenner, Y. Dai, F. Groeschel, *LiSoR irradiation experiments and preliminary post-irradiation examinations,* J. Nucl. Mater. 343 (2005) 267.

13 Summary

The above collected information describes the work of several partners in Task 5.2 of the MATISSE project and within the SAFE_COAT pilot project of EERA-JPNM. KTH and KIT further developed the composition of FeCrAl+RE alloys to optimize their behaviour in Pb-alloys aiming a corrosion resistant material for the temperature range Pb-alloy cooled nuclear reactors require. While KTH target bulk FeCrAl-RE alloys that require specific attention on formation of brittle sigma phases (Cr-content needs to be around 10wt%), the KIT approach to use an corrosion optimized FeCrAl+RE composition as base for surface alloying allows a wider range of compositions. Both explored the optimum composition that allows the formation of protective Al-rich oxide scales in Pb-alloys between 400 and 600°C at least. Avoiding the formation of Cr-carbides by controlling the C content and the ration between RE like Ti and Zr e.g. and C is on of the key issues for the formation of protective Al-rich scales. 10wt% Cr and 4 wt% Al, given that the RE and C concentrations are strictly controlled and optimized are the values to be respected. These results show that it is feasible to design ductile alumina-forming FeCrAl alloys as construction materials in corrosive environments at temperatures as low as 450°C. For Fe-Cr-Al-based alloys and modified surface layers exposed to molten lead with 10^{-6} wt.% oxygen in the 400-600°C temperature range an experimental criterion was defined concerning the aluminium and chromium content necessary to form a highly protective Al_2O_3 layer. It was found that higher Cr content leads to alumina formation at lower Al concentration. Outside this alumina stability domain, a concentration of 4 wt.% Al is sufficient, in synergy with 16 wt.% Cr content, to reduce drastically the growth rate of $Fe(Cr,Al)_2O_4$ sub-layer with spinel structure, on Fe-Cr-Al alloys exposed to oxygen-containing molten lead.

Two FeCrAl bulk tensile specimens were tested in PbBi and at both the fracture was fully ductile. That means that the potential problem with sigma formation was avoided. Beside ductile dimples, there were plate-like features that were connected with the specific fracture along the hot rolling direction. The surface of the specimens, where no cracks were detected, showed initiation of degradation, which might be due to the very low oxygen content that does not foster the formation of protective Al-rich oxide sales. Further tests especially with more material are required to address all open points in that development.

AlTiN coatings on T91 were tested in PbBi under harsh tensile load conditions (up to 550MPa) and exhibit almost no delamination. However, all the coatings cracked and the cracks usually stopped at the coating bulk interface. Only in notched areas crack formation in the bulk T91 was observed. The extreme high loads applied and the testing procedure does not allow to conclude on the allowable stress respectively strain until the coating starts cracking. Less severe stress levels or alternative testing procedure are required to explore the coatings further. Anyhow the non-delamination is a very promising results for such applied coatings.

The Detonation Gun process was investigated and optimized to coat 316 stainless steel plates and small tensile specimens. Especially the coating of small scaled substrates and the application of relatively thin (some tens of µm tick only) coatings was one of the major efforts and results of this exercise. Such coated specimens of 316L were loaded in air and PbBi at 550°C and showed that the coating was resistant. No delamination occurred, nor penetration of PbBi was observed, which both clearly shows the potential of this coating technology that requires further investigations.

The tensile tests of the 316L surface alloyed specimens showed in pre- and post investigation the missing of Al in the surface region. Knowing that at least 4wt% Al is required for protective scale formation, the results obtained in the tensile tests reflect the behaviour of uncoated 316L. Tests with proper surface alloyed steels having the required Al-content are required for meaningful and successful tensile test in liquid PbBi.

Slow strain tensile tests of surface alloyed T91 performed at RATEN clearly show the benefit of surface alloying. At the just coated side exfoliation at large strains is observed while the surface alloyed layer do not show such inappropriate behaviour. Slow strain tensile tests of 316l with an Al2O3 coating deposited by a detonation gun (ENEA) exhibit fully ductile behaviour of the bulk 316L while the coating did not show any delamination during the test.

Detailed TEM post investigations of surface alloyed FeCrAl coatings on T91 that were irradiated in contact with PbBi at 300°C with 72MeV protons to a dose of 2.5dpa were performed. Different precipitates (Al, Y, oxygen rich and Cr rich) were found throughout the surface alloyed layer varying in size, morphology and composition. This variation is attributed to the different cooling rates achieved at the surface alloying process. The hardening observed due to the

irradiation can not be attributed to this precipitates, but is expected to originate like for other ferritic materials in the defect structure of such materials. Fe irradiation done at HZDR at 300 and 450 °C and significant hardening is observed for all alloys at 300°C and 450°C. The combined effects of the Al mediated shift of the Cr solubility limit and potentially Cr content dependent partial suppressing of α'-phase precipitation by the implanted ions are considered as the main reasons for the variation of hardening observed for the different alloys. A significant contribution of impurity clusters to the observed hardening is expected.

Alumina forming alloys and surface layers and insoluble coatings are promising corrosion mitigation methods that showed their potential in this research. However, aspects like stress tolerance, delamination, irradiation stability are issues that require further attention. The investigations in this work are starting points that need to be continued to understand in detail the potential benefits and continue from such knowledge the optimization and the required scale up. Additional topics to be addressed are reliability, reproducibility and optimization that finally must end in a kind of standardization.